



AVISON (Analýza viditelnosti účastníků silničního provozu za účelem zvýšení jejich bezpečnosti za soumraku a v noci)

je projektem soutěže VI - Bezpečnostní výzkum České republiky 2015-2022 (2015 - 2022) vyhlášeného MVO - Ministerstvem vnitra (MV) s identifikačním číslem **VI20172019071** řešeným v období: 01.01.2017-31.12.2019. Jeho hlavní příjemcem je Vysoká škola báňská - Technická univerzita Ostrava / Fakulta elektrotechniky a informatiky, dalším účastníkem projektu je Centrum dopravního výzkumu, v. v. i. v roli dalšího účastníka projektu.



V Příloze č. 1 Smlouvy – Projekt, v části 5. 4. Vedlejší výsledky projektu:

DEFINICE DRUHŮ VÝSLEDKŮ

(Metodiky hodnocení výzkumných organizací a programů účelové podpory výzkumu, vývoje a inovací schválené usnesením vlády dne 8. února 2017 č. 107)

D - stať ve sborníku

Obsah:

- 1) VITASEK, J., J. JARGUS, S. HEJDUK, T. STRATIL, J. LATAL a V. VASINEK. Phosphor decay measurement and its influence on communication properties. In: 2017 19th International Conference on Transparent Optical Networks (ICTON). Girona: IEEE, 2017, s. 1-4. ISBN 978-1-5386-0859-3. DOI: 10.1109/ICTON.2017.8024951.
- 2) VITASEK, J., J. LATAL, T. STRATIL, S. HEJDUK, A. VANDERKA a L. HAJEK. Position of light sources for VLC. In: 2017 19th International Conference on Transparent Optical Networks (ICTON). Girona: IEEE, 2017, s. 1-4. ISBN 978-1-5386-0859-3. DOI: 10.1109/ICTON.2017.8024793.
- 3) KOLAR, J., LATAL, J., DHAR, A., PAUL, M.C., WILCEK, Z. Implementation of a thermally loaded EDFA amplifier into a WDM-PON optical network. In: 2017 19th International Conference on Transparent Optical Networks (ICTON). Girona: IEEE, 2017, s. 1-4. ISBN 978-1-5386-0859-3. DOI: 10.1109/ICTON.2017.8024952.
- 4) LATAL, J., VITASEK, J., HAJEK, L., VANDERKA, A., MARTINEK, R., VASINEK, V. Measurement of changes of polarization of optical beam affected by atmospheric effects. In: 2017 19th International Conference on Transparent Optical Networks (ICTON). Girona: IEEE, 2017, s. 1-4. ISBN 978-1-5386-0859-3. DOI: 10.1109/ICTON.2017.8024761.
- 5) BECAK, P., NOVAK, T., BALEJA, R. and SOKANSKY, K., Testing of the software goniophotometer in Wils - Building design computational programme, In: 2018 19th International Scientific Conference on Electric Power Engineering, EPE 2018 - Proceedings 2018, s. 1-5., ISBN: 978-153864611-3, DOI: 10.1109/EPE.2018.8395994.
- 6) BOS, P., BALEJA, R., SOKANSKY, K. and NOVAK, T., CCTV systems that work with the security lighting, In: 2018 19th International Scientific Conference on Electric Power Engineering, EPE 2018 - Proceedings 2018, s. 1-4., ISBN: 978-153864611-3, DOI: 10.1109/EPE.2018.8396020.
- 7) LATAL, J., WILCEK, Z., KOLAR, J. and J. VOJTECH. Measurement of IPTV Qualitative Parameters on EPON/VDSL2 Topology. In: 2018 International Conference on Broadband Communications for Next Generation Networks and Multimedia Applications, CoBCom 2018. Graz: IEEE, 2018, pp. 1-7. ISBN 978-1-5386-4157-6. DOI: 10.1109/COBCOM.2018.8443981.
- 8) LATAL, J., VITASEK, J., BOJKO, M., SKRINSKY, J., STRATIL, T., WILCEK, Z. and J. KOLAR. Simulation and Measurement of Atmospheric Effect on Optical Beam. In: 2018 20th International Conference on Transparent Optical Networks (ICTON). Bucharest: IEEE, 2018, pp. 1-8. ISBN 978-1-5386-6605-0. DOI: 10.1109/ICTON.2018.8473649.
- 9) LATAL, J., WILCEK, Z., KOLAR, J. and J. VOJTECH. Measurement of IPTV Services on a Hybrid Access Network. In: 2018 20th International Conference on Transparent Optical Networks (ICTON). Bucharest: IEEE, 2018, pp. 1-7. ISBN 978-1-5386-6605-0. DOI: 10.1109/ICTON.2018.8473724.
- 10) VITASEK, J., J. JARGUS, J. LATAL, T. STRATIL and Z. WILCEK. Illumination and Communication Characteristics of YAG: Ce Phosphor Powders. In: 2018 20th International Conference on Transparent Optical Networks (ICTON). Bucharest: IEEE, 2018, 2018, pp. 1-4. ISBN 978-1-5386-6605-0. DOI: 10.1109/ICTON.2018.8473800.

- 11) VITASEK, J., J. LATAL, T. STRATIL, J. JARGUS and Z. WILCEK. Fog Influence Simulation on Light Distribution from Street Lighting. In: 2018 20th International Conference on Transparent Optical Networks (ICTON). Bucharest: IEEE, 2018, pp. 1-4. ISBN 978-1-5386-6605-0. DOI: 10.1109/ICTON.2018.8473859.
- 12) VALICEK, P., NOVAK, T., BESEDA, J. and SOKANSKY, K., Modelling the Behavior of Lighting Systems Controlled at a Constant Level of Illuminance, 7th Lighting Conference of the Visegrad Countries, LUMEN V4 2018 - Proceedings 2018. ISBN: 978-153867923-4. DOI: 10.1109/LUMENV.2018.8520993.
- 13) BECAK, P., NOVAK, T., BALEJA, R. and SOKANSKY, K., Radiation of the Luminous Flux into the Upper Half-Space in Wils - Building Design, In: 7th Lighting Conference of the Visegrad Countries, LUMEN V4 2018 - Proceedings 2018, ISBN: 978-153867923-4, DOI: 10.1109/LUMENV.2018.8521116.
- 14) BALEJA, R., NOVAK, T., SOKANSKY, K., BOS, P. and BECAK, P., Measurement of Outdoor Lighting with a Focus on Watchdog Lighting System in the Area of Electric Station TR Čechy Střcd, In: 7th Lighting Conference of the Visegrad Countries, LUMEN V4 2018 - Proceedings 2018., ISBN: 978-153867923-4, DOI: 10.1109/LUMENV.2018.8521145.
- 15) DOLEJSI, O., BALEJA, R., BECAK, P., NOVAK, T., SOKANSKY, K., A comparison of light sources technologies of vehicles headlights illuminating a model road, *Proceedings of the 2019 20th International Scientific Conference on Electric Power Engineering, EPE 2019*, ISBN: 978-172811333-3, DOI: 10.1109/EPE.2019.8778112.
- 16) BECAK, P., WLOSOKOVA, J., PICHA, J., NOVAK, T., SOKANSKY, K., Modeling of luminous flux radiation to the upper hemisphere from real model of town, *Proceedings of the 2019 20th International Scientific Conference on Electric Power Engineering, EPE 2019*, ISBN: 978-172811333-3, DOI: 10.1109/EPE.2019.8778190.
- 17) VITASEK, J., T. STRATIL, Z. WILCEK, J. KOLAR a M. HUB. Comparison of Properties of White LED and Blue LED with External Phosphor Layer. In: *2019 21st International Conference on Transparent Optical Networks (ICTON)*. Angers: IEEE, 2019, pp. 1-4. ISBN: 978-172812779-8. DOI: 10.1109/ICTON.2019.8840376.
- 18) LATAL, J., J. VITASEK, M. BOJKO, L. HAJEK, Z. WILCEK, J. KOLAR, T. STRATIL A F. ŠARLEJ, "Measurement of Influence of Total Rainfall on Modulated Optical Beam in Laboratory FSO System," *2019 21st International Conference on Transparent Optical Networks (ICTON)*, Angers, France, 2019, pp. 1-5. ISBN: 978-172812779-8. DOI: 10.1109/ICTON.2019.8840436.
- 19) VITASEK, J., T. STRATIL, Z. WILCEK, J. KOLAR a M. HUB. Adjustment of Radiation Pattern of Street Luminaire. In: 2019 21st International Conference on Transparent Optical Networks (ICTON). Angers: IEEE, 2019, pp. 1-4. ISBN: 978-172812779-8. DOI: 10.1109/ICTON.2019.8840475M. .
- 20) J. LATAL, Z. WILCEK, J. KOLAR, F. SARLEJ A R. MARTINEK. Effect of Carbon Dioxide on SDR-Based Modulated Optical Beams for Free Space Optical Link. *International Symposium on Advanced Electrical and Communication Technologies ISAECT2019*. pp. 1-6. (bude publikováno).

- 21) R. MARTINEK, L. DANYS, R. JAROS, D. MOZNY, P. SISKÁ a J. LATAL. VLC channel equalization simulator based on LMS algorithm and virtual instrumentation. *International Symposium on Advanced Electrical and Communication Technologies ISAECT2019*. pp. 1-6. (bude publikováno).

Phosphor Decay Measurement and its Influence on Communication Properties

Jan Vitasek, Jan Jargus, Stanislav Hejduk, Tomas Stratil, Jan Latal, and Vladimir Vasinek

Department of Telecommunications, Faculty of Electrical Engineering and Computer Science,
VSB–Technical University of Ostrava, 17. listopadu 15, 708 33 Ostrava, Czech Republic

Tel: 00420 596 999 413, Fax: +420 596 991 650, e-mail: jan.vitasek@vsb.cz

ABSTRACT

The communication properties of the white Light Emitting Diodes (LED) above all depend on a phosphor decay. This article describes the measurement of rise and fall times of white light created by the blue LED and the YAG:Ce phosphors. Measured rise and fall times are compared to rise and fall time of the blue LED. We tested four kinds of phosphors which are able to create a white light. The phosphors were mixed in Poly-Di-Methyl-Siloxane (PDMS) polymer in the same concentration 1:35.

Keywords: communication, fall time, phosphor decay, rise time, white light, YAG.

1. INTRODUCTION

The illuminating engineering deals more and more with the white LEDs [1-2] which gradually replace the classical illumination sources (light bulbs and fluorescent lamps). Today there are readily available light bulbs with standard shape including white LEDs; the same is true for fluorescent lamps. The streetlights also have the white LEDs. The LEDs, not only white, are also used in automotive for Car-to-Car (C2C) communication. It is obviously that the usage of LEDs is very wide. Therefore there is an idea about adding another function; the LEDs could also provide the communication together with illumination, in comparison to classical illumination sources.

There are two ways how to create the white light in the LED. The first is using of blue, red and green LED. If the intensity levels of individual colour LEDs are set correct, the final light is white. This method is called colour mixing [3]. The other way is using of a wavelength converter. The converter converts the wavelength of the exciting light to the other wavelength [4-6]. In the white LEDs the yellow cerium-doped phosphor YAG:Ce (Yttrium Aluminium Garnet $Y_3Al_5O_{12}$) and blue light emitting source are used. A part of the blue light is converted in phosphor to the yellow light, the converted part together with the original blue part create the white light [7-9].

The general problem of phosphor as the wavelength converter is time delay [10]. After switching off of the exciting blue source the phosphor still emits the light relatively short time. This effect is absolutely irrelevant if the white LEDs are using for illumination, which is in the majority of cases. The phosphor delay has an influence, whether we want to send data (communicate) via the LEDs. The communication in terms of light is based on fast switching of light source (LED or laser diode). Generally, faster switching means faster bit rate and higher amount of transferred data. However, the phosphor decay extends the time of switching off of the light source, which limits the available bit rate.

At first glance it might seem that the phosphor influences only time of the decay, it means it extends the fall time. Nevertheless, the measurement showed that it also happen the extension of the rise time. The blue light is converted to yellow, therefore its amount decreases and the maximal intensity comes later together with the yellow light which the phosphor created. The creation of the yellow light takes also some time.

2. CREATION OF SAMPLES

This article compares four different phosphors. These phosphors are labelled QMK58/F-U1, QMK58/F-U2, QMK58/N-U6 and QUMK58/F-D1 [11]. The chemical composition of phosphors and median particle sizes are shown in Table 1. The provider is the company Phosphor Technology. These phosphors have working labels U1, U2, U6 and D1. These phosphors were mixed in Poly-Di-Methyl-Siloxane (PDMS) polymer.

Table 1. Rise times.

Phosphor	Chemical composition	Median particle sizes (μm)
QMK58/F-U1	$Y_3Al_5O_{12}$:Ce	4.0
QMK58/F-U2	$Y_3Al_5O_{12}$:Ce	3.5
QMK58/N-U6	$Y_3Al_5O_{12}$:Ce	11.0
QUMK58/F-D1	$(Y,Gd)_3Al_5O_{12}$:Ce	4.0

2.1 Poly-Di-Methyl-Siloxane

The used Poly-Di-Methyl-Siloxane (PDMS) names Sylgard 184 [12]. It is readily available product. The Sylgard 184 has two components, a PDMS base and a curing agent. Both these components are mechanically mixed in weight ratio 10:1. During the mechanical mixing some bubbles can appear. The bubbles could be removed by cooling in a refrigerator or in ultrasonic bath or in both. The phosphor powder was added to the Sylgard 184 in weight ratio 1:35. The mixture PDMS base-curing agent-phosphor was put in the laboratory shaker for the uniform distribution of all components before the heat hardening. The heat hardening happens by temperature around 85°C, it takes 30 minutes.

2.2 PDMS+Phosphor in Reflector

We also solved the problem how to suitable connect the PDMS+phosphor with the blue LED. For this purpose we used a reflector [13] for power LEDs. At the output aperture of the reflector there were a 2 mm thin layer of PDMS+phosphor. The reflector with the thin layer was then put on the blue LED. The procedure of preparation was following. The mixture PDMS+phosphor was poured in the Petri dish and it created the uniform layer. After that the reflector was put in the dish. The output aperture (wider) of the reflector was superimposed bottom of Petri dish. The dish was then put in the furnace. After the heat hardening the excess edges were removed. We repeated this procedure with all phosphors.

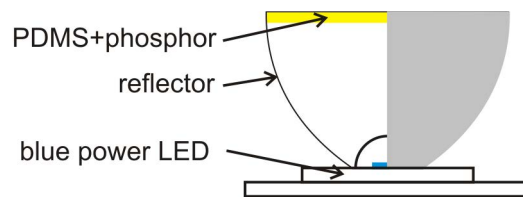


Figure 1. PDMS+phosphor in reflector.

3. ARRANGEMENT OF MEASUREMENT

We used the two blue power LEDs H2A1-H450 in the measurement. The two LEDs were used purposely because the measurement proceeded in parallel. The first LED has the reflector with PDMS+phosphor layer, the other LED has the empty reflector. Above the each LED there was placed the photodetector Thorlabs PDA36A-EC. Because we had two photodetectors their outputs were together connected to the two-channel oscilloscope Rohde Schwarz HMO1522. The LEDs were supplied by the forward current $I_f = 350$ mA from two-channel Programmable Power Supply Rohde Schwarz HM8143. The LEDs were switching on and off for detecting the rise and fall edges. For this purpose we used the Signal Generator Stanford Research Systems CG635. This signal generator was direct connected to the Programmable Power Supply. The frequency of the forward current was 1 Hz, which is enough for measurement of the rise and fall times. The oscilloscope can automatically detect the rise or fall edge of the signal with the stop running. The measured values were exported to the CVS files for further processing.

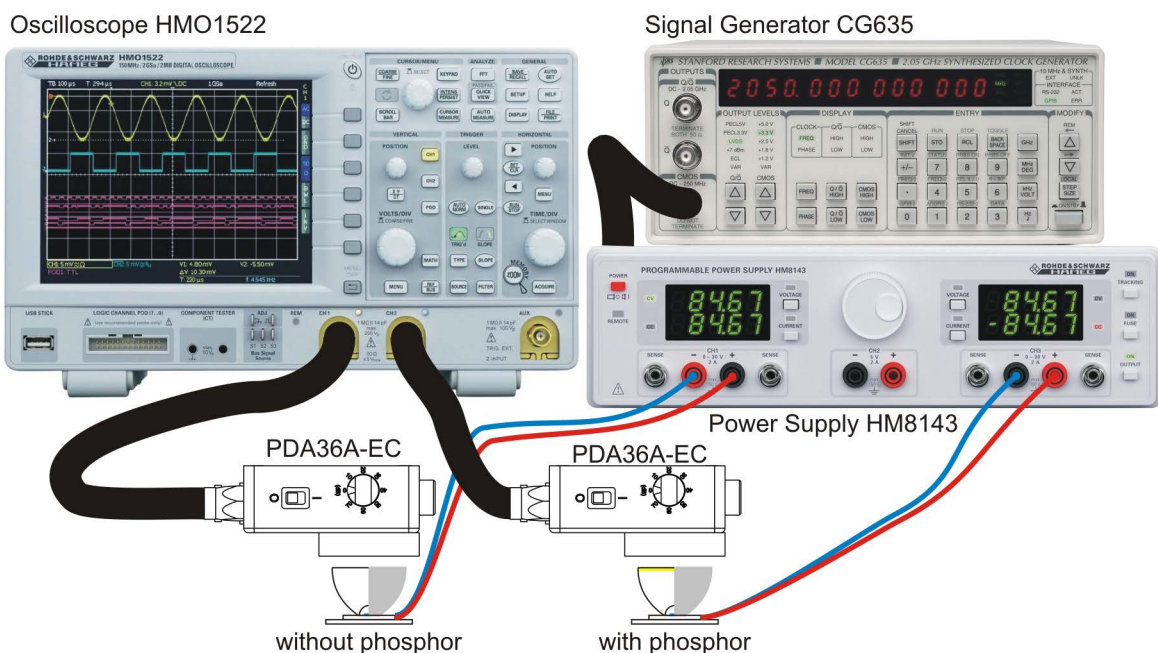


Figure 2. Arrangement of measurement.

4. RESULTS AND COMMENTS

At the beginning we had four prepared samples with phosphors U1, U2, U6 and D1. We measured the rise and fall times of the samples with different phosphors. The measured values are compared with rise and fall time of the blue LED. The phosphors caused the extension of rise and fall times. The measurement should show us, which phosphor has the shorter extension and if could be used for communication with white light.

Figure 3 shows the rise and fall edges measured with the phosphor U2.

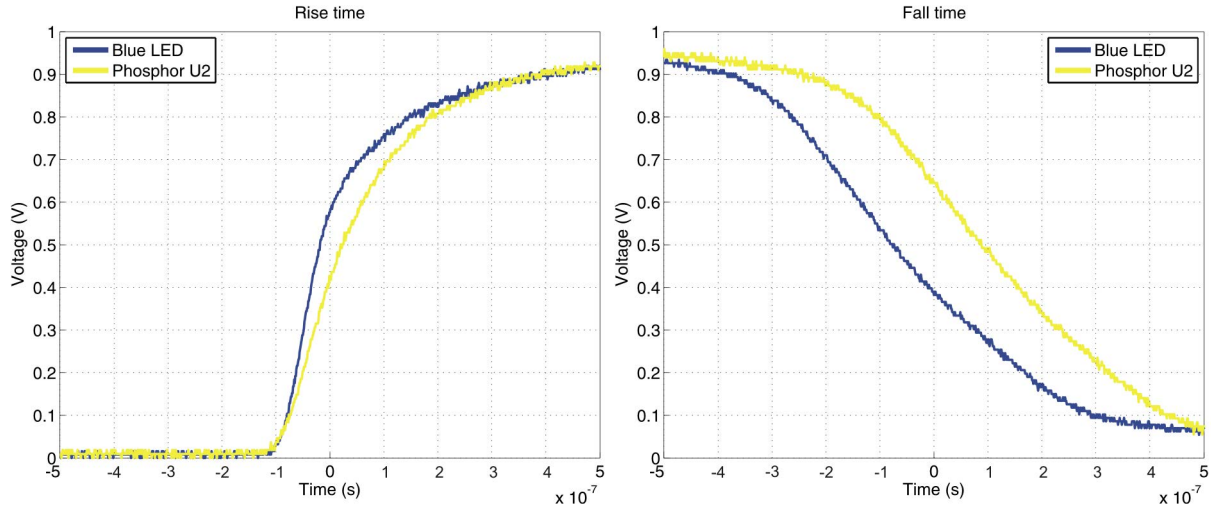


Figure 3. Rise and fall edges of phosphor U2 compared to LED.

The presence of phosphor has a negative influence on communication properties of the white light created by the phosphor layer. Table 2 shows the measured rise times. The rise time of the blue LED was $1.37 \cdot 10^{-7}$ s. For example, the rise time extended to $2.32 \cdot 10^{-7}$ s with the phosphor U1, the extension of the rise time caused by the phosphor is 95 ns, the rise time of the blue LED with phosphor U1 is almost 1.7 times. The extension of the fall time is 295 ns, which means 2.26 times longer time, see Table 3.

Table 2. Rise times.

	LED	U1	U2	U6	D1
rise time t_r (ns)	137	232	185	195	176
difference Δ (ns)	–	95	48	58	39
ratio R (-)	–	1.69	1.35	1.42	1.28

Table 3. Fall times.

	LED	U1	U2	U6	D1
fall time t_f (ns)	235	530	433	462	471
difference Δ (ns)	–	295	198	227	236
ratio R (-)	–	2.26	1.84	1.97	2.00

The difference Δ is calculated according to the relation:

$$\Delta = t_{r_U1} - t_{r_LED} \quad (1)$$

The ratio R is calculated according to the relation:

$$R = \frac{t_{r_U1}}{t_{r_LED}} \quad (2)$$

The theoretical bit rate of the blue LED should be

$$\text{bit rate} = \frac{1}{t_{r_LED} + t_{f_LED}} = \frac{1}{1.37 \cdot 10^{-7} + 2.35 \cdot 10^{-7}} = 2.7 \text{ Mb} \cdot \text{s}^{-1} \quad (3)$$

This value is low, if you add the phosphor to the blue LED, the bit rate decreases.

$$\text{bit rate} = \frac{1}{t_{r_U1} + t_{f_U1}} = \frac{1}{2.32 \cdot 10^{-7} + 5.30 \cdot 10^{-7}} = 1.3 \text{ Mb} \cdot \text{s}^{-1} \quad (4)$$

We compared four kinds of phosphors. The decay properties of phosphors are very similar. The shorter rise time has the phosphor D1, but the measured values of U2 and U6 are very similar. The shortest fall time has the phosphor U2, but it deals again the same, the measured values are very close.

5. CONCLUSIONS

This article dealt with the decay measurement of four different phosphors. It was similar phosphor thereof the results answer. We did not observe any expressive differences between rise times of phosphors, it could be only said that the phosphor U1 showed a little worse results. The same could be said about the fall times of the phosphors. All the four phosphors were mixed with PDMS in the same weight ratio 1:35. In the next step we want to test the influence of phosphor amount (concentration) on rise and fall times. Further we plan to measure the optical properties of the created white light (spectrum, Correlated Colour Temperature CCT, Colour Rendering Index R_a). The next possible step is to replace the blue LED by the blue laser diode and test the communication properties.

ACKNOWLEDGEMENTS

The authors would like to acknowledge the financial support of the Ministry of Education, Youth and Sports of the Czech Republic under Projects No. SP2017/79 and SP2017/97 of VSB–Technical University of Ostrava, Czech Republic. Our research was also supported by Projects No. VI20172019071, VI20152020008 and TA04021263. The work has been partially supported by Project No. CZ.1.07/2.3.00/20.0217.

REFERENCES

- [1] T. Novak, B. Socha, Z. Carbol, and K. Sokansky: Luminance evaluation of LED indoor luminaires for workspaces lighting, in *Proc. 13th International Scientific Conference Electric Power Engineering*, Brno, Czech Rep., May 2012.
- [2] R. Baleja, J. Sumpich, P. Bos, B. Helstynova, K. Sokansky, and T. Novak: Comparison of LED properties, compact fluorescent bulbs and bulbs in residential areas, in *Proc. 16th International Scientific Conference Electric Power Engineering*, Kouty nad Desnou, Czech Rep., doi: 10.1109/EPE.2015.7161181.
- [3] E. F. Schubert: *Light-Emitting Diodes*, Cambridge University Press, Cambridge, 2006.
- [4] L. Shirmane and V. Pankratov: Emerging blue-UV luminescence in cerium doped YAG nanocrystals, *Physica Status Solidi-Rapid Research Letters*, vol. 10, no. 6, pp. 475-479, Jun. 2016.
- [5] N. D. Q. Anh, T. H. Q. Minh, and N. H. K. Nhan: Enhancing lighting performance of white LED lamps by green emitting Ce,Tb phosphor, *Advances in Electrical and Electronic Engineering*, vol. 14, no. 5, pp. 609-614, Dec. 2016.
- [6] M. Skruodiene, M. Misevicius, M. Sakalauskaite, A. Katelnikovas, and R. Skaudzius: Doping effect of Tb³⁺ ions on luminescence properties of Y₃Al₅O₁₂:Cr³⁺ phosphor, *Journal of Luminescence*, vol. 179, pp. 355-360, Nov. 2016.
- [7] A. Dhar, A. Pal, S. Das, and R. Sen: Tm-Yb doped optical fiber performance with variation of host-glass composition, *Advances in Electrical and Electronic Engineering*, vol. 12, no. 6, pp. 582-589, Dec. 2014.
- [8] S. Mishra, D. S. Kshatri, A. Khare, and S. Tiwari: Nanocrystalline SrS:Ce³⁺ system for the generation of white light-emitting diodes, *Luminescence*, vol. 31, no. 8, pp. 1427-1432, Dec. 2016.
- [9] T. H. Q. Minh, N. H. K. Nhan, T. P. Vo, and N. D. Q. Anh: Enhancement of color rendering index for white light LED lamps by red Y₂O₃:Eu³⁺ phosphor, *Advances in Electrical and Electronic Engineering*, vol. 14, no. 3, pp. 340-344, Sep. 2016.
- [10] M. Rejman, V. Babin, R. Kucerkova, and M. Nikl: Temperature dependence of CIE-x,y color coordinates in YAG:Ce single crystal phosphor, *Journal of Luminescence*, vol. 187, pp. 20-25, Jul. 2017.
- [11] LED Phosphors, *Phosphor Technology* [online], <http://www.phosphor-technology.com/led-phosphors/>.
- [12] Sylgard 184 Silicone Elastomer Kit, *Dow Corning* [online], available at: <http://www.dowcorning.com/applications/search/default.aspx?R=131EN>.
- [13] Power LED reflectors, *Roithner LaserTechnik* [online], http://www.roithner-laser.com/datasheets/led_optics/clp17cr_clp20cr.pdf.

Position of Light Sources for VLC

Jan Vitasek, Jan Latal, Tomas Stratil, Stanislav Hejduk, Ales Vanderka, and Lukas Hajek

*Department of Telecommunications, Faculty of Electrical Engineering and Computer Science,
VSB-Technical University of Ostrava, 17. listopadu 15, 708 33 Ostrava, Czech Republic*

Tel: 00420 596 999 413, Fax: +420 596 991 650, e-mail: jan.vitasek@vsb.cz

ABSTRACT

White LED diodes are increasingly used. Thanks their features they are also used for illumination and gradually replace the classical light bulbs and fluorescent tubes. The one of advantages of white LED diodes is their availability for the Visible Light Communication. This article deals with study of suitable placing of light sources for indoor. The aim is a uniform light distribution and thereby a uniform distribution of VLC data signals. There were created light sources with LED diodes in software LightTools. These light sources were placed on the ceiling of room. The simulation found the positions of light sources in which the light distribution was the most uniform.

Keywords: LED, light distribution, LightTools, room, VLC.

1. INTRODUCTION

The illumination is an integral part of the present time. The light bulbs and fluorescent tubes are mainly used for the illumination. Except these classical illumination sources there also exist the light sources with Light Emitting Diodes (LED). The LEDs have several advantages in comparison with the classical incandescent and fluorescent light sources for illumination, the LEDs reach much higher efficiency and their further improvements are expected. The other advantages of the LEDs are their longer lifetime, higher tolerance to humidity, a smaller and compact size, minimum heat generation compared with the classical illumination sources, and lower power consumption. The LEDs are more ecological because they are mercury free [1]-[7].

With regard to using of current infrastructure and achieving of compatibility the LEDs are mounted in constructions with the identical shape which have the classical light bulbs and fluorescent tubes. It is obviously from the above described advantages that the LEDs are more and more used in practice. We can buy today the LED light bulb with the classical shape, thread and size [8]. The same also deals for the LED tubes [9]. These new LED illumination sources with the addition of a few relatively simple and cheap front end components could be directly installed and used.

The further advantage of the LED illumination sources is a possibility to provide the communication [1], [4]. In comparison to the classical illumination sources, the LED sources could be switched on and off relatively fast, which is the base of the communication. The LED sources are so able to provide the illumination and communication at the same time. This area is called Visible Light Communication (VLC). The VLC has a potential to provide the data and also illumination for indoor [10]. The VLC should replace the Wi-Fi in the future. The VLC has several advantages against the Wi-Fi. The visible light has 10 000 times greater spectrum than radio waves (Radio waves correspond to a frequency band of 3 kHz to 300 GHz, while the VLC correspond to a frequency band of 400 THz to 780 THz). The potential communication bandwidth of VLC is 400 THz, which is incomparably wider than the conventional RF bandwidth [10]. The VLC is safe and does not cause any interference with RF signals [11]. Thus this technology is perfectly suitable for communication in hospitals, power plants etc. [12]. The VLC is more secure. The RF waves pass through walls therefore are susceptible to snooping. Since light is confined to an area surrounded by opaque boundaries, there can be well defined coverage zones with enhanced security for VLC. The LEDs are energy efficient and highly controllable light sources, allowing them to be part of a Green technology. The LEDs roughly use one twentieth the amount of energy of a classical illumination source.

The VLC to be as efficient as possible it is also important to deal with a suitable distribution of light sources on the ceiling [5]. The uniform distribution of optical intensity in defined area is important for the mobility of users. The uniform optical intensity distribution does not put so demands on detectors of optical signal and the communication is more effective. The Signal to Noise Ratio (SNR) will be uniform therefore the bit rate and error rate will be also uniform.

2. ARRANGEMENT OF SIMULATIONS

At the beginning of this section it is necessary to say that we calculated the simulations which come from real grounds and the results would be usable in practice.

2.1 LightTools

The LightTools (LT) is a 3D optical engineering and design software product that supports virtual prototyping, simulation, optimization and photorealistic renderings of illumination applications. Its unique design and

analysis capabilities, combined with ease of use, support for rapid design iterations, and automatic system optimization, help to ensure the delivery of illumination designs according to specifications and schedule [13].

2.2 Dark Room

Our workplace disposes of the dark room with sizes $3.86 \times 2.46 \times 2.17$ m made from wood. This dark room is perfectly black-out against the ambient light, the photon counter received only seven photons per second. The identical room was also created in the LT software. The reflectance of walls was set to Lambertian scattering. The receiver plane was placed in height 80 cm above the floor, which is typical height of the table. The distance between the ceiling and the receiver plane is then 137 cm.

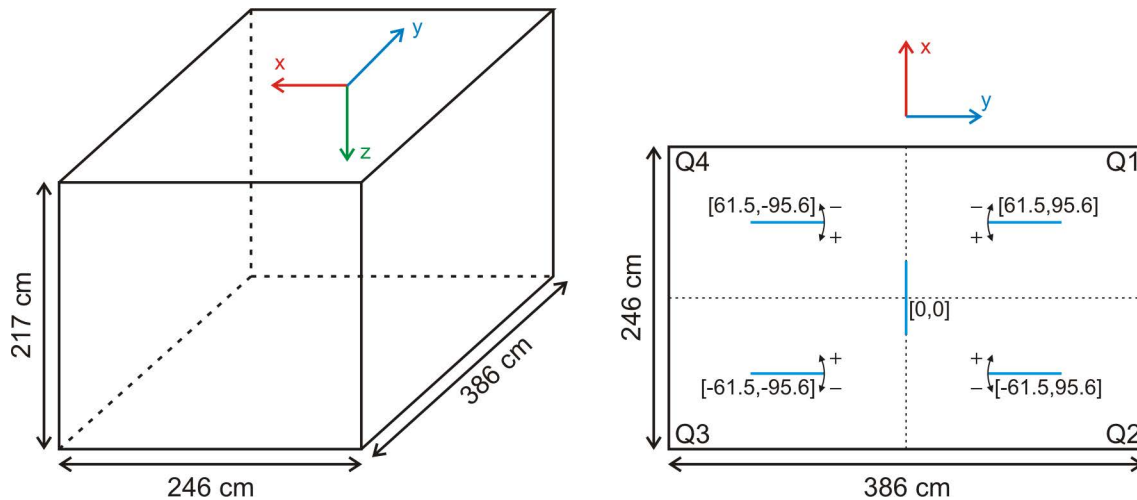


Figure 1. Dark room.

2.3 Light Sources

In the Introduction we mentioned two LED illumination sources, LED bulb [8] and LED tube [9]. These sources were modelled in LT software according to the real model. The LED bulb includes 10 SMD chips, each chip emits 47 lm and the total luminous flux is 470 lm. The colour temperature of the white light is 2700 K. The sizes are 97 mm length and 55 mm diameter. The LED tube is 600 mm long and the diameter of the tube is 26 mm. The LED tube has 44 SMD chips, each chip emits 18.18 lm and the total luminous flux is 800 lm. The colour temperature of the white light is 4000 K.

2.4 Position of Light Sources

The LED light sources were placed on the ceiling of the dark room. The ceiling was divided in four quadrants; the coordinate origin is in the centre of the ceiling, see Fig. 1.

The simulation calculated four variants in sum. The first variant contains 4 LED bulbs; each LED bulb is placed in the centre of each quadrant. The second variant has 5 LED bulbs, 4 LED bulbs are positioned in the centre of each quadrant, the fifth LED bulb is in the centre of the ceiling, in the coordinate origin. The third variant is the same as the first variant; the LED bulbs were replaced by the LED tubes. The last fourth variant has 5 LED tubes; the position is identical with the second variant, see Fig. 1. These variants describe the original positions before simulations.

2.5 Simulation

The LT software enables to make an optimization based on the required result. The required result is the most uniform distribution of the optical intensity on the receiver plane. It was set for the all variants that the shifts (distance) of the each LED source in the all quadrants were the same. In the variants with 5 LED sources, only the LED sources in quadrants could change their positions, the LED source in the coordinate origin was fixed. The LED tubes could change their position $[x,y]$ and also the rotation angle because their radiation pattern is asymmetric.

3. RESULTS AND COMMENTS

The Table 1 contains the final coordinates of LED sources after the optimization. Further we found the way how to compare the obtained results before and after optimization. At first, the LT software calculated the distribution of optical intensity before optimization, it means the original state. The receiver plane was divided in the grid 77×49 , which is 3773 values. The size of the mesh is 5×5 cm. Further we calculated the mean value of the optical intensity I_{avg} . Then we calculated the deviation Δ_n of each calculated optical intensity I_n from the mean value I_{avg} according to the equation (derived from the relative error):

$$\Delta_n = \left| \frac{I_n - I_{avg}}{I_{avg}} \right| \cdot 100 \tag{1}$$

These deviations Δ_n were then divided according to the value in intervals <0,5)%, <5,10)%, <10,15)%, <15,20)%. These divided values create a histogram.

Table 1. Coordinates after the optimization.

Coordinates	Before optimization	After optimization			
		4 LED bulbs	5 LED bulbs	4 LED tubes	5 LED tubes
x [cm]	61.5	64.32	70.36	64.51	70.72
y [cm]	96.5	94.61	109.46	94.42	110.50
angle [°]	0	–	–	6.7	-12.4

After that the optimization of position of LED illumination sources ran, the results are in Table 1. The LT software calculated the distribution of optical intensity after the optimization. The evaluation procedure was repeated. We calculated the mean value of the optical intensity I_{avg} after optimization. Further we calculated the deviations according to the Eq. (1). These deviations were divided in the same intervals.

The evaluation is following. The optimization should increase the account of deviations in interval <0,5)% and decrease the account in interval <15,20)%. The obtained results confirmed our presumptions.

Table 1 shows the improved positions of the LED sources for better distribution of optical intensity in receiver plane. We can see that new positions of 4 LED bulbs are very similar to the new positions of 4 LED tubes. The same we can say about 5 LED bulbs and 5 LED tubes. Moreover, the new positions of 4 LED sources differ little from the original positions. Figure 2 shows the improvement of distribution – it is more uniform. In the first variant 4 LED bulbs, the account of deviations increased in interval <0,5)%, the account of deviations decreased in <5,10)%, the account of deviations even slightly increased in interval <10,15)%. The deviations in interval <15,20)% almost disappeared. The similar results were obtained in variant 4 LED tubes. The optimization was very successful in variants 5 LED bulbs and 5 LED tubes. The improvement is expressive. The accounts of deviations are shown in Table 2.

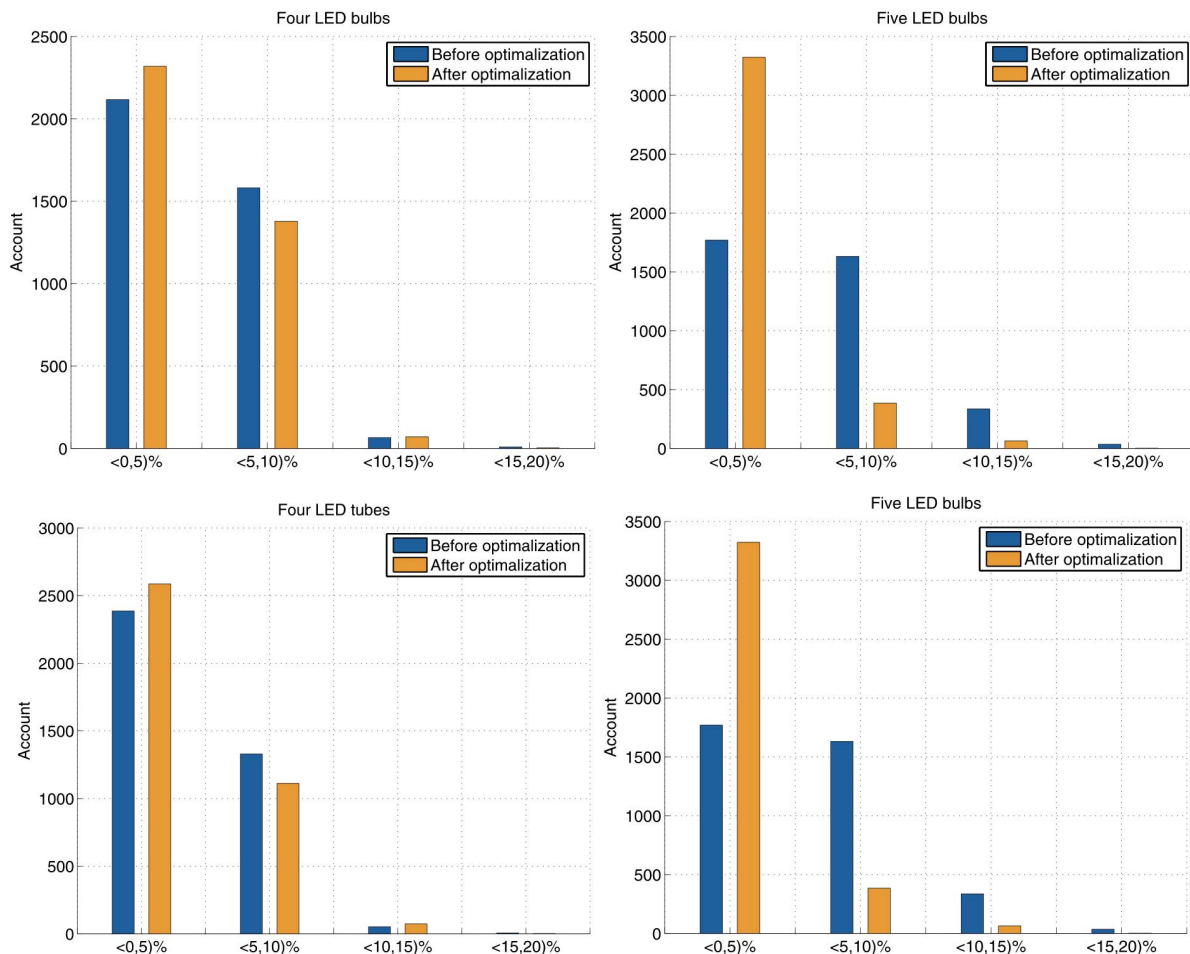


Figure 2. Histograms of results.

Table 2. Account of deviations.

interval	4 LED bulbs		5 LED bulbs		4 LED tubes		5 LED tubes	
	before	after	before	after	before	after	before	after
<0,5)%	2117	2319	1770	3323	2386	2586	1794	3436
<5,10)%	1581	1379	1631	385	1329	1112	1565	269
<10,15)%	66	71	337	63	52	73	363	64
<15,20)%	9	4	35	2	6	2	51	4

4. CONCLUSIONS

This article dealt with the suitable position of the illumination sources on the ceiling for the most uniform distribution of optical intensity on the receiver plane. The uniform distribution enables a better mobility of users with regard to the data transmission. The simulation came from the real grounds. The results showed that it is very advanced to using of 5 LED illumination sources when 91% (LED tubes) and 88% (LED bulbs) of receiver plane was covered by the optical intensity with deviation $\pm 5\%$, which is very good result. We would like to continue with the simulation of optical intensity distribution in our real office room.

ACKNOWLEDGEMENTS

The authors would like to acknowledge the financial support of the Ministry of Education, Youth and Sports of the Czech Republic under Projects No. SP2017/79 and SP2017/97 of VSB–Technical University of Ostrava, Czech Republic. Our research was also supported by Projects No. VI20172019071, VI20152020008 and TA04021263. The work has been partially supported by Project No. CZ.1.07/2.3.00/20.0217.

REFERENCES

- [1] P. Chvojka, S. Zvanovec, P. A. Haigh, and Z. Ghassemlooy: Channel characteristics of visible light communications within dynamic indoor environment, *Journal of Lightwave Technology*, vol. 33, no. 9, pp. 1719-1725, May 2015.
- [2] S. Hejduk *et al.*: Simple and universal current modulator circuit for indoor mobile free-space-optical communications testing, *Advances in Electrical and Electronic Engineering*, vol. 12, no. 1, pp. 66-74, Mar. 2014.
- [3] T. Novak, B. Socha, Z. Carbol, and K. Sokansky: Luminance evaluation of LED indoor luminaires for workspaces lighting, in *Proc. 13th International Scientific Conference Electric Power Engineering*, Brno, Czech Rep., May 2012.
- [4] T. Zhang, S. Guo, H. Chen, F. Zhong, and C. Ma: Enhancing the bit error rate of indoor visible light communication systems using adaptive channel estimation algorithm, *IET Communications*, vol. 9, no. 4, pp. 501-507, Mar. 2015.
- [5] A. Liner *et al.*: Software design of SMD LEDs for homogeneous distribution of irradiation in the model of dark room, *Advances in Electrical and Electronic Engineering*, vol. 12, no. 6, pp. 622-630, Dec. 2014.
- [6] R. Baleja *et al.*: Comparison of LED properties, compact fluorescent bulbs and bulbs in residential areas, in *Proc. 16th International Scientific Conference Electric Power Engineering*, Kouty nad Desnou, Czech Rep., 2015.
- [7] J. Kubicek, I. Bryjova, J. Moravec, J. Stetinsky, and M. Penhaker: The evaluation of light conditions influence and corrections upon Doppler blood perfusion imaging, *Advances in Electrical and Electronic Engineering*, vol. 14, no. 4, pp. 421-428, Nov. 2016.
- [8] PARATHOM advanced CLASSIC A, *OSRAM* [online], <http://www.osram.com/>.
- [9] SubstiTUBE T8, *OSRAM* [online], <http://www.osram.com/>.
- [10] H. Parikh, J. Chokshi, N. Gala, and T. Biradar: Wirelessly transmitting a grayscale image using visible light, in *Proc. International Conference on Advances in Technology and Engineering (ICATE)*, Mumbai, India, 2013, pp. 1-6.
- [11] S. Zhao, J. Xu, and O. Trescases: A dimmable LED driver for visible light communication (VLC) based on LLC resonant DC-DC converter operating in burst mode, in *Proc. 28th Annual IEEE Applied Power Electronics Conference and Exposition (APEC)*, Long Beach, California, USA, 2013, pp. 2144-2150.
- [12] H. Ma, L. Lampe, and S. Hranilovic: Integration of indoor visible light and power line communication systems, in *Proc. 17th IEEE International Symposium on Power Line Communications and its Applications (ISPLC)*, Johannesburg, South Africa, 2013, pp. 291-296.
- [13] LightTools, *Synopsys* [online], <https://optics.synopsys.com/lighttools/>.

Implementation of a Thermally Loaded EDFA Amplifier into a WDM-PON Optical Network

Jakub Kolar, Jan Latal, Anirban Dhar*, Mukul Chandra Paul*, and Zdenek Wilcek

Department of Telecommunications, Faculty of Electrical Engineering and Computer Science, VSB-Technical University of Ostrava, 17. listopadu 15, 708 33 Ostrava, Czech Republic

** Fiber Optics & Photonics Division, CSIR-Central Glass & Ceramic Research Institute, 196 Raja S. C. Mullick Road, Jadavpur, Kolkata-700 032, West-Bengal, India*

Tel: +420 597 325 845, e-mails: jakub.kolar@vsb.cz, jan.latal@vsb.cz

ABSTRACT

With deployment and continuous development of optical routes, the issues concerning the thermal loading of erbium-doped optical fibres become more and more relevant. As we were able to see a significant expansion of optical communication systems in the recent years, it was also necessary to find ways for bridging longer distances between individual points of the optical route. Modern optical telecommunication routes mainly use the DWDM system and optical transmission in the C and L bands. For this purpose, optical amplifiers that are mainly based on erbium doping are used. The aim of this paper is to point out the issues associated with the implementation of erbium-doped amplifying fibres into optical transmission routes that are made using the WDM-PON technology, with regard to the thermal load of these amplifying fibres.

Keywords: WDM-PON, erbium, temperature, power level, Mc-Cumber equation.

1. INTRODUCTION

Nowadays, we can see ever-increasing demands on optical transmission networks. The increasing demands are not only for higher transmission speeds, but also for the vital network capabilities that will enable to bridge longer distances. When a signal travels through an optical fibre, it is gradually attenuated by the effects of various physical or external influences. For this reason, it is sensible to insert optical amplifiers into the transmission route. There are various kinds of optical amplifiers available and one of them is an EDFA amplifier. The EDFA amplifiers are very often used in optical routes, primarily due to their properties and the resulting gain. There is also continuous development and improvements in the area of EDFA amplifiers, especially with the doped fibres used in them.

However, typical problems in constructing routes are the losses, which are caused by the laying of an optical distribution network or by its poorly secured active elements. It is the importance of securing the active elements sufficiently, especially with regard to the changes of climatic conditions, that can play the essential role in the correct functionality of the entire system. The active components are usually installed in telecommunication nodes, which have sufficient temperature stabilization provided by conditioning units with additional backup power supplies. The same is true for the installation of optical amplifiers, which are mostly implemented in the same place with the active elements, provided that they serve as power or end amplifiers in the optical route.

There are effects of temperature differences on optical filters, radiation sources and optical amplifiers, which are well known [1-4]. For these purposes, additional temperature sensing electronic circuits are placed in optical amplifiers, and their task is to balance the temperature gradients in case a change is sensed. Temperature dependence of an EDFA amplifier may pose a substantial problem, as the temperature affects the gain of the amplifier. In case the amplifier is deployed in DWDM operation, where it amplifies a few dozens of channels at the same time, it is very inconvenient if the gain in the individual channels changes. The changes in gains of the individual channels can cause even higher impact of non-linear effects in the optical fibres, and consequently deteriorate the communication across the entire transmission chain.

At first, this paper describes the theoretical formulations for temperature dependence of EDFA amplifying fibres, and then the authors focus on the description of the experimental measuring workplace. Finally, the last part describes the real measured values obtained for 4 optical fibres doped with Erbium with implementation into an optical route utilizing WDM-PON technology with a DWDM raster. Further steps and future research work are then introduced in the conclusion.

2. TEMPERATURE DEPENDENCE OF AN EDFA AMPLIFIER

Determining the temperature dependence of EDFA amplifiers is especially important for their use in optical WDM systems. For this purpose, we use a physical model with input parameters of energy density at a given energy level, the excitation coefficients between lower and higher energy levels and the distribution of electrons across the energy levels. In practice, however, these parameters are very complex to determine, therefore some simplification must be made so that we could use this model to determine the gain spectrum[5-9].

The EDFA temperature dependence in WDM systems manifests by changes of shape and level of emission and absorption spectra, which were tolerated in older systems. Nowadays, due to the technology advancement, more wavelengths, higher transmission speeds and longer distances are used, so it is more important for the amplifiers to work consistently regardless of the temperature changes. The rare earth elements in silicon materials are generally considered to be temperature independent, providing a gain of 15 dB to 45 dB, which serves as a compensation for the parasitic effects caused by the transmission of the signal through the medium. It has been found that if there is a one percent change in the EDF fibre gain coefficient caused by a temperature change, the result is a drop in gain of three tenths of a decibel for an amplifier with a 30 dB gain. This change is significant, because in order to achieve the global gain, a 1 dB gain difference for individual channels is tolerated [5-9].

The base parameters here are the concentration of active ions in the N medium and the probability that an electron will be present at a given energy level. The sum of probabilities for all involved levels must be equal to one. An electromagnetic wave with a given frequency ν and intensity I , travelling along the axis of the fibre is determined by the propagation equation [5-9]:

$$I(z) = I_0 \cdot e^{g \cdot z} \quad (1)$$

The gain coefficient denoted by g is determined by the population value, the emission value, the probability of the presence of an electron and the statistical value of the load for the lower and higher energy levels that are involved in the transition. If the energy levels are separated from each other by an energy difference determined by the product of the Planck constant and the frequency of the radiation, it is possible to make the sum of individual gain coefficients and determine the total gain in this way. Each energy level consists of vibrational sub-levels and the temperature dependence of the EDF fibres is caused by the different probability values of population density within each energy level. The value of population between two levels is then described by Boltzmann's rule using T the temperature on the Kelvin scale and k is the Boltzmann constant. Its most common form is written as a function of energy stated by:

$$P(E) = I_0 \cdot e^{-\left(\frac{E}{kT}\right)} \cdot f(T) \quad (2)$$

The temperature function $f(T)$ represents the temperature effect that meets the normalization condition. Due to the fact that each energy level has a finite range, it is possible to state that the sum of the population probabilities of all sub-levels of a given energy level must be equal to one. Using this rule, we can determine the values of the lowest and highest sub-levels:

$$\int \rho(E)P(E)dE \quad (3)$$

The energy density of all states is denoted by $\rho(E)$. This equation is the equivalent of the statement that the probability of the presence of an electron at a certain level is equal to one for all levels in total, however, here the effect of temperature is now included. Assuming the existence of two energy levels with the same energy densities, the respective condition for each of them can be determined using the relation Eq. (2). Using a transformation of the sum of the gain coefficients, it is then possible to determine their values for cases where most of the population is at a higher energy level and at a lower energy level. After that, the absorption and emission coefficients can be determined and by comparing them the following relation can be extracted:

$$g^* \cdot (\nu) = \alpha(\nu) \cdot e^{\left(\frac{\Delta E(T) - h\nu}{kT}\right)} \quad (4)$$

This is the McCumber relation, where $g^*(\nu)$ and $\alpha(\nu)$ represent the absorption and emission coefficients. However, all these rules are valid only in case that all the erbium ions are identical, have the same energy density $\rho(E)$ and the value of stimulated emission σ . But in real-life situations it is not possible to meet these conditions fully, as each erbium ion has slightly different surroundings. Therefore, the results of all equations should be averaged. Nevertheless, the experimental values have shown that the McCumber equation still represents the temperature dependence of EDF with high precision [5-9].

3. MEASUREMENT AND MEASURING WORKPLACE

A workplace for testing the thermal load of erbium-based amplifying optic fibres was created using a copper cube that consisted of two parts. The copper material was chosen for its very good thermal conductivity, which is 393 W/mK. Both parts of the copper cube can be easily separated to insert the amplifying fibres (see Table 1). One half of the cube has a milled-out groove where the amplifying fibres can be placed. After a fibre was inserted into the groove, the remaining space was filled with heat-conducting paste, not only to increase the heat transfer from outside into the copper cube, but also to prevent water condensation in the temperature chamber. To produce the desired temperature with good distribution, four Peltier cells were used. Cooling of Peltier cells was provided by copper coolers made for computer chipsets. After the fibre was inserted into the groove and covered by the heat-conducting paste, the copper cover was attached.

For measuring the temperature inside the temperature chamber we used a sensing system with a distributed temperature sensor. This was a commercially available distributed temperature sensing system. The system can measure temperatures along the entire length of the sensor fibre with a resolution of 0.01 °C per 1 meter of the optical fibre. Thanks to this system, we were able to assess the homogeneity of the temperature distribution inside the copper cube. An integral part of our workplace was formed by a pumping source, namely LD Pirelli E2-980, which was able to provide a pumping power of up to 125 mW at the wavelength of 980 nm, and also the use of a WDM coupler or an isolator. During our experiments, we used 4 amplifying optical fibres with the following specifications which were fabricated employing modified chemical vapour deposition (MCVD) system coupled with solution doping technique.

Table 1. Parameters of erbium-doped fibres.

Fibre ID	Shell composition	Core composition	Core diameter	Numeric aperture (NA)	Attenuation at 980 nm (dB/m)	Attenuation at 1530 nm (dB/m)	Optimum length (m)
SAE-1	SiO ₂ -P ₂ O ₅ -F	SiO ₂ -Al ₂ O ₃ -Er ₂ O ₃	5.2	0.15	~10	~20	~10-12
SAE-2	SiO ₂ -P ₂ O ₅ -F	SiO ₂ -Al ₂ O ₃ -Er ₂ O ₃	4.5	0.19	~15	~30	~10-12
SGAE-1	SiO ₂ -P ₂ O ₅ -F	SiO ₂ -GeO ₂ -Al ₂ O ₃ -Er ₂ O ₃	3.9	0.20	~5	~10	~15
SGAE-2	SiO ₂ -F	SiO ₂ -GeO ₂ -Al ₂ O ₃ -Er ₂ O ₃	5.0	0.17	~6	~12	~15

The complete connection of the designed erbium-doped amplifier was then placed on the Thorlabs board and incorporated into the overall system with all components designed for our measurement. This solution provides ideal conditions for all specified measurements and at the same time satisfies the condition of ability to move it, i.e. the mobility of the entire measuring station. The complete connection is shown in the following photograph (Fig. 1).

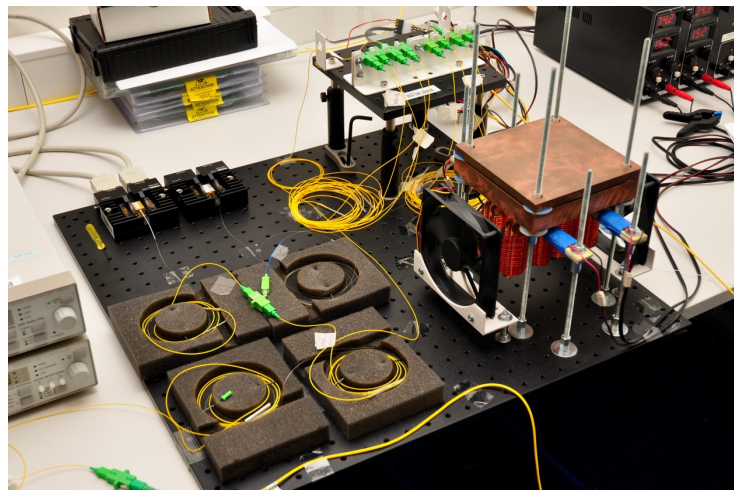


Figure 1. Complete connection of the measuring station (front view).

For testing of the amplifying ability of experimental erbium-doped fibres depending on the temperature during connection to WDM-PON network, we used OLT unit designated as EAST 1100 from LG Nortel company. [10] Further, it was necessary to use the athermal directional coupler AWG designated as WPF 1132c from LG Nortel company. As ONU units we used 6 end units designated EARU 1112, again from the same producer, LG Nortel company. To approximate a real topology as closely as possible, we created a transmission path measuring 13.292 km. The total transmission loss in the path is 10.37 dB. After setting of OLT unit EAST 1110, as well as six end units EARU 1112, it was necessary to connect and put to operation the whole experimental WDM-PON network. After completion and testing of functionality of experimental WDM-PON network, it was necessary to connect EDFA designed by us. EDFA was connected into the path in co-propagation direction in C band. Subsequently, spectrometer EXFO FTB-500 with module 7200D was connected to the output of splitter,

through which 10 % of input signal is transmitted, and the output of individual channels before EDFA amplifier was measured so that it is possible to compare the level of signal power before amplification. During the measurement, spectrometer EXFO FTB-500 with module 7200D was connected behind the amplified and connected again to the splitter through which 10 % of input signal is transmitted. The following image (Fig. 2) below shows the scheme of experimental WDM-PON network [11, 12, 13].

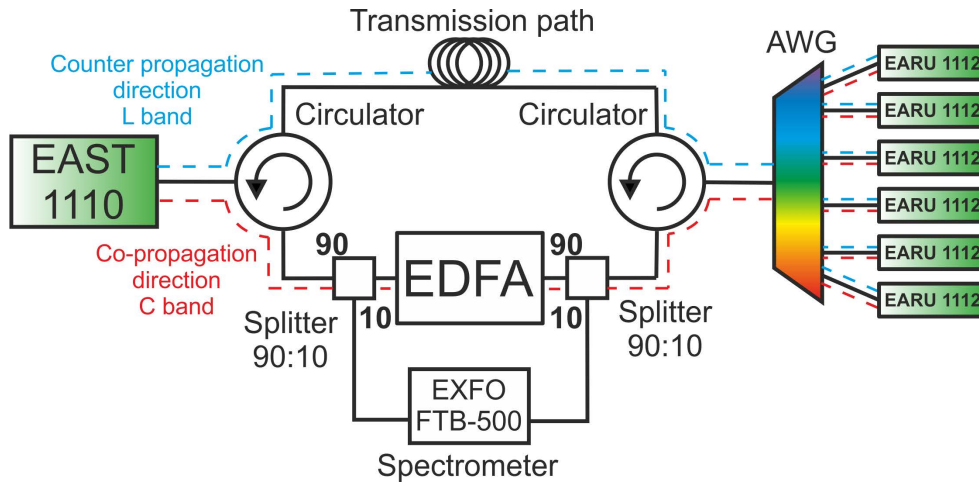


Figure 2. Experimental connection of testing WDM-PON network with connected EDFA amplifier.

4. MEASUREMENT EVALUATION

In order to compare individual fibres and enable better evaluation of the measured data, the fibres were mutually compared for two chosen temperatures, specifically, 25 °C and 90 °C. The results of this comparison were represented in individual graphs (Fig. 3-4) below. In these graphs is shown behaviour of the experimental fibres within real topology.

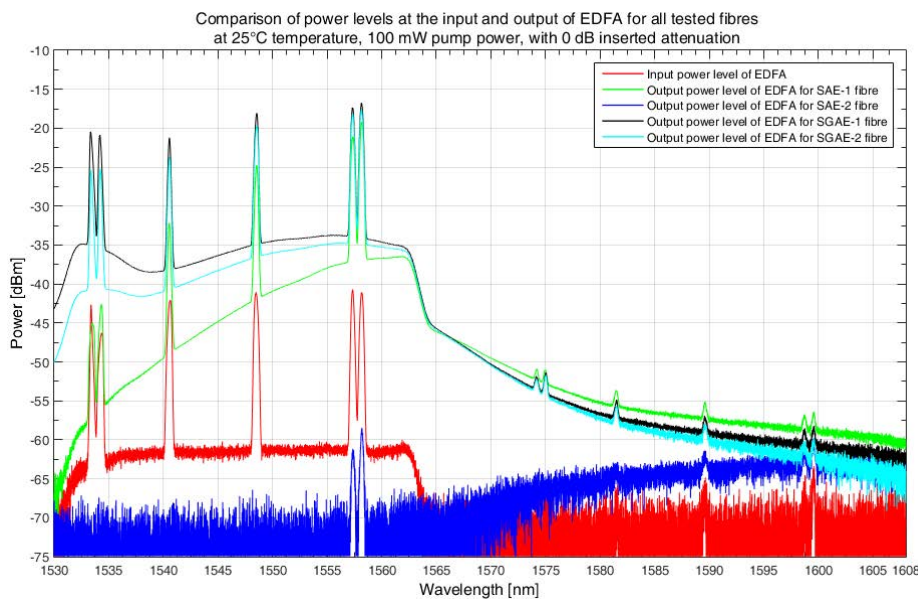


Figure 3. Comparison of the power levels at the input and output of EDFA for all tested fibres at 25°C temperature, 100 mW pump power and with 0 dB inserted attenuation.

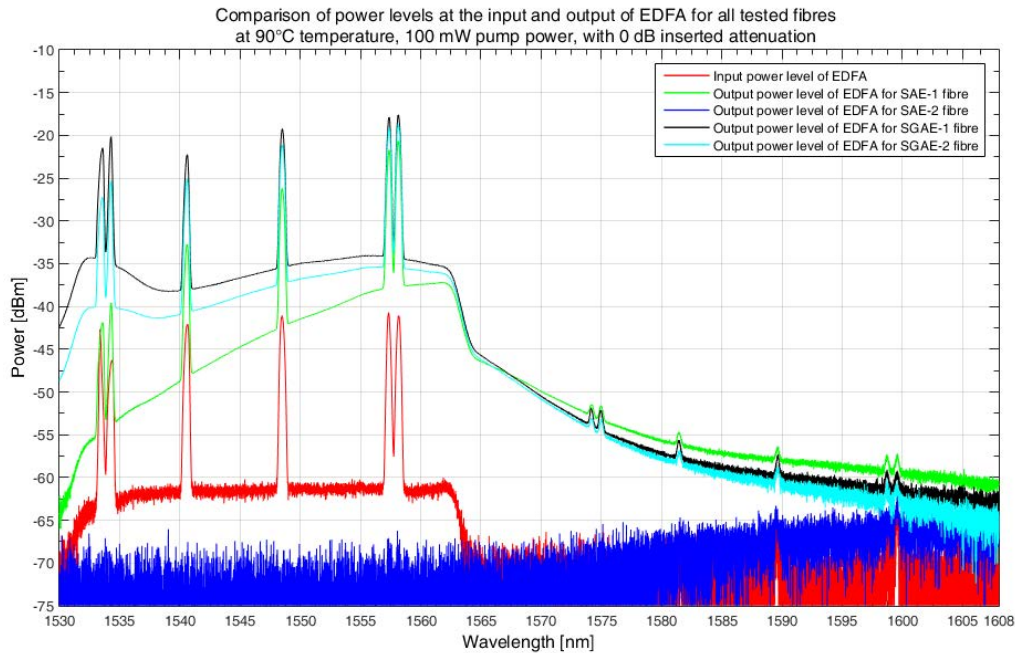


Figure 4. Comparison of the power levels at the input and output of EDFA for all tested fibres at 90°C temperature, 100 mW pump power and with 0 dB inserted attenuation.

Experimental erbium-doped fibres were first compared with each other at 25 °C temperature and 100 mW output. We can see (Fig. 3) that erbium-doped SGAE-1 fibre achieved the best level of amplification of output power in these parameters. The value of amplification for individual channels ranges from 20 to 25 dBm. Erbium-doped SGAE-2 fibre has a similar amplification curve as SGAE-1 fibre. When comparing the levels of amplification, however, erbium-doped SGAE-2 fibre achieves worse results than SGAE-1 fibre. The difference is 2 – 3 dBm for wavelengths ranging from 1540 nm to 1565 nm. The difference is higher between wavelengths 1530 nm and 1540 nm, specifically 5 – 6 dBm compared to erbium-doped SGAE-1 fibre. When we look closer at erbium-doped SAE-1 fibre, we can notice that the amplification curve is absolutely different from the above-described fibres SGAE-1 and SGAE-2. It is obvious from the amplification curve that erbium-doped SAE-1 fibre is not excited sufficiently to amplify signal adequately in the entire C band.

We can see in Fig. 3 that this insufficient excitement is manifested especially for wavelengths ranging from 1530 nm to 1540 nm, with a big difference in the amplification level apparent in the comparison of fibres SGAE-1 and SGAE-2. Insufficient amplification of this erbium-doped SAE-1 fibre is given by two factors. First, the high inserted attenuation of the fibre itself, which is 10 dB for 980 nm wavelength, and 20 dB for 1530 nm wavelength. Second, insufficient pump power for this fibre. As for erbium-doped SAE-2 fibre, we can see that the amplifying ability of the fibre is fully attenuated. Compared to other fibres, and in comparison with the value of power at the input of EDFA, we can see in Fig. 3 that this SAE-2 fibre attenuates signal in the entire C band. This is given, similarly as in case of SAE-1 fibre, by the value of inserted attenuation of the fibre itself, as well as by insufficient pump power for this fibre. The value of inserted attenuation for SAE-2 fibre is 15 dB for 980 nm wavelength, and as much as 30 dB for 1530 nm wavelength.

Comparison of individual erbium-doped fibres at 100 mW pump power exposed to 90 °C temperature is available in Fig. 4. We can see that 90 °C temperature attenuated the level of output almost equally and for all erbium-doped fibres, approximately by 1 – 3 dBm. It is clear that temperature caused higher attenuation in erbium-doped SAE-2 fibre, both in C band, where not even the last two channels are distinguishable, and in L band, which is attenuated even more.

5. CONCLUSIONS

Within our measurements, we have described the issues associated with the implementation of erbium-doped amplifying fibres into optical transmission routes that are made using the WDM-PON technology, with regard to the thermal load of these amplifying fibres. The real measured values, plotted in the graphs in Figs. 3 and 4, have thus confirmed the theoretical assumptions that increasing temperature produces decreasing gain of EDFA amplifiers or EDF fibres. In the future, we would like to perform further measurements for other temperatures, including their negative values, and subsequently compare the results with simulations made in the OptiWave OptiSystem application.

ACKNOWLEDGEMENTS

The research described in this article could be carried out thanks to the active support of the projects no. SP2017/79, SP2017/97, VI20172019071, VI20152020008, TA03020439 and TA04021263. This article was prepared within the frame of sustainability of the project No. CZ.1.07/2.3.00/20.0217 "The Development of Excellence of the Telecommunication Research Team in Relation to International Cooperation" within the frame of the operation programme "Education for competitiveness" that was financed by the Structural Funds and from the state budget of the Czech Republic.

REFERENCES

- [1] M. Kihara, S. Tomita, and T. Haibara: Influence of wavelength and temperature changes on optical performance of fiber joints with small gap, *IEEE Photonics Technology Letters*, vol. 18, no. 20, pp. 2120-2122, 2006.
- [2] J. Chovan, F. Uherek, R. Kurinec, A. Satka, J. Pavlov, and D. Seyringer: Temperature characterization of passive optical components for WDM-PON FTTx, *Advances in Electrical and Electronic Engineering*, vol. 9, no. 3, pp. 143-149, 2011.
- [3] L. Scholtz, L. Ladanyi, and J. Mullerova: Interfacial roughness and temperature dependence of narrow band thin film filters for the DWDM passive optical networks, *Advances in Electrical and Electronic Engineering*, vol. 14, no. 1, pp. 75-82, 2016.
- [4] M. Papes, P. Šiška, A. Liner, J. Látal, P. Koudelka, J. Vitasek, M. Fajkus, and V. Vašinek: Measurement of attenuation changes of PON elements with temperature, in *Proc. SPIE – The International Society for Optical Engineering*, 8697, Ostravice, Czech Republic, Sep. 2012, art. no. 86971R.
- [5] M. Bolshtyansky, P. Wysocki, and N. Conti: Model of temperature dependence for gain shape of erbium-doped fiber amplifier, *Journal of Lightwave Technology*, vol. 18, no. 11, pp. 1533-1540, 2000.
- [6] N. Kagi, A. Oyobe, and K. Nakamura: Temperature dependence of the gain in erbium-doped fibers, *Journal of Lightwave Technology*, vol. 9, no. 2, pp. 261-265, 1991.
- [7] M. Yamada, M. Horiguchi, and M. Okayasu: Temperature dependence of signal gain in Er³⁺-doped optical fiber amplifiers, *IEEE Journal of Quantum Electronics*, vol. 28, no. 3, pp. 640-649, 1992.
- [8] M. Yucel and H.H. Goktas: Determination of minimum temperature coefficient of C band EDFA, *Journal of Applied Sciences*, vol. 8, no. 23, pp. 4464-4467, 2008.
- [9] C. Berkdemir and S. Ozsoy: An investigation on the temperature dependence of the relative population inversion and the gain in EDFAs by the modified rate equations, *Optics Communications*, vol. 254, no. 4-6, pp. 248-255, 2005.
- [10] R. Poboril, P. Siska, J. Latal, M. Smrz, J. Cubik, S. Kepak, and V. Vasinek: Measuring optimal length of the amplifying fiber in different working conditions of the amplifier, *Advances in Electrical and Electronic Engineering*, vol. 12, no. 6, pp. 557-566, 2014.
- [11] R. Sifta, P. Munster, O. Krajsa, and M. Filka: Simulation of bidirectional traffic in WDM-PON networks, *Przegląd Elektrotechniczny*, vol. 90, no. 1, pp. 95-100, 2014.
- [12] J. Putrina, S. Olonkins, and V. Bobrovs: Investigation of in-line EDFA performance dependence on channel spacing in WDM transmission systems, in *Proc. Advances in Wireless and Optical Communications (RTUWO)*, Riga, Latvia, Nov. 2016, art. no. 7821848.
- [13] V. Bobrovs and S. Berezins: EDFA application research in WDM communication systems, *Elektronika ir Elektrotehnika*, vol. 19, no. 2, pp. 92-96, 2013.

Measurement of Changes of Polarization of Optical Beam Affected by Atmospherically Effects

Jan Latal, Jan Vitasek, Lukas Hajek, Ales Vanderka, Radek Martinek*, and Vladimir Vasinek

Department of Telecommunications, Faculty of Electrical Engineering and Computer Science, VSB-Technical University of Ostrava, 17. listopadu 15, 708 33 Ostrava, Czech Republic

** Department of Cybernetics and Biomedical Engineering, Faculty of Electrical Engineering and Computer Science, VSB-Technical University of Ostrava, 17. listopadu 15/2172, Ostrava-Poruba, Czech Republic*

Tel: +420 597 325 845, e-mail: jan.latal@vsb.cz

ABSTRACT

In this article the composite author dealt with measurement possibilities of polarization states of light source emitting 1550 nm which was affected by atmospherically transmission environment in special acrylate box 2.5 m long. The Polarimeter Thorlabs TXP 5004 and the External Sensor Head PAN5710IR3 measured the changes of polarization parameters, ellipticity and azimuth, defining placement on the Poincaré sphere for the light source emitting 1550 nm with marking ML925B45F. The statistical analysis was done from these parameters and by the help of testing of hypotheses was set, whether the difference between reference environment without turbulences and affecting of atmospherically effects is statistically significant.

Keywords: FSO, temperature, polarization, turbulences, ellipticity, azimuth.

1. INTRODUCTION

In the last year we can observe the rapid increase using of the optical communications, both in fibre or fibreless area. The optical systems enable a large capacity of data transmission and also higher data rates. The main benefit of installing of photonic networks except the above mentioned is resistance to electromagnetic interference. As time goes on, the telecommunication operators began deal with possibilities of mobile spread of high-speed signal for the end users, with internet increasing. This caused an up rise of mobile networks which provide today up to 100 Mb/s. Further improvement is expecting in new 5G technology promising data rate up to 20 Gb/s and the response decreased to units of milliseconds.

The problem of all mobile networks is too great regulation of frequency band on the part of national and international telecommunication authority. This leads to division across states and problems with certification of communication devices.

The great advantage of optical fibreless systems (FSO) is working in non-license band therefore they are not regulated. The operators do not pay for using these frequency/optical bands [1]. Nevertheless, the FSO links also have several disadvantages. One of them is a transmission medium, the atmosphere. The atmosphere brings several problems in form of plenty physical phenomena which affect the optical beam. The atmosphere is a chaotic and unpredictable environment with dynamic changes. Many negative effects are in the atmosphere. These effects degrade the optical power or the beam shape. The fog, mist, turbulences and other atmospheric phenomena can affect the FSO link [3,4,5]. Modern methods of switching between FSO and RF are using for reliability and immunity improvement. Hybrid FSO/RF link has much better reliability and immunity against atmospheric effects. Besides the communications, the FSO links are used also for sensor networks [2]. The sensor network building is usually performed regardless of polarization state of the transmitted beam. The features of polarization state depend above all on the type of used light source. The optical beam of FSO link has Gaussian or Top-hat shape with elliptical polarization. The polarization state and the coherence is then better in gas lasers than in solid-state light sources. The ellipticity of gas lasers usually gets near to zero and the coherence length depends on resonance mirrors used in lasers. The polarization state is also important due to the using of new modern modulation formats for communication when the polarization states carry different optical power.

In this article the composite author focused on the hypothesis whether the turbulences (thermal of mechanical) could affect the polarization state, azimuth, ellipticity of optical beam from semiconductor laser emitting wavelength 1550 nm for different modulation formats. The measured data of polarization states, azimuth and ellipticity were processed by the help of statistical method (exploration analysis).

2. POLARIZATION OF OPTICAL RADIATION AND ITS INTERACTION WITH ENVIRONMENT

It is necessary to respect certain conventional rules for correct study of polarization of optical radiation. The infraction of these rules could lead to mistaken evaluation of studied effects and experimentally obtained data. The polarization is defined motion of the endpoint of vector of electric and magnetic field. There are three kinds of the polarization [8, 9, 10]:

- Linear – the endpoints of vector describe the line.
- Circular – the endpoints of vector describe the circle.

- Elliptical – the endpoints of vector describe the ellipse.

The mode in fibre is divided in two components due to birefringence. In the coordination system, the each polarized light could be resolved on a part which is only in x-direction and a part which is only in y-direction. Axis z is a propagation direction. The polarization has an influence on interaction of light with environment, for example:

- Amount of light reflected on interface of two environments/materials depends on polarization.
- Amount of absorbed light depends on polarization.
- Dispersion on light is sensitive on polarization.
- Refractive index of anisotropic materials. Different polarized light spreads with different velocities and shows different phase shifts. The polarization ellipse changes by spreading [11,12].

3. MEASUREMENT AND MEASURING WORKPLACE

For our experiments we put together the apparatus shown in Fig. 1. It was comprised of a measurement box made from acrylate 2.5 m long, 0.5 m high and 0.5 m wide, with 120 mm openings on all sides (separated from each other by 625 mm), to position ventilators or allow air conduction. The upper side of the set-up is removable to allow for the placement of the measurement box into the apparatus during experimentation. To generate thermal turbulences, CTH-5000 Empire fan heaters with the following specifications were used: 2 kW power, hot air temperature ~48°C, and convection speed = 3.5 m·s⁻¹. For our experiments many different scenarios were set by changing position of Hot-Air heaters along one side of laboratory box. In different measurement scenarios, the position of the heaters was changed along the box openings. Totally, it was arranged 6 positions of Hot-Air heaters. Each part was measured for three levels of ventilator rpm. In the first three steps, only the thermal turbulent source was run. In each step the turbulent source was placed in different place. Thanks to different ventilator rpm the hypothesis could be tested if the air velocity and air temperature have some effect on the polarization of modulated beam. In the fourth and fifth step we added the second thermal ventilator. Then the length of beam affected by the thermal turbulence was extended. In the last sixth step we added also the third thermal turbulent source. The turbulences affected on the whole length.

The exploration analysis of measured values in separated steps for laser emitting 1550 nm is summarized in Table 1 and Table 2, where the number before underline is position of the Hot-Air heater according the diagram of measurement and the number after underline is rpm 1 = 35%, 3 = 100%. When the rpm ventilator was 35%, the mean temperature was 50°C and air velocity was 2.9 m·s⁻¹. When the rpm ventilator was 70%, the mean temperature was 45.7°C and air velocity was 5.5 m·s⁻¹. When the rpm ventilator was 100%, the mean temperature was 42°C and air velocity was 8.2 m·s⁻¹. When the rpm was set 35%, the thermal ventilator had constant rpm. After rpm increasing the warm air was cooled therefore higher rpm caused lower temperature. This means that greater influence on polarization of the optical beam has the temperature of turbulence than air velocity.

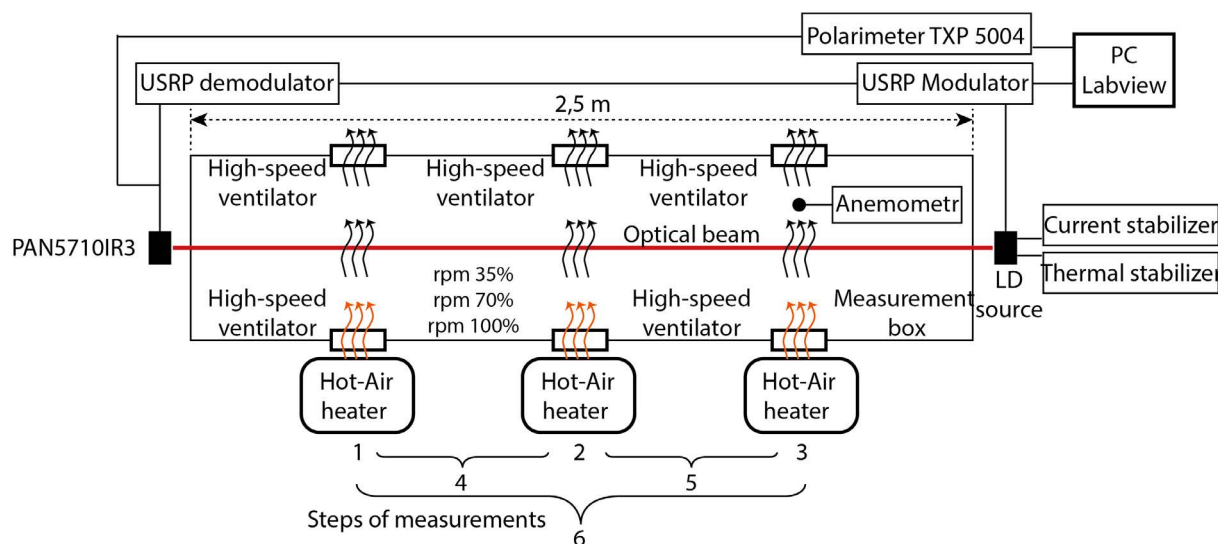


Figure 1. Diagram of measurement of turbulent effects on modulation format.

Warm air generated by heaters was blown into the box by using a high-speed ventilator (SUNONPDM 1212PBM 1-A DC12V) [6] and was removed through another ventilator on the opposite side. With this arrangement, a warm air stream could be generated to change the local refractive index parameter in the measurement box. Subsequently, the measurement box was placed on an iron mounting in front of it, the holder of the laser diode was installed on an aluminium structure, with the laser diode shooting at a right angle through

the front of the measurement box. The laser beam, ended on the head of photodetector (PAN5710IR3) from polarizer, which was also placed on its own aluminium structure for ensuring maximal stability. The measurement box was used to measure the effects of the thermal and mechanical turbulences on the optical modulated beam that travelled in its middle part and ensured that a stable conduction environment could be maintained for various heater placements. To ensure thermal and current stabilization of the laser diode (LD) on the transmission side, a Thorlabs set was used (TDC205C – setting regular part of stream, TED200C – setting operating temperature, TLCLDM9 – holder of laser diode with input for modulating voltage) [8].

To generate the PRBS (pseudo-random bit sequenced) signal, a USRP NI 2920 (more details can be find there) was used: its output was linked to the LD and could change the size of the modulation voltage for the laser diode. Modulation of the laser diode was achieved using the RF input on the holder TCMLD9, which was driven by the current and thermal controller. Laser diode was placed inside laser driver TCMLD9, where circuit Bias-T is placed. This circuit allows bring together DC component from current driver and modulation signal from RF input. This laser driver is also stabilized by temperature driver. To the RF input that was supplied by a SMA connector with an impedance ending of about 50 Ω , the modulating signal with a frequency up to 50 MHz could be added and sample rate is 500 kHz, number of symbols was set to 500. This signal directly modulated the laser diode installed in front of the holder (TLCLDM9) equipped with a collimator (type marking A220TM-B) to focus the optical beam. On the transmission side, the operating wavelength (1550 nm) of the light source with a ML925B45F marking could be selected. The magnitude of the transmitted power of the LD was set to 6 mW and the divergence of the optical beam FWHM was set to 25° for parallel beam transmission and 30° for perpendicular transmission. The atmospheric effects (mechanical turbulences, thermal turbulences) influenced the polarization of the laser beam as it travelled through the simulating box. The affected laser beam was converted back to an electrical signal by stimulating a photodetector (Thorlabs PAN5710IR3) and then was demodulated in the second device (USRP NI 2920). A computer connected to the controlled device (USRP NI 2920) provided the reading of the changes in the symbol speed or modulation format. During measurement of the thermal turbulences the simulated box was hermetically sealed to ensure uniform decomposition temperatures inside the box and at the same time to maintain stable conductions.

4. MEASUREMENT OF OPTICAL BEAM POLARIZATION CHANGES CAUSED BY ATMOSPHERIC PHENOMENA

Following chapter is dealing with measured results of simulated atmospheric phenomena influences on the modulated optical beam with regards to polarization change. The main emphasis was put on azimuth and ellipticity changes of the optical beam. Behavior of simulated atmospheric phenomena was then evaluated with the help of basic statistical methods.

4.1 Polarization measurement in reference static environment

Measurement was performed so that in laboratory box were switched off all ventilators and all inlets were covered to achieve as static environment in the box as was possible. Therefore, in the box was environment without turbulences with constant room temperature of 25°C. Under these conditions were measured optical beam polarization states for eight different modulation formats and subsequently were performed basic statistical tests whether used modulations have any effect on beam polarization. As is shown in the Tab. 1 there is no significant effect of used modulation format on the resultant polarization in the static environment.

Table 1. Ellipticity and azimuth values of different modulation formats in reference static environment.

		QPSK	$\pi/4$ DQPSK	8PSK	16PSK	4QAM	16QAM	32QAM	64QAM
Ellipticity (deg)	Average	2.27	2.28	2.27	2.27	2.27	2.27	2.27	2.27
	Mean-root-square error	0.04	0.04	0.04	0.04	0.03	0.03	0.03	0.03
	Number of samples	2000	2000	1993	1968	2000	2000	2000	2000
Azimuth (deg)	Average	7.15	7.15	7.15	7.15	7.15	7.15	7.15	7.15
	Mean-root-square error	0.04	0.04	0.04	0.04	0.04	0.04	0.04	0.04
	Number of samples	2000	2000	1987	1987	2000	2000	1999	1999

4.2 Influence of mechanical a thermal turbulences

Our performed measurement consists of seven steps. First one is reference static environment, then three mechanical turbulent environments (different air flow velocity) and three thermal turbulences (different temperature and air flow velocity). On the ground of finding that there is no significant effect of used modulation

format on the resultant polarization was from each modulation group chosen one modulation format (QPSK and 16QAM), which were used for measurement of turbulences influence on the modulated optical. Measurement scheme is shown on the Fig. 1. Every measurement step took 15 minutes. First were measured mechanical turbulences at three different rotation speeds and subsequently were performed similar measurements with added heaters. In the box were measured temperature and by anemometer velocity of air flow.

Table 2. Measured results exploration analysis of turbulences influence for individual steps.

		Without turbulence	Mechanical turbulence			Thermal turbulence		
			2.5 m·s ⁻¹	4.2 m·s ⁻¹	5.4 m·s ⁻¹	50 °C 2.9 m·s ⁻¹	45.7 °C 5.5 m·s ⁻¹	42 °C 8.2 m·s ⁻¹
QPSK Ellipticity (deg)	Average	2.27	2.27	2.22	2.19	1.84	1.89	1.96
	Mean-root-square error	0.02	0.06	0.05	0.74	1.49	0.93	0.82
	Number of samples	29999	29901	29915	30000	29996	29997	30000
16QAM Ellipticity (deg)	Average	2.27	2.27	2.22	2.19	1.81	1.89	1.96
	Mean-root-square error	0.02	0.05	0.05	0.72	1.35	0.93	0.83
	Number of samples	29996	29937	29978	30000	29998	29999	30000
QPSK Azimuth (deg)	Average	7.82	7.8	7.79	7.76	7.78	7.72	7.75
	Mean-root-square error	0.02	0.07	0.06	0.16	2.73	1.78	1.48
	Number of samples	28267	29877	29954	29998	29998	30000	30000
16QAM Azimuth (deg)	Average	7.82	7.8	7.79	7.77	7.75	7.74	7.76
	Mean-root-square error	0.03	0.06	0.05	0.16	2.46	1.79	1.49
	Number of samples	28104	29959	29983	29999	29999	29999	29999

In the Tab. 2 is shown exploration data analysis of individual measured steps for both modulations. Prior to hypotheses testing statistical comparison of QPSK modulation with 16QAM modulation was performed. Because from obtained results they are statistically similar hypothesis testing was then performed only for one modulation. First of all it is necessary evaluate measured results. From measured Average results can be said that in case of mechanical turbulences there are no significant changes. For example the worst mechanical turbulence result of Average was at air flow velocity of 5.4 m·s⁻¹ and this change (for QPSK modulation) was 0.08° for ellipticity and 0.06° in case of azimuth. However change in mean-root-square error increased markedly for mechanical turbulences. This means larger values variation, but average is still approximately about initial values of reference static environment. Notable changes are then observed in case of thermal turbulences. Average change for this kind of turbulence reached up to 0.46° for ellipticity and 0.1° for azimuth. Thermal turbulences also largely increased mean-root-square error, which is in this case in order of units, while in case of mechanical turbulences was in order of hundredths and in worst case tenths. From evaluation of these results we can say that influence of mechanical and thermal turbulences are statistically significant, which is verified with the help of Poincare's sphere.

Interesting finding, in case of thermal turbulences, was that increase in ventilator rotation speed caused fall of air flow temperature from the heater. From measured results can be seen that larger influence has air temperature then velocity of air flow. In our measurement of thermal turbulence there was difference of 8 °C in temperature and 5.3 m·s⁻¹ in air flow velocity in between first and third step, but worst results occurs in case of lowest air flow velocity, but with highest temperature. On the other hand best results showed thermal turbulence measurement with lowest temperature with highest air flow velocity. At the Fig. 2 above are data displayed at Poincare's sphere for visualization how are individual data distributed through Stokes vectors. From comparison between reference static environment and environment with mechanical turbulences is evident that data varied only slightly from initial values, which is obvious from Tab. 2. More interesting is look on environment with thermal turbulences where results displayed points of Stoke's vectors considerably distributed, which is caused by larger mean-root-square error.

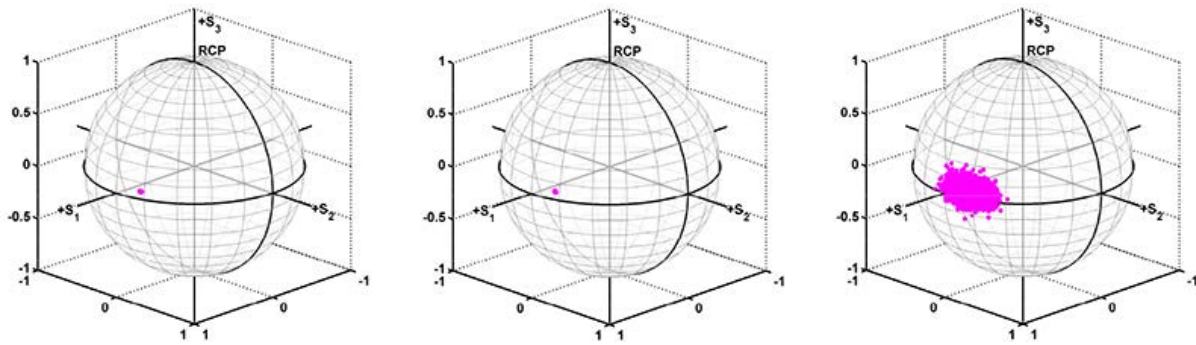


Figure 2. Measured data displayed at Poincaré's sphere, from left to right: reference environment, mechanical turbulence and thermal turbulence.

5. CONCLUSIONS

Research presented in this article confirmed theoretical expectations that thermal turbulences changing local refractive index of the atmosphere, whereby occurs optical intensity fluctuations or changes of polarization parameters respectively. Modulated optical beam with wavelength of 1550 nm displayed for different modulation formats worsened polarization changes through Stoke's vectors as well as worsened azimuth and ellipticity. With regards to progress in cryptography and utilization of modulations with quantum keys it is necessary to observe and pay attention to solutions and behavior of optical beams polarization states for free space optical communication.

ACKNOWLEDGEMENTS

The research described in this article could be carried out thanks to the active support of the projects no. SP2017/79, SP2017/97, TG01010137, MP1401, VI20172019071, VI20152020008, TA04021263. This article was prepared within the frame of sustainability of the project No. CZ.1.07/2.3.00/20.0217 "The Development of Excellence of the Telecommunication Research Team in Relation to International Cooperation" within the frame of the operation programme "Education for competitiveness" that was financed by the Structural Funds and from the state budget of the Czech Republic.

REFERENCES

- [1] R. Ramirez-Iniguez, S.M. Idrus, and Z. Sun: *Optical Wireless Communications: IR for Wireless Connectivity*, CRC Press, 2008.
- [2] I.I. Kimand and E.J. Korevaar, "Availability of free-space optics (FSO) and hybrid FSO/RF systems," in *Proc. International Symposium on the Convergence of IT and Communication (ITCom 2001)*, International Society for Optics and Photonics, 2001.
- [3] L.B. Stotts *et al.*, "Progress towards reliable free-space optical networks," in *Proc. Military Communications Conference (MILCOM 2011)*, IEEE, 2011.
- [4] A.K. Majumdar and J.C. Ricklin, Eds.: *Free-Space Laser Communications: Principles and Advances*, vol. 2, Springer Science & Business Media, 2010.
- [5] A. Vanderka *et al.*, "Design, simulation and testing of the OOK NRZ modulation format for free space optic communication in a simulation box," *Advances in Electrical and Electronic Engineering* 12.6, 604-616 (2014).
- [6] <http://www.digikey.com/product-detail/en/PMD2409PMB1-A.%282%29.GN/259-1424-ND/1249297>
- [7] <http://sine.ni.com/nips/cds/view/p/lang/cs/nid/212995>
- [8] F. Dvorak and J. Diblík, "Study of the temperature turbulences effect upon the optical beam in atmospheric optical communication," *Radioengineering* 20(3), 575–580 (2011).
- [9] W.A. Shurcliff: *Polarized Light, Production and Use*, Harvard University Press, Cambridge, MA, (1962).
- [10] A. Krische, M. Schulz, C. Knothe, and U. Oechsner, "Polarization analyzer for fiber optics and free beam applications," *Optik & Photonik* 8(1), 54–57 (2013).
- [11] F. Dvorak, J. Maschke, and C. Vlcek, "The analysis of fiber sensor of temperature field disturbance by human body part access," *Advances in Electrical and Electronic Engineering* 12(6), 575–581 (2014).
- [12] F. Dvorak, J. Maschke, and C. Vlcek, "The response of polarization maintaining fibers upon temperature field disturbance," *Advances in Electrical and Electronic Engineering* 12(2), 168–176 (2014).

Testing of the Software Goniophotometer in Wils – Building Design Computational Programme

Petr Becak, Tomas Novak, Richard Baleja, Karel Sokansky

Faculty of Electrical Engineering and Computer Science

VSB-TU Ostrava

Ostrava, Czech Republic

petr.becak@vsb.cz, tomas.novak1@vsb.cz, richard.baleja.st@vsb.cz, karel.sokansky@vsb.cz

Abstract – The article deals with the testing of the beta version extension of the BUILDING DESIGN computational programme. The superstructure was conceived as the possibility of inserting a network of calculating points in the shape of a sphere. Points showing normal illuminance towards the centre of the sphere. The goal of implementing such a network of calculation points is to extend the possibilities of a computational program for modelling the luminous intensity curves of existing luminaires as well as newly composed of many discrete optical systems installed in different directions of radiation and having different luminous fluxes in order to achieve the desired resultant characteristic already in a model form. There will be considerable cost savings in the development of such types of luminaires. In the future, the use of this network of computing points and the modelling of the light output emitted into the upper half-space from outdoor lighting systems is the goal. It will be the basis for further astronomical calculations that focus on distracting light and increased sky luminance.

Keywords - software goniophotometer, luminous intensity curves, direct luminous flux, reflected luminous flux

I. INTRODUCTION

The aim of this article is to demonstrate the functionality of a software goniophotometer in the Wils - Building Design computational program by Astra MS Software [4]. At present, there are a number of other computational programs involved in the modelling of lighting systems or separate luminaires, such as the computational programs of the German company DIALux or Swiss RELUX, but none of these softwares allow the calculation of illumination or more precisely luminance for the display of light intensity curves of light source or luminaires, because the network of calculation points are flat lands in these programs. VŠB-TUO in cooperation with Astra MS Software, it was possible to insert computational points network in the shape of a sphere with computational points showing normal illumination in the direction to the center of the sphere. The system thus designed duplicates the function of a real goniophotometer, a photometric laboratory instrument that measures luminous intensity or luminous intensity curves.

Work is partially supported by Grants SGS SP2018/117 - BroadbandLIGHT - Public Lighting in SMART City and VI20172019071 - Analysis of Visibility of Transport Infrastructure for Safety Increasing during Night, Sunrise and Sunset

The principle of a goniophotometer is that it allows to measure the luminous intensity in different planes and at different angles, which can be easily interpreted by a sphere with a network of calculation points. The density of the calculation points can be entered in an angular step according to the standard luminaire measurement plan C, γ .

All calculations in the program testing and computational procedures were performed with a maintenance factor of 1 so that input and output data could be compared, in particular from the point of view of the energy conservation law, and there was no aging of the luminaires and light sources.

II. VERIFYING THE PROGRAMME FUNCTION – MEASURING THE DIRECT COMPONENT OF LUMINAIRE LUMINOUS FLUX

Verification of the programme functionality was solved by comparing the luminous intensity curve of selected luminaire with that of the luminaire generated by a software goniophotometer. Comparison was made from the viewpoint of verifying the shape of the luminous intensity curve and from the viewpoint of the total luminous flux that is generated in the space from the obtained LDT data. LDT data represents Eulumdat photometric data of luminaires. This is a data file which is used by users of computational programs for illumination. Among the parameters stored in these data, we can find, for example, the dimensions of the luminaire and the luminous area, the power input, the luminous flux, the colour rendering index, the correlated colour temperature of the light source, the light cover and efficiency, and last but not least the luminous intensity curves of the luminaire itself.

For the purpose of comparing the functionality of the program, the VYRTYCH 1VV-70S-DINGO-E was fitted with a 70 W high-pressure sodium discharge lamp. The luminaire has radiation pattern corresponding to the classical pattern of the street lighting luminaire, shown in Figure 1.

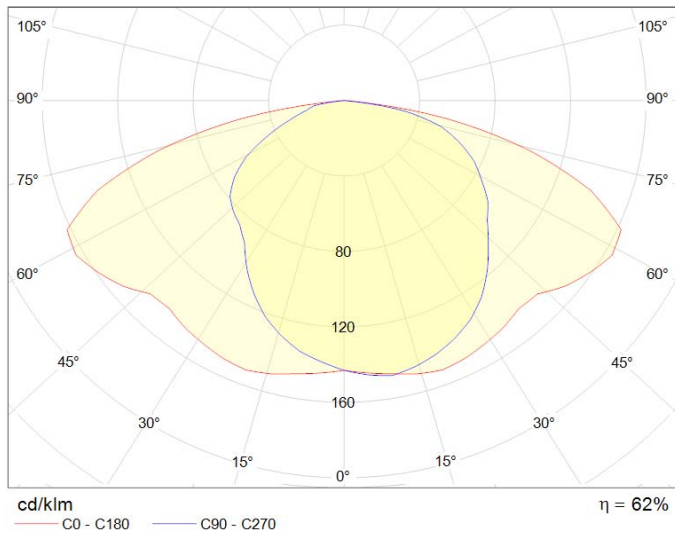


Fig. 1. Radiation pattern of the luminaire from manufacturer's LDT data

Input data from a manufacturer's LDT data that was crucial for verifying the functionality of a software goniophotometer is the shape of the radiation pattern, or more precisely luminous intensity values for given planes with the given step and, last, but not least, the resultant value of luminous flux of the luminaire. The above data are shown in Table I and the luminous intensity values for individual planes are selected in Table II.

TABLE I. INPUT DATA OF THE LUMINAIRE

Power input of the light source (W)	70
Luminous flux of the source (lm)	5600
Luminaire efficiency (%)	61,6
Luminous flux of the luminaire (lm)	3450
Luminaire dimensions (mm)	460 x 310 x 260

TABLE II. LUMINOUS INTENSITY VALUES FOR INDIVIDUAL PLANES OBTAINED FROM MANUFACTURER'S LDT DATA

I (cd/klm)	C270°	C300°	C330°	C0°	C30°	C60°	C90°
0°	143	143	143	143	143	143	143
15°	129	134	141	150	151	148	146
30°	103	115	135	149	154	143	134
45°	83	92	123	145	150	123	108
60°	60	75	122	164	193	110	84
75°	21	36	77	101	143	82	53
90°	0	0	0	0	0	0	0

For the verification of the properties of the computational programme, the above specified luminaire was placed in the centre of the sphere formed by the calculation points distributed in planes C0 - C180 and C90 - C270 by 5° and in gamma planes also by 5°. The radius of the computing sphere has been selected at 10 m so that the tested luminaire can be viewed as a point source. This is shown in the following Figure.

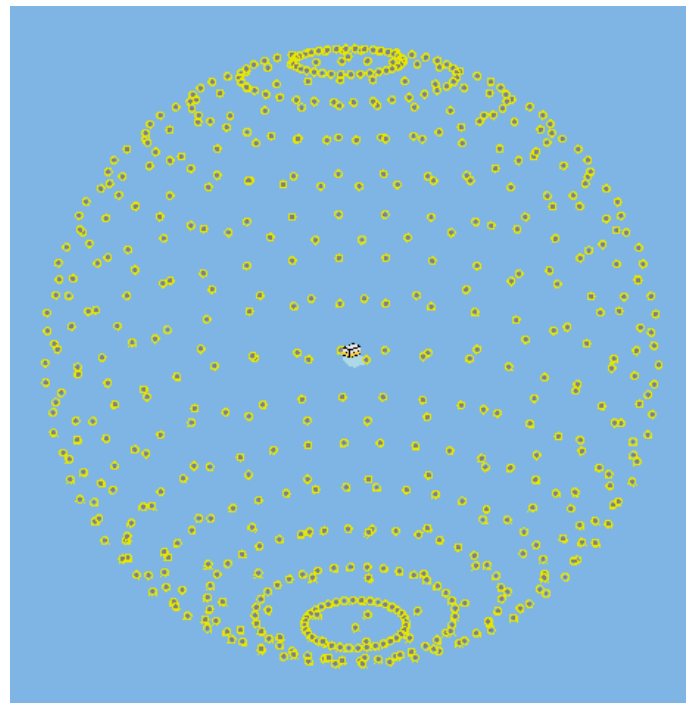


Fig. 2. Model situation of location of the luminaire against the reference plane in the Wils programme

The luminous intensity values obtained for individual planes were selected from the LDT data to match the LDT manufacturer data steps. These luminous intensity values are listed in the following Table.

TABLE III. LUMINOUS INTENSITY VALUES FOR INDIVIDUAL PLANES OBTAINED FROM LDT DATA CALCULATED BY THE WILS PROGRAMME

I (cd/klm)	C270°	C300°	C330°	C0°	C30°	C60°	C90°
0°	142	142	142	142	142	142	142
15°	128,1	132,9	139,9	148,6	149,7	146,8	144,9
30°	102,6	114,4	134,1	148	152,8	142,1	133,3
45°	82,8	91,9	122,4	144,1	149	122,8	107,9
60°	60,4	75,3	121,4	163,1	191	110,2	84,2
75°	21,5	36,7	77,6	102,6	144,2	82,8	53,7
90°	0	0	0	0	0	0	0

Based on the data obtained from the computational program (software goniophotometer) for individual planes, the radiation pattern of the luminaire was obtained, as shown in the following Figure.

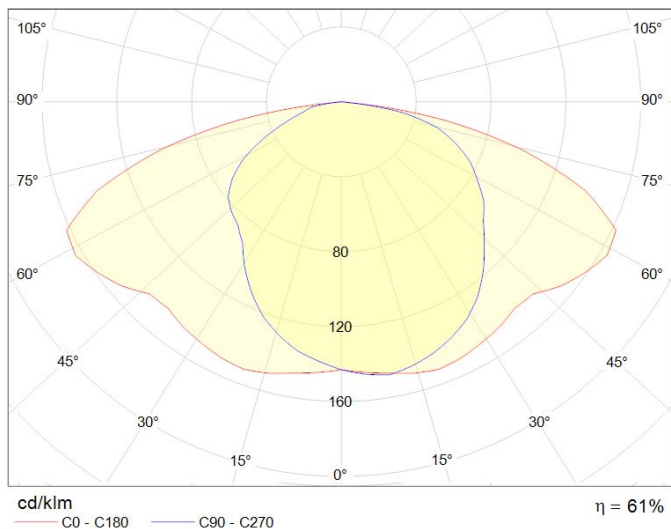


Fig. 3. Radiation pattern of the luminaire from LDT data computed by Wils programme

From the above-mentioned lighting and technical parameters of the original luminaire and the lighting and technical parameters of the luminaires obtained from a software goniophotometer, the following can be stated to verify the behaviour of the programme:

- By comparing the luminous flux of the original luminaire (3450 lm) and the luminous flux obtained by the method of the band factors from the luminous intensity curve of the newly measured (3390 lm) we concluded that the deviation at the above-described density of the calculation points is less than 2 %. [1].
- Shape and size of luminances of the calculated radiation pattern corresponds to the original radiation pattern and it can be stated that the deviations from the original values are minimal and the behaviour of network of the calculation points can be also attributed.

combination luminaire-reflective material was the same as the luminous flux coming out of the luminaire located in a system 1 m above the reflecting surface. Larger distance from a reflective surface (2 m or more) would result in a direct luminous flux in the half-space, which would be undesirable for the experiment. Due to the expected diffuse reflection of the simulated reflective area, we also expected a substantial change in radiation pattern from lower half-space radiation to upper half-space radiation, and a change in shape of the radiation pattern from wide pattern for street lighting to a pattern that approaches a diffusive radiator.

Model situation of location of the luminaire against the illuminated surface is illustrated in the following Figure.

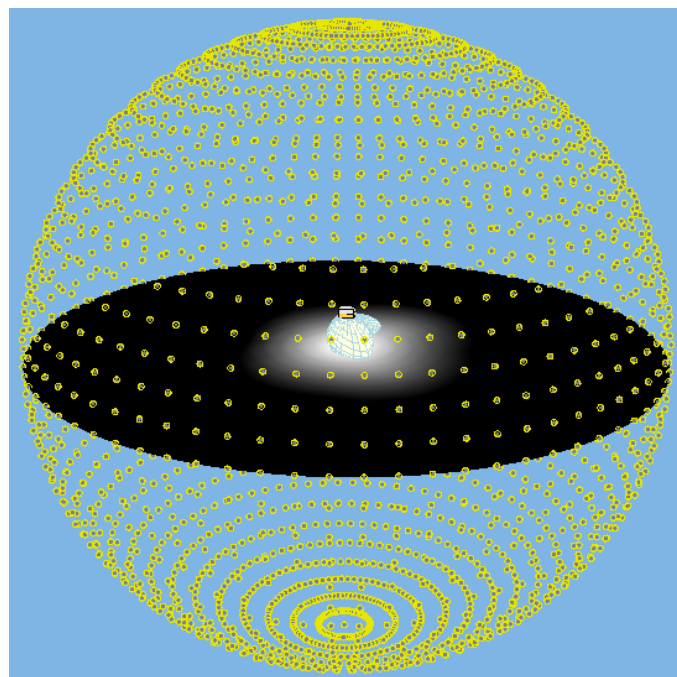


Fig. 4. Model situation of luminaire location against illuminated surface with 100 % in Wils programme

III. VERIFYING THE PROGRAMME FUNCTION – MEASURING THE INDIRECT COMPONENT OF LUMINAIRE LUMINOUS FLUX

In the future, the purpose of this application is to use the calculation points for modelling radiation of luminous flux spreading into the upper half-space from outdoor lighting systems as the basis for further astronomical calculation [5] that focus on disturbing light and increased sky brightness. Therefore, it is necessary to address not only the direct component but also the component reflected from the objects located near the lighting systems. Verification of software function was also done using the calculation with the reflected luminous flux component for the identical luminaire tested for the direct component of the luminous flux, i.e. the VYRTYCH 1VV-70S-DINGO-E luminaire. The number of reflections was set to 3 in the software, which is sufficient enough for testing. The calculation points distributed in the planes were the same as the previous case. For the model, a reflecting surface with 100% reflection was used to avoid any loss during luminous flux reflection and total luminous flux coming out into the

The luminous intensity values obtained in the upper half-space due to reflection from the illuminated surface are recorded in the following Table.

TABLE IV. LUMINOUS INTENSITY VALUES OBTAINED FROM REFLECTION FOR INDIVIDUAL PLANES OBTAINED FROM LDT DATA CALCULATED BY THE WILS PROGRAMME

<i>I</i> (cd/klm)	C270°	C300°	C330°	C0°	C30°	C60°	C90°
90°	0	0	0	0	0	0	0
105°	50,1	51,5	54,8	58,1	59,7	58,3	57,1
120°	94,2	95,9	100,2	104,5	106,5	105,5	104,5
135°	130,3	131,8	135,5	139,4	141,4	141,3	140,8
150°	157,4	158,4	160,8	163,5	165,2	165,7	165,7
165°	174,8	175,2	176,3	177,6	178,6	179,1	179,3
180°	182,2	182,2	182,2	182,2	182,2	182,2	182,2

Based on the luminance data obtained from software goniophotometer for individual planes, the radiance pattern of the fictitious luminaire was obtained, all of whose luminous

flux was reflected in the upper half-space where it was captured by the spherical computing network of the software goniophotometer. This pattern is illustrated in the following Figure.

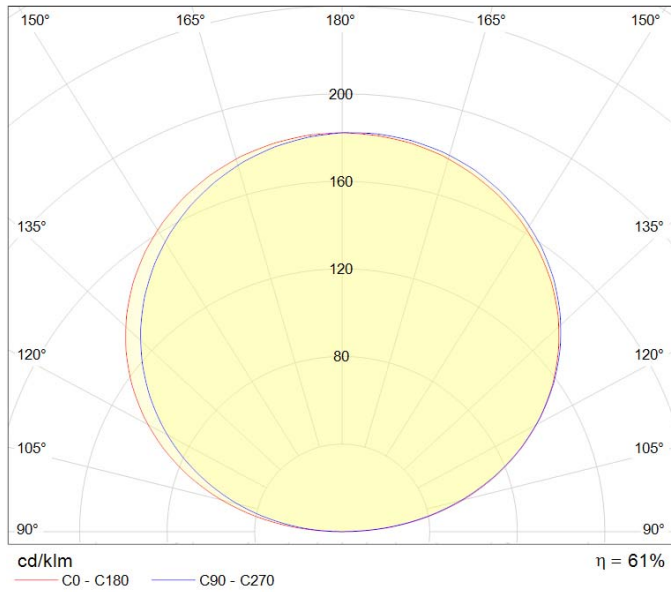


Fig. 5. Radiation pattern of the fictitious luminaire into the upper half-space calculated by the Wils software at 100% reflection of the illuminated area.

From the above-mentioned lighting and technical parameters of the original luminaire and the lighting and technical parameters of combination luminaire-reflective surface obtained from a software goniophotometer, the following can be stated to verify the behaviour of the programme:

- By comparing the luminous flux of the original luminaire (3450 lm) and the luminous flux obtained by the method of the band factors from the luminous intensity curve of the newly measured (3390 lm) we concluded that the deviation at the above-described density of the calculation points is again less than 2 %.
- Shape and size of luminous intensities of the calculated radiation pattern corresponds to the assumptions. The calculated luminous intensity curve radiates only to the upper half-space, and its shape approaches the diffusive (cosine) radiator. Expected deviations from the shape of the cosine function are visible from the curve unbalance and is caused by the unbalanced light radiation of the luminaire, and by using the reflective surface throughout the examined radius, the resulting combination of light radiation of luminaire and reflective surfaces does not act as a point source.

IV. VISION FOR THE FUTURE

On the basis of an experiment with the calculation of the direct component of the luminous flux, it will be possible in the future to use the test grid of computing points forming a software goniophotometer as an extension of Wils computational programme capabilities for modelling the

luminous intensity curves of new luminaires composed from many discrete optical systems installed together in different directions of radiation and having different luminous fluxes [2] so as to achieve the desired resultant pattern already in the form of a model [3]. There will be a significant reduction in the cost of developing such types of luminaires, which is welcomed by developers and manufacturers of luminaires around the world.

On the basis of an experiment with the calculation of the indirect component of the luminous flux using software goniophotometer, it will be possible to model the radiation of luminous flux passing into upper half-space from outdoor lighting systems [6], which has the greatest contribution to increased sky brightness and also amount of disturbing light. We must not forget the other sources of this disturbance, including illumination of interiors – radiated luminous flux to the outside of the window, illumination of airports, illumination of outdoor sport grounds, illumination of outdoor workplaces, architectural lighting and, last but not least, advertising lighting. All this will be possible to model in the software, including the installation of lighting systems by real-world luminaires using LDT data from manufacturers. Experiments using the above-mentioned models will serve for further astronomical calculations that focus on obtrusive light, or more precisely increased sky luminance. Based on this vision, the whole development of this software was conceived between the VŠB – Technical University of Ostrava and Astra MS Software.

V. CONCLUSION

Software running on the principle of a virtual goniophotometer is in the testing phase and constantly evolving from the viewpoint of optimization, accuracy of calculations and the development of graphical user interface.

Specifically, from this article dealing with program testing, based on the above experiments and the knowledge of the lighting and technical parameters of the original VYRTYCH 1VV-70S-DINGO-E luminaire with lighting and technical parameters of the luminaire obtained from a software goniophotometer, it can be stated that the software works as expected and does not show errors in numerical calculations.

By comparing the luminous flux of the original luminaire (3450 lm) and the luminous flux obtained by the method of the band factors from the luminous intensity curve of the newly measured (3390 lm) we concluded that the deviation at the above-described density of the calculation points was less than 2 %, both in the direct component experiment (3390 lm) and when respecting the reflective component (3410 lm) of the luminaire's luminous flux. The deviation in both cases is acceptable for calculation estimates.

REFERENCES

- [1] L. Lipnický, D. Gašparovský, R. Dubnička, "Influence of the calculation grid density to the selected photometric parameters for road lighting", Proceedings of 2016 IEEE Lighting Conference of the Visegrad Countries, Lumen 2016 Karpacz, Poland, DOI: 10.1109/LUMENV.2016.7745555
- [2] R. Dubnička, L. Lipnický, M. Barčík, D. Gašparovský, "Comprehensive view of LED products in luminaires", Published in: Diagnostic of

Electrical Machines and Insulating Systems in Electrical Engineering (DEMISEE), 2016 Papradno, Slovakia, DOI: 10.1109/DEMISEE.2016.7530467

- [3] T. Pavelka, M. Ptacek, P. Baxant, "Static model of LED behaviour depending on operating conditions", Published in: Electric Power Engineering (EPE), 2016 17th International Scientific Conference, 2016 Prague, Czech Republic, DOI: 10.1109/EPE.2016.7521774
- [4] J. Sumpich, T. Novak, Z. Carbol, K. Sokansky, "Software calculation tool for light savings in the buildings compared with real measured data", 2013, 14th International Scientific Conference on Electric Power Engineering 2013, EPE 2013, Pages 677-680
- [5] M. Kocifaj, F. Kundracik, "Modeling the night sky brightness distribution via new SkyGlow Simulator", Proceedings of 2016 IEEE Lighting Conference of the Visegrad Countries, Lumen 2016 Karpacz, Poland, DOI: 10.1109/LUMENV.2016.7745553
- [6] P. Žák, S. Vodráčková, "Conception of public lighting", Proceedings of 2016 IEEE Lighting Conference of the Visegrad Countries, Lumen 2016 Karpacz, Poland, DOI: 10.1109/LUMENV.2016.7745514

CCTV Systems that Work with the Security Lighting

Petr Bos, Richard Baleja, Karel Sokansky, Tomas Novak

Faculty of Electrical Engineering and Computer Science

VSB - Technical University of Ostrava

Ostrava, Czech Republic

petr.bos@vsb.cz, richard.baleja.st@vsb.cz, karel.sokansky@vsb.cz, tomas.novak1@vsb.cz

Abstract—Nowadays, there is an access to unattended operation in the area of outdoor electric power stations. With this type of operation, it is necessary to keep an eye on the station's activities not only during the day, but especially at night. Since the operation of the entire lighting system under normal conditions is highly inefficient and causes light pollution, there is a solution that in continuous night operation, the lighting system only provides illumination around a fence. In cooperation with the lighting system set up in this way, surveillance cameras should also be used to monitor the surroundings around the fence and provide information about potential disruption perimeter of the power station.

Keywords—electric power stations, camera system, lighting system, spectral sensitivity, luminance map

I. INTRODUCTION

This article discusses the issue of appropriate choice and mutual cooperation of the lighting system and the surveillance cameras system. The chosen issue does not only concern electrical stations, but generally it is the introduction of CCTV systems in industrial applications that are subject to artificial lighting settings in selected areas. Besides these issues, the article will also discuss the main principles that are important to observe when designing lighting systems. The lighting system serves not only to provide visual tasks for workers and operators, but also for surveillance or diagnostic camera systems.

A suitable choice of lighting systems is important especially for the proper operation of the camera, a legible image, and a sharp record. Camera systems can be used in different areas. In addition to the above-mentioned areas of electric station perimeters, camera systems can be used also for diagnostic purposes. In this respect, CCTV systems are used, for example, to control defects. The cameras used for diagnostics guarantee high performance, not based solely on high-speed image acquisition and processing, but also provide the user with reliable and repeatable performance even in the most demanding machine vision applications. Camera diagnostic systems have various ways of working; their great merit includes high performance and resolution, machine vision tools, connectivity to other systems, automatic selecting features, setting parameters, and operating in real-world conditions with no need for setup.

One of the most important parameters of every camera is its sensitivity, which determines under what minimum light conditions the camera chip can capture the image. The lower

This article was prepared with the support of the projects "Broadband LIGHT - Public Lighting in SMART City" SP2018/117 and "Analysis of Visibility of Transport Infrastructure for Safety Increasing during Night, Sunrise and Sunset" VI20172019071, by institution of VSB-TU Ostrava.

the sensitivity of the camera chip, the better it can capture images at low ambient light intensities. Other important parameters include adjusting the light colour of the camera's spectral sensitivity light system and the correct design of the lighting system regarding the deployment of camera systems.

II. SPECTRAL ADAPTATION OF THE LIGHT COLOUR OF ARTIFICIAL LIGHT SENSITIVITY OF CAMERA CHIPS

Due to the rapid development of LED lights used in public lighting, it is necessary to think about the issue of maximum use of radiated energy from lighting systems by individual camera systems. The individual chips that are used in camera systems have a spectral sensitivity that does not resemble the sensitivity curve of the human eye. The maximum sensitivity of the camera chips is beyond 555nm, as is the case of a with the human eye, and their spectral sensitivity can also reach areas of infrared or ultraviolet radiation. In contrast to other sources, spectrum colour of the lighting systems using LED illumination can be changed, and thus the use of incident radiation on the camera chip can be maximized. By optimizing the choice of LED spectral radiation, it is possible to achieve light technical parameters for both the human eye at task area and a sufficient incidental radiant flux on the camera chip in maximum spectral sensitivity. The article presents a procedure and a practical example of solving the spectral adaptation of colour temperature of a lighting system fitted with LEDs to a particular chip used in a CCTV system used for surveillance lighting in an outdoor power station and a camera chip used that is used for diagnostic purposes.

III. REQUIREMENTS FOR THE LOCATIONS OF CAMERAS REGARDING THE LIGHTING SYSTEM OF ARTIFICIAL LIGHTING

The following part describes the proposal for the location of surveillance cameras. With respect to cameras installation, it is necessary to meet the basic principles for their location and all the sensing needs in order to increase the safety of power stations. In addition to these basic principles, it is also important to address their position from the point of view of possible glare with high luminances from the luminaires of the lighting system itself. This condition is very important because the camera will monitor the selected area in the direction of maximum light distribution from the lighting system. Therefore, it is essential to choose properly the location of not only cameras but also luminaires to preserve the correct function and proper recording of a clear and sharp image. Due to the reflective properties of the materials, it is assumed that the monitored subjects will have the maximum reflections in

the backward direction to the camera and will therefore maximize the excitation of the camera chips.

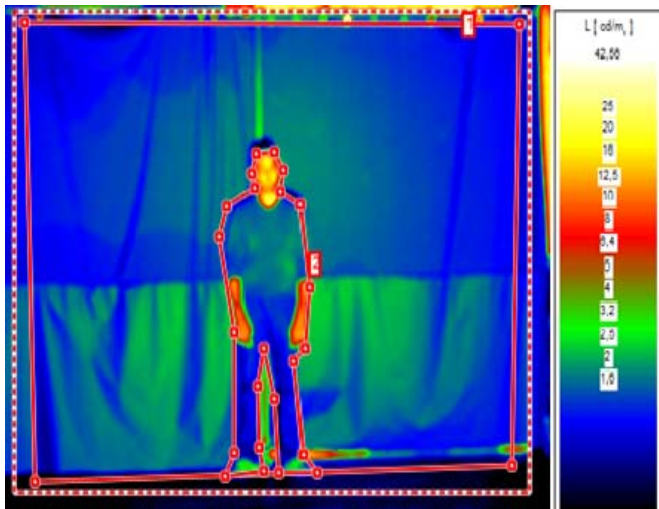


Fig. 1. Luminance map - very dark background and dark clothes

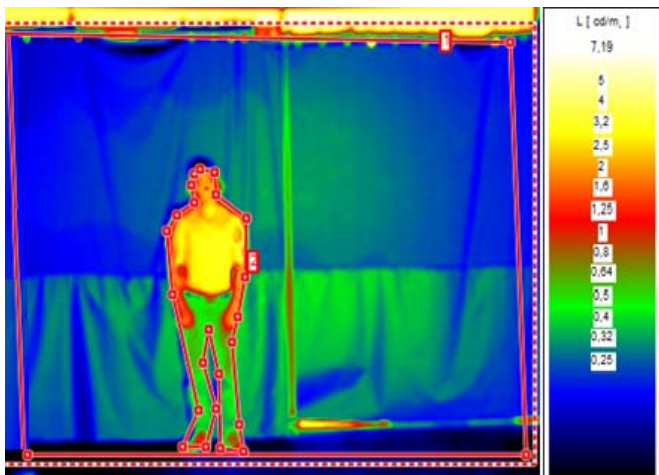


Fig. 2. Luminance map - very dark background and light clothes

- Ev...vertical illuminance (lx)
- Lav...average luminance (cd/m²)
- ρ...real situation could only approach these limits of reflection. There are laboratory limits of it.

TABLE I. EVALUATION OF LIGHT PARAMETERS IN THE COURSE OF CAMERA SWITCHING WITH VERY DARK BACKGROUND

Dark background (ρ is lower than 0.03)		
	From RGB to BW mode	From BW to RGB mode
Ev camera (lx)	4	2.3
Ev captured surface (lx)	37	200
Lav dark pedestrian (cd/m ²)	0.46	2.55
Lav background (cd/m ²)	0.28	1.56
Lav light pedestrian (cd/m ²)	1.48	7.52
Lav background (cd/m ²)	0.34	1.83

TABLE II. EVALUATION OF LIGHT PARAMETERS IN THE COURSE OF CAMERA SWITCHING WITH VERY LIGHT BACKGROUND

Light background (ρ is higher than 0.95)		
	From RGB to BW mode	From BW to RGB mode
Ev camera (lx)	0.19	1
Ev captured surface (lx)	4.6	22
Lav dark pedestrian (cd/m ²)	0.13	0.655
Lav background (cd/m ²)	0.84	3.98
Lav light pedestrian (cd/m ²)	-	1.78
Lav background (cd/m ²)	-	4.1



Fig. 3. Example of camera view at night

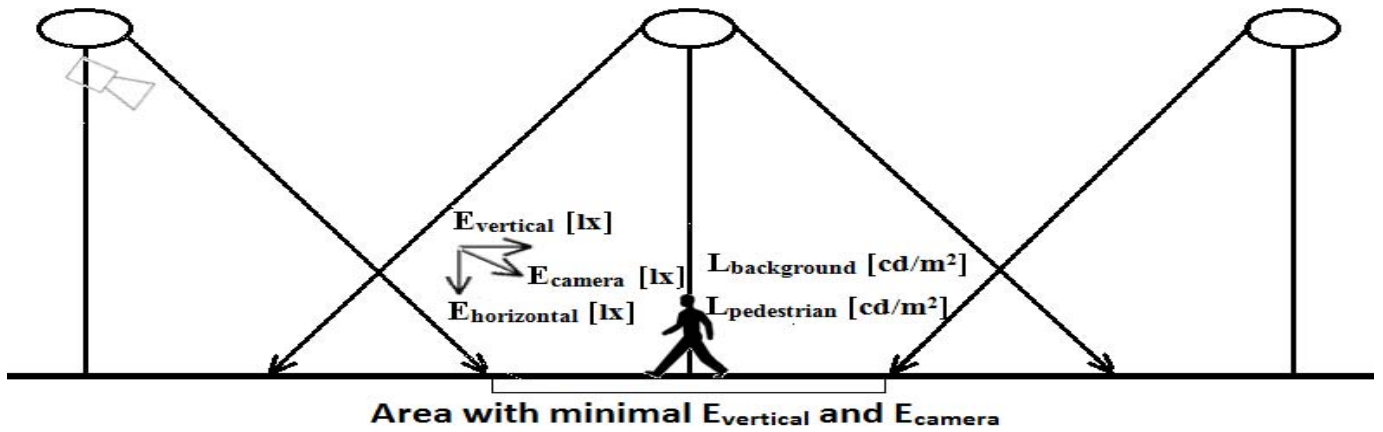


Fig. 4. Standard lighting systems

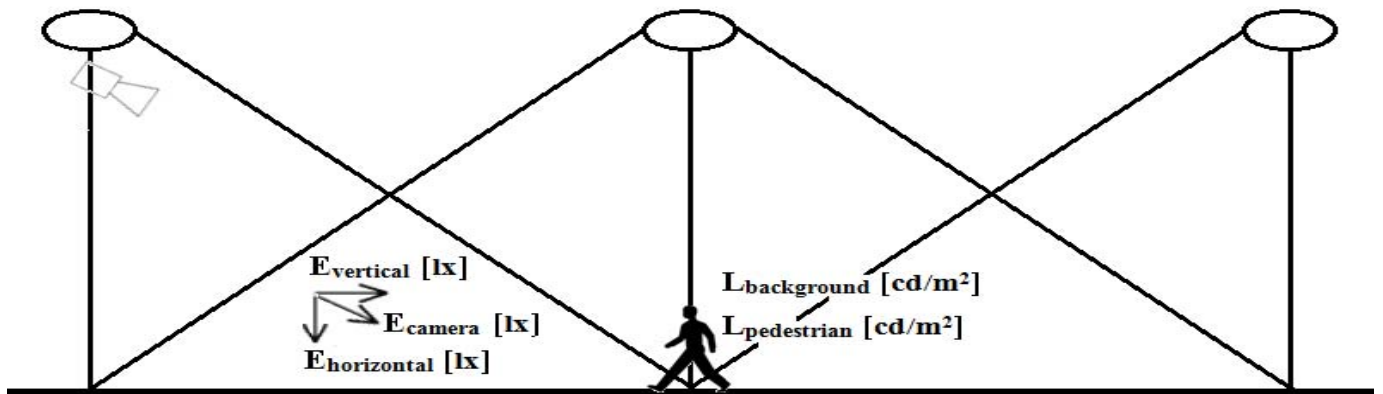


Fig. 5. Philosophy of lighting system from the perspective of the camera system

IV. CHANGING THE PHILOSOPHY OF THE DESIGN OF LIGHTING SYSTEMS FOR SURVEILLANCE LIGHTING

According to the above-mentioned, the lighting systems, which work synergistically with surveillance camera systems, must meet not only requirements for humans' visual tasks, but primarily, they must meet requirements for camera systems recording. With respect to the requirements for visual performance, adequate horizontal illumination must be maintained between the individual columns of the lighting system, and even distribution must be achieved in the observed section. From the point of view of the camera, it is important to ensure so-called camera illumination in the monitored area. In the standard design of the lighting systems, shown in Figure 4, there are different requirements for the position of surveillance, different task area and different requirements for distribution of luminous flux of the luminaires. The problem is that in the monitored section between two luminaires, the desired camera component of the illumination does not have to be recognized, even though normative regulations are observed. The article illustrates how to design a lighting system of security lighting so that both the horizontal and the camera illumination throughout the monitored area are respected. This recommendation is depicted in Figure 5. [1] [2] [3] [6]

V. RELATION BETWEEN CAMERA MANUFACTURER REQUIREMENTS AND LIGHTING STANDARDS

The last part of this article summarizes the requirements for the combination of CCTV systems and public lighting luminaires that use LED lighting. These requirements are complemented by calculations and measurements of luminance ratios as well as real outputs of CCTV systems installed on the security lighting of an outdoor power station. [4] [5]

VI. MEASUREMENT OF SPECTRAL CHARACTERISTICS OF LED LIGHT SOURCES

The spectral characteristics of each LED that were used in the measurements are: LED with correlated colour temperatures 3000 K, 4000 K that are used in power stations and 3000 K, 6000 K that are used in the diagnostics. Spectral radiant exitance moves to higher wavelengths with rising correlated colour temperature. Constant x said on vertical axis of spectral characteristics is relative to radiant output. Calculation was done to find out the maximal adaptation of luminaires to camera. Calculation of constant x :

$$x \cdot \sum_{400}^{750} A \cdot \Delta B = P \quad (1)$$

$$x = \frac{P}{\sum_{400}^{750} A \cdot \Delta B} \quad (2)$$

- x...constant
- A...relative spectral energy distribution [%]
- B...wavelength [nm]
- P...output [W]

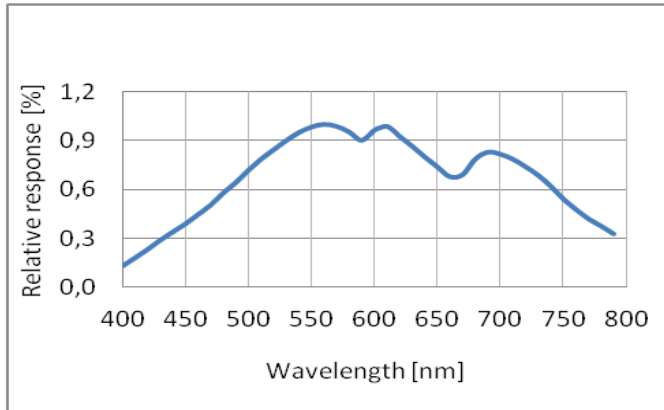


Fig. 6. Spectral characteristic of the camera chip used in power stations

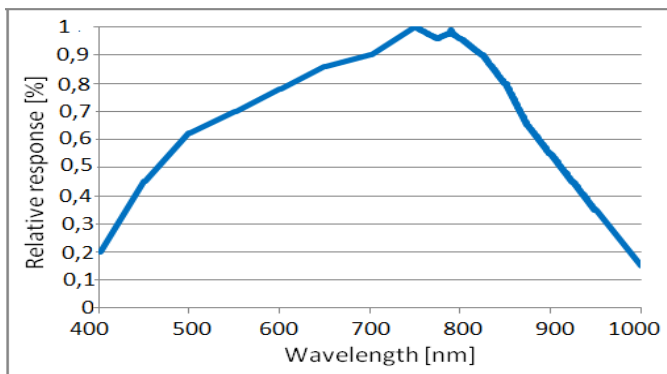


Fig. 7. Spectral characteristic of the camera chip used in the diagnostics

TABLE III. TRANSFER FUNCTION FOR CAMERA SENSOR USED IN POWER STATIONS AND IN THE DIAGNOSTICS

Luminaire type	Transfer function of camera sensors
Correlated colour temperature and area	
3000K – power station	88,90%
4000K – power station	85,90%
3000K - diagnostics	79,3%
6000K - diagnostics	68,7%

The transfer functions for the LEDs used in the power stations were comparable. The transfer function for LEDs with correlated colour temperature 3000 K was 88.9 %. For

correlated colour temperature 4000 K, the transfer function was 85.9 %. From the above measurements, it is evident that the increasing correlated colour temperature of the LEDs decreases the transfer function. The reduction of the transfer function is minimal for these LEDs. However, it is important that the transfer function is maximal for the correct setting of cameras and lighting systems in power stations.

The transfer functions for LEDs used in diagnostics were different. The best transfer function was for the correlated colour temperature 3000 K and it 79.3 %. As the correlated colour temperature of LED increases, the transfer function decreases. These assertions were demonstrated in LEDs with correlated colour temperature 6000 K, where the transfer function was only 68.7 %. The decrease was 10.6 %. The value 100 % is relative to values of ideal spectral sensor speed at all wavelengths.

VII. CONCLUSION

Both in electrical stations and diagnostics, it is important to preserve the correct settings between the cameras and the lighting systems. This article proposes recommendations for correct setting of lighting systems and cameras. Designing lighting systems emphasizes the right choice of correlated colour temperature to ensure the best possible transfer function between the lighting system and the camera. Decreasing transfer function reduces the resolution of the camera and may cause a very low visibility of the camera. Other important parameters in the design of lighting systems include horizontal illuminance, vertical illuminance and camera illuminance. From the point of view of the design of lighting systems must be ensured the horizontal illuminance and uniformity. From the point of view of camera settings is important preservation of camera illuminance in the working area.

REFERENCES

- [1] I. Ullman, P. Bos, J. Ullman, "New outdoor lighting-Operation and maintenance," 17th International Scientific Conference on Electric Power Engineering, 2016, art. no. 7521823, ISBN 978-150900907-7.
- [2] P. Bos, R. Baleja, K. Sokansky, T. Novak, I. Ullman, "Selection of lighting systems for electrical stations CEPS in connection with the introduction of LED," 8th International Scientific Symposium on Electrical Power Engineering, 2015, pp. 220-223.
- [3] P. Bos, R. Baleja, K. Sokansky, T. Novak, I. Ullman, "Outdoor lighting versus surveillance camera systems in electrical substations CEPS," 16th International Scientific Conference on Electric Power Engineering, 2015, pp. 464-467.
- [4] I. Ullman, J. Otypka, T. Mlcak, "New development in control system CEPS, a.s. electrical substation outdoor lighting," 15th International Scientific Conference on Electric Power Engineering, 2014, art. no. 6839516, pp. 649-654.
- [5] I. Ullman, "Implementing new outdoor lighting in electrical stations according to CEPS a. S. Standards," 14th International Scientific Conference on Electric Power Engineering, Kouty Nad Desnou, pp. 63-67.
- [6] K. Sokansky, T. Novak, I. Ullman, Z. Medvec, "Lighting of outdoor electrical stations philosophy," 10th International Scientific Conference on Electric Power Engineering, 2009, pp. 202-206.

Measurement of IPTV Qualitative Parameters on EPON/VDSL2 Topology

Jan Latal*, Zdenek Wilcek*, Jakub Kolar*, Josef Vojtech**

*VSB—Technical University of Ostrava, Faculty of Electrical Engineering and Computer Science,
Department of Telecommunications, 17. listopadu 15, Ostrava, 708 33, Czech Republic

**CESNET, a. i. e., Zikova 1903/4, 160 00, Prague 6, Czech Republic

jan.latal@vsb.cz, zdenek.wilcek.st@vsb.cz, jakub.kolar@vsb.cz, josef.vojtech@cesnet.cz

Abstract—The future of telecommunication networks lies in the area of multimedia services that are offered to end customers. The article discusses the possibilities of deploying IPTV service for a hybrid type of telecommunication topology, which is formed by EPON/VDSL2 systems. The advantage of such topologies is the use of already existing telecommunication network and verification of qualitative features of the distributed IPTV data flows at the same moment. Therefore, the main outputs of this article are the possibilities of distributing data packets by means of multicast or unicast operations. The basic qualitative parameters of the video and data flows (PSNR, MSE, and SSIM) were evaluated with the help of the software tool - MSU Video Quality Measurement Tool.

Index Terms—EPON, VDSL2, IPTV, PSNR, MSE, SSIM, unicast, multicast, MPEG

I. INTRODUCTION

Nowadays the analogue broadcast is gradually coming to an end and the developing digital broadcast is ascending. The digital broadcast has several forms—satellite broadcast (DVB-S, DVB-S2), cable broadcast (DVB-C/2), digital terrestrial broadcast (DVB-T/2), and mobile broadcast (DVB-H/2). Another way to monitor the digital broadcast is to use IPTV technology. The IPTV (Internet Protocol Television) represents the television broadcast, video on demand (VoD) and audio content (of the radio) over high-speed telecommunication networks. For the end user, the IPTV service seems to be and works as a standard television broadcast. From the point of view of an IPTV provider, the service represents processing and secure provision of the video content/streaming by means of data networks that are based on the IP protocol. It seems appropriate to use the EPON Network (IEEE 802.3ah) which fully supports the transmission of the data through IP packets for this purpose. The EPON networks are relatively often used within the telecommunication networks as access networks or last mile networks (EFM) [1]. Among other things, their advantage lies in sufficient bandwidth for data transmission along with low transmission responses [2], [3]. As the demand for multimedia services grows, it is strictly necessary for telecommunication operators to dimension their transmission networks with respect to meeting QoS parameters. This has already posed a problem as the operators are extensively trying to use the possibilities of already existing telecommunication infrastructures for distribution of broadband services. Nevertheless, there are problems with older system types, such

as xDSL technology that should have played a different role in the past. Although the EPON networks are preferentially installed as access networks through FTTH, within the FTTE, the FTTC can be the xDSL systems for end users. However, the problem starts now because such systems operate with completely different methods, and the coexistence of the EPON/xDSL hybrid topology hides some risks in the form of, for instance, the loss of packets due to attenuation along the route or time delays, etc. This article focuses on the issue of hybrid connection for the EPON/VDSL2 systems, when different route lengths of both optical and metallic parts are simulated as well as the distribution of data transmission by unicast or multicast. In addition, two transmission profiles for the VDSL2 (ITU G.993.2) system are also selected to monitor the behaviour of the video flow broadcasting. In such a developed network by means of the distributed video-flows on the VLC server, where the video samples are stored, they are examined by using objective methods (PSNR, MSE, and SSIM) to see if they meet the transmission criteria.

II. RELATED WORKS

Another team focused on the study of a complex simulation infrastructure (Stockholm, Oslo and Copenhagen). It tested the coexistence of a number of telecommunication systems, such as SDH, 10G Ethernet, 1G optical, and 100M of the Ethernet confronting the distribution of multimedia service packages in the form of Triple Play with respect to limit values for individual types of services. It was found out that complicated distribution transmission networks can be used for broadcasting of multimedia services with respect to the QoS and QoE parameters [4]. The authors focused on using the wavelet transformation to study the IPTV data traffic during the 2006 FIFA World cup, when a large amount of the data was distributed. Based on their research it was discovered that there was a direct link between the data transmission and the scalability of the TCP traffic, while the static behaviour without significant changes in the traffic or communication was detected for the UDP [5]. Other teams have dealt with the possibilities of coexistence of the WAN in the form of Wi-Fi or 3G networks, broadcasting the IPTV data flow of end customers with access network. It was found out that both the radio networks show significant differences for the IPTV distribution [6]. The article includes the possibilities

of inter- and intra-ONU support of the QoS on the EPON network. It was demonstrated that the QoS cannot be maintained throughout the communication, especially at high load of the EPON network through different methods of bandwidth allocation for this type of network [7]. Under normal conditions, the distribution of multimedia content through multicast technology without QoS degradation is mainly used for the IPTV. However, it was discussed whether the use of different types of distribution of flows may offer new options (on the application layer) of how to approach the issue of directing (unicast, multicast) the IP packets with multimedia content to end users [8]. In the article by I-Shyan Hwang and colleagues, they found a new way of algorithm for allocating LLIDs for individual IPTV data flows (channels) on the basic topology. The basic topology is the EPON network that provides Ethernet on its transport layer of the protocol (defined according to IEEE 802.3). The results from their simulations showed that the proposed mechanism can improve the QoS metrics in terms of bandwidth, packet loss and queue length [9]. The article by Dohoon Kim and colleagues focuses on studying the possibilities of DSL lines for the QoS of multimedia services with the aim of achieving higher QoE quality through the House of Quality framework combined with the Analytic Hierarchy Process [10].

The IEEEtran class file is used to format your paper and style the text. All margins,

III. METHODS FOR DETERMINING THE QUALITY OF IPTV

There is a number of recommendations for the assessment of the image quality and video signal. One of the best known ones is, e.g. ITU-T P.910. The advantage of this measurement is that one can describe the image based on the reality and, as a result, the information that is imperceptible to the human eye is limited. Subjective measurement is influenced by a number of factors and it is difficult to carry out repeated subjective measurement. There are a few approaches to measure the IPTV quality, e.g. MSE, PSNR, SSIM, MDI or MPQM (Moving Pictures Quality Metric) from the range of objective methods. Within the scope of our measurements we primarily focused on the objective methods for the IPTV quality assessment, specifically on the MSE, PSNR and SSIM that are described in more detail below and the actually measured values are provided in the subsequent chapters [11, 12, 13].

A. MSE (Mean Square Error)

The MSE represents the mean square error of the received video signal in comparison with the original one. This formula is used for the calculation:

$$MSE = \frac{1}{MN} \sum_{j=0}^{M-1} \sum_{i=0}^{N-1} (x_{ij} - y_{ij})^2, \quad (1)$$

where x is the original image, y is the received image, elements i, j are the elements of the image matrix, M is the number of pixels per image height, and N is the number of pixels per image width.

B. PSNR (Peak Signal to Noise Ratio)

The PSNR represents the ratio between the highest value and the MSE and is expressed on the basis of the formula:

$$\begin{aligned} PSNR &= 10 \cdot \log_{10} \left(\frac{m^2}{MSE} \right) = \\ &= 20 \cdot \log_{10}(m) - 10 \cdot \log_{10}(MSE), \end{aligned} \quad (2)$$

where m is the maximum value, which a pixel can receive.

C. SSIM (Structural Similarity Index)

The SSIM parameter takes into account the human visual system. It measures the similarity between two images. The SSIM was designed to improve traditional metrics, such as the MSE and PSNR, which proved to be in contradiction with human perception. The reference values are in the interval of $< 0, 1 >$, where 0 represents a zero relation to the original image, and is achieved when comparing two identical images.

$$SSIM(x, y) = [l(x, y)]^\alpha [c(x, y)]^\beta [s(x, y)]^\gamma, \quad (3)$$

The element $l(x, y)$ is used to compare the signal brightness, element $c(x, y)$ compares the signal contrast, and $s(x, y)$ is used to measure the structural correlation that is calculated from the relations:

$$l(x, y) = \frac{2\mu_x \cdot \mu_y + C_1}{\mu_x^2 + \mu_y^2 + C_1}, \quad (4)$$

$$c(x, y) = \frac{2\sigma_x \cdot \sigma_y + C_2}{\sigma_x^2 + \sigma_y^2 + C_2}, \quad (5)$$

$$s(x, y) = \frac{\sigma_{xy} + C_3}{\sigma_x \cdot \sigma_y + C_3}. \quad (6)$$

where μ_x and μ_y represent the average of the samples x and y , σ_x and σ_y represent the standard deviation of the samples x and y . The constants C_1 , C_2 and C_3 are used for stabilization in case the average and variance are very small. The parameters $\alpha > 0$, $\beta > 0$ and $\gamma > 0$ are used to set the relative importance of the three elements. These elements do not depend on each other, therefore, the change in brightness and contrast has little effect on the structure of the image. This parameter settings $\alpha=0$, $\beta=0$, $\gamma=0=1$ and $C_3=C_2/2$ are used to simplify the SSIM, then (3) reduces to (7):

$$SSIM(x, y) = \frac{2\mu_x \cdot \mu_y + C_1 \cdot (2\sigma_{xy} + C_2)}{(\mu_x^2 \cdot \mu_y^2 + C_1) \cdot (\sigma_x^2 \cdot \sigma_y^2 + C_2)}, \quad (7)$$

The SSIM index is calculated for each pixel (i, j) . The quality of the entire image is calculated by using the medium SSIM index.

$$MSSIM = \frac{1}{M} \sum_i \sum_j SSIM(i, j). \quad (8)$$

where M is the total number of local SSIM indexes.

IV. IPTV QUALITY MEASUREMENT

The software tool MSU Video Quality Measurement Tool was used for our purposes to measure the qualitative parameters of IPTV services on a real route. By using the objective methods SSIM, PSNR and MSE it evaluates the quality of delivered or distributed video flows in the given topology of the telecommunication network. In case of the hybrid topology of the network and IPTV broadcasting, the unicast and multicast operation was investigated with respect to the type of the tested video sample. In the Tab. I the properties of the used video samples are specified. The given types of the video samples were chosen on purpose with respect to the types of compression codecs for video flows from Internet providers. These are MPEG-2 HD, MPEG-2 SD, and MPEG-4 HD of the highest quality. The MPEG-4 allows you to save up to 50 percent of the bandwidth. That is why it is a choice of new IPTV providers, while existing MPEG-2 applications are slowly moving towards MPEG-4.

TABLE I
VIDEO SAMPLES FOR IPTV TESTING

Testing IPTV	Video Sample Parameters			
	File	Frame/sec.	Resolution	Codec
MPEG-2 HD	MPEG	59	1280x720	MPEG-2
MPEG-4 HD	AVI	23	1280x720	MPEG-4
MPEG-2 SD	MPEG	25	720x576	MPEG-2

V. IMPLEMENTED TOPOLOGY FOR MEASURING IPTV QUALITATIVE PARAMETERS

It was necessary to use two topologies for the IPTV measurement. The first connection (see Fig. 1) was used for the unicast operation and the second one (see Fig. 2) for the multicast operation. The reason was to connect AXS-200/625 device to the topology for multicast traffic analysis. The given topologies were created from an optical and metallic part, where the optical part, which was formed by optical paths created by fibres G.652B, was variable with a setting of 0 to 10 km, and the metallic part (type cable SYKY 2x2x0.5) was selected up to 100 meters, as the attenuation in the form of degradation of the VDSL2 transmission properties of the system appeared. The length of the 100-meter metallic route was chosen, where the degradation of the signal is not so apparent. Both the topologies consist the following parts, and the Server, on which the individual tested video samples are stored, is the core. By using the VLC Player in broadcast mode the IPTV video flows are distributed to the EPON/VDSL2 hybrid topology to end units (PC) / EXFO AXS 200/625 measuring device. At the end of the network, there is a participating computer, which detects and processes the operation into the visual form by means of the VLC Player programme. As an active system the OLT unit of the EPON technology type 2 with the following basic parameters was used: the range of about 20 km, the maximum defined split ratio of 1:32 at the used wavelengths 1310 nm (upstream), 1490 nm (downstream) and a transmission rate of 1 Gb·s⁻¹ or

1.25 Gb·s⁻¹, where 250 Mb·s⁻¹ is used for overhead needed for data transmission and administration [1]. The transmis-

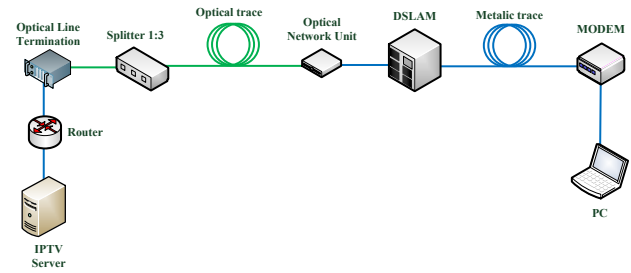


Fig. 1. Topology of hybrid network EPON/VDSL2 unicast operation.

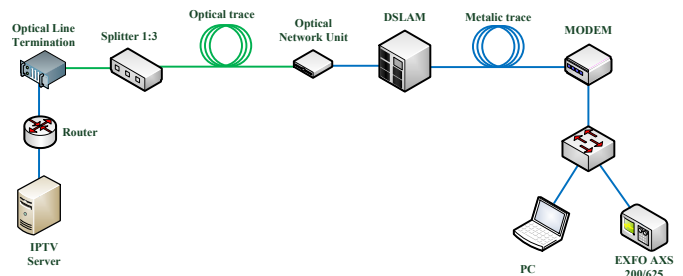


Fig. 2. Topology of hybrid network EPON/VDSL2 multicast operation.

sion profiles with the speeds of the upstream 32 Mb·s⁻¹ and downstream 32 Mb·s⁻¹ in the form of symmetrical service and unsymmetrical one with the speed of the upstream 45.44 Mb·s⁻¹ and downstream 80 Mb·s⁻¹. The requirements for network traffic of the IPTV in the real time are different to other services, such as the VoIP (Voice over IP) and the high-speed Internet access. Therefore, the unicast and multicast operations were used for distribution of video flows on the given connections (see Figures 2 and 3). The aim of selecting the IP datagrams distribution was to find out whether the mode selection had impact on the quality of the IPTV data flow transmissions with selected codecs and topology parameters. It is common for the implementation of multimedia applications, which include the IPTV, to distribute an identical intense data flow to a smaller or large group of recipients during their operation. The support for the multicast is useful on such a network. Group broadcasting or multicast mean the possibility of broadcasting to a particular group of recipients. Unlike omnidirectional broadcasting (broadcasting), when a packet can be sent to all recipients on the local network, the multicast is not limited by the border of the local network. The recipients of the multicast may be spread over a large network. The multicast is ideal to be used for the IPTV system, where one data flow (TV programme) needs to be delivered to a group of recipients, who are interested in the given programme at some point of time without having to send individual data flows that carry independently the required information from the source to all interested parties. In this case, the source generates only one data flow that only sends

the elements of the network infrastructure to the directions, where the parties interested in the data are located. Thanks to multicasting the used bandwidth is significantly smaller than if the broadcast source generated a single data flow separately for individual recipients. The unicast communication principle is not used intensively nowadays. It is a transmission between two stations, when one of them is the source of the broadcast, and the other is the recipient. If there is another station that wants to communicate with the broadcast source, the source station will have to create a new packet. This means that the source must send the data as many times as the number of the recipients on the network is. This type of communication is not used for the IPTV technology due to a large number of users. If there are too many unicast transmissions used the network is congested. The IPTV uses the unicast communication, for instance, for interactive services (VoD, VCR).

VI. MSU VIDEO QUALITY MEASUREMENT TOOL

Testing by means of the software was performed by comparing the streaming videos (see samples in Tab. I) recorded by the VLC player to the original video. The samples were compared by using the objective methods MSE, PSNR, and SSIM. The higher the value of the MSE, the more different the sample is from the original video. Regarding the PSNR parameter, the sample is the same as the original video if the value is 100 dB. The lower the PSNR value, the less similar the tested samples are. The SSIM parameter takes into account the human visual system. The value 1 means the match of the compared samples. The value 0 indicates the zero relation to the original image. In Fig. 3 to Fig. 5 we can observe the effect of the route length on the MSE, PSNR and SSIM values. Regarding the multicast operation on the EPON/VDSL2, we can clearly see that the operation is not affected by the length of the route in the profile A at all. This indicates that the transmission capabilities of the system are sufficiently dimensioned to transmit all types of video samples. In the Fig. 3 we can see that the MPEG4-HD video achieves only the value MSE 0.9 at 100 meters of a metallic path, when the attenuation of the metallic path appears. It is

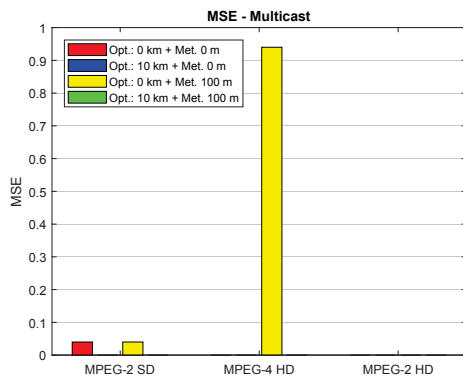


Fig. 3. The values of the MSE parameters for multicast operation, VDSL2 profile A.

necessary to take into account that the HD video flows are very dependent on the bandwidth provided for the transmission. The value is almost zero for the remaining combinations of route lengths as well as for other types SD/HD MPEG-2 videos. The PSNR value is close to the value 100 dB and the SSIM is almost equal (see Fig. 4 and Fig. 5). In case of the unicast operation for the VDSL2 transmission profile we can observe changes in the form of an increase of the MSE values, when the deviation of the received video signal from the original one is considerable for all types of tested samples, see Figure 6. This also applies to the other qualitative parameters PSNR and SSIM, see Figures 7 and Fig. 8. In the Figures 7 and Fig. 8 we can see that changes of these parameters in comparison with the tested routes and types of the chosen video flow/sample. As we can see in the Fig. 6, the MSE is growing considerably for the video sample with the codec MPEG-2 SD at three variants of the network topology, when only one topology with the minimum optical path length and the 100 m metallic part has a low MSE value. The MSE value grew to 664 and the PSNR dropped to 22.5 dB. The completely opposite situation occurs in the sample, when the codec MPEG-4 HD for the MSE is used. Then the situation of the MPEG-2 HD sample, when the MSE shows the same or similar values for the topologies with

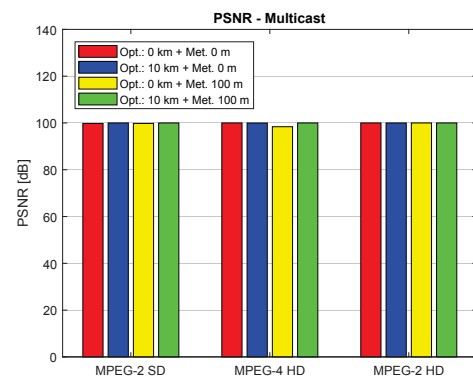


Fig. 4. The values of the PSNR parameters for multicast operation, VDSL2 profile A.

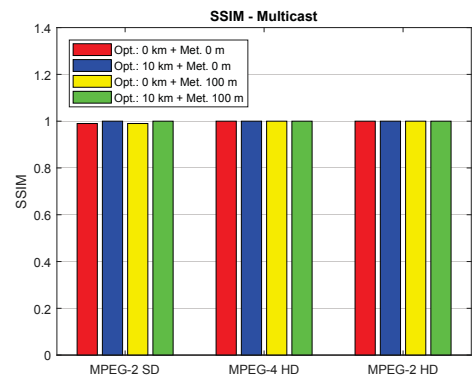


Fig. 5. The values of the SSIM parameters for multicast operation, VDSL2 profile A.

the set route lengths, is also interesting. Regarding the PSNR, see Fig. 7, all the samples more or less behave similarly, only the MPEG-2 HD with the minimum route length setting of the tested routes, the maximum match of the video appears. The last testing is then via the SSIM, see Fig. 8, when it is possible to observe very similar tendencies for all tested video samples and simulated routes. Only in case of the SD video, the SSIM drops to 0.7. In case of the speed profile B, the MSE value increases and the signal to noise ratio decreases for the codec MPEG4-HD (see Fig. 9). These fluctuations occur when optical paths of the 10 km length are connected. However, based on the SSIM value in the Fig. 10 the deviation in these two coefficients is probably imperceptible to the human eye.

This is convenient for the end user, who is not deprived of

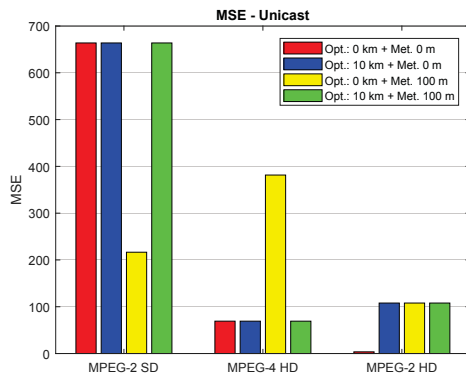


Fig. 6. The values of the MSE parameters for unicast operation, VDSL2 profile A.

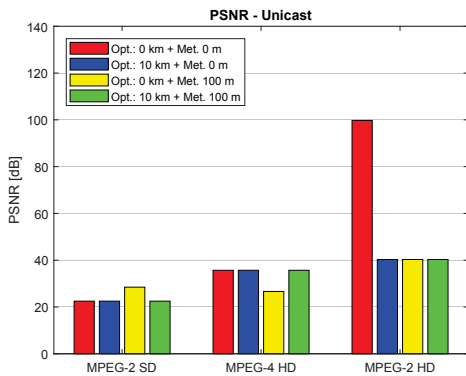


Fig. 7. The values of the PSNR parameters for unicast operation, VDSL2 profile A.

the QoE quality for each type of the tested video sample. The PSNR values, see Figure 11, confirm the fact that the IPTV multicast operation and video sample spreading show very similar values and the quality of the transmitted video is very high. It is possible to see considerable changes only in the MPEG-4 HD, when the PSNR value dropped to 38 dB in case of the optical path setting to 10 km and metallic path setting to 100 m. If we observe the MSE in the Figure 12 in case of the unicast operation, we see that the MPEG-2 SD video

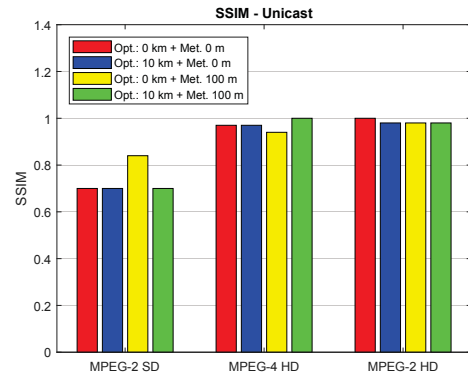


Fig. 8. The values of the SSIM parameters for unicast operation, VDSL2 profile A.

sample is experiencing a significant increase. Afterwards, it

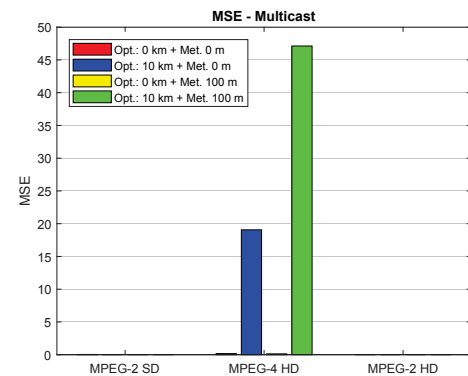


Fig. 9. The values of the MSE parameters for multicast operation, VDSL2 profile B.

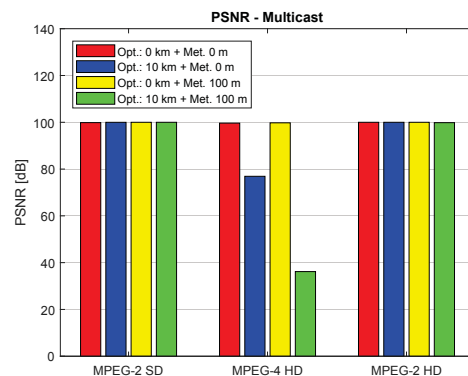


Fig. 10. The values of the PSNR parameters for multicast operation, VDSL2 profile B.

led to the degradation of the original video in comparison with the transmitted one, and, therefore, to the decline in subjective assessment of the video quality. The values of the PSNR correspond with it in the Figure 13, when they are very low 22.5 dB. Regarding the SSIM, see Figure 14, the results

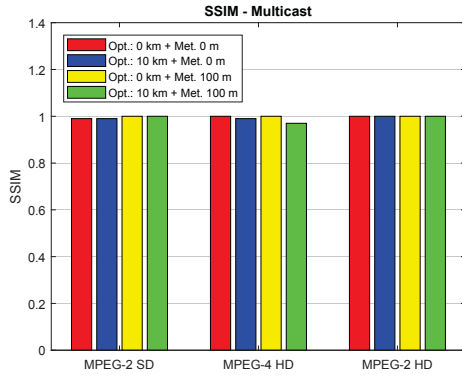


Fig. 11. The values of the SSIM parameters for multicast operation, VDSL2 profile B.

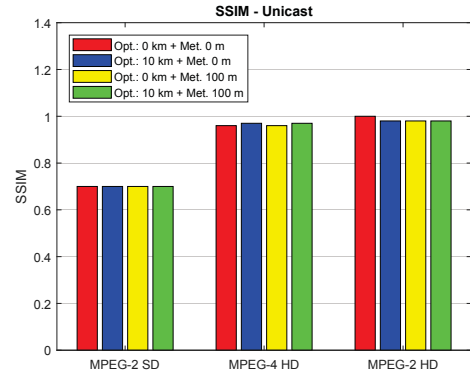


Fig. 14. The values of the SSIM parameters for unicast operation, VDSL2 profile B.

of the measurements are more or less balanced for all types of videos and selected compression codecs.

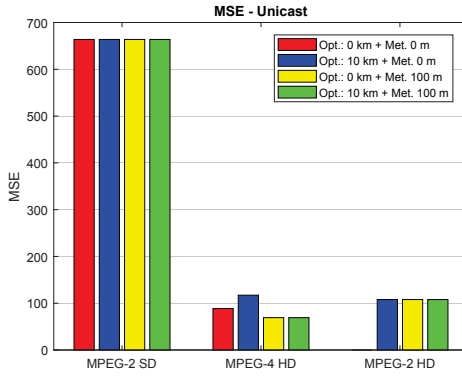


Fig. 12. The values of the MSE parameters for multicast operation, VDSL2 profile B.

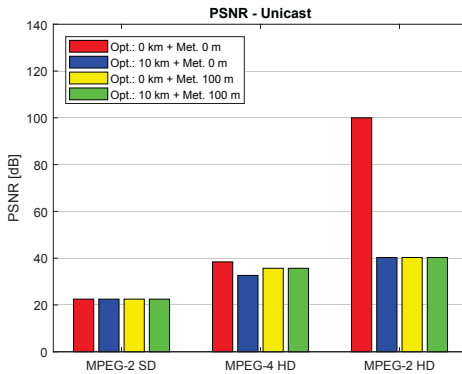


Fig. 13. The values of the PSNR parameters for unicast operation, VDSL2 profile B.

VII. ANALYSIS OF THE IPTV OPERATION BY MEANS OF EXFO-200/625

The analysis of the multicast operation was performed, when the device recorded the bitrate of each video type. The

measurement lasted two minutes, and in Table II and Tab. III we can find the average bitrate for each combination of the hybrid topology and the distribution of the IPTV data flows. The profiles of the MPEG-2 HD sample achieved the highest values of the data flow.

TABLE II
VDSL2 PROFILE A.

VDSL - Profile A	Bit Rate Mb·s ⁻¹		
	MPEG-2 SD	MPEG-4 HD	MPEG-2 HD
Opt. 0 km + Met. 0 km	3.374	3.486	15.566
Opt. 10 km + Met. 0 km	3.406	3.666	15.541
Opt. 0 km + Met. 0.1 km	3.391	3.431	15.498
Opt. 10 km + Met. 0.1 km	3.372	3.592	15.584

TABLE III
VDSL2 PROFILE B.

VDSL - Profile B	Bit Rate Mb·s ⁻¹		
	MPEG-2 SD	MPEG-4 HD	MPEG-2 HD
Opt. 0 km + Met. 0 km	3.388	3.775	15.655
Opt. 10 km + Met. 0 km	3.386	3.555	15.604
Opt. 0 km + Met. 0.1 km	3.391	3.579	15.627
Opt. 10 km + Met. 0.1 km	3.389	3.585	15.502

VIII. CONCLUSION

The future of the IPTV or Triple Play is unquestionable with respect to increasing demands of end users for this service. With the development of 5G the more massive use of multimedia data transmission will take place and telecommunication operators must be prepared to face this fact. The article describes the possibilities of distribution of different video types and compression codecs with regard to simulated path lengths for the optical or metallic parts of the distribution network. The EPON/VDSL2 hybrid network appears to be viable if more video flows are not used on the given line at one moment. They would overload the bandwidth and thus degrade the QoS and QoE parameters. It was also pointed out that the IPTV multicast operation is far more convenient

than the unicast, which imposes greater requirements on the telecommunication network. The future research will focus on creating other types of networks with the assessment by means of the distribution functions of used video types and the use of modern types of compression codecs for the video [14] to [18].

ACKNOWLEDGMENT

The research described in this article could be carried out thanks to the active support of the projects no. VI20172019071, 614R1/2017, SP2018/117 and SP2018/184. The work has been partially supported by Project No. CZ.1.07/2.3.00/20.0217. This work was supported partially by the Ministry of Education, Youth and Sport of the Czech Republic by the project "E infrastructure CESNET - modernization", reg. nr. CZ.02.1.01/0.0/0.0/16_013/0001797.

REFERENCES

- [1] L. G. Kazovsky, N. Cheng, W. Shaw, D. Gutierrez and Wong Shing-Wa, *Broadband Optical Access Networks*. Canada: Wiley, 2011. pp. 283.
- [2] R. Agalliu and M. Lucki, Transmission Transparency and Potential Convergence of Optical Network Solutions at the Physical Layer for Bit Rates from 2.5 Gbps to 256 Gbps, *Advances in Electrical and Electronic Engineering*, vol. 15, no. 5, pp. 877–884, 2018.
- [3] C. Burtscher, D. Seyringer and M. Lucki, Comparison of Splitting Properties of Various 1x16 Splitters, *Advances in Electrical and Electronic Engineering*, vol.15, no. 1, pp. 107–113, 2017.
- [4] G. Baltoglou, E. Karapistoli and P. Chatzimisios, Real-world IPTV Network Measurements," in *Proceeding of 2011 IEEE Symposium on Computers and Communications (ISCC)*, Greece, Kerkyra, 2011, pp. 830–835.
- [5] T. Silverston, O. Fourmaux and K. Salamatian, Characterization of P2P IPTV Traffic: Scaling Analysis, *Technical Report v2*, 2007.
- [6] Y. Li, Y. Zhang and R. Yuan, Measurement and analysis of a large scale commercial mobile internet TV system, in *Proceeding of IMC '11 Proceedings of the 2011 ACM SIGCOMM conference on Internet measurement conference*, Germany, Berlin, 2011, pp. 209–224.
- [7] C. Assi, M. Maier and A. Shami, Toward Quality of Service Protection in Ethernet Passive Optical Networks: Challenges and Solutions, in *IEEE Network*, vol. 21, iss. 1, pp. 12–19, 2007.
- [8] S. A. Hadiwardoyo, An overview of multicast routing techniques for group communications applications, in *Proceeding of 2017 25th Telecommunication Forum (TELFOR)*, Belgrade, Serbia, 2017, pp. 1–4.
- [9] I. S. Hwang, A. Nikoukar, A. T. Liem and K. C. Chen, A new architecture for multicasting live IPTV traffic in ethernet passive optical network, in *Proceeding of 2013 International Conference on Electronics, Computer and Computation (ICECCO)*, Ankara, Turkey, 2013, pp. 60–63.
- [10] D. Kim, Application of the HoQ framework to improving QoE of broadband internet services, *IEEE Network*, vol. 24, iss. 2, pp. 20–26, 2010.
- [11] S. Winkler and P. Mohandas, The Evolution of Video Quality Measurement: From PSNR to Hybrid Metrics, *IEEE Transactions on Broadcasting*, vol. 54, pp. 660–668, 2008.
- [12] Z. Wang, A.C. Bovik, H.R. Sheikh and E.P. Simoncelli, Image quality assessment: from error visibility to structural similarity, *IEEE Transactions on Image Processing*, vol. 13, iss. 4, pp. 600–612, 2004.
- [13] H. R. Sheikh and A.C. Bovik, Image information and visual quality, *IEEE Transactions on Image Processing*, vol. 15, iss. 2, pp. 430–444, 2006.
- [14] J. Vodrazka, P. Lafata, Transmission Delay Modelling of Packet Communication over Digital Subscriber Line, *Advances in Electrical and Electronic Engineering*, vol. 11, no. 4, pp. 260–265, 2013.
- [15] J. Bienik, M. Uhrina, M. Vaculik, T. Mizdos, Perceived Quality of Full HD Video - Subjective Quality Assessment, *Advances in Electrical and Electronic Engineering*, vol. 14, no. 4, pp. 437–444, 2016.
- [16] M. Uhrina, J. Hlubik and M. Vaculik, Correlation between Objective and Subjective Methods Used for Video Quality Evaluation, *Advances in Electrical and Electronic Engineering*, vol. 11, no. 2, pp. 135–146, 2013.
- [17] M. Uhrina, J. Frnda, L. Sevcik, M. Vaculik, Impact of H.264/AVC and H.265/HEVC Compression Standards on the Video Quality for 4K Resolution, *Advances in Electrical and Electronic Engineering*, vol. 12, no. 4, pp. 545–551, 2014.
- [18] M. Uhrina, J. Bienik and M. Vaculik, Impact of GoP on the Video Quality of VP9 Compression Standard for Full HD Resolution, *Advances in Electrical and Electronic Engineering*, vol. 14, no. 4, pp. 445–452, 2016.

Simulation and Measurement of Atmospheric Effect on Optical Beam

Jan Latal¹, Jan Vitasek¹, Marian Bojko², Jan Skrinsky³, Tomas Stratil¹, Zdenek Wilcek¹, and Jakub Kolar¹

¹Department of Telecommunications, Faculty of Electrical Engineering and Computer Science, VSB-Technical University of Ostrava, 17. listopadu 15, 708 33 Ostrava, Czech Republic

²Department of Hydromechanics and Hydraulic Equipment, Faculty of Mechanical Engineering, VSB-Technical University of Ostrava, 17. listopadu 15, 708 33 Ostrava, Czech Republic

³Energy Research Centre, VSB-Technical University of Ostrava, 708 33 Ostrava - Poruba, Czech Republic
Tel: +420 597 325 845, e-mail: jan.latal@vsb.cz

ABSTRACT

The basic atmospheric phenomena (mainly fog) influencing the optical beams, which are generated by laser diodes at wavelengths of 650 and 850 nm, will be introduced in this article. Also the possibilities of the Software Defined Radio utilization, which can create different types of modulation (M-QAM, M-PSK) and can be used for evaluation of the influences of artificial atmospheric effect on the modulated optical beam in the acrylate box, will be presented. The results from the real measurements compared with ANSYS software models will be shown as well.

Keywords: FSO, fog, MER, modeling, modulation, scattering.

1. INTRODUCTION

Optical Wireless Communications (OWC) systems became a new type of telecommunication networks in recent years. The OWC are not regulated by any national regulator of Radio frequency (RF) spectrum and provide high bandwidth. This makes the OWC as an attractive transmission tool for telecommunication operators. The unlicensed bands of OWC are very advantageous, nevertheless, there are problems with the transmission environment, which is the atmosphere. The atmosphere compounds of several layers. From 0 to 80-90 km of altitude, there is a homosphere, above the homosphere there is the heterosphere. The three main layers of the atmosphere are defined in the homosphere; the troposphere, the stratosphere and the mesosphere. These three layers are separated by a temperature gradient which depends on the altitude. The Free Space Optic (FSO) links operate in the troposphere as the lowest layer of the atmosphere. The atmosphere causes several problems in form of plenty physical phenomena which affect the optical beam. The atmosphere is a chaotic and unpredictable environment with dynamic changes. Many negative effects are in the atmosphere. Mechanical and thermal turbulences create cellulars in which the local refractive index changes, resulting in fluctuations of power levels of a transmitted signal, a deflection of the beam from its path, or a scattering of light. Aerosols in the atmosphere cause the scattering of light, which happens on their particles. The scattering is described according to the Mie linear scattering which appears on particles comparable to the wavelength of light. These effects degrade the optical power or the beam shape. The fog, mist, turbulences and other atmospheric phenomena can affect the FSO link [1-3]. Modern methods of switching between FSO and RF are using for reliability and immunity improvement. Hybrid FSO/RF link has much better reliability and immunity against atmospheric effects [4,5].

In this article, the author's team focused on the effect of simulated atmospheric phenomenon, which was a glycerine fog, on the modulated optical beam Phase-Shift Keying or Quadrature Amplitude Modulation (PSK and QAM) with respect to the communication parameter Modulation Error Ratio (MER). At the same time, the possibilities of ANSYS Fluent numerical software are presented for a prediction of behavior of the artificial fog in an acrylate box.

2. THEORY OF FOG EFFECT ON OPTICAL BEAM

The fog is the most negative phenomenon effecting on the FSO links because the fog consists of small water droplets with size close to near IR wavelengths used in the FSO. Depending on the particle sizes from which the fog is compound, we divide the different types of the fog. The fog is a phenomenon when the meteorological visibility decreases between 0 and 2 km. If the visibility is more than 2 km, this type is called "haze". The visible and near infrared light is attenuated by the fog, the fog decreases the optical power of the FSO link, and in some cases it may interrupt the communication completely. Nowadays, other methods for a characterization of the fog are used, such as measuring the size of fog particles and their density. Fog visibility methods were taken from measurements which are usually done at airports. These methods have a certain disadvantage, they do not include microclimatic environments, such as rivers and ponds. The results of airport measurements can be used to estimate optical conditions [1-3].

Modeling of an attenuation caused by the fog is a relatively complex issue because the distribution and density of the fog particles may vary with an altitude, which makes the modeling even more complex. The three main parameters used for attenuation of the fog and haze are a visibility, a relative humidity and a temperature. The most important parameter is the meteorological visibility. However, there are several models that enable the attenuation calculation based on the meteorological visibility for different wavelengths.

The two most used models are the Kruse and Kim models. The attenuation can be calculated by use of this equation and the q coefficient is used according to the model:

$$\alpha_{fog} = \frac{13}{V[km]} \left(\frac{\lambda}{\lambda_0} \right)^{-q} [dB \times km^{-1}], \quad (1)$$

where:

$$q \text{ for Kruse model: } q = \begin{cases} 1.6 & \text{if } V > 50 \text{ km} \\ 1.3 & \text{if } 6 \text{ km} < V < 50 \text{ km} \\ 0.585V^{1/3} & \text{if } V < 6 \text{ km} \end{cases} \quad (2)$$

$$q \text{ for Kim model: } q = \begin{cases} 1.6 & \text{if } V > 50 \text{ km} \\ 1.3 & \text{if } 6 \text{ km} < V < 50 \text{ km} \\ 0.16V + 0.34 & \text{if } 1 \text{ km} < V < 6 \text{ km} \\ V - 0.5 & \text{if } 0.5 \text{ km} < V < 1 \text{ km} \\ 0 & \text{if } V < 0.5 \text{ km} \end{cases}, \quad (3)$$

where the variables in the equations are defined as follows: V – meteorological visibility, λ – wavelength, λ_0 – reference wavelength. The fog can be further divided according to the Al-Naboulsi model into an advective and a convective (radiation) fog. The advective fog is created by a stream of warm and humid air above a cold surface. The air is cooled down and a condensation of water vapor occurs. The attenuation for the advective fog is given by the following relation:

$$\gamma_{ADV}(\lambda) = \frac{0.11478\lambda + 3.8367}{V} \quad (4)$$

The convective fog is created by cooling a warm surface of the Earth by cold air at very slow wind speeds and high humidity. Air contact with the warm surface causes a condensation of a water vapor. The attenuation of this fog is given by the relationship:

$$\gamma_{KON}(\lambda) = \frac{0.18126\lambda^2 + 0.13709\lambda + 3.7502}{V} \quad (5)$$

3. MODULATIONS

Modulation formats are important issues of each communication system. The dominant optical modulations used in the FSO are the On-Off Keying (OOK) and Non-Return-to-Zero (NRZ) with the Direct Detection (DD) in Intensive Modulation (IM) systems [1, 11]. For the system with DD, the received optical power is instantly transformed into an electrical signal. While the Intensity Modulation, we can change the intensity of the optical radiation in accordance with the amplitude of the electrical signal. The oscillations of the carrier optical wave are not affected by modulation and demodulation. In the transmitter, only the optical power changes that is detected in the receiver.

Recent research of advanced optical modulations was motivated by demand on higher transmission capacity, better system reliability and optimal working conditions. The higher order modulation may result in higher spectral efficiency due to reduced symbol rate and narrowing of spectrum.

For example in the [6-10], the authors' team focused on study of the influence of strong fog on optical link in laboratory conditions. At the same time, we tested various types of modulation for suppression of scintillation effect on the optical beam. Some other types of modulations, such as SIM, PoLSK, BPSK, have also been used [12-17]. All these simulated laboratory atmospheric effects are created for the purpose to develop a high-quality OWC link that will be more resistant to changes in atmospheric medium and have a low bit error rate BER.

4. MEASUREMENT OF FOG EFFECT ON FSO LINK

We used the measuring (acrylate) box for our fog measurement experiment with the modulated FSO link in the laboratory. This acrylate box has a length of 2.5 m and 0.5 m in height and 0.5 m in width. The box is used for stable conditions during experimental measurements. The glycerin generator Antari F-80Z generated the artificial fog. The greatest specification was the time that the fog disappear. The fog produced by the glycerin generator decays very slowly, due to its composition. Parallel to fog creation, the particle size distribution of the fog was also measured. Based on this, we are able to determine whether it is possible to quantitate the amount of

fog (from a glycerin generator) into the acrylate box. Figure 1 shows the measurement scheme of fog effect on the FSO link.

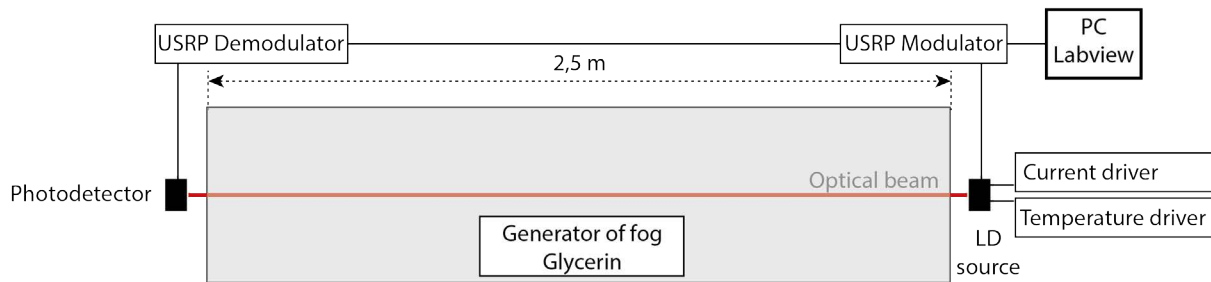


Figure 1. Measurement of fog influence on FSO link.

Subsequently, the acrylate box was placed on an iron mounting in front of it, the holder of the laser diode was installed on an aluminium structure, with the laser diode shooting at a right angle through the front of the measurement box. To ensure thermal and current stabilization of the laser diode (LD) on the transmission side, a Thorlabs set was used (TDC205C – setting regular part of stream, TED200C – setting operating temperature, TLCLDM9 – holder of laser diode with input for modulating voltage). Two types of light sources with wavelength of 650 and 850 nm (types 650543A and L850P010) were used. The LD 650 nm the output power was 5 mW and the LD operating at 850 nm the output power was 10 mW. To generate the PRBS (pseudo-random bit sequenced) signal, a USRP NI 2920 was used: its output was linked to the LD and could change the size of the modulation voltage for the laser diode. Modulation of the laser diode was achieved using the RF input on the holder TCMLD9, which was driven by the current and thermal controller. Laser diode was placed inside laser driver TCMLD9, where circuit Bias-T is placed. This circuit allows bring together DC component from current driver and modulation signal from RF input. This laser driver is also stabilized by temperature driver. To the RF input that was supplied by a SMA connector with an impedance ending of about 50 Ω , the modulating signal with a frequency up to 50 MHz could be added and sample rate is 500 kHz, number of symbols was set to 500, any shaping filter was not used and the gain of the signal was set to 0 dB. This signal directly modulated the laser diode installed in front of the holder (TLCLDM9) equipped with a collimator (type marking A220TM-B) to focus the optical beam. The fog generator fueled the fog into the acrylate box. The optical beams went through the box.

On the receiver side, there was a photodetector InGaAs Fixed Gain Detector PDA10CF-EC. The photodetector bandwidth was 150 MHz. The affected laser beam was converted back to an electrical signal by stimulating a photodetector and then was demodulated in the second device (USRP NI 2920). A computer connected to the controlled device (USRP NI 2920) provided the reading of the changes in the symbol speed or modulation format and qualitative parameter MER.

4.1 Evaluate parameter MER

As the bit error rate BER parameter evaluates communication, we have another parameters for modulations that allow us to evaluate how much the modulated optical beam was affected by the negative effects of the transmission medium. These parameters include the Modulation Error Ratio (MER) parameter and the Error Vector Magnitude (EVM) amplitude parameter. Both these parameters are related to the constellation diagram. In the ideal constellation diagram there are only the ideal positions. Whereas in real conditions, due to the different effects of the noise, we do not reach this ideal positions and the individual points in the constellation diagram deviate from the ideal positions and consequently it appears as if the given point is spread out.

The MER parameter is defined (according to [18]) as the ratio of the sum of the squares of the amplitudes of the ideal symbol vectors to the sum of squares of the amplitudes of the error symbol vectors. This parameter is analogous to the SNR in digitally modulated signals and is also usually expressed in decibels.

$$MER = \frac{\sum_{j=1}^N (\tilde{I}_j^2 + \tilde{Q}_j^2)}{\sum_{j=1}^N [(I_j - \tilde{I}_j)^2 + (Q_j - \tilde{Q}_j)^2]} \quad (4)$$

where: \tilde{I}_j is the size of the ideal symbol component on the constellation I axis, I_j is the size of the real symbol component on the constellation I axis, \tilde{Q}_j is the size of the ideal symbol component on the constellation Q axis, Q_j is the size of the actual symbol component on the Q axis of the constellation diagram.

5. MEASUREMENT OF INFLUENCE OF ARTIFICIAL GLYCERINE FOG ON MODULATION FORMATS

The fog created by the fog generator is very concentrated and decays slowly, therefore the fulfilling by the fog took only three seconds. Subsequently, each modulation format was measured for thirty minutes to see how the

fog decays with time and the MER qualitative communication parameter improves. The fog generation process is shown in Figure 2. On the left, there is the empty box before the fog fulfilling. In the middle, the fog is blown into the acrylate box. For a certain time, the fog holds at the top of the box and then begins to scatter slowly over the entire box volume. The scattered fog can be seen in the picture on the right. Even after thirty minutes the fog is not completely decayed, as will be seen in graphs of the MER parameter as well as quantification of the fog particles.



Figure 2. Fog generation process.

In the above graphs, there are time slopes of the MER parameter for the given PSK modulations which are influenced by fog in the acrylate box. It is clear from the graphs that modulations with fewer states are more resistant to atmospheric effects in the form of aerosol or fog. Comparison of QPSK and $\pi/4$ DQPSK to 8PSK and 16PSK shows, that the MER value more oscillates in case of more complex modulation formats than simpler modulation formats. This behavior is logical because the more states modulations are more influenced than the modulation formats with a lower number of states. Also from the point of view of the lowest achieved MER value after the fog decay are better QPSK (see Fig. 3) and $\pi/4$ DQPSK (see Fig. 4). It is clear from the graphs that after the fog fulfilling, the MER parameter gradually decreased until the fog dispersed throughout the box. Subsequently, over a period of about 200 to 300 seconds, the MER values slowly rised but even after half an hour they have not reached the original values.

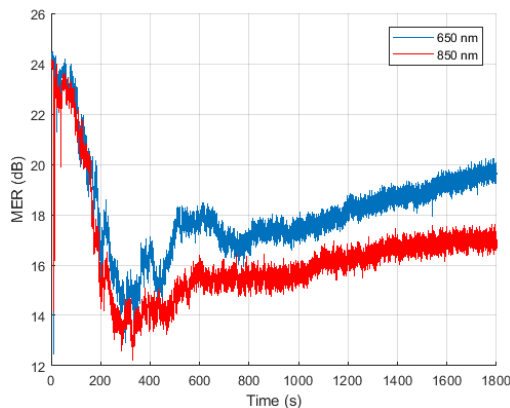


Figure 3. MER time waveform by fog influence on QPSK.

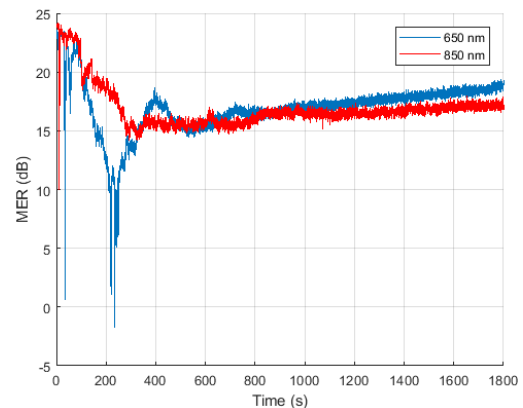


Figure 4. MER time waveform by fog influence on $\pi/4$ DQPSK.

As in case the PSK modulations (see Figs. 5, 6), the same behavior occurs when low state modulation after reaching the lowest level slowly increases without any greater oscillations of the MER parameter. For more complex modulations [16QAM (see Fig. 8) and more (see Figs. 9, 10)], a large oscillations of values occur throughout the half-hour interval. It is obvious that the values slowly improve, but values are very variable against 4QAM (see Fig. 7). It is interesting, that the 32QAM modulation (see Fig. 9) was more unstable than the 64QAM modulation, see Fig. 10, which could be expected to produce worse results. The minimum is reached after about 200 seconds, then the MER value increased with the gradual fog decay.

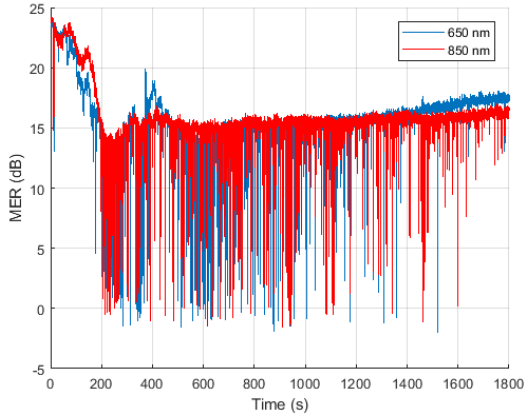


Figure 5. MER time waveform by fog influence on 8PSK.

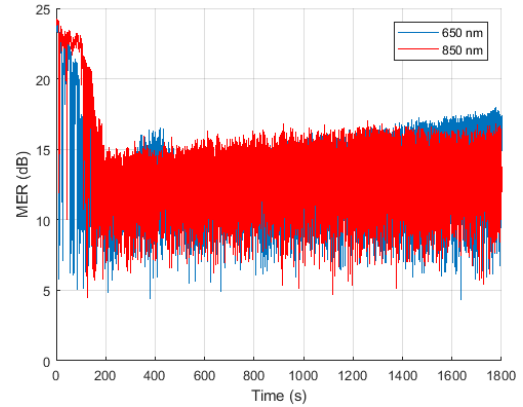


Figure 6. MER time waveform by fog influence on 16PSK.

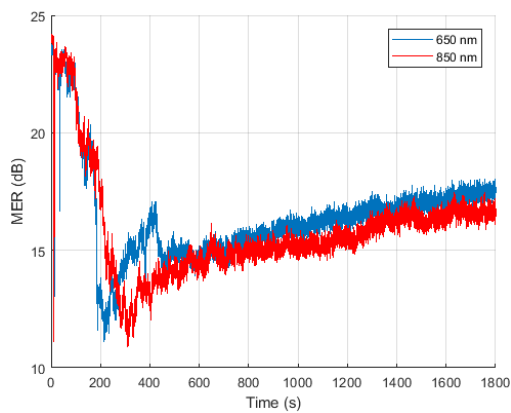


Figure 7. MER time waveform by fog influence on 4QAM.

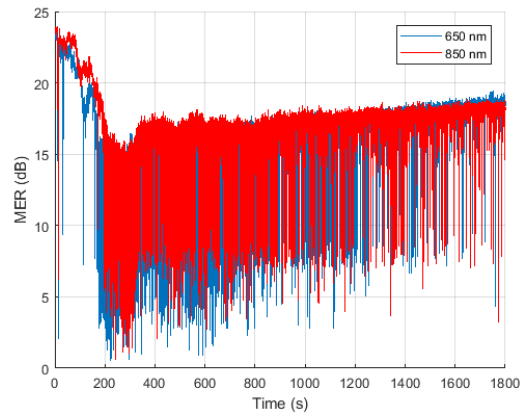


Figure 8. MER time waveform by fog influence on 16QAM.

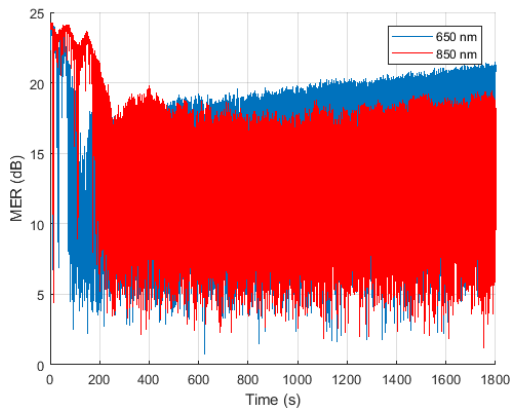


Figure 9. MER time waveform by fog influence on 32QAM.

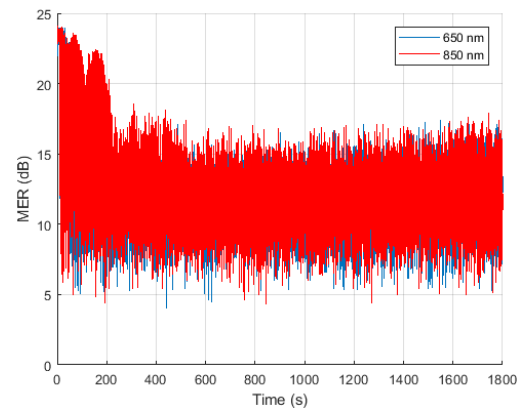


Figure 10. MER time waveform by fog influence on 64QAM.

6. PARTICLE SIZE MEASUREMENT OF THE GLYCERINE FOG IN THE ACRYLATE BOX

Particle number measurement was done by use of SMPS and OPS devices. These instruments were used for measurement of particles produced by the Antari F-80/Z fog generator. The devices SMPS 3080, CPC3772 and OPS 3330 measured the three-second amount of the fog, which has been used for the aforementioned fog effect on the modulation formats. We used three devices due to extend the range of particle diameter which can be measured. But there was a problem with data interpretation because the OPS has the range of 0.3 to 9 μm divided into 16 classes while the SMPS has a range of 21.7 to 593.5 nm, divided into 64 classes. By the help of particle counting, it was possible to analyze the particles produced by the Antari F80/Z fog generator, from the results it is possible to determine the size, weight and number of particles that affect the modulated optical beam

and the quality parameter MER of communication. It is clear from the measurements that the particle amount in time portion 2s is distributed to the larger and smaller groups of particles, the smaller particles gradually sublimate faster than the larger particles (see Fig. 11).

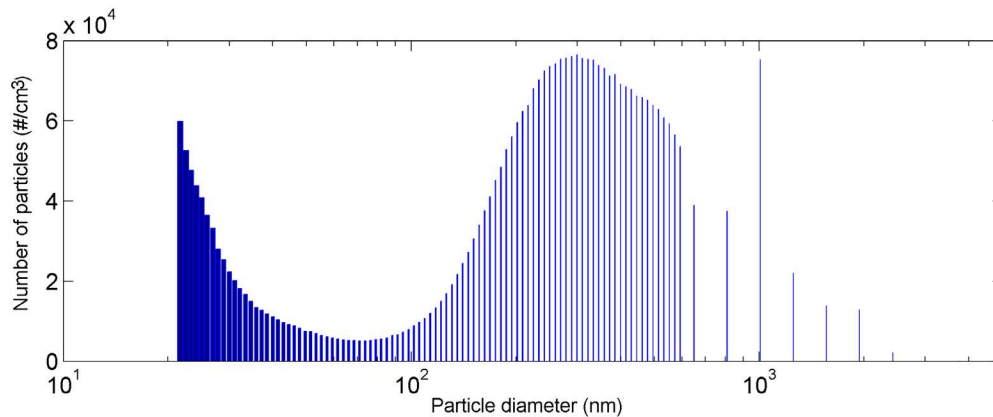


Figure 11. Particle quantification of the fog after 2 minutes

7. NUMERICAL MODEL OF PARTICLE FLUX IN TIME

A mathematical modeling was used to compare the visual behavior of the fog and distribution in the acrylate box. The mathematical modeling was done in ANSYS Workbench (ANSYS Fluent) and CATIA V5. In defining the model, it was most important to specify the boundary conditions of particle composition, a mass flow, a particle velocity and a density. This was done by the help of measurements for verification of the numerical model with real measurement. The Antari F-80/Z fog generator uses glycerine, where the simplified composition can be defined as a 70% distilled water and 30% glycerine (sometimes also glycol). The distilled water serves as a carrier of glycerine droplets after heating. From the available numerical turbulence models that could be used, a turbulent model $k-\epsilon$ relizable, see Figure 12, was chosen as a representative model, see Figure 12, which corresponds most to the real measurement shown in Figure 13. This model is a modification of the $k-\epsilon$ standard. It is known from the theory that it uses an alternative formulation of equations for turbulent kinetic energy and a transport equation for dissipation rate. The model was selected based on a visual comparison with the actual measurement (video) for each time step. In case that a different particle size value could be selected for the graphical output, then we would be closer to the actual measurement in terms of visual comparison. The particles are of different sizes according to the defined Rosin-Rammler distribution, but they are plotted as constant-radius particles by graphical output. By visual observation we can say that the numerical model corresponds to the real fulfilling of the glycerine fog into the acrylic box.

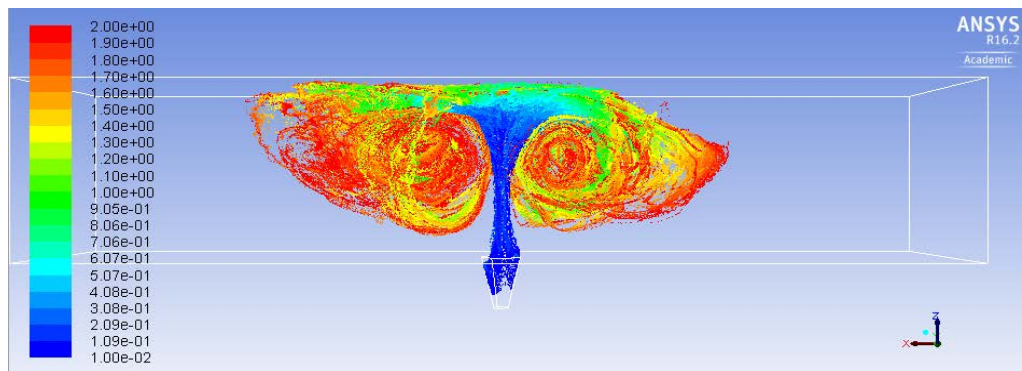


Figure 12. Discrete phase trajectory for the turbulent model $k-\epsilon$ relizable in time 2s.



Figure 13. Real measurement of particles from fog generator in time 2s.

8. CONCLUSIONS

This article aims to the problematic associated with the fog effect on FSO link in laboratory conditions. Based on the experimental work of glycerine fog effect on the modulated optical beam by the PSK and QAM modulation formats it was found, that higher modulation formats are less resistant to particle sizes of the simulated fog. At the same time, for a better image of the particle size distribution of generated fog, the measurements of particle distribution were done in the time domain. An integral part of the work is a new approach to modeling of behavior of atmospheric phenomena through numerical models in ANSYS. These models help us to understand the problem of simulated phenomena more closely in laboratory conditions. The future direction of research will be focused on new types of modulation formats such as OFDM and optimization of numerical models.

ACKNOWLEDGEMENTS

The authors would like to acknowledge the financial support of the Ministry of Education, Youth and Sports of the Czech Republic under Projects No. SP2018/117 and SP2018/184 of VSB–Technical University of Ostrava, Czech Republic. Our research was also supported by Projects No. VI20172019071. This article was prepared within the frame of sustainability of the project No. CZ.1.07/2.3.00/20.0217 within the frame of the operation programme "Education for competitiveness" that was financed by the Structural Funds and from the state budget of the Czech Republic. This work was supported by the European Regional Development Fund in the Research Centre of Advanced Mechatronic Systems project, project number CZ.02.1.01/0.0/0.0/16_019/0000867. This work would not have been possible without the financial support of Innovation for Efficiency and Environment - Growth, reg. no. LO1403 supported by National Programme for Sustainability and financed by the Ministry of Education, Youth and Sports.

REFERENCES

- [1] Ramirez-Iniguez, Roberto, Sevia M. Idrus, and Ziran Sun. *Optical wireless communications: IR for wireless connectivity*. CRC press, 2008.
- [2] Majumdar, Arun K., and Jennifer C. Ricklin, eds. *Free-space laser communications: principles and advances. Vol. 2*. Springer Science & Business Media, 2010.
- [3] Stotts, Larry B., et al. "Progress towards reliable free-space optical networks." *Military Communications Conference, 2011-MILCOM 2011*. IEEE, 2011.
- [4] Nadeem, F., Kvicera, V., Awan, M. S., Leitgeb, E., Muhammad, S. S., & Kandus, G. (2009). Weather effects on hybrid FSO/RF communication link. *IEEE Journal on Selected Areas in Communications*, 27, 1687–1697.
- [5] Ritu Gupta, Preeti Singh (2017) *Performance Analysis of FSO System for Different Fog Conditions*. In: Singh R., Choudhury S. (eds) *Proceeding of International Conference on Intelligent Communication, Control and Devices. Advances in Intelligent Systems and Computing*, vol 479. Springer, Singapore.
- [6] M. A. Esmail, H. Fathallah and M. S. Alouini, "Outage Probability Analysis of FSO Links Over Foggy Channel," in *IEEE Photonics Journal*, vol. 9, no. 2, pp. 1-12, April 2017.
- [7] E. Leitgeb, H. Ivanov, T. Plank, P. Pezzeri and C. Pock, "Implementation of a testbed with a hardware channel emulator for simulating the different atmospheric conditions to verify the transmitter and receiver of Optical Wireless systems," *2017 19th International Conference on Transparent Optical Networks (ICTON)*, Girona, 2017, pp. 1-4.
- [8] B. Kebapci, F. Miramirkhani, H. Nouri and M. Uysal, "A custom-design atmospheric channel emulator for the performance evaluation of free space optical communication systems," *2017 19th International Conference on Transparent Optical Networks (ICTON)*, Girona, 2017, pp. 1-5.
- [9] Ijaz, M., Ghassemlooy, Z., Pesek, J., Fiser, O., Minh, H. L., & Bentley, E. (2013). Modeling of fog and smoke attenuation in free space optical communications link under controlled laboratory conditions. *Journal of Lightwave Technology*, 31, 1720–1726.
- [10] Ali, M. A. A. (2015). Performance analysis of fog effect on free space optical communication system. *IOSR Journal of Applied Physics*, 7, 16–24.
- [11] Vanderka, Ales, et al. "Design, Simulation and Testing of the OOK NRZ Modulation Format for Free Space Optic Communication in a Simulation Box." *Advances in Electrical and Electronic Engineering* 12.6 (2014): 604-616
- [12] W.O. Popoola, Z. Ghassemlooy: BPSK subcarrier intensity modulated free space optical communications in atmospheric turbulence, *Journal of Lightwave Technol.*, vol. 27, iss. 8, April 2009, pp. 967–973, doi: 10.1109/JLT.2008.2004950
- [13] J. Li, et al.: Optical communication using subcarrier PSK intensity modulation through atmospheric turbulence channels, *IEEE Transaction on Communication*, vol. 55, iss. 8, Aug. 2007, pp. 1598–1606, doi: 10.1109/TCOMM.2007.902592
- [14] A. M. Mbah, et al.: Performance evaluation of digital pulse position modulation for wavelength division multiplexing FSO systems impaired by interchannel crosstalk, *IET Optoelectronics*, vol. 8, iss. 6, Dec. 2014, pp. 245-255, doi: 10.1049/iet-opt.2013.0145
- [15] R. Agalliu, M. Lucki: Benefits and Limits of Modulation Formats for Optical Communications, *Advances in Electrical and Electronic Engineering*, vol. 12, no. 2, Jun. 2014, pp. 160-167, doi: 10.15598/aeec.v12i2.992
- [16] X. Tang, Z. Ghassemlooy, S. Rajbhandari, W. O. Popoola, M. Uysal, D. Wu, "Experimental demonstration of polarisation shift keying in the free space optical turbulence channel", *Communications in China Workshops (ICCC) 2012 1st IEEE International Conference on*, pp. 31-36, 2012.
- [17] S. Rajbhandari et al., "On the study of the FSO link performance under controlled turbulence and fog atmospheric conditions," *Proceedings of the 11th International Conference on Telecommunications*, Graz, 2011, pp. 223-226.
- [18] National Instruments, Modulation Error Ratio (MER) and Error Vector Magnitude (EVM), <http://www.ni.com/white-paper/3652/en/>.

Measurement of IPTV Services on a Hybrid Access Network

Jan Latal*, Zdenek Wilcek*, Jakub Kolar*, and Josef Vojtech**

**Department of Telecommunications, Faculty of Electrical Engineering and Computer Science, VSB-Technical University of Ostrava, 17. listopadu 15, 708 33 Ostrava, Czech Republic*

** *CESNET, a. l. e., Zikova 1903/4, 160 00 Prague 6, Czech Republic*

Tel.: +420 597 325 845, E-mail: jan.latal@vsb.cz

ABSTRACT

Future telecommunication networks will be formed by means of different types of telecommunication systems that were used in the past. Considering expanding options of today's smart mobile phones there is increasing pressure on telecommunication operators, who face a challenge how to cooperate across different telecommunication systems within their networks. The work focuses on the expansion of IPTV data flow on a hybrid network that is formed by the EPON and ADSL technologies. Along with the hybrid topology we focus on comparing multicast and unicast expansion of IPTV data traffic within this work.

Keywords: IPTV, hybrid network, EPON, ADSL, MSE, PSNR, SSIM.

1. INTRODUCTION

In recent years, new possibilities of distribution of data or multimedia services to end customers appear. The term multimedia services means the distribution of services known as Triple Play (IPTV, VoIP, Data). As demand for their deployment from end users rapidly grows, the pressure on telecommunication operator increases. They face the decision on how to move towards (CAPEx) investment into telecommunication infrastructure taking into account its return and effective management (OPEx). The simplest approach is to use already existing infrastructure and its maximum utilization. Nevertheless, this leads to coexistence of different types of telecommunication systems.

The IPTV is one of the key Internet applications and it has been used substantially during the last decade due to the introduction of a new technology of video stream spreading on the television networks. The IPTV can offer a greater possibility of interactivity to end users by means of the IP protocol. It is believed that the video stream transmission will cover approximately 1 million minutes of data per second in 2017, accounting roughly for 80–90% of the total data volume on the networks. The IPTV service needs an appropriate solution to bandwidth throttling in the access part of telecommunication networks. The IPTV consists of live TV, time-shifted TV, and video on demand (VoD). Based on the type we divide them into controlled and uncontrolled categories [1-7]. In the article, the team of authors mainly focused on the real creation of the hybrid topology of the telecommunication system for access networks of end users. This is a combination of the EPON technologies in an optical domain with a metallic part of the network in the form of ADSL 2+. Different profiles of multimedia streams represented by different types of video compression (MPEG2,4 SD/HD) were tested on the given topology. The basic video quality parameters (PSNR, MSE, SSIM) were evaluated afterwards by means of the software tool MSU Video Quality Measurement Tool.

2. STATE OF THE ART

The team of authors lead by the C.A.A. studied the QoS possibilities on the created topology of the LTEa EPON network with regard to dynamic assignment requirements [8]. In this article, the authors focused on creating a topology that was formed by a WDM-RoFSOPON connection with transmission of the TP services. In order to improve performance and extend the route, they have optimised the use of the RSOA amplifier [9]. On the EPON – WLAN (WiMAX) topology, the team of the authors has simulated the possibility of improvement of the QoS metrics for the future FiWi networks from traffic class mapping, scheduling, and resource management to advanced aggregation techniques, congestion control, and layer-2 path selection algorithms [10]. The authors monitored the QoS parameters for spreading data streams on the hybrid topology that was formed by the EPON network and the WiMAX radio network. It has been revealed that the given topologies must be necessarily combined appropriately and the dynamic bandwidth allocation algorithm, an intra ONU-BS (integrated optical network unit and WiMAX base station) scheduling algorithm, and a QoS mapping mechanism need to be implemented [11].

In the article by Dohoon Kim [12] and the colleagues, the possibilities of DSL lines for the QoS of multimedia services were investigated with the aim to achieve higher QoE quality through the House of Quality framework combined with the Analytic Hierarchy Process. In the article by I-Shyan Hwang [13] and the colleagues, they have found a new way of algorithm for allocating LLID for individual IPTV data streams (channels) on the basic topology. The basic topology refers to the EPON network, which operates on transport layer with the Ethernet protocol (defined by IEEE 802.3). The results from their simulations showed that the proposed mechanism can improve the QoS metrics in terms of the bandwidth need, packet loss and queue length.

The authors' team concentrated on the issue of the DBA solution on the PON networks for multimedia services with regard to the QoS. The aim of the work was to distribute the bandwidth controlling from only OLT to inside each ONU in an intelligent way [14]. A special algorithm of the P2P application-aware mechanism in EPON for lowering the cost Inter-ISP traffic and improving overall system performances, such as delay, was proposed in the article [15]. In the OPNET software, another team of authors attempted to simulate a prediction of the interaction between technical parameters of the QoS versus QoE telecommunication network under realistic conditions of the Triple Play network with the use of the IPTV protocol [16]. Under the normal conditions, the distribution of multimedia content is mainly used for the IPTV through the multicast technology without decreasing the quality of QoS. However, it has been discussed whether the use of other types of flow distribution may offer new options (on application layer) of how to approach the issue of IP packet routing (unicast, multicast) with multimedia content to end users [17].

3. TRIPLE PLAY

Telephone operators are now using new strategies for providing new services to their customers by using the networks of new generation. The entire service package includes a fixed line in combination with the Internet access, IP television, video on demand, and other applications. All of these services are distributed through the IP protocol (3rd layer of the ISO/OSI model) on the Ethernet (2nd layer of ISO/OSI model) network. The services are differentiated by the use of the transport layer (4th layer of the ISO/OSI model). The TCP protocol (Transmission Control Protocol), which ensures a joint and reliable data transfer, is used for the transmission of data service. In case of the data loss, the lost data is sent back again. The multimedia services VOIP and IPTV use the UDP protocol, which is disjoint and unreliable character of the data distribution. In case of the loss, the lost data is not sent back. This eliminates the delay, but degrades the service, which then results in the image defect or audio quality degradation. It follows from the foregoing that it is necessary to pay proper attention to these services within the telecommunication networks and based on the needs of end customers it is necessary to adjust the parameters of the network. Various measurements and evaluation methodologies were defined in order to meet the conditions of the service quality.

4. METHODS FOR DETERMINING THE QUALITY OF IPTV

There is a recommendation to evaluate the image quality and video signal, e.g.: ITU-T P.910. Subjective measurement of image quality and video signal is based on the factor of human perception. The advantage of this measurement is that a person is able to describe the image based on the reality and, as a result of this, the information, which is imperceptible to the human eye, is limited. The subjective measurement is influenced by a number of factors and it is difficult to take repeated subjective measurements. There are a few approaches to IPTV quality measurements, such as MSE, PSNR, SSIM, MDI, or MPQM (Moving Pictures Quality Metric) from a range of objective methods. The group of subjective IPTV quality assessment methods includes the MOS (Mean Opinion Score), DSCQS (Double Stimulus Continuous Quality Scale), DSIS (Double Stimulus Impairment Scale), ACR (Absolute Category Rating). Within our measurements we primarily focused on the objective IPTV quality assessment methods, specifically on the MSE, PSNR, and SSIM, which are described below in more detail, and, subsequently, their real-time values are delivered within the next chapters [18-20].

4.1 DCR (Degradation Category Rating)

Degradation Category Rating is also described in the ITU-T Recommendation P.910. In comparison with the ACR the difference is that the evaluators watch the reference video first. This video is played again before each evaluated sample. The participants evaluate the video according to the Tab. 1. The final outcome is again the average rating of a particular video [18-20].

Table 1. Scale of aggravation for DCR.

Grading value	Estimated impairment level
5	imperceptible
4	perceptible, but not annoying
3	slightly annoying
2	annoying
1	very annoying

4.2 DSCQS (Double Stimulus Continuous Quality Scale)

Double Stimulus Continuous Quality Scale method is standardized in the ITU-R Recommendation BT.500, and is widely used to assess the systems used for television broadcasting. The subject is shown a couple of videos, including the reference video, twice in a row. The videos are presented in random order and the evaluators have no idea, which of them is the reference one. The subject evaluates the video in the range of five categories. The

assessment scale is standardized to a range of 0-100 and the assessment of the evaluated video is subtracted from the assessment of the reference video. The resulting values are further averaged. A smaller value means a better video, i.e. a smaller difference from the reference video [18-20].

4.3 MSE (Mean Square Error)

The MSE represents the mean square error of the received video signal in comparison with the original one. This formula is used for the calculation:

$$MSE = \frac{1}{MN} \sum_{j=0}^{M-1} \sum_{i=0}^{N-1} (x_{ij} - y_{ij})^2 [-] \quad (1)$$

where x is the original image, y is the received image, the elements i, j are the elements of the image matrix, M is the number of pixels per height of the image and N is the number of pixels per width of the image.

4.4 PSNR (Peak Signal to Noise Ratio)

The PSNR represents the ratio between the highest value comparing to the MSE and is expressed by the formula:

$$PSNR = 10 \cdot \log_{10} \left(\frac{m^2}{MSE} \right) = 20 \cdot \log_{10} (m) - 10 \cdot \log_{10} (MSE) [dB] \quad (2)$$

where m is the maximum value that a pixel can get.

4.5 SSIM (Structural Similarity Index)

The SSIM parameter takes into account the human visual system. It measures the similarity between two images. The SSIM was designed to improve traditional metrics, such as the MSE and PSNR, which proved to be in conflict with human perception. The reference values are in the interval $<0,1>$, where 0 means a zero relation to the original image and 1 is achieved by comparing two identical images.

$$SSIM(x, y) = [l(x, y)]^\alpha [c(x, y)]^\beta [s(x, y)]^\gamma \quad (3)$$

The element $l(x, y)$ is used to compare the signal brightness, the element $c(x, y)$ compares the signal contrast, and the element $s(x, y)$ serves to measure the structural correlation that is calculated from the relations:

$$l(x, y) = \frac{2\mu_x \cdot \mu_y + C_1}{\mu_x^2 + \mu_y^2 + C_1} \quad (4)$$

$$c(x, y) = \frac{2\sigma_x \cdot \sigma_y + C_2}{\sigma_x^2 + \sigma_y^2 + C_2} \quad (5)$$

$$s(x, y) = \frac{\sigma_{xy} + C_3}{\sigma_x \cdot \sigma_y + C_3} \quad (6)$$

where μ_x and μ_y represent the average of the samples x and y , σ_x and σ_y represent the standard deviation of the samples x and y . The constants C_1 , C_2 and C_3 are used for stabilization in case the average and variance are very small. The parameters $\alpha > 0$, $\beta > 0$ and $\gamma > 0$ are used to set the relative importance of the three elements. These elements do not depend on each other, therefore the change in brightness and contrast has little effect on the structure of the image. These parameter settings $\alpha = \beta = \gamma = 1$ and $C_3 = C_2/2$ are used to simplify the SSIM, then (3) reduces to (7):

$$SSIM(x, y) = \left(\frac{2\mu_x \cdot \mu_y + C_1}{2\mu_x^2 \cdot \mu_y^2 + C_1} \right) \cdot \left(\frac{2\sigma_x \cdot \sigma_y + C_2}{2\sigma_x^2 \cdot \sigma_y^2 + C_2} \right) \quad (7)$$

The SSIM index is calculated for each pixel (i, j) . The quality of the entire image is calculated by using a medium SSIM index.

$$MSSIM = \frac{1}{M} \sum_i \sum_j SSIM(i, j) \quad (8)$$

where M is the total number of local SSIM indexes.

5. IPTV QUALITY MEASUREMENT

The measurement of the quality services on the real route was carried out by software tools. In case of the IPTV, the MSU Video Quality Measurement Tool was used. In case of the IPTV, the unicast and multicast operation was examined. Both of these types of the operation were examined by means of the MSQ VQMT. The Table 2 lists the characteristics of the examined video samples. These types of the video samples were intentionally

chosen with respect to the types of compression codex for video streams by providers of the Internet connection. These are MPEG-2 HD, MPEG-2 SD and the highest quality of MPEG-4 HD.

Table 2. Video samples for IPTV testing.

Testing IPTV	File	Frames/sec.	Resolution	Codec
MPEG-2 HD	MPEG	59	1280×720	MPEG-2
MPEG-4 HD	AVI	23	1280×720	MPEG-4
MPEG-2 SD	MPEG	25	720×576	MPEG-2

6. TOPOLOGY FOR IPTV MEASUREMENT

The topology, see Fig. 1 below, was used for the IPTV measurement. The given topology was formed by an optical and metallic part, where the optical part was variable with a setting of 0 to 10 km and the metallic part (typified cable SYKY 2x2x0.5) was selected in reach of 2 km. The length of the 2-kilometer metallic path, where the signal degradation is still not so evident, was chosen. The transfer profile with the speeds of 4096 Kbit/s and downstream 32000 Kbit/s was used for the ADSL2+. The topology includes a server that uses the VLC player to distribute the IPTV traffic into the given topology. At the end of the network, there is a participant's computer, which also detects and processes the operation into a visual form by means of the VLC Player Programme. The optical path was formed by an optical fibre of the G.652D type. As an active system, the OLT unit of the EPON technology type 2 with the following basic parameters: the range of about 20 km, the maximum defined split ratio of 1:32 at the used wavelengths – 1310 nm (upstream), 1490 nm (downstream) and a transmission rate of 1 Gbps or 1.25 Gbps, where 250 Mbps is used for overhead needed for data transmission and administration [5]. On the connection (see Fig. 1) the unicast and multicast traffic were used for the distribution of the video stream. The goal of selecting IP datagrams distribution was to determine whether mode selection affects the quality of the IPTV data transmission with selected codecs and topology parameters. The IP multicast is a method of forwarding the IP datagrams from one source to a group of multiple end stations. Instead of sending each datagram to each destination, only a single datagram is sent. The unicast indicates sending packets only into one destination (node, station) on the computer network. In case you need do deliver the same data to multiple nodes at the same time, it is more convenient to use multicast or broadcast (for example, audio or video streaming for conference calls, IPTV, etc.).

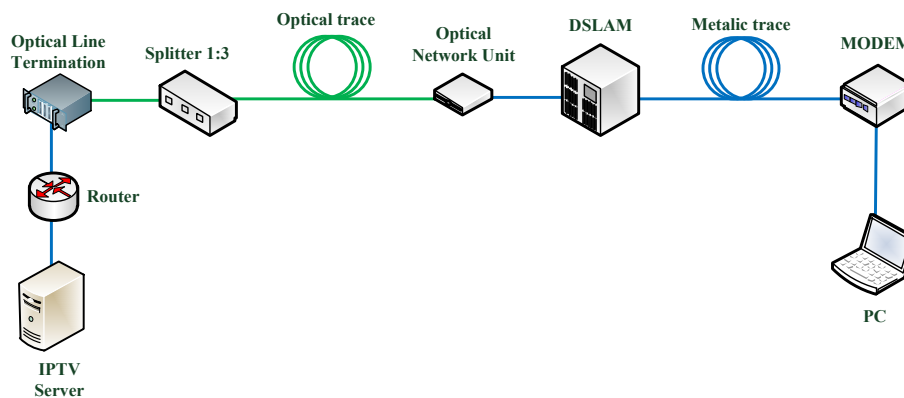


Figure 1. Topology of hybrid network.

7. MSU VIDEO QUALITY MEASUREMENT TOOL

Testing by means of this software was carried out by comparing the stream video (see samples in Tab. 2) recorded by the VLC player with the original video. The samples were compared by using the objective MSE, PSNR and SSIM methods. In both cases we can see that chosen path lengths for either optical or metallic part have almost no effect on the quality of the SDTV video (MPEG-2 SD). The MPEG4-HD video sample gets worse by adding a metallic path, as well as the MPEG2-HD video sample. The only difference can be seen in video quality on a route with simulated 2 km length. The resulting MPEG4-HD sample quality is many times worse in comparison with the 2 km real route. On the contrary, the MPEG2-HD sample shows better quality by using a simulated route. In the Fig. 3 we can see the influence of the routes on the value of the SSIM parameter that measures the similarity between the two images, and takes into account the human visual system. We can notice a slightly more significant drop in the MPEG2-HD video when adding a metallic path.

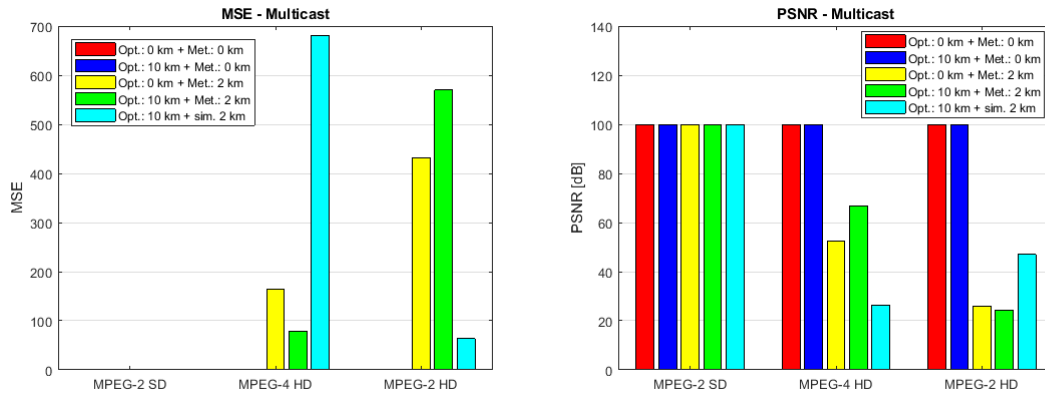


Figure 2. ADSL – Multicast, MSE (left) and PSNR (right).

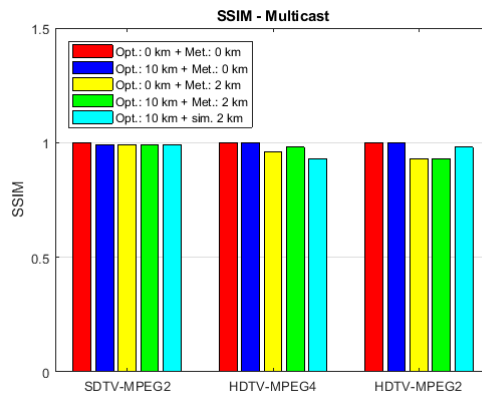


Figure 3. ADSL – Multicast, SSIM.

In Fig. 4 we can notice a significant drop in the SDTV video quality in the unicast traffic. This quality, however, does not change with the extension of the route. So, we can assume that the problem is that the video was multiplexed before the streaming itself. It mostly affected the MPEG2-SD video quality, when the value of the peak signal to noise ratio (PSNR) dropped from 100 dB to 22.5 dB. This must have been necessarily reflected by the SSIM parameter (see Fig. 5), which has fallen to 0.7. The MPEG4-HD and MPEG2-HD are also not significantly affected by the length of the route, but rather by the implemented multiplex. The exception is the MPEG2-HD video without a route that achieves the quality of the original video.

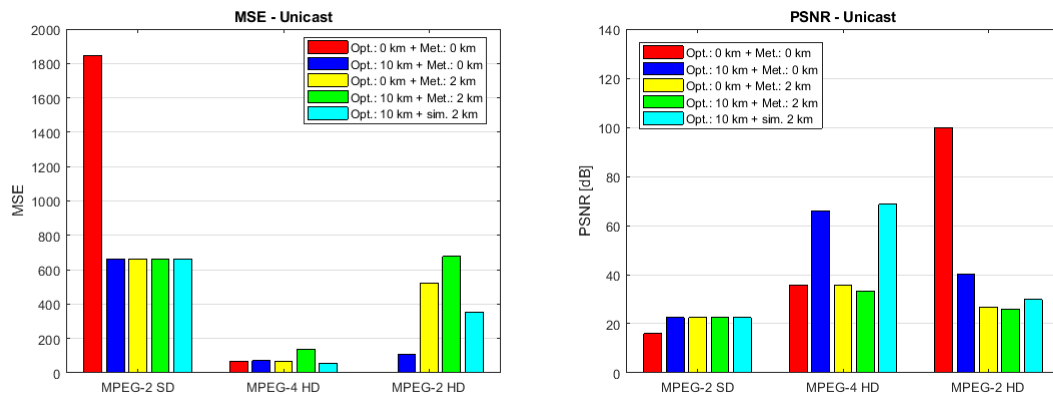


Figure 4. ADSL – Unicast, MSE (left) and PSNR (right).

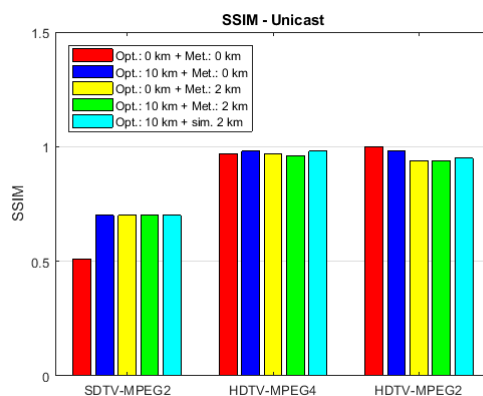


Figure 5. ADSL – Unicast, SSIM.

8. CONCLUSIONS

The actual real measurements confirmed the fact that the EP-type networks combined with the ADSL2+ may transmit the multi-media stream with the video either in SD or HD quality for MPEG2 or MPEG4 without any major difficulties through the IPTV protocol with regard to objective video quality assessment. Unfortunately, there is a problem with the metallic part. If the end user was at a great distance from the DSLAM, the video could be significantly degraded, which results in a decrease in the QoS parameters of the telecommunication network. The future works will focus more deeply on the issue of studying the QoS network, observation of the QoE, and also the usage of other types of topologies including new types of the video compression codecs.

ACKNOWLEDGEMENTS

The research described in this article could be carried out thanks to the active support of the projects no. VI20172019071, CESNET 614R1/2017, SP2018/117 and SP2018/184. The work has been partially supported by Project No. CZ.1.07/2.3.00/20.0217. This work was supported partially by the Ministry of Education, Youth and Sport of the Czech Republic by the project "E infrastructure CESNET - modernization", reg. nr. CZ.02.1.01/0.0/0.0/16_013/0001797.

REFERENCES

- [1] P. Bhaumik, A. Sayeem Reaz, and B. Mukherjee, "Performance of 10G-EPON in streaming IPTV," in Proc. *2012 IEEE International Conference on Advanced Networks and Telecommunications Systems (ANTS)*, Bangalore, India, pp. 30-32.
- [2] J. Litvik, I. Dolnak, M. Dado, and M. Kuba, "Computational effective numerical models of the active semiconductor components in the optical communication systems," in Proc. *2017 Conference on Microwave Techniques (COMITE)*, Brno, Czechia, pp. 1-6.
- [3] L. D. Lamb, "Status and evolution of EPON: From IPTV today to 10Gb/s and beyond," in Proc. *2006 European Conference on Optical Communications*, Cannes, France, pp. 1-2.
- [4] Yaling Nie, "A multicast QoS control scheme and system in EPON system," in Proc. *2007 6th International Workshop on Design and Reliable Communication Networks*, La Rochelle, France, pp. 1-4.
- [5] L. G. Kazovsky, N. Cheng, W. Shaw, D. Gutierrez, and W. Shing-Wa, *Broadband Optical Access Networks*, Canada, Wiley, p. 283, 2011.
- [6] C. Burtscher, D. Seyringer, and M. Lucki, "Comparison of splitting properties of various 1×16 splitters," *Advances in Electrical and Electronic Engineering*, vol. 15, no. 1, pp. 107-113, 2017.
- [7] R. Agalliu, C. Burtscher, M. Lucki, and D. Seyringer, "Optical splitter design for telecommunication access networks with triple-play services," *J. of Electrical Engineering*, vol. 69, no.1, pp. 32-38, 2018.
- [8] C. A. Astudillo and N. L. S. Da Fonseca, "Standard-compliant QoS provisioning scheme for LTE/EPON integrated networks," *IEEE Wireless Communications*, vol. 21, no. 3, pp. 44-51, Jun. 2014.
- [9] G. Ch. Mandal, R. Mukherjee, B. Das, and A. S. Patra, "Next-generation bidirectional triple-play services using RSOA based WDM radio on free-space optics PON," *Optics Communications*, vol. 411, pp. 138-142, 2018.
- [10] M. Maier and N. Ghazisaidi, "QoS provisioning techniques for future fiber-wireless (FiWi) access networks," *Future Internet*, vol. 2, no. 2, pp. 126-155, 2010.
- [11] C. Ranaweera, E. Wong, C. Lim, and A. Nirmalathas, "Quality of service assurance in EPON-WiMAX converged network," in Proc. *2011 International Topical Meeting on Microwave Photonics* jointly held with *2011 Asia-Pacific Microwave Photonics Conference*, Singapore, 2011, pp. 369-372.

- [12] D. Kim, "Application of the HoQ framework to improving QoE of broadband internet services," *IEEE Network*, vol. 24, no. 2, 2010.
- [13] I. S. Hwang, A. Nikoukar, A. T. Liem, and K. C. Chen, "A new architecture for multicasting live IPTV traffic in Ethernet passive optical network," in Proc. *2013 International Conference on Electronics, Computer and Computation (ICECCO)*, Ankara, pp. 60-63.
- [14] S. K. H. Sadon, S. M. Mitani, T. Kanesan, H. M. Hizan, and R. Mohamed, "Quality of service (QoS) analysis for decentralized passive optical network (PON) intelligent algorithm," *WSEAS Transactions on Communications*, vol. 15, pp. 202-205, 2016.
- [15] A. T. Liem, I. S. Hwang and, A. Nikoukar, "Peer-to-peer application-aware mechanism for enhancing video streaming in enhanced EPON," in Proc. *2015 International Conference on Electrical Engineering and Informatics (ICEEI)*, Denpasar, Indonesia, pp. 590-593.
- [16] M. Nuhbegović, A. Čolaković, and A. Hasković, "Validating IPTV service quality under realistic triple play network conditions," in Proc. *2014 X International Symposium on Telecommunications (BIHTEL)*, Sarajevo, pp. 1-6.
- [17] S. A. Hadiwardoyo, "An overview of multicast routing techniques for group communications applications," in Proc. *2017 25th Telecommunication Forum (TELFOR)*, Belgrade, Serbia, pp. 1-4.
- [18] S. Winkler and P. Mohandas, "The evolution of video quality measurement: From PSNR to hybrid metrics," *IEEE Transactions on Broadcasting*, vol. 54, no. 3, pp. 660-668, 2008.
- [19] Z. Wang, A. C. Bovik, H. R. Sheikh and E. P. Simoncelli, "Image quality assessment: from error visibility to structural similarity," *IEEE Transactions on Image Processing*, vol.13, no. 4, pp. 600-612, 2004.
- [20] H. R. Sheikh and A.C. Bovik, "Image information and visual quality," *IEEE Transactions on Image Processing*, vol.15, no. 2, pp. 430-444, 2006.

Illumination and Communication Characteristics of YAG:Ce Phosphor Powders

Jan Vitasek, Jan Jargus, Jan Latal, Tomas Stratil, and Zdeněk Wilček

Department of Telecommunications, Faculty of Electrical Engineering and Computer Science,
VSB–Technical University of Ostrava, 17. listopadu 15, 708 33 Ostrava, Czech Republic

Tel: 00420 596 999 413, Fax: +420 596 991 650, e-mail: jan.vitasek@vsb.cz

ABSTRACT

This article deals with a comparison of illumination and communication characteristics of white light which is created by excitation of phosphor powder by blue power LED. There are tested two phosphor powders with little different chemical composition. The communication parameters are rise, fall, and photoluminescence decay times. Illumination parameters are colour coordinates and Colour Correlated Temperature. These characteristics are important for VLC technology. The phosphor powders were mixed with Poly-Di-Methyl-Siloxane (PDMS).

Keywords: blue LED, YAG:Ce, VLC, white light.

1. INTRODUCTION

Light Emitting Diodes (LEDs) are more and more used in everyday life. LED light bulbs and LED strips are used inside, LEDs are used in headlamps and tail lamps of cars, are used in lamps for street illumination. The classical light bulbs and fluorescent lamps are gradually replaced by LED light sources due to their better features and characteristics. If we compare the classical and LED illumination sources, we can say that LEDs reach much higher efficiency and their further improvements are expected. The other advantages of the LEDs are their longer lifetime, a smaller and compact size, minimum heat generation compared with the classical illumination sources, higher tolerance to humidity, and lower power consumption [1-4].

The other advantage of LEDs is their possible using for communication purposes. LEDs could be fast switched on and off in comparison to the classical light bulbs and fluorescent lamps. Therefore, the LEDs could be applied in automotive for Car-to-Car (C2C) communication and Car-to-Infrastructure (C2I) communication. Great potential is placed in Visible Light Communication (VLC) which should replace the Wi-Fi in the future. VLC technology combines two functions together, illumination and communication [1,5-8].

Creation of white light in LEDs is possible by two methods. The first method uses three colour chips (red, green and blue). Correct setting of intensity levels makes white light. This method is called as Colour Mixing, LEDs are labelled as RGB-LEDs. The other method is based on a conversion of light. A blue light emitting chip excites a yellow phosphor; a part of the blue light is converted in the yellow light which together with rest of blue light create white light. YAG:Ce materials are used as a converter. These LEDs are labelled as pc-LEDs (phosphor-converted) [1-3]. The disadvantage of the pc-LEDs is a photoluminescence (PL) decay. This article deals with features of white light created by the phosphor-converted method. We kept at disposal two YAG:Ce phosphor powders with little different chemical composition, QMK58/F-U2 ($Y_3Al_5O_{12}:Ce^{3+}$) and QUMK58/F-D1 ($(Y,Gd)_3Al_5O_{12}:Ce$). Manufacturer of these phosphor powders is Phosphor Technology Ltd.

These phosphor powders were mixed with Poly-Di-Methyl-Siloxane (PDMS) [9] polymer in the same weight concentration 1:35. The phosphor powders were excited by the blue power LED H2A1-H450 [10]. The results parameters were final spectra, colour coordinates x , y and also Correlated Colour Temperature (CCT). The parameters in communication domain was a rise time, fall time and PL decay time.

2. PHOTOLUMINESCENCE IN A PHOSPHOR POWDER

After light excitation by correct wavelengths, the electron transitions 5d-4f happen in YAG:Ce phosphor powders with large emission spectrum. Ce^{3+} has a valence electron configuration of $4f^1$, which gives rise to the $^2F_{5/2}$ and $^2F_{7/2}$ low-lying energy states. Consequently, the visible emission is a composite of two bands due to an electronic transition from the lowest lying 5d energy level down to the $^2F_{5/2}$ and $^2F_{7/2}$ states. Since the emission is due to an allowed 5d-4f electronic transition, it has a short lifetime of ca. 20 ns [11]. The Ce^{3+} activator ions substitute some of the Y^{3+} ions which are coordinated by eight O^{2-} anions in the host lattice of YAG. The Ce^{3+} ions consequently occupy sites of D_2 point group symmetry and the resulting crystal field causes the energies of the 5d orbitals to be split [12-13]. Five absorption bands at 204.6, 225.4, 261, 339.7 and 457.5 nm were observed in the absorption spectrum of YAG:Ce by Tomiki *et al.* [14] which were assigned to transitions from the $^2F_{5/2}$ ground state to each of the 5d levels. YAG:Ce phosphors can contain together with yttrium Y also Gadolinium Gd. Gd^{3+} ions are larger than Y^{3+} which causes a red shift of the Ce^{3+} emission due to the increased crystal field. Conversely, substitution of Al^{3+} ions for the larger Gd^{3+} ions on the octahedral sites gives a blue shift due to a weaker crystal field for the Ce^{3+} ions [11].

3. EXPERIMENTAL ARRANGEMENT

3.1 Poly-Di-Methyl-Siloxane Polymer

We needed to create some layer with phosphor powders. For this purpose, we used Poly-Di-Methyl-Siloxane (PDMS) names Sylgard 184 [9]. The Sylgard 184 has two components, a PDMS base and a curing agent. The phosphor powder was added to the Sylgard 184 in weight ratio 1:35. The mixture PDMS base-curing agent-phosphor was put in the laboratory shaker for the uniform distribution of all components. The heat hardening happens at temperature around 85 °C, it takes 30 minutes. The PDMS is optically transparent from the near UV up to NIR region of the spectra.

For the measurement, we used a reflector [15] for power LEDs. The mixture of PDMS+phosphor powder was poured into Petri dish. The output aperture of the reflector was also placed in Petri dish. After hardening, it the reflector was a 2 mm thin layer of PDMS+phosphor powder, Fig. 1.

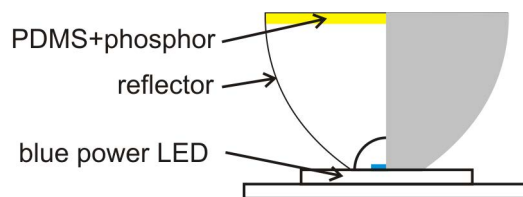


Figure 1. PDMS+phosphor powder in a reflector.

3.2 Illumination characteristics measurement

The blue power LED H2A1-H450 (peak wavelength 450 nm and FWHM 35 nm by forward current 350 mA) [10] was continually supplied by forward current from 50 mA to 350 mA with step 50 mA through a High Power Mounts TCLDM9 (Thorlabs) and Benchtop LD Current Controller LDC240C (Thorlabs). The total optical spectrum, colour coordinates x , y , and CCT was recorded for each forward current by the spectrometer Avantes HS2048XL together with an integrating sphere.

3.3 Communication characteristics measurement

The blue power LED H2A1-H450 [10] was modulated by a square signal (frequency 150 kHz, U_{\max} 10 V, U_{\min} 0 V). The power LED was supplied through High Power Mounts TCLDM9 (Thorlabs) and Benchtop LD Current Controller LDC240C (150 mA). The square signal was lead to TCLDM9 through RF input (50 Ω). That means, the high level was 350 mA (0.150 + 10/50), the low level was 150 mA. The photodetector was PDA36A-EC (Thorlabs), and output of this photodetector was connected to the oscilloscope LeCroy 204Xi, which automatically detected rise and fall edges.

The rise time is time, in which the intensity of signal rises from 0.1 to 0.9. Likewise, fall time is time, in which the intensity of signal falls from 0.9 to 0.1. The PL decay time is time, in which the intensity of signal falls from 1.0 to 0.386 [14].

4. ILLUMINATION CHARACTERISTICS RESULTS

The forward current of the excitation blue LED was gradually increased from 50 mA to 350 mA. At first, we measured the phosphor powder QMK58/F-U2. The measured values are summarized in Table 1. The same measurement was done with the phosphor powder QUMK58/F-D1, which includes moreover Gd element. The results are in Table 2. Figure 2 shows the final spectra of both phosphor powders, Fig. 3 shows measured x and y values in diagram CIE1931.

Table 1. Illumination characteristics of the phosphor powder QMK58/F-U2.

I_f (mA)	50	100	150	200	250	300	350
x (-)	0.3723	0.3711	0.3701	0.3692	0.3684	0.3679	0.3675
y (-)	0.4519	0.4483	0.4454	0.4430	0.4411	0.4398	0.4392
CCT (K)	4567.0	4580.8	4594.4	4606.4	4617.1	4625.7	4632.1

Table 2. Illumination characteristics of the phosphor powder QUMK58/F-D1.

I_f (mA)	50	100	150	200	250	300	350
x (-)	0.3756	0.3735	0.3716	0.3701	0.3690	0.3684	0.3689
y (-)	0.3826	0.3778	0.3740	0.3709	0.3687	0.3672	0.3672
CCT (K)	4176.4	4206.4	4235.9	4260.7	4280.9	4290.0	4274.4

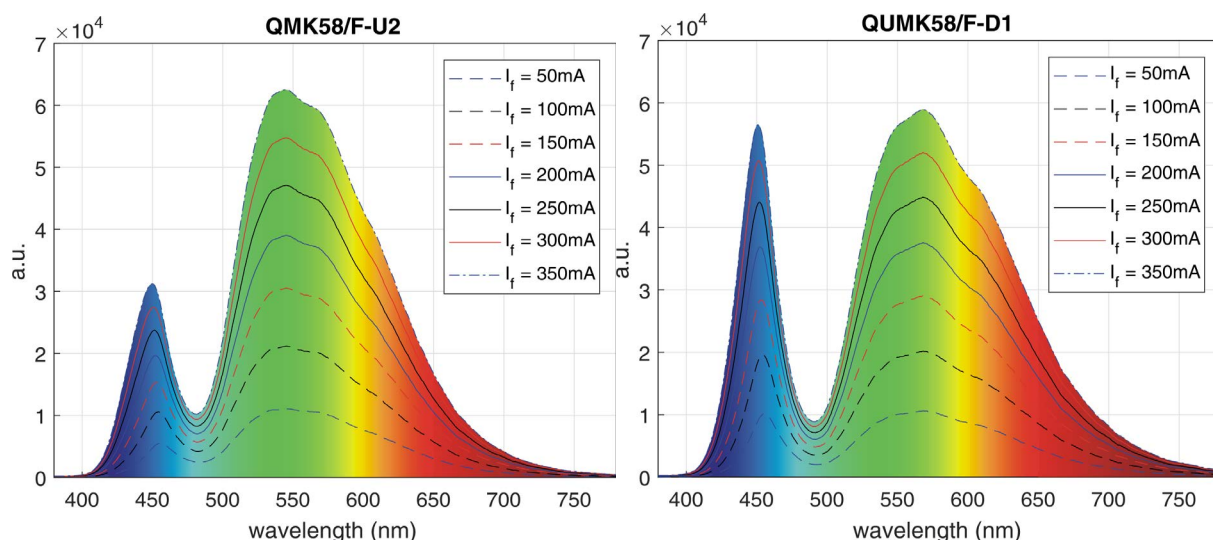


Figure 2. White spectra with phosphor powders QMK58/F-U2 (left) and QUMK58/F-D1 (right).

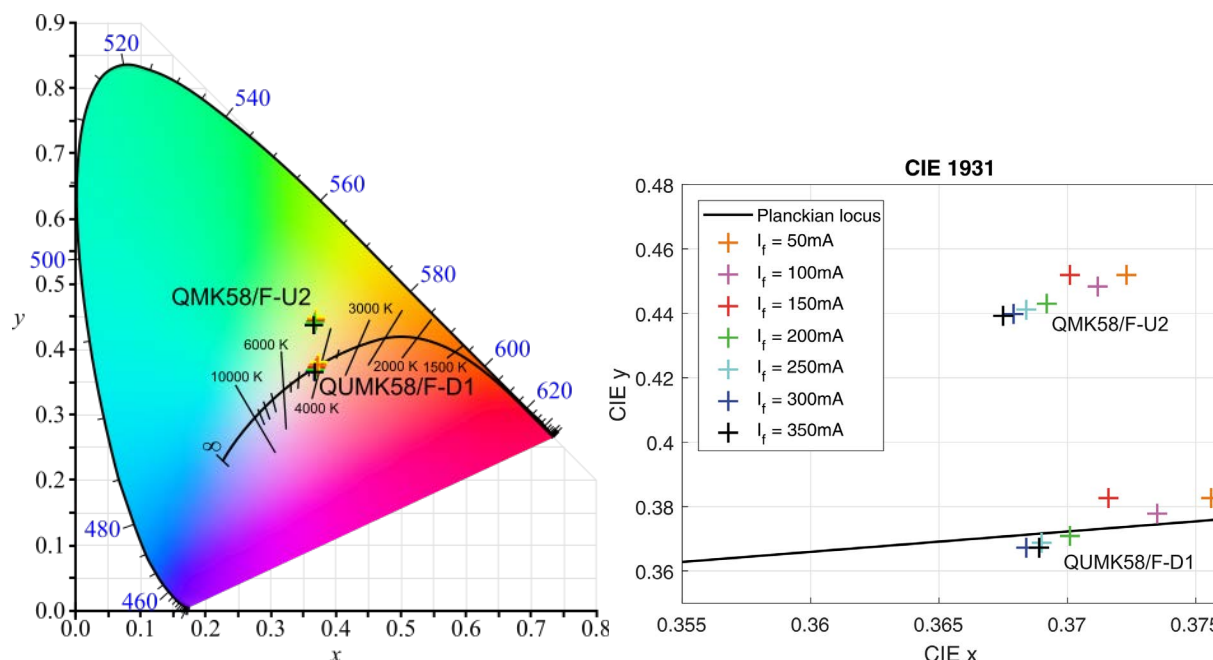


Figure 3. White spectra with phosphor powders QMK58/F-U2 (left) and QUMK58/F-D1 (right).

5. COMMUNICATION CHARACTERISTICS RESULTS

The exciting LED was modulated by the square signal described above. Measured values of rise, fall and PL decay times are in Table 3. Figure 4 shows a fall time and PL decay time of the phosphor powder QUMK58/F-D1.

Table 3. Rise, fall and PL decay times of phosphor powders QMK58/F-U2 and QUMK58/F-D1.

	Rise time t_r (ns)	Fall time t_f (ns)	Decay time t_d (ns)
QMK58/F-U2	115.72	122.97	78.80
QUMK58/F-D1	118.38	121.58	81.60

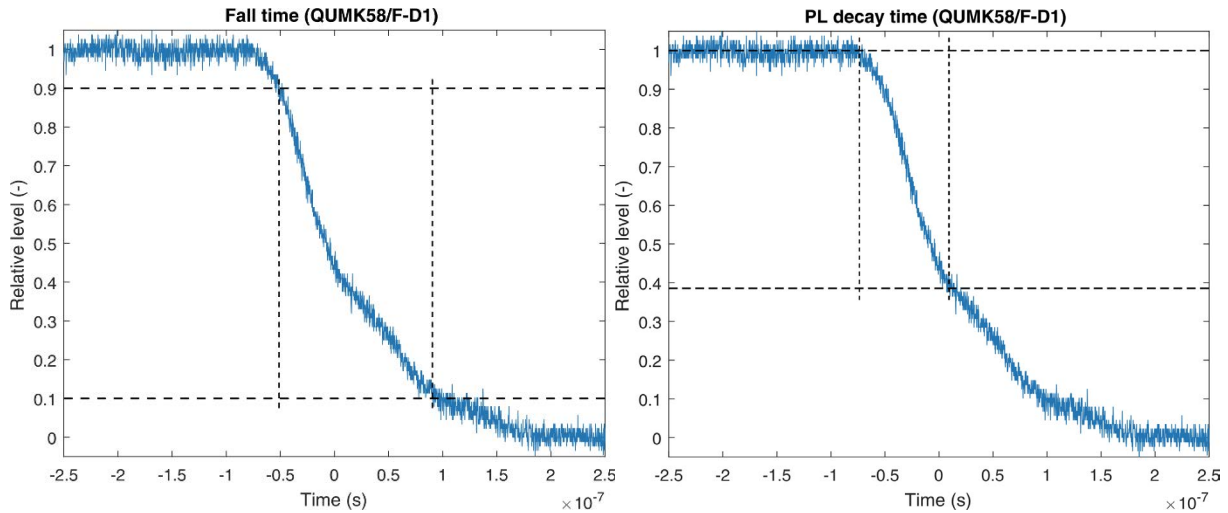


Figure 4. Fall (left) and PL decay (right) times of the phosphor powder QUMK58/F-D1.

6. DISCUSSION

The illumination characteristics of both phosphor powders are very similar. The CCT changed minimally with increasing forward current. The change could be calculated according to the relation (1), which is derived from the relative error

$$\Delta(\%) = \frac{CCT_{I_f=50mA} - CCT_{I_f=350mA}}{CCT_{I_f=350mA}} \quad (1)$$

where $CCT_{I_f=200mA}$ is the value of CCT measured by forward current 50 mA and $CCT_{I_f=350mA}$ is the value of CCT measured by forward current 350 mA. The difference Δ of CCT was 1.5% (QMK58/F-U2) and 2.3% (QUMK58/F-D1) respectively. These changes are very small and human eye is not able to recognize them. The CCT independence on the forward current is very good for modulation because the CCT stays practically constant.

The CCT of the phosphor powder QMK58/F-U2 is cooler than QUMK58/F-D1. The average CCTs were 4603.4 K (QMK58/F-U2) and 4246.4 K (QUMK58/F-D1) respectively. Therefore, both phosphor powders are usable for illumination purposes. Also, we can see the spectral red shift in QUMK58/F-D1 caused by Gd in Fig. 2. Therefore, the CCT of the QUMK58/F-D1 is warmer.

The communication characteristics of both phosphor powders are also very similar. The PL decay times are longer than is mentioned in books but this is probably caused by modulation features of the exciting power LED.

7. CONCLUSIONS

This article describes testing of two YAG:Ce phosphor powders for using in VLC. The tested parameters were illumination characteristics (spectra, colour coordinates and CCT) and communication characteristics (rise, fall and PL decay times). The used excitation light source was the blue power LED. Both phosphor powders created white light which is usable for illumination purposes. The average CCTs were 4603.4 K and 4246.4 K respectively, which is close to a day light. The communication characteristics were also very similar, there were not found any important difference between both phosphor powders. We can say, that both phosphor powders could be used for illumination and communication purposes.

ACKNOWLEDGEMENTS

The authors would like to acknowledge the financial support of the Ministry of Education, Youth and Sports of the Czech Republic under Projects No. SP2018/117 and SP2018/184 of VSB–Technical University of Ostrava, Czech Republic. Our research was also supported by Projects No. VI20172019071, VI20152020008 and TA04021263. The work has been partially supported by projects CZ.1.07/2.3.00/20.0217 and CZ.02.1.01/0.0/0.0/16_019/0000867.

REFERENCES

- [1] E. F. Schubert: *Light-Emitting Diodes*, Cambridge University Press, Cambridge, 2006.
- [2] T. Novak, B. Socha, Z. Carbol, and K. Sokansky: Luminance evaluation of LED indoor luminaires for workspaces lighting, in *Proc. 13th International Scientific Conference Electric Power Engineering 2012*, Brno, Czech Republic, May 2012.

- [3] R. Baleja, J. Sumpich, P. Bos, B. Helstynova, K. Sokansky, and T. Novak: Comparison of LED properties, compact fluorescent bulbs and bulbs in residential areas, in *Proc. 16th International Scientific Conference Electric Power Engineering 2015*, Kouty nad Desnou, Czech Republic, 2015.
- [4] T. Stratil, P. Koudelka, R. Martinek, and T. Novak: Active pre-equalizer for broadband over visible light, *Advances in Electrical and Electronic Engineering*, vol. 15, no. 3, pp. 553-560, Mar. 2017.
- [5] S. Arnon: Optimised optical wireless car-to-traffic-light communication, *Transactions on Emerging Telecommunications Technologies*, vol. 25, no. 6, pp. 660-665, Jun. 2014.
- [6] B.W. Kim and S.Y. Jung: Vehicle positioning scheme using V2V and V2I visible light communications, in *Proc. IEEE 83rd Vehicular Technology Conference*, Nanjing, 2016, pp. 1-5.
- [7] N. D. Q. Anh, T. H. Q. Minh, and N. H. K. Nhan: Enhancing lighting performance of white LED lamps by green emitting ce,tb phosphor, *Advances in Electrical and Electronic Engineering*, vol. 14, no. 5, pp. 609-614, Dec. 2016.
- [8] P. Jing, W. Huang, and L. Chen: Car-to-pedestrian communication safety system based on the vehicular ad-hoc network environment: A systematic review, *Information*, vol. 8, no. 4, pp. 1-8, Dec 2017.
- [9] Sylgard 184 Silicone Elastomer Kit, Dow Corning [online], available at: <http://www.dowcorning.com/applications/search/default.aspx?R=131EN>.
- [10] H2A1-H450, Roithner Lasertechnik [online], http://www.roithner-laser.com/datasheets/led_highsingle/h2a1-h450.pdf.
- [11] R. Withnall and J. Silver, *Handbook of Visual Display Technology: Luminescence of Phosphors*, Springer, Berlin, 2012, pp. 1013-1028.
- [12] T. Teplicky, M. Danisova, M. Valica, D. Chorvat, and A. Marcek Chorvatova: Fluorescence properties of chlorella sp. algae, *Advances in Electrical and Electronic Engineering*, vol. 15, no. 2, pp. 352-357, Jun. 2017.
- [13] X. Xiao, H. Tang, T. Zhang, W. Chen, W. Chen, D. Wu, R. Wang, and K. Wang: Improving the modulation bandwidth of LED by CdSe/ZnS quantum dots for visible light communication, *Optics Express*, vol. 24, no. 19, pp. 21577-21586, 2016.
- [14] T. Tomiki, H. Akamine, M. Gushiken, Y. Kinjoh, M. Miyazato, T. Miyazato, N. Toyokawa, M. Hiraoka, N. Hirata, Y. Ganaha, and T. Fudemma: Ce³⁺ centres in Y₃Al₅O₁₂ (YAG) single crystals, *Journal of the Physical Society of Japan*, vol. 60, no. 7, pp. 2437-2445, 1991.
- [15] Power LED reflectors, *Roithner LaserTechnik* [online], http://www.roithner-laser.com/datasheets/led_optics/clp17cr_clp20cr.pdf.

Fog Influence Simulation on Light Distribution from Street Lighting

Jan Vitasek, Jan Latal, Tomas Stratil, Jan Jargus, and Zdenek Wilcek

Department of Telecommunications, Faculty of Electrical Engineering and Computer Science,

VSB–Technical University of Ostrava, 17. listopadu 15, 708 33 Ostrava, Czech Republic

Tel: +420 596 999 413, Fax: +420 596 991 650, e-mail: jan.vitasek@vsb.cz

ABSTRACT

This article deals with a study of the influence of fog on street lighting. Modern luminaires of street lighting use LED diodes to illumination. The LEDs have several advantages in comparison to traditional light sources, one of their main advantage is an ability to transmit data and engage so in concept "Smart City". The disadvantage of outdoor optical links could be a presence of contrary meteorological conditions as a fog. In software LightTools, a model of street lighting luminaire was created according to real model and also four kinds of fog. The fog is divided according to its influence on the distribution of light.

Keywords: fog weather, LightTools, meteorological visibility, street lighting.

1. INTRODUCTION

Illumination is one of the main topics which are currently developed. It refers to outdoor and indoor. The light bulbs and fluorescent lamps were used for illumination purposes a long time. These light sources are gradually replaced by LEDs. The reason for this replacement is above all the features of LEDs. LEDs reach much higher efficiency and their further improvements are expected. The other advantages of the LEDs are their longer lifetime, a smaller and compact size, minimum heat generation compared with the classical illumination sources, higher tolerance to humidity, and lower power consumption. The LEDs are mercury free. That are the reasons why the LEDs gradually replace the traditional illumination sources. We can meet them in shape of LED light bulbs and fluorescent lamps or in head and tail lamps of cars and also the street lighting is not an exception [1-6].

The next great advantage of LEDs against to traditional light sources is their ability to provide a communication. LEDs could be switched on and off very fast; human eye is not able to make out these changes. Fast enough switching on and off is important presumption for data transmission. Thus, LEDs are able to provide two functions at the same time, illumination and communication. LED using in street lighting so can provide traditional illumination and data for pedestrians or road users. The street lighting luminaires so could be one of a key element of "Smart" and engage in concept "Smart City". Further, it is possible to regulate the emitting power of street lighting and decrease their power consumption [1-4,7].

2. ATMOSPHERIC EFFECTS INFLUENCING ON PROPAGATION OF LIGHT

The biggest disadvantage of optical atmospheric links is the transmission environment itself, the atmosphere. In the atmosphere, there can appear meteorological effects which can markedly influence on propagation of light. The worst effect is a fog. The fog consists of fine water droplets; their diameter is comparable with the wavelength of used light. The diameter of fog droplets is in range 1 – 10 μm , concentration in 1 mm^3 is 10 – 100 [8]. The Mie scattering happens on fog droplets because the diameter and wavelength are similar. The scattering is asymmetrical, a front lobe dominates in case of greater particles, a back lobe is smaller. This effect is contrary in case of smaller particles [9].

The influence of the fog on optical beam could be set by the help of an extinction coefficient [10]. The extinction coefficient could be expressed by a meteorological visibility V_M . The meteorological visibility is defined as a distance, at which the transmittance reaches a value $T = 0.02 = 2\%$ at the wavelength 555 nm. A general relation between meteorological visibility V_M and extinction coefficient α_e (km^{-1}) is

$$\alpha_e \approx \frac{3.91}{V_M} \left(\frac{\lambda}{555} \right)^{-q} \quad (1)$$

where λ is the wavelength of used light and parameter q is determined by empirical models. Parameter q is defined according to Kruse or Kim model in dependence on meteorological visibility. The extinction coefficient α_e could be converted into an attenuation coefficient α ($\text{dB} \cdot \text{km}^{-1}$) according to the relation

$$\alpha = \frac{\alpha_e}{0.23} = \frac{17}{V_M} \left(\frac{\lambda}{555} \right)^{-q} \quad (2)$$

The extinction coefficient α_e exponentially decreases the optical intensity according to the relation

$$I_1 = I_0 \exp(\alpha_e \cdot z) \quad (3)$$

where z is distance. The extinction coefficient α_e could be also expressed by the help of the meteorological visibility

$$\alpha_e = \frac{-\ln T}{V_M} \quad (4)$$

where T is transmittance of the atmosphere $T = 0.02$ and V_M is the meteorological visibility.

3. SIMULATION SETTING

3.1 LightTools

The LightTools (LT) is a 3D optical engineering and design software product that supports virtual prototyping, simulation, optimization and photorealistic renderings of illumination applications. Its unique design and analysis capabilities, combined with ease of use, support for rapid design iterations, and automatic system optimization, help to ensure the delivery of illumination designs according to specifications and schedule [11].

3.2 Boos Naica Luminaire

We have the real street lighting luminaire Boos Naica [12] for testing. The technical parameters of this luminaire are: colour temperature 4000 K, luminous flux 47000 lm, size 675×421×124 mm (L×B×H). The luminaire includes 144 LEDs arranged in a rectangle. A model of this luminaire was created in LightTools software for following simulations and evaluations.

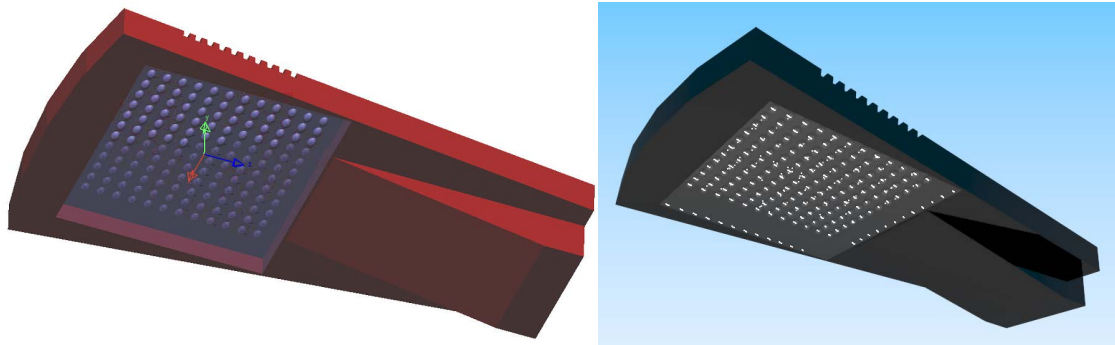


Figure 1. Boos lamp simulated in LightTools.

3.3 Calculation and Setting of the Fog

In the technical books and articles, we can find several kinds of the fog according to the attenuation coefficient [4]: dense fog 315 dB·km⁻¹, thick fog 75 dB·km⁻¹, moderate fog 28.9 dB·km⁻¹ and light fog 18.3 dB·km⁻¹. At first, we found the meteorological visibility V_M for these attenuation coefficients α according to the Eq. (2). The knowledge of meteorological visibility V_M enables to calculate the extinction coefficient α_e according to the Eq. (4) and subsequently attenuation at a distance 5m according to Eq. (3). The calculations are summarized in Table 1.

Table 1. Parameters of the fogs.

Fog type	Attenuation coefficient α (dB·km ⁻¹)	Meteorological visibility V_M (km)	Extinction coefficient α_e (km ⁻¹)	Attenuation at 5 m (-)
Dense	315	0.054	72.40	0.6963
Thick	75	0.227	17.23	0.9175
Moderate	28.9	0.594	6.82	0.9665
Light	18.3	0.981	3.99	0.9803

According to these calculations, we created the above mentioned kinds of the fog in LightTools software. The LightTools enables to create a material (environment) with particles on which Mie scattering occurs. The parameters are particle size distribution (PSD), refraction index, particle number density in 1 mm³. In our laboratory, we measured the PSD of an artificial fog based on glycerine by the apparatus Scanning Mobility Particle Sizer (SMPS) Model 3936 (Aerosol. Neut 3088+CPC) which is able to analyse particles with the diameter in range 8 – 1000 nm. Figure 2 shows a histogram of measured PSD.

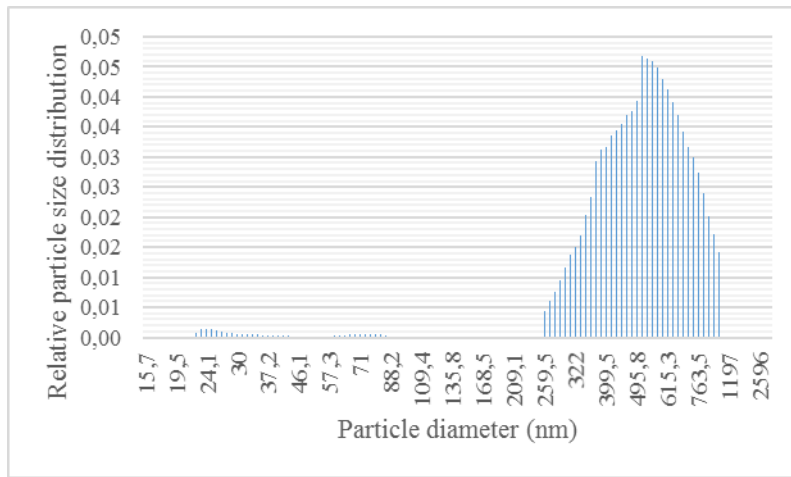


Figure 2. Histograms of measured PSD.

The real part of the refractive index of particles was set 1.33, the imaginary part 2.47×10^{-9} . Particle number density in 1 mm^3 was a variable value and determines the kind of the fog. The dense fog has 133 particles, the thick fog 32 particles, the moderate fog 13 particles and the light fog 7 particles in 1 mm^3 . The particle numbers were found in LightTools by an optimization process according to the attenuation at 5m mentioned in Table 1.

4. RESULTS AND COMMENTS

The target of the simulation was to find out how the different kinds of the fog effects on the distribution of light. The luminaire Boos Naica was placed in height 5m, the receiver plane had size $10 \times 10 \text{ m}$. Gradually we simulated dense, thick, moderate and light fogs and also clear air. The greatest light intensity is directly under the luminaire. There are not any important differences in kind of fog for street lighting luminaire Boos.

But the boundary conditions are also important. The intensity of light decreases with increasing distance from the centre. At the same time, the technical standards define the values of minimal intensity which has to be measured in given areas like roads, footpaths or pedestrian crossings. These values are different for different areas. For example, the intensity 400 lx is in distance 4.3 m from the centre in the clear air. The similar distance was observed for thick, moderate and light fog. The dense fog shortens the distance in 3.9 m.

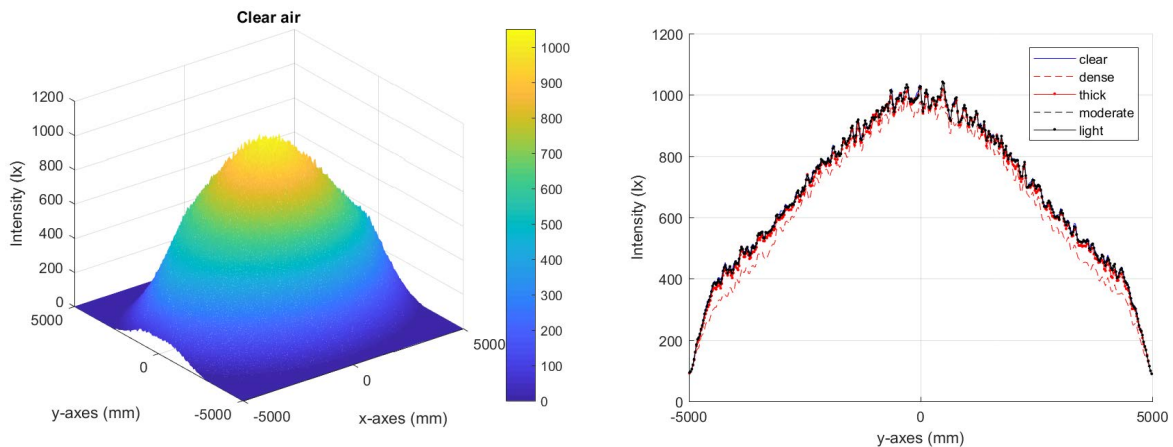


Figure 3. Distribution of light in different fogs.

The simulations of influence and kind of fog are a useful tool for placement of luminaires for meeting with sufficient and safe illumination conditions given by technical standards for given rural areas. The results of simulations showed that there is not any great difference between light, moderate and thick fog and clear air. The biggest problems and attenuation are caused by the dense fog which decreases a range of street lighting.

5. CONCLUSIONS

This article deals with the influence of four kinds of the fog on illumination features of street lighting. We have a real model of luminaire Boos Naica. This luminaire was also modeled in LightTools software. Further, we created four kinds of the fog according to the attenuation coefficient in this software. We simulated how the fogs effect on the distribution of light from the street lighting luminaire. The results showed that there are not any

differences between light, moderate, thick fog and clear air. But the dense fog influences on the distribution of light. We will continue with laboratory measurements of the same luminaire.

ACKNOWLEDGEMENTS

The authors would like to acknowledge the financial support of the Ministry of Education, Youth and Sports of the Czech Republic under Projects No. SP2018/117 and SP2018/184 of VSB–Technical University of Ostrava, Czech Republic. Our research was also supported by Projects No. VI20172019071, VI20152020008 and TA04021263. The work has been partially supported by projects CZ.1.07/2.3.00/20.0217 and CZ.02.1.01/0.0/0.0/16_019/0000867.

REFERENCES

- [1] E. F. Schubert: *Light-Emitting Diodes*, Cambridge University Press, Cambridge, 2006.
- [2] R. Baleja, J. Sumpich, P. Bos, B. Helstynova, K. Sokansky, and T. Novak: Comparison of LED properties, compact fluorescent bulbs and bulbs in residential areas, in *Proc. 16th International Scientific Conference Electric Power Engineering 2015*, Kouty nad Desnou, Czech Republic.
- [3] N. D. Q. Anh, T. H. Q. Minh, and N. H. K. Nhan: Enhancing lighting performance of white LED lamps by green emitting Ce,Tb phosphor, *Advances in Electrical and Electronic Engineering*, vol. 14, no. 5, pp. 609-614, Dec. 2016.
- [4] Z. Ghassemlooy, W. Popoola, and S. Rajbhandari: *Optical Wireless Communications: System and Channel Modelling with Matlab*, New York: CRC Press. 2013.
- [5] A. Liner, M. Papes, J. Jaros, F. Perecar, L. Hajek, J. Latal, P. Koudelka, and V. Vasinek: Software design of SMD LEDs for homogeneous distribution of irradiation in the model of dark room, *Advances in Electrical and Electronic Engineering*, vol. 12, no. 6, pp. 622-630, Dec. 2014.
- [6] D. Sobola, S. Talu, P. Sadovsky, N. Papez, and L. Grmela, Application of AFM measurement and fractal analysis to study the surface of natural optical structures, *Advances in Electrical and Electronic Engineering*, vol. 15, no. 3, pp. 569-576, Sep. 2014.
- [7] T. H. Do and M. Yoo: Visible light communication based vehicle positioning using LED street light and rolling shutter CMOS sensors, *Optics Communications*, vol. 407, pp. 112-126, Jan. 2018.
- [8] R. Ramirez-Iniguez, S. M. Idrus, and Z. Sun: *Optical Wireless Communications: IR for Wireless Connectivity*, New York, CRC Press, 2007.
- [9] M. Bass, C. Macdonald, G. Li, C. M. Decusatis, and V. N. Mahajan: *Handbook of Optics: Atmospheric Optics, Modulators, Fiber Optics, X-Ray and Neutron Optics*, New York, McGraw-Hill Companies, 2010.
- [10] M. Grabner and V. Kvicera: Multiple scattering in rain and fog on free-space optical links, *Journal of Lightwave Technology*, vol. 32, no. 3, pp. 513-520, Feb. 2014.
- [11] LightTools, Synopsys [online], <https://optics.synopsys.com/lighttools>.
- [12] Boos Naica, Boos [online], <http://www.booslight.com/products/naica>.

Modelling the Behavior of Lighting Systems Controlled at a Constant Level of Illuminance

Pavel Valíček, Tomáš Novák, Jiří Beseda, Karel Sokanský
VŠB - Technical University of Ostrava
Ostrava-Poruba, Czech Republic
pavel.valicek@vsb.cz, tomas.novak1@vsb.cz, jan.vanus@vsb.cz, karel.sokansky@vsb.cz

Abstract—The paper deals with the issue of the dimming of lighting systems of the artificial lighting controlled to a constant level of illuminance based on contributions of daylight.

It solves the issue of differences, which arise when setting the existing lighting systems without daylight and their subsequent operation in dimming to a constant illuminance level with the presence of daylight. This issue is addressed in the paper by means of modelling the illuminance systems of the artificial lighting and CIE overcast sky producing different illuminance of an outdoor, unshielded surface.

The modelling took place based on the contributions of the equally cloudy sky to the interior. The article analyses the influence of the location and reception characteristics of the light sensor on the course of illuminance and the uniformity by solving the interior spaces at various levels of outdoor lighting.

Primarily, the simplest types of lighting systems dimmed as a whole based on the input of one illuminance sensor were modelled there.

Keywords—*daylight, artificial light, illuminance, uniformity, controlling, dimming, sensor*

I. THE DESCRIPTION OF THE MODELLED SPACE

An existing room, located at premises of VŠB - Technical University of Ostrava, namely the Faculty of Civil Engineering, was used for the design of the system. The location of the building within the urban development can be seen in Fig. 1, which is oriented to the north. For behavioural modelling, the BuildingDesign software from Astra MS Software s. r. o., with the Wils (version 7.0.238) extension for artificial lighting calculation and Wdls (version 5.0.124) was used to calculate the daily lighting [1][2].



Fig. 1. The airplane picture of the location of the building within the Faculty of Civil Engineering of VŠB - TU Ostrava

The room no. LPOI302 is used according to the standard ČSN EN 12464-1 (Light and Lighting - Workspace Lighting - Part 1: Interior Workspaces) as a classroom or consulting room with a prescribed minimal maintained illuminance of 300 lx. One side of the room, from the sill height of 950 mm to the ceiling, has two windows with the size of 2425 x 2150 mm (left window and 5600 x 2150 mm (right window) facing north. In Figure 2, it can be seen a comparison between a real photo taken in the room and a 3D model made in the BuildingDesign environment. The environment has been simplified to the elements that describe the characteristics of the reflecting surfaces in the room.

Inside the room, the lighting system is installed and it is realized by the luminaires with fluorescent lamps of HORMEN, type VOIIDA T5 with installed 2x58W power. The room is fitted with eight luminaires fitted to the ceiling at the height of 3100 mm.

This paper has been elaborated in the framework of the project SP2018/117 of Student Grant System, VSB-TU Ostrava. The work has been partially supported by Projects No. CZ.1.07/2.3.00/20.0217 and VI20172019071.



Fig. 2. The example of a real room and the 3D model

II. SENSORS USED IN EXAMINATION OF BEHAVIOUR OF THE LIGHTING SYSTEM

The modelling of the reception characteristics of the used sensors was based on a survey of the sensors available on the Czech market. The values for the calculation were chosen according to the most commonly used reception characteristics [4]. A basic overview of the most common sensors available on the Czech market, their way of communication and the angle of reception characteristics is given in the Tab. 1.

TABLE I. THE BASIC OVERVIEW OF THE LIGHTING SENSORS AVAILABLE ON THE CZECH MARKET[5][6][7][8]

Producer	Type	Means of Communication	Angle for reception characteristic
Osram	DUO	1...10 V	110°
	DIM MULTI	1...10 V	110°
	DIM PICO	1...10 V	50°
	DIM MICO	1...10 V	80°
ZUMTOBEL	ED-EYE	DALI	30°
TRIDONIC	basicDIM ILD 5DPI 14f	DALI	60°

	basicDIM ILD 16 DPI 69f	DALI	13°
	SMART senzor 5D 19f	PCA EXCEL one4all	42°
	SMART senzor 5D 19fe	PCA EXCEL one4all	31°
	SMART senzor 10DPI 19fe	PCA EXCEL one4all	38°
BEG	LUXOMAT MiniClip LR-1	1...10 V	140°

To simulate the control of the lighting system in a constant level of the illuminance in the 3D model of the room LPOI302, the reception angles values of 30°, 60°, 110°, 180° were used in accordance to the Cosine reception pattern Fig. 3.

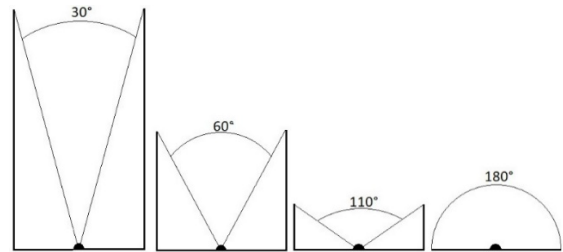


Fig. 3. Layout of individual cases of shielding of the sensing point by the tube in a 3D model

In the LPOI302 testing room, seven sensor positions were selected. Six positions are located on the ceiling at the height of 3100 mm and one is located on the table level at the height of 750 mm. The positions of the sensors were chosen to reflect the diversity of lighting conditions in the room due to daylight access to the room the best.

The positions of the sensors L_1, L_2, P_1, P_2 were selected in the centres axes of each window. The sensors L_1 and P_1 are located in 1/3 of the length of the room and the sensors L_2 and P_2 then in the 2/3 of the room length. These positions were intentionally chosen as the most appropriate positions for the uniformity of daylight on both sides. These positions were evenly spaced from the luminaires.

On the contrary, the position of the sensor S_1 in the centre of the room was suggested as the most frequent positions chosen while installing light sensors. This is the approximate centre of the room with a centre line location of the luminaires. The position S_2 was selected as a complement to compare the result of the centre position with the location in the centre of the window centres.

Fig. 4 shows the individual positions of the sensors in the room. At the P_2 position, the table has two sensors with the same position differing in the height position and orientation of the reception characteristics, which can be seen well in Fig. 5. The matching position has been selected for an easier comparison of the results with the ceiling sensor, where no difference is caused by the different room position.

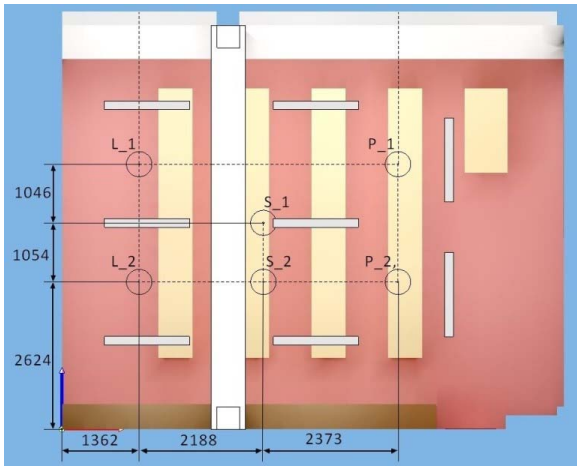


Fig. 4. The graphic layout of the sensor position within the LPOI302 room



Fig. 5. The 3D view of the location of the light sensors

III. MODELING THE OPTIMAL LIGHTING SENSOR POSITION

When modelling the lighting system's behavior, the default value of the control, and hence the required value of the maintained room illuminance value, was chosen as 453 lx. This is the value, which was achieved by the illuminance system of artificial lighting for 100% end-of-life power.

The outdoor illuminance increased steadily in modelling according to the 0, 50, 100, 150, 200, 300, 500, 750, 1500, 3000, 5000, 7500, 10000, 15000, 20000 lx series. [3]

IV. EVALUATION OF SENSOR LOCATION

The graph in Fig. 7, presents the fact that not all the locations of the illuminance sensor can provide control information leading to the correct regulation of the system.

From the viewpoint of maintaining the required value of 453 lx at a constant surface reflection value, the sensor best located at S1 position with a reception angle of 60° was best suited.

This process copied the required value with the smallest deviation. Further, these sensors S_1 30°, L_2 60°, L_2 30°, P_2 60°, S_2 60° and P_2 30° have passed as well. Other placement and reception characteristics are not suitable as the value of the maintained illuminance value dropped below the required limit during the control.

In general, it can be said that it is not advisable to place the sensors close to the windows, as the lighting system is then under-regulated and the required room lighting is not achieved in the room as a whole. The best placement of the sensor in this room is the centre of the room or the distance of 2/3 of the length of the room from the windows. However, the most suitable position of the sensor depends on the spatial character of the room.

From the data obtained during the modelling it is also possible to figure out which reception angle is the best suited for sensing the lighting in the room. For clarity, we will remove only sensor values for the position S_1, which came out as the most appropriate, from the graph Fig. 6.

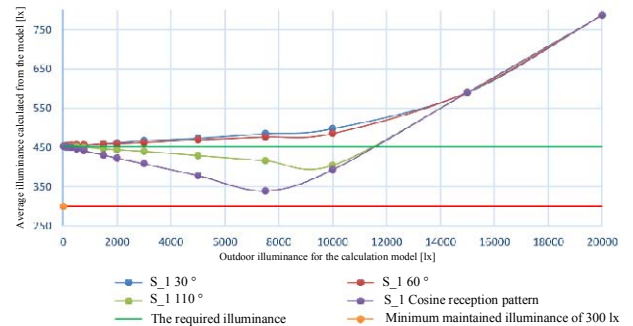


Fig. 6. Graph of control of the lighting system when changing the angle of reception characteristics

The results for the sensor position S_1 is depicted in Fig. 6 coincide with the other positions on the ceiling. The best angle of reception is the angle of 60°. An angle of 30° is already extinguished by the room, while the 110° angle and the Cosine reception pattern of the lighting system are under-regulated and the room lighting then does not reach the required values.

The inadequacy of wide reception characteristics is caused by the presence of large windows across the room that partially dazzle these sensors, which consequently do not provide credible information on the level of illuminance of the reference level. The opposite extreme is then the 30° receiving angle, which, on the contrary due to its small sensor surface cannot measure a sufficient area with a relevant room value and therefore its results are distorted.

The opposite case is the positioning of the sensor at the level of the desk with the scan direction upwards. The reverse trend was demonstrated here, namely the suitability of the broadest reception characteristics. It is therefore ideal to place the sensor on the table the Cosine reception pattern that respects both the location and reception characteristic of the photometer and actually evaluates the illuminance at the point of vision.

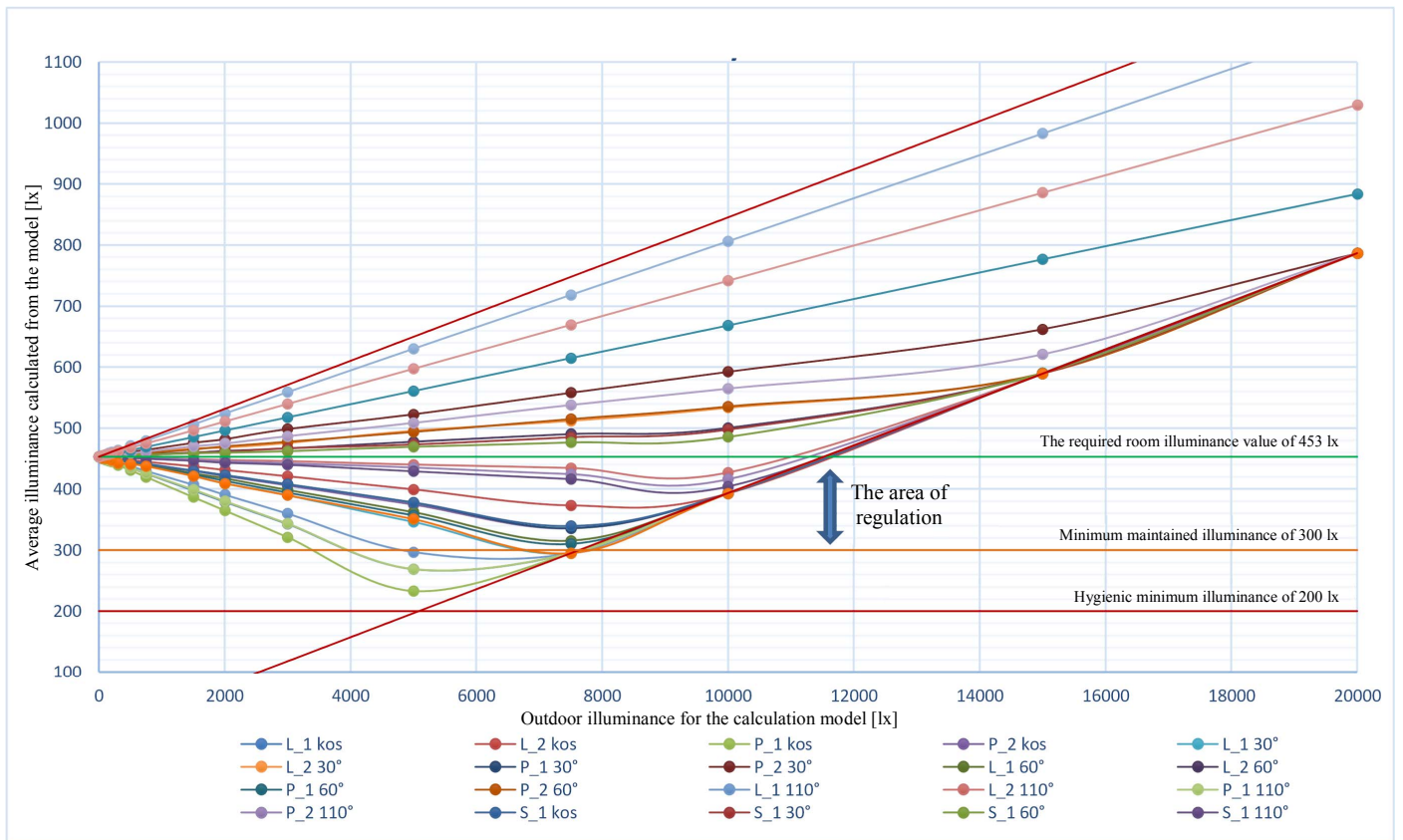


Fig. 7. Graph of even illuminance dependency on outdoor illuminance for each sensor.

V. CONCLUSION

The aim of the paper was to find out the ideal combination of position of the illuminance sensor and its reception characteristics for the existing room LPOI302 serving as a classroom. The purpose of this modelled environment with a controllable lighting system was to maintain the required room illuminance value at a constant level of 453 lx at a constant reflection of surfaces.

As the most optimal position of the sensor, with an emphasis on uniformity of lighting, is in the center of the room on the ceiling. This position is marked as S_1. Other acceptable positions of the light sensors are located in 2/3 of the length of the room from the windows in positions L_2 and P_2. On the contrary, the obtained data verified the fact that the position near the windows is not suitable due to the low level of illuminance in the remaining parts of the room and the resulting non-compliance with the normative requirements for illuminance of the whole working space.

During the optimization of the reception characteristics of the light sensors, the most suitable reception characteristics with a 60 ° spatial angle and a 30 ° angle are also available for a ceiling location. Wider characteristics are inappropriate for ceiling location because the room is under-regulated then and the required lighting conditions are not achieved at the end. When using a sensor in the worktable level, the

reception pattern is the opposite and preferably, it regulates the sensor system with the Cosine reception pattern and 110° sensors.

REFERENCES

- [1] D. Gasparovsky, J. Raditschova, "Proposal of a method for assessment of energy performance of home lighting", 2016, IEEE Lighting Conference of the Visegrad Countries, Lumen V4 2016
- [2] J. Sumpich, T. Novak, Z. Carbol, K. Sokansky, "Software calculation tool for light savings in the buildings compared with real measured data", 2013, 14th International Scientific Conference on Electric Power Engineering 2013, EPE 2013, Pages 677-680
- [3] P. Valicek, T. Novak, J. Vanus, K. Sokansky, R. Martinek, "Measurement of illuminance of interior lighting system automatically dimmed to the constant level depending on daylight", 2016, 6th International Conference on Environment and Electrical Engineering, EEEIC 2016, Article number 7555604, DOI: 10.1109/EEEIC.2016.7555604
- [4] J. Habel, P. Zak, "Energy performance of lighting systems", 2011, Przeglad Elektrotechniczny Volume 87, Issue 4, 2011, Pages 20-24
- [5] Osram DIM, In: Osram [online] 2018. https://www.osram.com/ds/ecat/DIM%20MULTI-Stand-alone%20sensors-Light%20management%20systems-LED%20technology/com/en/GPS01_1035602/PP_EUROPE_Europe_eCat/ZMP_1002745/
- [6] Zumtobel ED-EYE, In: BEG [online] 2018. https://www.zumtobel.com/com-en/products/product_popup.html?22154682

- [7] Tridonic BasicDIM ILD 16DPI 69f. In: TRIDONIC [online].
Dornbirn: TRIDONIC, 2018. [http://www.tridonic.com/
com/en/products/basicdim-ild-16dpi-69f.asp#tab4](http://www.tridonic.com/com/en/products/basicdim-ild-16dpi-69f.asp#tab4)
- [8] BEG LUXOMAT MiniClip LR-1 . In: BEG [online] 2018.
[https://www.beg-luxomat.com/cz/produkty/luxomat/soumrakove-
spinace/dim/miniclip-lr1/](https://www.beg-luxomat.com/cz/produkty/luxomat/soumrakove-spinace/dim/miniclip-lr1/)

Radiation of the Luminous Flux into the Upper Half-space in Wils – Building Design

Petr Becak, Tomas Novak, Richard Baleja, Karel Sokansky
Faculty of Electrical Engineering and Computer Science
VSB-TU Ostrava

Ostrava, Czech Republic

petr.becak@vsb.cz, tomas.novak1@vsb.cz, richard.baleja@vsb.cz, karel.sokansky@vsb.cz

Abstract—The article focuses on the further verification of the software goniophotometer in the BUILDING DESIGN computational program in terms of the possibility of calculating the radiation of the luminous flux flowing into the upper half-space from public lighting systems [1]. Software goniophotometer was tested by the previous verification for the accuracy of calculations of the direct and indirect component of luminaire luminous flux. The superstructure was conceived as the possibility of inserting a network of calculating points in the shape of a sphere. We can imagine the points showing normal illuminance towards the centre of the sphere as a lux meter sensor. The system thus designed duplicates the function of a real goniophotometer, a photometric laboratory instrument that measures luminous intensity or luminous intensity curves. The principle of a goniophotometer is that it allows to measure the luminous intensity in different planes and at different angles, which can be easily interpreted by a sphere with a network of calculation points. The density of the calculation points can be entered in an angular step according to the standard luminaire measurement plan C, γ . The goal of implementing such a network of calculation points is to extend the possibilities of a computational program for modelling the luminous intensity curves of existing luminaires as well as newly composed luminaires. The main goal is calculating the radiation of the luminous flux flowing into the upper half-space from the outdoor lighting systems. It will be the basis for further astronomical calculations that focus on distracting light and increased sky luminance. Based on the testing, it will be possible to create model of lighting system in some city or district of the city by inserting LDT data of real luminaires, thus creating a real lighting system with real building models. From the resulting model, it will be possible to quantify the proportion of the direct and indirect luminous flux flowing into the upper half-space.

Keywords—software goniophotometer, modeling, radiation curves, upper half-space, LED lighting system, sodium lighting system

I. INTRODUCTION

The aim of the article is to showcase the usage of the sphere network of computing points used to model the radiation of the luminous flux from a public lighting system pointing to the top of the half-space. The first step was to design a lighting system that used LED radiating only to the bottom of the half-space for which an Artechnic Schröder VOLTANA 2 5102 – 16 LG Innotek 3535 luminaire was used. The following lighting system was designed with the use of high pressure sodium luminaires radiating to both parts of the half-space. The tape of luminaire used for this lighting system was VYRTYCH

Work is partially supported by Grants SGS SP2018/117 - BroadbandLIGHT - Public Lighting in SMART City and VI20172019071 - Analysis of Visibility of Transport Infrastructure for Safety Increasing during Night, Sunrise and Sunset

BETY-150S [2]. This issue focuses on the obtrusive light and increased sky brightness which are commonly discussed topics.

Obtrusive light may be defined simply as unwanted light. More specifically, it may include light that falls onto the property of others, sometimes called spill light or light trespass, and glare, or excessive light from luminaires that hinders vision in consequence of amount, direction or spectral composition.

The opinions on obtrusive light clash between the astronomical public and illumination experts (especially caretakers or owners of the outdoor lighting systems) which is what brings the issue to the public. Citizens in many places often complain about the obtrusive light radiating into their homes. The energetic concept of individual states as well as the multinational one both add to the issue [3].

Obtrusive light represents a total luminous flux that spreads to the upper half-space and therefore increases sky brightness. It is formed by direct and indirect (reflected) luminous flux from the terrain and particular objects. The most important thing is the evaluation of the luminous flux that is distributed directly to the upper half-space by ULR, see equation 1 below:

$$ULR = \frac{ULOR}{ULOR + DLOR} \quad (1)$$

where:

ULR - proportional direct luminous flux radiated to the top of the half-space

ULOR - luminous flux radiated directly from the luminaire to the top of the half-space

DLOR - luminous flux reflected from the surfaces of the surrounding objects

ULOR + DLOR - total luminous flux radiated to the top of the half-space

II. MODEL OF A CITY WITH ROADS M5

A city with a road and a build-up area was used as a base of the design. The class of the road was set to be M5. The built-up area is composed of residential houses and an industrial building situated near the road. The built-up area as well as the road with a pavement are obstacles with a certain reflectivity for a lighting system and the spread of its luminous flux.

Ground plan and the parameters of the model city created in the program Wils are shown below.

TABLE I. PARAMETERS OF THE MODEL CITY

Parameter	Length (m)	Width (m)	Height (m)	Reflectivity (%)
Road	150	7	0,05	10
Pavement	150	1	0,1	30
House	10	10	5	30
Industrial building	100	30	10	30
Grass	150	90	0,01	10

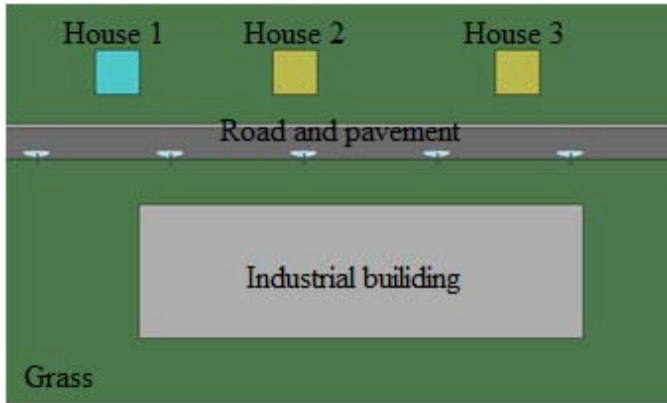


Fig. 1. Ground plan of the model city

The network of the computing points for both direct and reflected components was set to be five times the longest dimension of the model city to allow it to be seen as a point source (see figure 2).

All of the computations were done with maintenance factor 1 which allows the comparison between input and output data. This was done to make sure that the aging of the luminaires and light sources would not affect the data. However, the lighting system was always designed to work with a maintenance factor in a real situation.

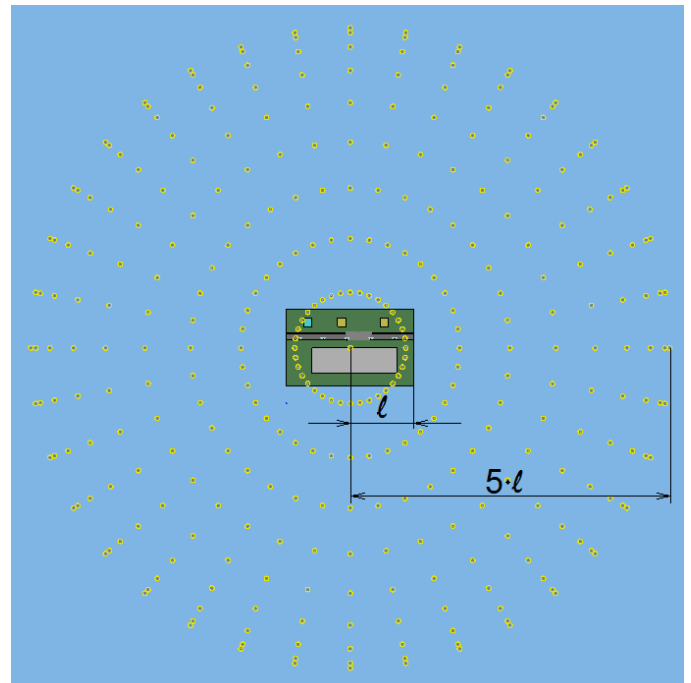


Fig. 2. Model situation of location of the city model against the reference plane in the Wils programme

III. ILLUMINATION OF THE ROAD USING LED LUMINAIRES

The road M5 was designed to be in accordance with the standards. The illuminators are situated on poles 30m away in a height of 7m. The lighting system is composed of 5 poles with luminaires whose parameters are shown in the table 2. As was previously mentioned these illuminators radiate only to the bottom of the half-space and are specifically designed to illuminate roads. It can therefore be assumed that the entire luminous flux of this lighting system that gets to the top of the half-space is reflected from the model objects and surfaces [4].

TABLE II. PARAMETERS OF THE LED ILLUMINATION SYSTEM

Luminaire	5x Artechnic Schröder VOLTANA 2 5102 – 16 LG Innotek 3535
Size of the luminaire (mm)	135 x 505 x 70
Power consumption of the luminaire (W)	28
Power consumption of the lighting system (W)	140
Luminous flux of the source (lm)	3154
Luminous flux of the lighting system sources (lm)	15770
Efficiency (%)	85,6
Luminous flux of the luminaire (lm)	2700
Luminous flux of the lighting system (lm)	13500

The luminaire with distribution curves of a common road luminaire is shown in the figure 3.

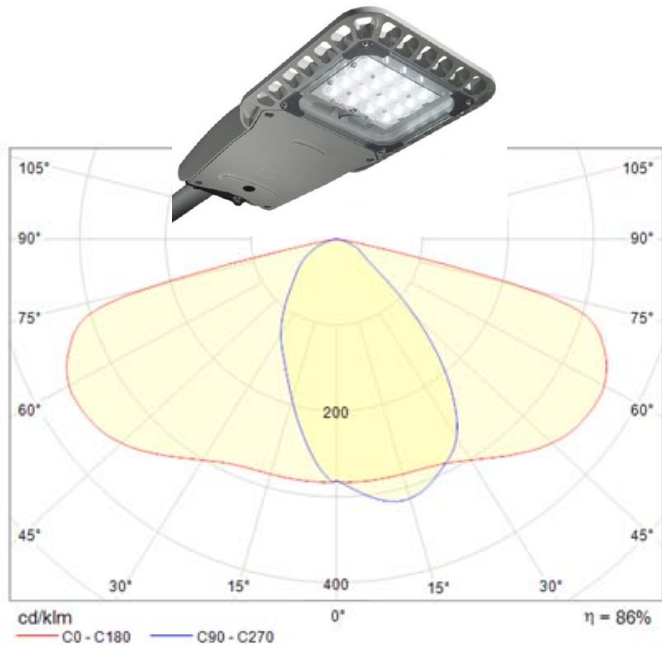


Fig. 3. Luminaire VOLTANA 2 5102 – 16 LG Innotech 3535 and its distribution curves from LDT manufacturer data

Table 3 shows computed luminous intensity values of the city for the chosen plates obtained from LDT Wils program data.

TABLE III. LUMINOUS INTENSITY OF THE CITY FOR CHOSEN PLATES OBTAINED FROM LDT WILS PROGRAM DATA

<i>I</i> (cd/klm)	C0°	C60°	C120°	C180°	C240°	C300°
90°	0,1	0,2	1,4	2,1	1,3	0,5
100°	0,6	1	3,8	4,6	3,9	1,6
110°	1,3	3,1	7,7	7,8	8	4
120°	2,2	8,4	10,7	11,3	11,1	8,8
130°	8,3	11	13,2	14	13,6	11,5
140°	12,1	13,3	15,2	16	15,6	13,7
150°	14,6	15,3	16,7	17,4	17	15,6
160°	16,2	16,7	17,7	18,2	17,9	16,9
170°	17,4	17,6	18,1	18,5	18,2	17,7
180°	18,1	18,1	18,1	18,1	18,1	18,1

Based on the luminous intensity of the individual plates that were computed by the software goniophotometer, it is possible to construct the distribution curves of the city with LED lighting system. These curves is shown in the figure 4.

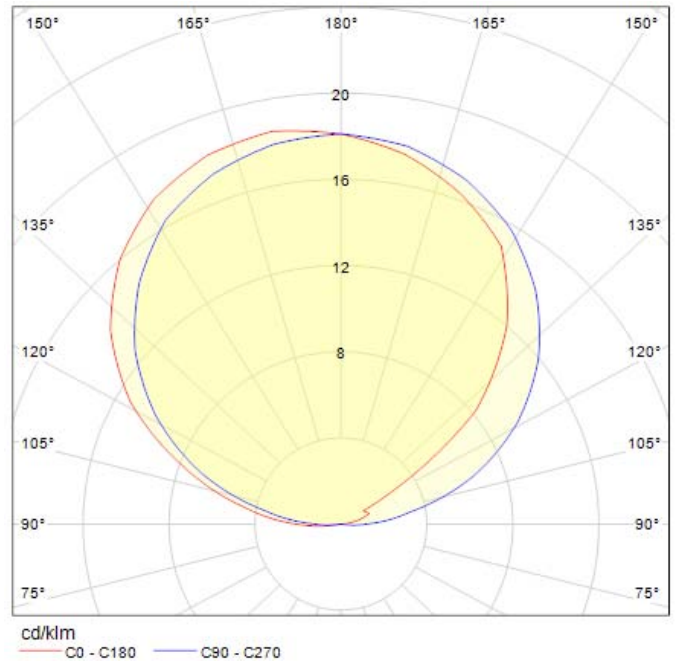


Fig. 4. Distribution curves of the city with LED lighting system VOLTANA 2 5102 – 16 LG Innotech 3535

Based on the above mentioned parameters of the lighting system and the parameters of the combination of lighting system - reflective surface obtained from the software goniophotometer, the following can be stated:

- The shape and size of the luminous intensity computed from the distribution curves of the city corresponds with the previous assumptions. The computed luminous intensity curve radiates only to top of the half-space and its shape is close to that of diffusing (cosine) radiator. The assumed deviations from the shape of cosine are visible in asymmetry of the curves that is caused by asymmetric radiation of the luminaires in the lighting system and by the fact that the computation respects the reflective characteristics of the materials defined in the table 1. This causes the deformation of the curve which is visible in the palnes C0-C180.

- The ratio of the total luminous flux to the top of the half-space was computed to be 8,12 % of the total luminous flux of the luminaires in the lighting system. This percentage corresponds to 1096 lm of the luminous flux [5].

IV. ILLUMINATION OF THE ROAD USING HIGH PRESSURE SODIUM LUMINAIRES

A lighting system that uses park luminaires with rotary symmetrical distribution curve and primary radiation to the top of the half-space was used to compare differences of the distribution curves of the city model for the illumination of the same road in a same geometrical layout.

It can therefore be assumed that the luminous flux of this lighting system gets to the top of the half-space both directly

and by reflection from the model objects. The parameters of this particular lighting system are shown in table 4.

TABLE IV. PARAMETERS OF THE HIGH PRESSURE SODIUM ILLUMINANCE SYSTEM

Luminaire	5x VYRTYCH BETY-150S
Size of the luminaire (mm)	540 x 540 x 660
Power consumption of the luminaire (W)	150
Power consumption of the lighting system (W)	750
Luminous flux of the source (lm)	17200
Luminous flux of the lighting system sources (lm)	86000
Efficiency (%)	58,2
Luminous flux of the luminaire (lm)	10010
Luminous flux of the lighting system (lm)	50050

The luminaire with its distribution curve set to illuminate parks is shown in figure 5.

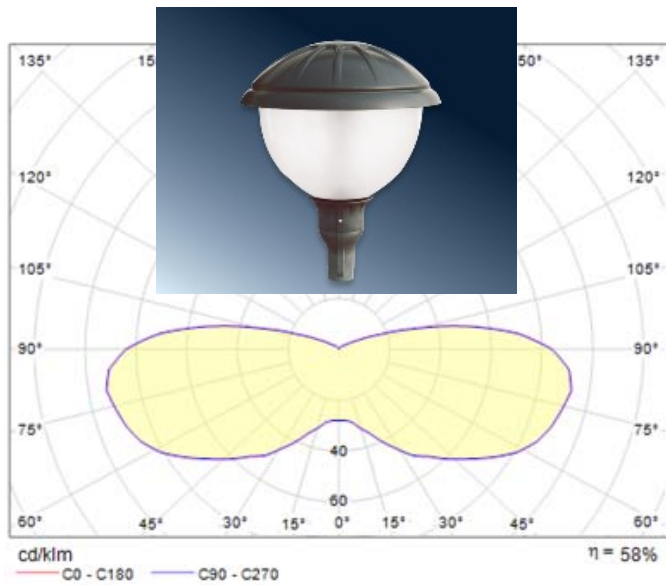


Fig. 5. Luminaire BETY-150S and its distribution curves from the LDT manufacturer data

Table 5 shows the computed luminous intensity values of the model city for chosen plates obtained from LDT Wils program data.

TABLE V. LUMINOUS INTENSITY OF THE CITY FOR CHOSEN PLATES OBTAINED FROM LDT WILS PROGRAM DATA

I (cd/klm)	C0°	C60°	C120°	C180°	C240°	C300°
90°	10,3	17	74,4	78,3	76,9	33,5
100°	7,2	44,5	50,9	54,8	52,1	46,1
110°	7	17,8	22,2	24,8	22,3	17,7
120°	2,9	6,8	11,5	13,1	11,6	7,2
130°	3,6	5,2	9,2	11	9,4	5,6
140°	4,4	5,4	8,4	10,7	8,5	5,6
150°	4,8	5,2	7,4	8,9	7,5	5,4
160°	5,2	5,3	6,8	8	6,9	5,5
170°	5,5	5,6	6,3	7	6,3	5,6
180°	5,7	5,7	5,7	5,7	5,7	5,7

Based on the luminous intensity for individual plates computed by the software goniophotometer, it is possible to construct distribution curves of luminous intensity of a city with high pressure sodium lighting system. This distribution curve is shown in the figure 6.

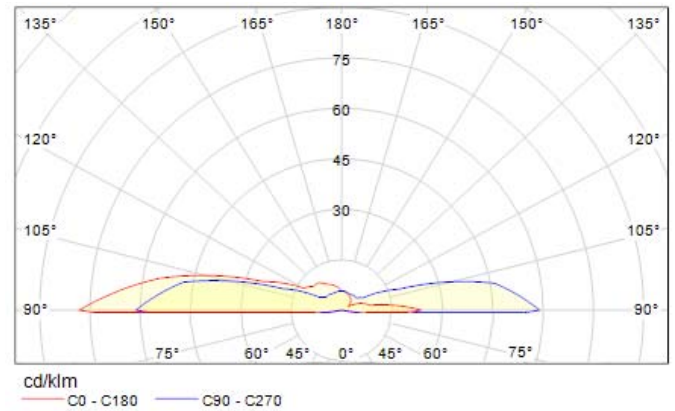


Fig. 6. Distribution curves of the city with high pressure sodium lighting system BETY-150S

Based on the above mentioned parameters of the lighting system and the parameters of the combination of lighting system - reflective surface obtained from the software goniophotometer, the following can be stated:

- The shape and size of the luminous intensity computed from the distribution curves of the city corresponds with the previous assumptions. The computed luminous intensity curve radiates only to top of the half-space and its shape differs distinctively from the previous case. The reason behind that is the amount of luminous flux radiated directly to the top of the half-space.

- The ratio of the total luminous flux to the top of the half-space was computed to be 29,8 % of the total luminous flux of the luminaires in the lighting system. This percentage corresponds to 14915 lm of the luminous flux. This luminous flux can be then divided into a direct component ULOR and reflected component DLOR. The direct component is 23 %

(11512 lm) and the reflected one is the remaining 6,8 % (3403 lm) from the total luminous flux of the lighting system.

V. CONCLUSION

Even though both of the lighting systems were designed to have approximately the same level of maintained illuminance, the high pressure sodium lighting system has 5,4 times greater power consumption (3,7 times greater luminous flux) which in the end means much higher expenses from the economic point of view.

It can also be stated that the level of obtrusive light is affected the most by the radiation direction of the individual luminaires and its geometry. The total luminous flux that was radiated to the top of the half-space by the high pressure sodium lighting system is 13,6 times greater than in the case of LED lighting system. It is also important to mention that while using the high pressure sodium lighting system, the luminous flux going to the top of the half-space (14915 lm) is greater than the total luminous flux of the LED lighting system (13500 lm).

The following table shows the final comparison between the two designed lighting systems with two different types of luminaires. The individual computed components of the luminous flux going to the top of the half-space are the key entries for this work.

TABLE VI. THE FINAL COMPARISON BETWEEN THE TWO DESIGNED LIGHTING SYSTEMS FOR THE CITY MODEL.

Parameter	LED lighting system	Sodium lighting system
Maintained road illuminance (lx)	8,98	8,65
Power consumption of the lighting system (W)	140	750
Luminous flux of the lighting system (lm)	13500	50050
Luminous flux going to the top of the half-space (%)	8,12	29,8
Luminous flux going to the top of the half-space (lm)	1096	14915
Direct luminous flux <i>ULOR</i> (%)	0	23
Direct luminous flux <i>ULOR</i> (lm)	0	11512
Reflected luminous flux <i>DLOR</i> (%)	8,12	6,8
Reflected luminous flux <i>DLOR</i> (lm)	1096	3403

REFERENCES

- [1] J. Sumpich, T. Novak, Z. Carbol, K. Sokansky, "Software calculation tool for light savings in the buildings compared with real measured data", 2013, 14th International Scientific Conference on Electric Power Engineering 2013, EPE 2013, Pages 677-680
- [2] P. Žák, S. Vodráčková, "Conception of public lighting", Proceedings of 2016 IEEE Lighting Conference of the Visegrad Countries, Lumen 2016 Karpacz, Poland, DOI: 10.1109/LUMENV.2016.7745514
- [3] M. Kocifaj, F. Kundracik, "Modeling the night sky brightness distribution via new SkyGlow Simulator", Proceedings of 2016 IEEE Lighting Conference of the Visegrad Countries, Lumen 2016 Karpacz, Poland, DOI: 10.1109/LUMENV.2016.7745553
- [4] L. Lipnický, D. Gašparovský, R. Dubníčka, "Influence of the calculation grid density to the selected photometric parameters for road lighting", Proceedings of 2016 IEEE Lighting Conference of the Visegrad Countries, Lumen 2016 Karpacz, Poland, DOI: 10.1109/LUMENV.2016.7745555
- [5] T. Pavelka, M. Ptacek, P. Baxant, "Static model of LED behaviour depending on operating conditions", Published in: Electric Power Engineering (EPE), 2016 17th International Scientific Conference, 2016 Prague, Czech Republic, DOI: 10.1109/EPE.2016.7521774

Measurement of Outdoor Lighting with a Focus on Watchdog Lighting System in the Area of Electric Station TR Čechy Střed

Richard Baleja, Tomas Novak, Karel Sokansky, Petr Bos, Petr Becak
Department of Electrical Engineering
FEECS, VŠB-TU Ostrava
Ostrava, Czech Republic

richard.baleja@vsb.cz, tomas.novak1@vsb.cz, karel.sokansky@vsb.cz, petr.becak@vsb.cz, petr.bos@vsb.cz

Abstract—The use of camera and security systems has been becoming a standard part of facilities equipment. Companies protect their property against potential damage and theft and also want to have information about who, when and where was located. These systems are especially used to protect strategic objects whose threat or destruction would have an obvious impact on a society. This group of buildings clearly includes electric stations where the eventual shutdown or destruction would result in a power outage in the regions or a total blackout of the whole country. Therefore, when designing security and camera systems, consideration should be given to all possibilities of space disturbance and to designing the system so that any intruder can be detected in time. In this paper, we will deal in detail with the watchdog lighting system of an electric station that works together with camera systems TSFO. At the very beginning, the right choice of security cameras is essential - they should have a sufficient sensitivity and a resolution to detect objects properly in both day and night hours. The designing of a watchdog lighting system is necessary for the camera system TSFO to work reliably and to provide expected information. The watchdog lighting system is designed with respect to the position and height of the monitoring cameras and by this calculation is set the height of the luminaires, their pitch and the appropriate type and power of the luminaire. At present, most of the lighting systems are provided by LED lights, which, compared to the high-pressure sodium lamps, have many benefits, mainly in the wide range of luminance curve characteristics. The subject of this article is a measuring of watch lighting system in the site of the electric station TR Čechy střed, which uses high-pressure sodium lamps for watchdog lighting system as well as the design of optimization of this lighting system by using LED luminaires capable of distributing the camera lighting component throughout the whole range of the monitored area between the lighting points.

Keywords—luminance camera, colour rendering index, watch lighting system, TSFO system

I. INTRODUCTION

The high-quality design of the lighting systems in the area of electric station is important especially for safety reasons. It is about the safety of the whole electric station, which should be protected against potential intruders, as well as the safety of employees who have to move in places with high voltage. This is not just a design watchdog lighting project to ensure the proper functioning of the security cameras, but also the design

This article was prepared with the support of the project "BroadbandLIGHT - Public Lighting in SMART City" SGS SP2018/117 by institution of VSB-TU Ostrava.

of lighting systems, whose role is to illuminate individual areas within the station. For example, these are entrance gates, roads, transformers and various measuring devices that need to be checked regularly. Lighting requirements are often very specific, and therefore, when designing the watchdog lighting systems, it is necessary to respect, in addition to Czech technical standards, technical standards that deal with the issue in more detail. ČEPS, a.s. in cooperation with VŠB TU - Ostrava, worked out a technical standard, which deals with the lighting issues at the premises of electric stations. This standard is available under the designation TN/59/2016 Revision 3 Venkovní a vnitřní osvětlení v objektu elektrických stanic PS and is valid from 1.5.2016. According to this standard, outdoor lighting in electric stations is divided into three types, such as watchdog lighting, road lighting and operational lighting. This standard defines the requirements of each type of the lighting system and also describes its correct design. The obtrusive light problematics, which has become more and more current, is also described. It is recommended to use flat-faced luminaires so that the proportion of light emitted from the luminaire to the upper half-space is as small as possible, ideally equal to zero.

II. WATCHDOG LIGHTING AND LIGHTING REQUIREMENTS

Luminaires for public lighting are used for a watchdog lighting systems, either with high-pressure sodium lamps or with LED. The watchdog lighting serves to illuminate the perimeter of the premises of the electric station in order to ensure the functionality of the security camera systems (TSFO) of the security guard. The watchdog lighting is installed along the entire fence of the electric station, including the entrances to the houses and the central house, the entrances and along the fencing, which separates the foreign legal entity from ČEPS premises. Luminaires with the photometric distribution curve for public lighting systems are used for illuminating the strip along the fencing to provide the watchdog lighting system. The lighting points are located inside a station 2.5 to 4 meters from the fence. Luminaires are directed towards the fence.

Requirements for the watchdog lighting are defined according to the technical standard TN/59/2016 of revision No. 3 as follows: the average maintained vertical illumination must be at least 10 lx. The illumination is evaluated from the point of view of the security camera at a height of 1 m above the terrain. The average maintained horizontal illumination of the reference section between the two light points must be at least

10 lx. Uniformity requirements for both cases are $U_o = 0.4$. The limit value of the glare rating limits GRL shall not be greater than 45. The colour rendering index of the lighting sources used must be at least 20. When lighting is proposed, it is recommended that the luminaires be placed in a higher vertical level as a security camera. Luminaires must be placed in such a way that they do not cause the camera to glare and cause the camera to pass into a saturated state.

The functionality of security cameras is that it picks up the luminances of illuminated objects. The greatest luminance is achieved when the luminous flux enters the illuminated object from the viewpoint of the camera. Standard cameras have a minimum sensitivity for colour mode $E = 0.4$ lx and for black and white mode $E = 0.05$ lx. This is illumination on the chip of security camera. According to specialists, these values are however very low and their generalization may cause camera malfunctions. For example, switching from the colour mode to the black and white mode.

In order to ensure the optimal and correct functioning of the camera and the contrast, it is necessary that the illumination value for the colour mode is at least 15 lx and for black and white 10 lx. This illumination must be at least 70% of the area occupied by the scene. To avoid overturning, and thus reduce an image resolution, it is necessary to balance the illumination, i.e. the ratio of maximum intensity to minimum intensity, in a ratio of 6 : 1, at 4 : 1 (zoomed out) points.

III. THE MEASUREMENT OF WATCHDOG LIGHTING

In order to verify the quality of the proposed lighting systems, the light parameters are measured. The measurement is always carried out after eclipse to avoid the contribution of daylight. The measurements include all spaces and places that are in the electric station. These are premises of transformers, measuring devices, roads and so on.



Fig. 1. Area of TR electrical station Čechy střed

Several light parameters are measured for watchdog lighting system. It is the camera illuminance (vertical illuminance of the camera), the horizontal illuminance at ground level and the measuring of luminances from the view of the security camera. The values of illumination are measured using a luxmeter. The measurement of the vertical illumination

is providing by using a tripod. Luminances are measured using a luminance camera located as close as possible to the security camera. From this position, the luminance analyses are made for the different distance of the figures from the security camera.

The measurement of the lighting parameters was carried out at the electric station TR Čechy střed. The area of the electric station is illustrated in Figure 1. The red colour shows the line of the watchdog lighting. The yellow colour mark the areas of the electric substations, transformers and roads where the horizontal illumination was evaluated. The watchdog lighting system is realized in the area of the electric station using luminaires with high-pressure sodium lamps with a power of 70 W. Luminaires are located at a height of 6 meters at a distance between the lighting points is 15 meters.

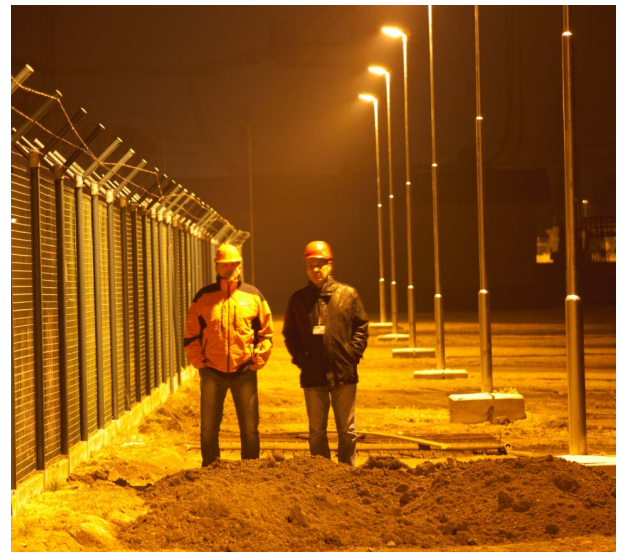


Fig. 2. View of the watchdog lighting system

Due to the same height of luminaires and their pitch, only the reference sections were selected for the measurement. The position of the reference sections is marked in figure 1. (sections 2A, 2B and 2C). As was mentioned above, the proper function of the security cameras depends on the luminances of objects. For this reason, the quality of the watchdog lighting was also verified by means of a luminance camera. The luminance camera was placed in the approximate position of the security camera so that the observation conditions of the luminance camera corresponded to the monitoring conditions of the security camera.

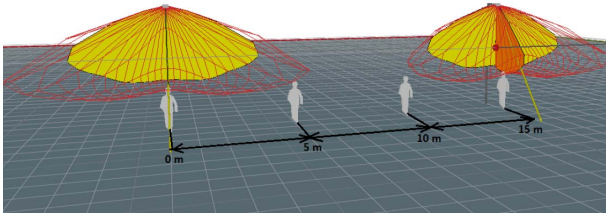


Fig. 3. Schematic outline of figures positions for the measurement of luminance analysis (4 positions)

The luminance camera views correspond to possible views of security cameras. These views were chosen as the most critical views of security cameras, whose role is to monitor the area of the electric station. To evaluate the luminance analysis, figures with different garment reflections, which gradually changed their positions at a spacing of approximately 5 m were used. For each reference section of the watchdog lighting, the luminance analysis was made for 4 positions of the figure. An example of the luminance analysis of the figures is shown in figure 4. The figure with a lighter clothing is placed on the left; the figure with a dark clothing is placed on the right. The following figure 5 shows a record from the security camera.

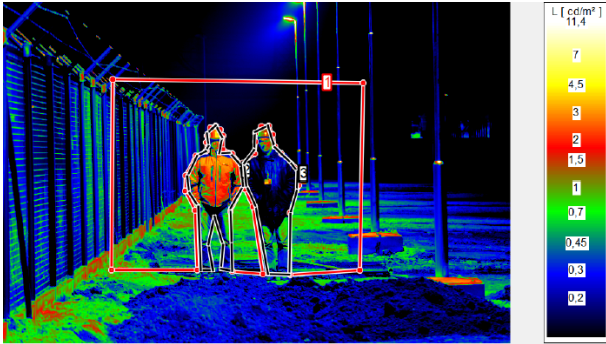


Fig. 4. Luminance analysis of figures



Fig. 5. Record from the security camera

TABLE I. CALCULATED VALUES FROM THE LUMINANCE ANALYSIS OF THE FIGURES

	Luminance analysis of figures				
	Average luminance of figurine		Average background luminance (cd/m ²)	Contrast of figures and background	
	Left (cd/m ²)	Right (cd/m ²)		Left (-)	Right (-)
Position 2	1.14	0.31	0.33	2.45	0.06

TABLE II. CALCULATED VALUES OF VERTICAL AND HORIZONTAL ILLUMINATION

	Measurement of illumination	
	Average horizontal illumination of the referent section (lx)	Average vertical illumination of figures in position (lx)
Position 2	24.1	25

IV. CONCLUSION

From the measured luminance analyses of the figures in the field of vision of the security camera, the contrasts between the background and the figurines were calculated. The calculated contrasts between the figure and the background are relatively low, so in some cases recording and recognizing pedestrians in the field of vision of the security camera can be difficult. From the measurements of the luminance contrast and based on the measured vertical illuminances of figures, in the case of measurements on the reference section 2A, 2B and 2C, it is obvious that the highest luminances values, contrast and also vertical illumination take the figures in position 2 (according to figure 3). On the other hand, the lowest values are in position 3 (figure 3). It is caused by the distribution of the luminous flux (photometric distribution curves) of the luminaires of watchdog lighting system, as it is illustrated in figure 3. For designing watchdog lighting systems, it is preferable to use LED luminaires for better distribution of luminous flux through the lens. These days a large number of luminaires with different photometric distribution curves are available on the market. They are capable of distributing the luminous flux so that it can be used with the highest possible efficiency.

REFERENCES

- [1] Technical standards of CEPS a.s., TN/59/2016 Revision 3 Venkovni a vnitri osvetleni v objektu elektrickych stanic PS and is valid from 1.5.2016.
- [2] I. Ullman, P. Bos, J. Ullman, "New outdoor lighting-Operation and maintenance," 17th International Scientific Conference on Electric Power Engineering, 2016, art. no. 7521823, ISBN 978-150900907-7.
- [3] P. Bos, R. Baleja, K. Sokansky, T. Novak, I. Ullman, "Outdoor lighting versus surveillance camera systems in electrical substations CEPS," 16th International Scientific Conference on Electric Power Engineering, 2015, pp. 464-467.
- [4] K. Sokansky, T. Novak, I. Ullman, Z. Medvec, Lighting of outdoor electrical stations philosophy: 10th International Scientific Conference Electric Power Engineering, Kouty nad Desnou, 2009, pp 202-206, ISBN 978-80-248-1947-1.

A Comparison of Light Sources Technologies of Vehicles Headlights Illuminating a Model Road

Ondrej Dolejsi, Richard Baleja, Petr Becak, Tomas Novak, Karel Sokansky
Faculty of Electrical Engineering and Computer Science
VSB-TU Ostrava

Ostrava, Czech Republic

ondrej.dolejsi.st@vsb.cz, richard.baleja.st@vsb.cz, petr.becak.st@vsb.cz, tomas.novak1@vsb.cz, karel.sokansky@vsb.cz

Abstract—The paper presents courses of measured values of vertical and horizontal illuminance on a sample section of a road. The model road was created at LIBROS safe driving polygon in Ostrava within the Comparative Measurement of Night Traffic Area, which was organized as part of the research task VI2VS/571 of BV III/1-VS programme entitled "Analysis of Road Traffic Participants Visibility so that it is possible to increase their safety in dusk and night". Measurements were made for two model situations of road lighting: vehicle low beam headlights and a combination of road lighting and low beam headlights. Vehicles of the same type with low beam headlights with halogen, xenon and LED sources were used for the measurements.

Keywords—road lighting, low beam headlights, vertical illuminance

I. INTRODUCTION

In November 2018 a comparative measurement of night traffic area took place at the LIBROS safe driving polygon in Ostrava. In this action, a model situation was created where a straight section of the traffic area is illuminated by the low beam headlights of vehicles with different light source technologies while road lighting is switched on or switched off. The lighting of the road corresponded to the real conditions that can occur on the roads in normal operation. Luminance analysis [1] and vertical and horizontal illuminance measurements (E_v and E_h) were performed on the model road [2].

The aim of this work is to assess the illuminated area of the headlights of different technologies and to compare the distribution of measured values of E_v between the different technologies.

II. METHOD

The aim of the measurement was to compare the distribution of the E_v in the model section of the road, which was illuminated by low beam headlights with different light source technologies. Three Škoda Octavia vehicles of the same series with halogen, xenon and LED light sources in headlights were selected for the measurements. E_v values were measured

Article was written within the framework of the research grant VI2VS/571 "Analysis of Visibility of Road Participants in Order to Increase Their Safety at Dusk and at Night" provided by the Ministry of the Interior and supported by the Traffic Police Service of the Police Presidium of the Czech Republic.

for the following situations:

TABLE I. OBJECTS PARAMETERS CALCULATED IN MODEL

Headlights	Situation
Halogen	Low beam without road lighting
	Low beam with road lighting
Xenon	Low beam without road lighting
	Low beam with road lighting
LED	Low beam without road lighting
	Low beam with road lighting

The lighting system was one-sided with luminaires fitted with metal-halide lamps with a correlated color temperature T_c 4000 K. To classify the sample section to the corresponding lighting class according to EN 13201-2 [3], a horizontal illuminance measurement was made on the road. The horizontal illuminance measurement was performed in accordance with EN 13201-4 [4]. There was a coherently illuminated road [5].

A straight road section with two lanes was chosen as the model case. The total width of the road was 7.2 m. The total length of the model section was 50 m and the spacing of the luminaires was 30 meters [6,7]. For the measurement of the vertical illuminance, ten rows were selected on the section with the measured points marked in each row with letters A to H. The layout of the measured points is schematically shown in the Figure 1.

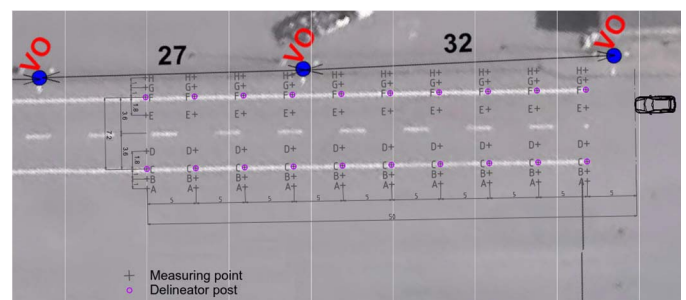


Fig. 1. The grid of measuring points on the model road for vertical illuminance measurement.

III. GRAPHS

In total, six situations were modeled for the case of vertical illuminance measurements, as mentioned in the chapter above. For each variant, a graph of the E_v distribution in space was compiled. For better orientation, the graphs were supplemented with illustrations of delineator posts, vehicles and road lighting luminaires. In the case of measuring the horizontal illuminance of the sample section, a graph of the E_h distribution was compiled.

A. Sample Section of Lighting Illuminated by the Road Lighting

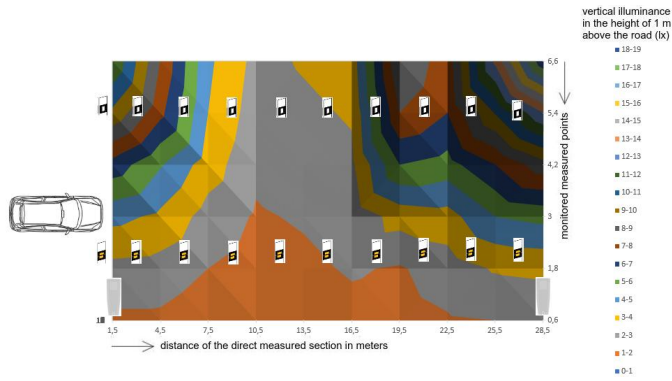


Fig. 2. The course of horizontal illuminance of the model road section, illuminated by the road lighting.

In this situation, the roadway is illuminated only by the road lighting. The type of lighting system, luminaires and sample section dimensions are given in the previous chapter. The distribution of E_h on the sample road section is shown in the Figure 2. On the road, the measured average illuminance was $E_{hm} = 4.6$ lx, with a total uniformity of $U_o = 0.26$.

B. Space Illuminated by the Low Beam Headlights

In this situation, the road is illuminated only by the low beam headlights of the vehicle. Thus, a model situation is created that occurs in a rural area or in a poorly illuminated urban area. The E_v distribution for each headlight technology is shown in the graphs below. The distribution of the measured values E_v for the low beam headlight is shown in the Figure 3.

Vertical illuminance E_v measured at point F, i.e. on the right edge of the road in the direction of drive of the vehicle, was less than 1 lx at a distance of 40 m from the vehicle. The classic halogen lamp is able to light up to about 35m in front of a driver. However, it is important to note that in the right and left boarding zones the area is only about 20 - 25 m.

The distribution of the measured values of E_v for the xenon low beam headlight is shown in the Figure 4. In the given model situation, at a distance of 30 m at point F, the E_v value was less than 1 lx. Xenon has excellent light beam trimming that reduces the dazzling of oncoming vehicles. However, there may occur a situation (headlight adjustment) where the low beam headlights only illuminate the area in front of the driver up to a distance of 30 m.

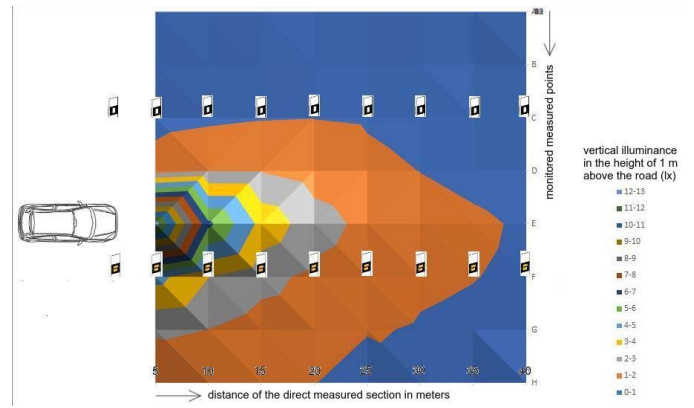


Fig. 3. The course of vertical illuminance of the measured model road cutout without the road lighting. Illuminated by the halogen low beam headlights.

The boarding zones situation is very good. High T_c of xenon headlights is suitable for peripheral vision areas at low adaptation luminance.

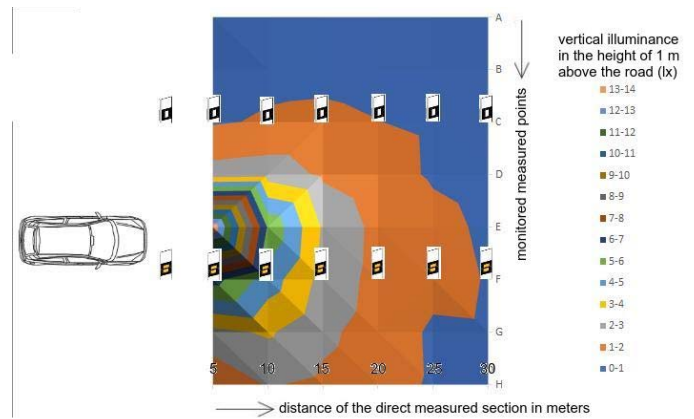


Fig. 4. The course of vertical illuminance of the measured model road cutout without the road lighting. Illuminated by the xenon low beam headlights.

The distribution of the measured values of E_v for the LED low beam headlight is shown in Figure 5. The E_v value was measured at a distance of 45 m from the vehicle headlights. The LED headlights provides high-quality illumination of the boarding zones in the peripheral area both from the illuminance and T_c point of view, while providing luminous flux up to the area of 40 m in front of a driver.

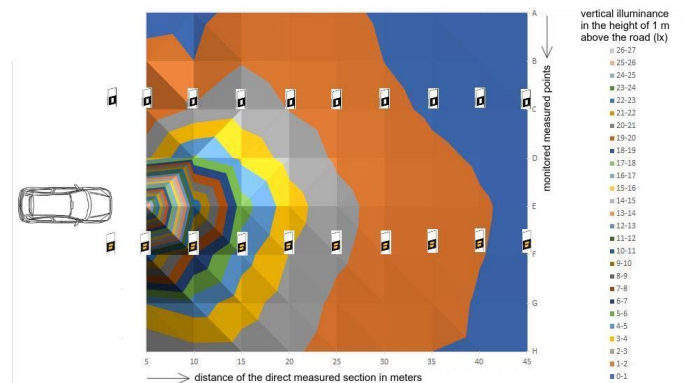


Fig. 5. The course of vertical illuminance of the measured model road cutout without the road lighting. Illuminated by the LED low beam headlights.

For halogen and xenon headlights the maximum vertical E_v values are up to 15 lx. For LED headlights the maximum value is almost double. LED and xenon headlights have a similar vertical illuminance distribution in space. However, in the LED headlights, the value of E_v at point F dropped below 1 lx by 10 m further than in the case of xenon headlights and it also illuminated the left space of the road up to a distance of 30 m. A shorter illumination of the left side of the road can be seen in the halogen headlight. The left space outside the road is almost unilluminated.

C. Space Illuminated by Both Low Beam Headlights and the Road Lighting Luminaires

In the last model situation, the road cutout was illuminated by the low beam headlights of the vehicle simultaneously with the road lighting. The average illuminance measured on the sample section was 4.6 lx. The road lighting is realized by luminaires with metal-halide lamps with a correlated color temperature T_c 4000 K. The spacing between the light points is 30 m. The model simulated the conditions that occur in urban areas. The E_v distribution for each headlight technology is shown in the graphs below.

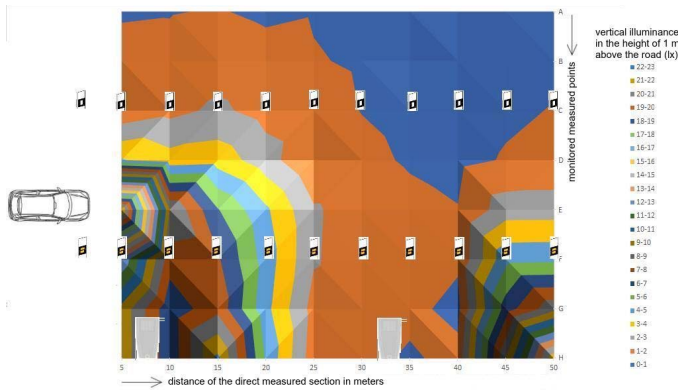


Fig. 6. The course of vertical illuminance of the measured model road cutout with the road lighting. Illuminated by the halogen low beam headlights.

The measured values of E_v for halogen headlights are shown in the Figure 6, for the xenon headlights are shown in the Figure 7 and for the LED in the Figure 8. In the case of xenon headlights compared to the other technologies, the value E_v of points F in the entire length was not more than 1 lx. At a distance of 35 m and 40 m, there was a mentioned decrease.

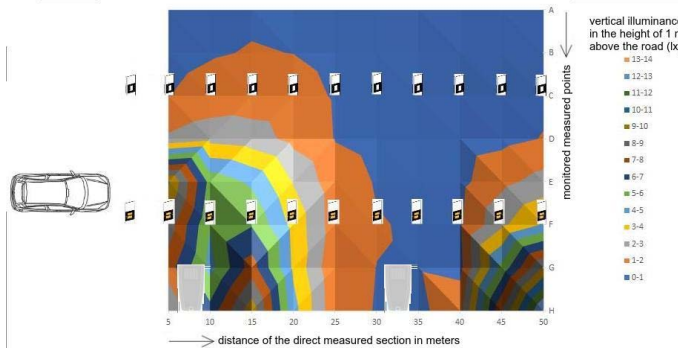


Fig. 7. The course of vertical illuminance of the measured model road cutout with the road lighting. Illuminated by the xenon low beam headlights.

From the above mentioned results it is obvious that the combination of the vehicle low beam headlights and the road lighting system will increase the E_v in the entire sample road section. At points F, the value of E_v dropped below 1 lx only for xenon headlights at distances of 35 m and 40 m from the vehicle. This option is rather to have an idea of E_v progress in space, since it always depends on the particular geometric setting and lights of the particular system.

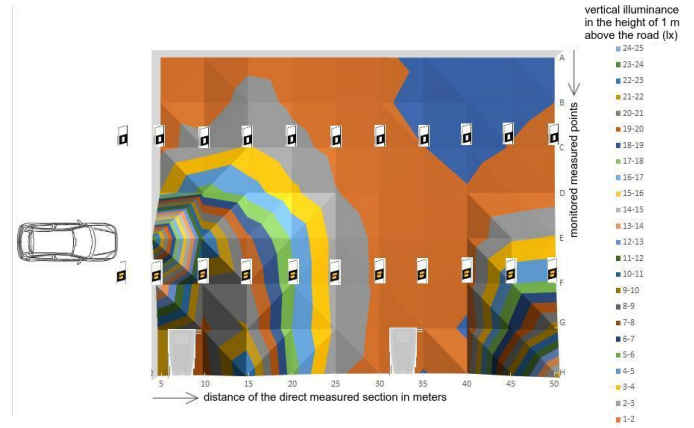


Fig. 8. The course of vertical illuminance of the measured model road cutout with the road lighting. Illuminated by the LED low beam headlights.

This group of results draws attention to the fact that the combination of low beam headlights and road lighting may not provide sufficient illuminance on a potential roadside obstacle and that its visibility in front of a road lighting luminaire can be minimal.

IV. CONCLUSION

The measurements have shown that the visibility of the obstacle in the right-side lane in the direction of drive with the low beam headlights without road lighting is up to 40 m from the vehicle. This is an alarming result, as we are able to stop the vehicle on wet road only at speeds up to 55 km/h.

By illuminating the road by combining the vehicle low beam headlight and the road lighting, the E_v value at point F was bigger than 1 lx in an entire length of the section. The condition was not met only for xenon when it was measured 0.9 lx at distances of 35 m and 40 m.

From these values, it would seem that in model situations, LED low beam headlights clearly surpassed the other headlights. However, by subjective observations during the measurement, sharp shadows were observed in sources with higher correlated color temperature, which were made by road directional posts. Furthermore, due to the high luminous flux of the headlights, there was a strong dazzling compared to the halogen and xenon headlights. As part of the development of headlights, it would be advisable to test a possibility of a combined headlight where the low beam would have the characteristics of a halogen headlight and the remote mode of the LED headlight. The reason for using a low beam halogen light would be due to the satisfactory E_v values and lower dazzling. The issue of dazzling of the above-described light source technologies will be discussed in detail in the following outputs, which will deal with the luminance analysis of the described and other model situations. It is important to note

that even a well-illuminated road does not guarantee that the obstacle will be visible on the road or in the boarding zone.

In the follow-up work, it would be fitting to focus on the shadows created by the directional posts and to compare the dazzling of other road users. Furthermore, in order to compare suitable technology for car headlights better, a larger sample of vehicles would need to be measured.

REFERENCES

- [1] P. Baxant, S. Sumeč, and J. Skoda, "Contrast analysis in lighting technology," Proceedings of 2016 IEEE Lighting Conference of the Visegrad Countries, Lumen 2016 Karpacz, Poland, ISBN: 978-150903305-8, DOI: 10.1109/LUMENV.2016.7745507.
- [2] L. Lipnický, D. Gasparovský, and R. Dubnická, "Influence of the calculation grid density to the selected photometric parameters for road lighting," Proceedings of 2016 IEEE Lighting Conference of the Visegrad Countries, Lumen 2016 Karpacz, Poland, ISBN: 978-150903305-8, DOI: 10.1109/LUMENV.2016.7745555.
- [3] EN 13201-2, "Road Lighting: Part 2: Requirements," Czech standardization institute, Prague, 2016.
- [4] EN 13201-4, "Road Lighting: Part 3: Calculation," Czech standardization institut, Prague, 2016.
- [5] Road traffic regulations, "Road traffic regulations - duties of persons enjoying diplomatic privileges and immunities in the Czech Republic," Act No. 361/2000 concerning road traffic and amending certain acts (Road Traffic Act), 2000.
- [6] ČSN CEN/TR 13201-1, "Road Lighting: Part 1: Guidance for selecting lighting classes," Czech standardization institute, Prague, 2016.
- [7] ČSN 73 6110, "Design of local roads," Czech standardization institute, Prague, 2006.

Modeling of Luminous Flux Radiation to the Upper Hemisphere from Real Model of Town

⁽¹⁾Petr Becak, ⁽²⁾Jana Wlosokova, ⁽³⁾Jan Picha

^(1,3)Faculty of Electrical Engineering and Computer Science

⁽²⁾Faculty of Mining and Geology

VSB-TU Ostrava

Ostrava, Czech Republic

petr.becak@vsb.cz, jana.wlosokova@vsb.cz, jan.picha@vsb.cz

⁽⁴⁾Tomas Novak, ⁽⁵⁾Karel Sokansky

^(4,5)Faculty of Electrical Engineering and Computer Science

VSB-TU Ostrava

Ostrava, Czech Republic

tomas.novak1@vsb.cz, karel.sokansky@vsb.cz

Abstract—Article targets to show potential of software goniophotometer from point of view calculation of the luminous flux leads to the upper hemisphere from road lighting system. Basis for this article was real model of blocks of flats in Frydek-Mistek. Software goniophotometer was originally checked in terms of accuracy for calculation direct and reflected part of the luminous flux [1]. In next step was creating of basic model formed from several objects including buildings and road lighting system realized by five luminaires [2]. Software upgrade allows possibility of inserting calculation grid in sphere shape. These points represented normal illuminance in direction to the middle of sphere and behave like an imagine luxmeter sensors. Aim of implementation this net is update simulation program for calculation of the luminous flux radiated to the upper hemisphere from artificial lighting systems as basis for next astronomic calculation which are deeply focused on night sky luminance description [3]. Using this model will possible to do models of the artificial light radiation of whole towns contains not only road light systems, but other artificial light sources too. Principle is to include radiation characteristics of these big units to LDT file as a one luminaire with information about luminous flux and shape of luminous intensity distribution. This LDT file could be used for next calculations which will evaluate influence of big light sources to night sky luminance.

Keywords—software goniophotometer, obtrusive light, road lighting, luminous flux, radiation, upper hemisphere

I. INTRODUCTION

The aim of the article is description of the software goniophotometer possibilities. It will show modelling of the luminous flux in upper hemisphere generated by outdoor light sources. The model was prepared because of necessity to predict behaviour of lighting systems from the point of view obtrusive light. Until this time it was possible to do only some partial short or long term measurements [4].

For this article was used the district Kolarikovo in town Frydek-Mistek. There is very high amount of old lighting

systems with high pressure sodium lamps (HPS) with sphere shape. These lighting systems radiate directly to the upper hemisphere luminous flux nearly 50 % of their total luminous flux. Therefore we can say that this blocks of flats is "good" example because of big source which can produce luminous flux to the upper hemisphere. It could leads to sky luminance increasing [5]. The obtrusive light is not possible avoid, because of the reflected luminous flux but with well directed lightning systems usage it is possible reduce it. The prevent improvement is installation of lighting systems with downward radiation only, which will lited only needed areas.

It is necessary to understand that outdoor lighting consists with many kinds of the light sources. The obtrusive light produces not only road lightings but also architectural lighting, billboards, illumination of sport facilities and parking places, warehouses, industrial buildings, etc. The obtrusive light is also emitted from interiors of buildings (windows) [6] and car headlamps. So generally, we can say that all artificial light (not only road lighting) can have negative influence and could have unpleasant effect for astronomers and environmentalists. Therefore it is necessary to verify all light sources from the point of view of the obtrusive light.

This article is aimed on calculation of the luminous flux radiated to the upper hemisphere only from road light systems. Other kind of light sources of the obtrusive light will be modeld and inserted in the future. All calculations were done with maintenance factor 1. It represent the worst case of the obtrusive light level.

II. FUNCTION OF SOFTWARE GONIOPHOTOMETER

Upgrade of software enable to insert calculation grid in sphere shape. Each calculated point describe normal illuminance in direction to the middle of sphere. This system duplicate function of the real goniophotometer. Principal of the goniophotometer is in possibility to measure luminous intensity in different levels and in different angles. It can be to interpret by sphere with calculation grid. The software goniophotometer duplicates this function only with difference, that is possible insert LDT file of luminaire or city LDT file with unbounded size. New possibility is option to choose density of calculation

Work is partially supported by Grants SGS SP2019/143 - BroadbandLIGHT - Public Lighting in SMART City and VI20172019071 - Analysis of Visibility of Transport Infrastructure for Safety Increasing during Night, Sunrise and Sunset

grid in angle step according standard used levels for luminaire measurement in C, γ planes. For correct calculation it is necessary to take each object as simple point source. It means that object has insignificant dimensions against distance of point which is calculated. In praxis is this ratio requested higher than 5 so as light source was taken as simple point source. Picture 1 shows situation of simple point source (model of blocks of flats) regarding to calculation grid of the software goniophotometer. When the longest distance of model is 625 meters, then diameter of calculation points is 5000 meters. The distance is longer then requirement and that it is why the calculation fulfill needed condition.

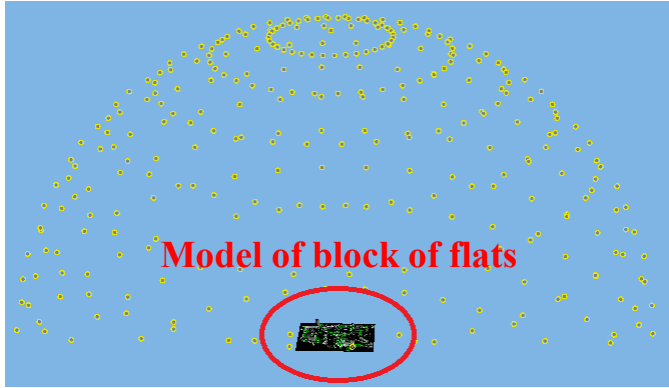


Fig. 1. Model of blocks of flats placed under the software goniophotometer.

It is necessary to repeat that the calculation grid displayed normal illuminance in direction to the middle of sphere and represent imagine luxmeter sensors. This fact shown figure 2.

Software is working on basis of inverse square law (1). It means that each calculation point of the grid represented normal illuminance and after it is converted to luminous intensity in solved direction. Output is final luminous intensity distribution for whole calculated lighting system, which is possible exported to the LDT file.

$$E = \frac{I}{l^2} \quad (1)$$

where:

- E Illuminance (lx)
- I Luminous intensity (cd)
- l Distance (m)

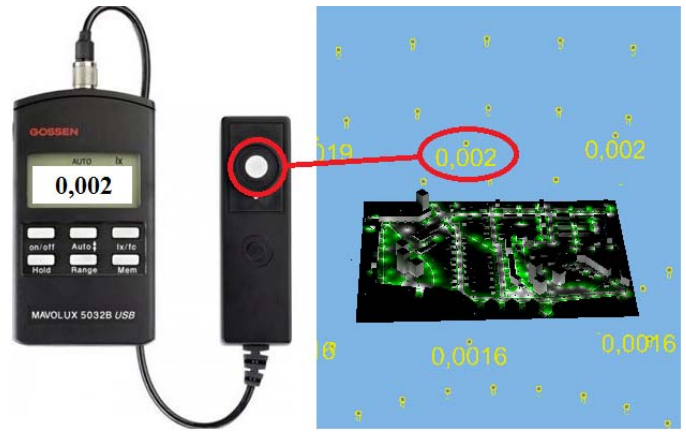


Fig. 2. Calculation grid showing normal illuminance of the software goniophotometer.

III. THE DISTRICT WITH BLOCKS OF FLATS KOLARIKOVO DESCRIPTION

Basis for model is part of town Frydek-Mistek with roads and build up area. The district is placed on GPS coordinates 49°40'30.4"N 18°20'03.6"E. Build up area is generally formed by blocks of flats and family houses. All surfaces like roads, houses and green spaces are described by their average reflectivity. Specification of it is in table 1.

TABLE I. OBJECTS PARAMETERS CALCULATED IN MODEL

Objects	Count (pcs)	Surface (m ²)	Reflectivity (%)
Buildings	170	-	30
Roads and parking places	-	50 000	10
Footpaths	-	11 000	20
Grass	-	137 000	10

The district includes big amount of luminaires radiated luminous flux to the upper hemisphere. Therefore it was appropriate this fact to check and verify by calculation, which ratio of luminous flux is going to the upper hemisphere. After calculation of this ratio it is possible to determine how much of luminous flux is going to the upper hemisphere directly and how much by reflection from modeled objects with regard on diffused reflection. Figure 3 shows 3D model of the district Kolarikovo. This model was taken from DWG data's with accurate placement of buildings, roads, and luminaires (with mounting height and luminaires directions) [7].

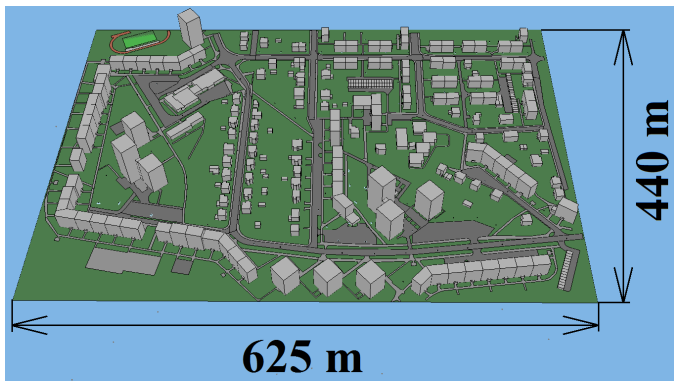
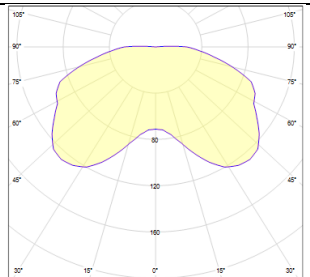
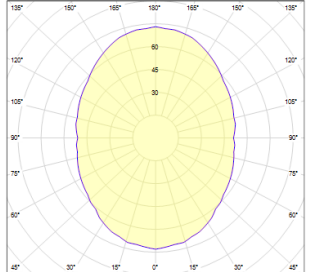


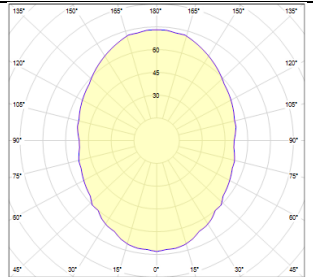
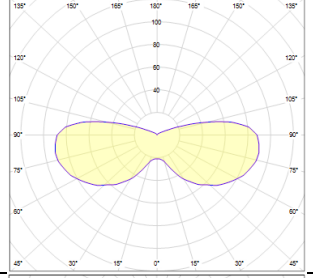
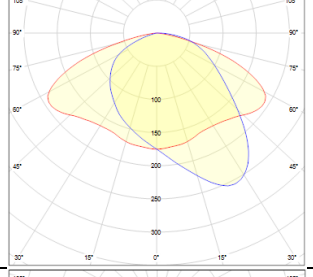
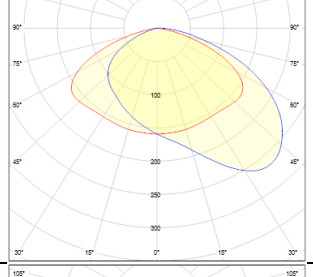
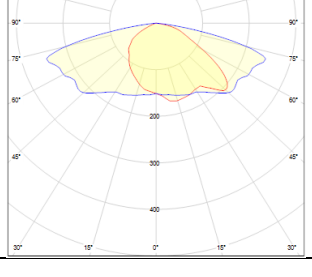
Fig. 3. 3D model of the district Kolarikovo with marked dimensions.

Used luminaires are placed on poles with height 5, 6 and 8 meters above ground. Each luminaire was inserted via LDT file. Total count and ration of the luminous flux radiated to the upper hemispheres (ULR) is described in table 2.

According table 2 ensues that 3 types of the luminaires are unfit for illumination of roads and paths, because their primary radiation to the upper hemisphere is very high. We are speaking about luminaires from companies Elektrosvit and Humaco. Those luminaires are “historical” and in time of installation was not accentuate on elimination of the obtrusive light, anyway in this time. For calculation was ignore tilting of luminaires (slope of outrigger is 0°), because of minimum amount of luminaires were tilted.

TABLE II. LUMINAIRES TYPES, THEIR COUNT AND LUMINOUS FLUX RADIATION

Luminaire type	Count (pcs)	ULR (%)	Luminous flux distribution
Elektrosvit 4460570	4	1,3	
Elektrosvit 4461602	30	50,1	

Elektrosvit 4461902	94	50,4	
Humaco EP 50W RAL	4	25,3	
Elstav Lunoide 70 SHC	46	0	
Elstav Lunoide 100 SHC	8	0,1	
Artechnic-Schreder M2A-S 100 SHC	6	0	

On table 2 basis is possible to say that in studied area is 192 luminaires in total. Total initial luminous flux of all luminaires in model is 845 868 lm with total electrical power 16 810 W. It shows next table.

TABLE III. LUMINOUS FLUX AND POWER OF LIGHTING SYSTEMS

Luminaire type	Luminaire power (W)	System power (W)	Luminaire luminous flux (lm)	System luminous flux (lm)
Elektrosvit 4460570	85	340	3 306	13 224
Elektrosvit 4461602	85	2 550	4 234	127 020
Elektrosvit 4461902	85	7 990	4 234	397 996
Humaco EP 50W RAL	85	340	3 960	15 840
Elstav Lunoide 70 SHC	85	3 910	4 032	185 472
Elstav Lunoide 100 SHC	120	960	7 030	56 240
Artechnic-Schreder M2A-S 100 SHC	120	720	8346	50 076

IV. RESULTS FROM CALCULATION OF DISTRICT RADIATION

Complete aim of experiment is to calculate luminous flux ratio emitted to upper hemisphere. Calculation in software makes it possible calculate only direct element of this luminous flux and direct element including reflected luminous flux, so total luminous flux going to the upper hemisphere. Calculation of reflected luminous flux is valid only in condition for diffused reflection. Following graphs show amount and shape of radiated luminous flux which is produced by whole amount of lighting sources inside the model of the district.

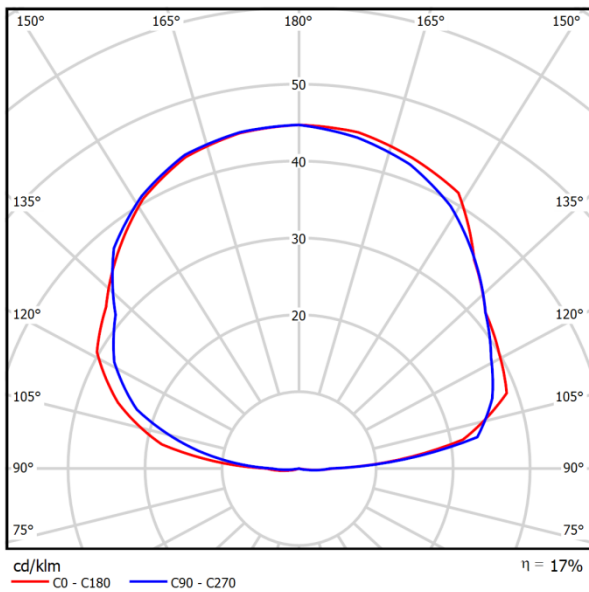


Fig. 4. Luminous intensity distribution included only direct luminous flux from luminaires to the upper hemisphere.

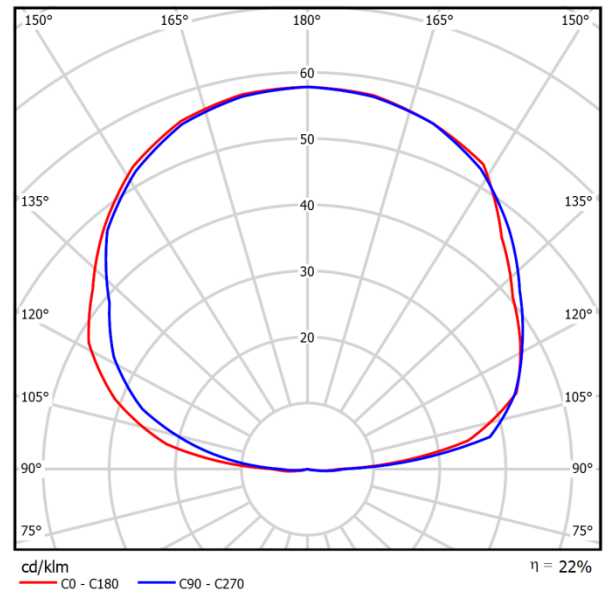


Fig. 5. Luminous intensity distribution included direct and reflected luminous flux from luminaires to the upper hemisphere.

Based on previous information it is possible establish:

Shapes and luminous intensity sizes calculated from the district model is responding to presumption. Calculated luminous intensity distribution radiate only to the upper hemisphere and its shape approximates to cosine (diffuse) radiator. Expected deviations from cosine shape are visible in curves asymmetry between planes C0 and C90 of the model. This effect is caused by asymmetric luminaires and by geometry of the model.

Ratio of direction luminous flux radiated to the upper hemisphere was calculated by software on 17 % from total luminous flux of whole lighting system. It represents value 143 798 lm. Major influence on this fact have luminaires which emits approximately 50 % of luminous flux directly to the upper hemisphere. In this study we have 124 these luminaires from total 194 luminaires.

Total luminous flux radiated to the upper hemisphere was calculated on 22,7 % from overall luminous flux radiated from used luminaires. It represents 192 012 lm. Reflected element is possible calculate and in this case it is 5,7 % of total luminous flux. It represents 48 214 lm. This fact confirms that influence of direct luminous flux is higher than reflected one.

V. CONCLUSION AND VISION FOR THE FUTURE

Following table describes overview calculation parameters, which deals with luminous flux radiation to the upper hemisphere. It was calculate on the base of the district Kolarikovo model with real lighting systems.

TABLE IV. SUMMARY OF CALCULATION PARAMETERS OF THE DISTRICT KOLARIKOVO

Parameters	HPS lighting system
Total electrical power of lighting systems (W)	16 810
Total luminous flux of lighting systems (lm)	845 868
Luminous flux radiated to the upper hemisphere (%)	22,7
Luminous flux radiated to the upper hemisphere (lm)	192 012
Direct luminous flux radiated to the upper hemisphere (%)	17
Direct luminous flux radiated to the upper hemisphere (lm)	143 798
Reflected luminous flux radiated to the upper hemisphere (%)	5,7
Reflected luminous flux radiated to the upper hemisphere (lm)	48 214

In software it is possible to change old lighting system by modern LED [8, 9] lighting system with the same parameters and observe differences in luminous flux radiation to the upper hemisphere.

Aim for future is to complete model for all potential sources of obtrusive light and calculate and verify ratio of luminous flux from those sources against road lighting systems. This vision shows figure 6.

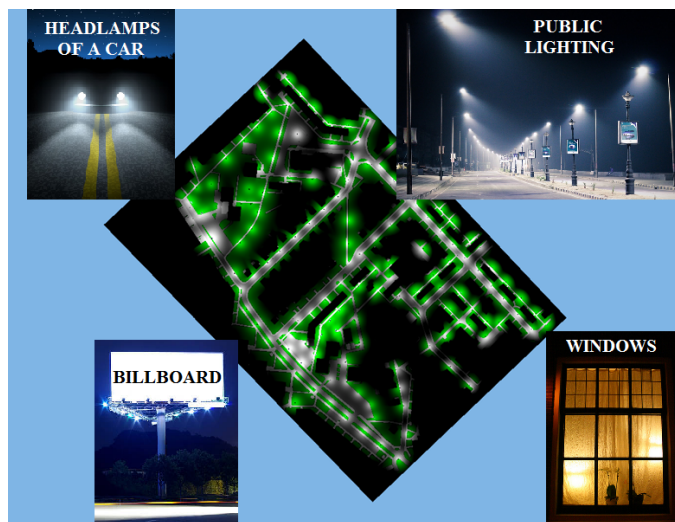


Fig. 6. All light sources of potential obtrusive light, which will be implemented to the model in future.

REFERENCES

- [1] P. Běčák, T. Novák, R. Baleja, K. Sokanský, "Testing of the Software Goniophotometer in Wils - Building Design Computational Programme", Published in: Electric Power Engineering (EPE), 2018, 19th International Scientific Conference, 2019Bmo, Czech Republic, ISBN: 978-1-5386-4612-0
- [2] P. Běčák, T. Novák, R. Baleja, K. Sokanský, "Radiation of the Luminous Flux into the Upper Half-Space in Wils - Building Design", Proceedings of 7th Lighting Conference of the Visegrad Countries, LUMEN V4 2018, 2018, Grand HotelTrebic Czech Republic, ISBN: 978-153867923-4
- [3] M. Kocifaj, F. Kundracik, "Modeling the night sky brightness distribution via new SkyGlow Simulator", Proceedings of 2016 IEEE Lighting Conference of the Visegrad Countries, Lumen 2016 Karpacz, Poland, DOI: 10.1109/LUMENV.2016.7745553
- [4] L. Lipnický, D. Gašparovský, R. Dubníčka, "Influence of the calculation grid density to the selected photometric parameters for road lighting", Proceedings of 2016 IEEE Lighting Conference of the Visegrad Countries, Lumen 2016 Karpacz, Poland, DOI: 10.1109/LUMENV.2016.7745555
- [5] F. Dostal, K. Sokanský, T. Novák, "Long-term measurements of night sky illuminance", 2010, 1 2010 9th International Conference on Environment and Electrical Engineering, DOI: 10.1109/EEEIC.2010.5489919
- [6] S. Darula, P. Oberman, "Jas okna v noci", Kurz osvětlovací techniky XXVII, Kouty nad Desnou, ISBN 978-80-248-2087-3
- [7] P. Žák, S. Vodráčková, "Conception of public lighting", Proceedings of 2016 IEEE Lighting Conference of the Visegrad Countries, Lumen 2016 Karpacz, Poland, DOI: 10.1109/LUMENV.2016.7745514
- [8] R. Dubníčka, L. Lipnický, M. Barčík, D. Gašparovský, "Comprehensive view of LED products in luminaires", Published in: Diagnostic of Electrical Machines and Insulating Systems in Electrical Engineering (DEMISEE), 2016 Papradno, Slovakia, DOI: 10.1109/DEMISEE.2016.7530467
- [9] T. Pavelka, M. Ptacek, P. Baxant, "Static model of LED behaviour depending on operating conditions", Published in: Electric Power Engineering (EPE), 2016 17th International Scientific Conference, 2016 Prague, Czech Republic, DOI: 10.1109/EPE.2016.7521774

Comparison of Properties of White LED and Blue LED with External Phosphor Layer

Jan Vitasek, Tomas Stratil, Zdenek Wilcek, Jakub Kolar, and Michal Hub

Department of Telecommunications, Faculty of Electrical Engineering and Computer Science,

VSB–Technical University of Ostrava, 17. listopadu 15, 708 00 Ostrava, Czech Republic

Tel: +420 596 999 413, Fax: +420 596 991 650, e-mail: jan.vitasek@vsb.cz

ABSTRACT

This article deals with comparison of illumination and communication properties of white LED (5500K) and blue LED with external phosphor layer. At the start, the illumination properties of phosphors (internal, external) were measured after excitation by square signal. Based on these values, suitable frequencies of communication signal were determined. Further, frequency of modulation signal was increased with regard on final white signal. The voltage transmission was also calculated for both white light sources.

Keywords: LED, modulation, phosphor, rise and fall times, VLC.

1. INTRODUCTION

Light Emitting Diodes (LEDs) are more and more used. The primary purpose their use is illumination. We can meet the LEDs in light bulb, are used for street lighting, automotive uses them in headlamps and in tail lamps. The LEDs replace the standard illumination sources because they have better characteristics. LEDs have longer lifetime, a smaller and compact size and minimum heat generation compared with the classical illumination sources. The power consumption is lower, they are tolerant to humidity and they have higher efficiency [1-4].

Except the illumination properties, the LEDs have also communication properties. We can say that LEDs are multifunctional. LEDs could be fast switched on and off in comparison to the classical light bulbs and fluorescent lamps. This can be used for Vehicle-to-Vehicle (V2V) communication and Vehicle-to-Infrastructure (V2I) communication. Great potential is placed in Visible Light Communication (VLC) or in Light Fidelity (Li-Fi) which can replace the Wi-Fi (radio based). The VLC technology combines two functions together, illumination and communication [5-7].

There are two ways, how to create white light. The first way is use of three (red, green and blue) or more colour chips. Correct intensity levels of chips make white light. This way is called Colour Mixing. The other way uses conversion of light from short wavelengths to longer wavelengths. A blue light emitting chip (short wavelengths, higher energy) excites a yellow phosphor; a part of the blue light is converted in the yellow light (longer wavelengths, lower energy) which together with rest of blue light create white light. YAG:Ce materials usually serve as a converter. The disadvantage of the conversion of light is a photoluminescence (PL) decay [1,3].

This article compares properties of white light created by blue emitting LED with external phosphor layer QMK58/F-U1 ($Y_3Al_5O_{12}:Ce^{3+}$) and properties of white light from white LED (internal phosphor). It was known from the previous measurement, that the phosphor QMK58/F-U1 creates white light with Colour Correlated Temperature (CCT) around 5100 K. The commonly available white LED with CCT 5500 K was chosen for comparison. This white LED is labelled in text as LED5500 K.

2. ARRANGEMENT OF MEASUREMENT

2.1 Poly-Di-Methyl-Siloxane Polymer

The phosphor powder QMK58/F-U1 was mixed with a Poly-Di-Methyl-Siloxane (PDMS) names Sylgard 184 [8] which serves as a carrier. The Sylgard 184 compounds of two parts, a PDMS base and a curing agent. The mixture of PDMS base, curing agent, phosphor QMK58/F-U1 was put in the shaker for the uniform distribution. The heat hardening happens at temperature around 85°C, it takes 30 minutes.

Before the heat hardening, the mixture of PDMS+phosphor created thin layer at the end of the reflector which can be easily put to the power LED.

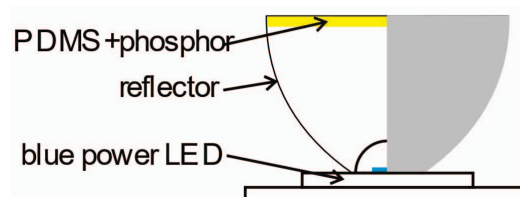


Figure 1. PDMS+phosphor in a reflector.

2.2 Illumination properties measurement

The blue power LED H2A1-H450 [9] with external phosphor layer and the white LED5500K [10] was supplied (continually) by forward current from 50 mA to 350 mA (with step 50 mA) through a High Power Mounts TCLDM9 (Thorlabs) and Benchtop LD Current Controller LDC240C (Thorlabs). We recorded the total optical spectrum, colour coordinates x , y , and CCT by the spectrometer Avantes HS2048XL.

2.3 Communication properties measurement

The power LEDs (H2A1-H450, LED5500K) were supplied and modulated through the High Power Mounts TCLDM9 (Thorlabs), which includes Bias-T RF input (50Ω). Thanks to this component it is possible to add a DC and AC component into LED. The Benchtop LD Current Controller LDC240C (Thorlabs) served as DC component source (150 mA). The AC component created a signal generator HMF2550 (Rohde&Schwarz). It was a square signal ($f=1\text{MHz}$, $U_{\max}=10\text{V}$, $U_{\min}=0\text{V}$). That means a high forward current was 350 mA, a low forward current was 150 mA. We used the photodetector PDA36A-EC (Thorlabs), its output was connected to the oscilloscope LeCroy 204Xi for signal evaluation.

The measured parameters were rise and fall times. According this we determined a maximal frequency of modulation signal.

3. RESULTS OF ILLUMINATION PROPERTIES

This chapter summarizes results of measurement of illumination properties of the white LED5500K and the blue LED with the external phosphor layer. The forward current gradually increased from 50 mA to 350 mA with a step 50 mA. The measured results are in Table 1 and Table 2. Figure 2 shows spectra of created white lights for different forward currents. The results showed that the blue LED with the external phosphor layer emits more invariable white light (CCT changed less) than the white LED with internal phosphor layer.

Table 1. Illumination properties of the blue LED with the external phosphor layer QMK58/F-U1.

I_f (mA)	50	100	150	200	250	300	350
x (-)	0.3481	0.3468	0.3457	0.3449	0.3443	0.3439	0.3436
y (-)	0.4043	0.4000	0.3967	0.3942	0.3924	0.3915	0.3904
CCT (K)	5036.9	5065.7	5091.7	5112.4	5128.0	5135.9	5145.3

Table 2. Illumination properties of the white LED5500K.

I_f (mA)	50	100	150	200	250	300	350
x (-)	0.3385	0.3348	0.3330	0.3318	0.3310	0.3306	0.3298
y (-)	0.3511	0.3467	0.3432	0.3403	0.3379	0.3360	0.3340
CCT (K)	5256.4	5402.1	5477.4	5528.3	5564.4	5586.1	5621.0

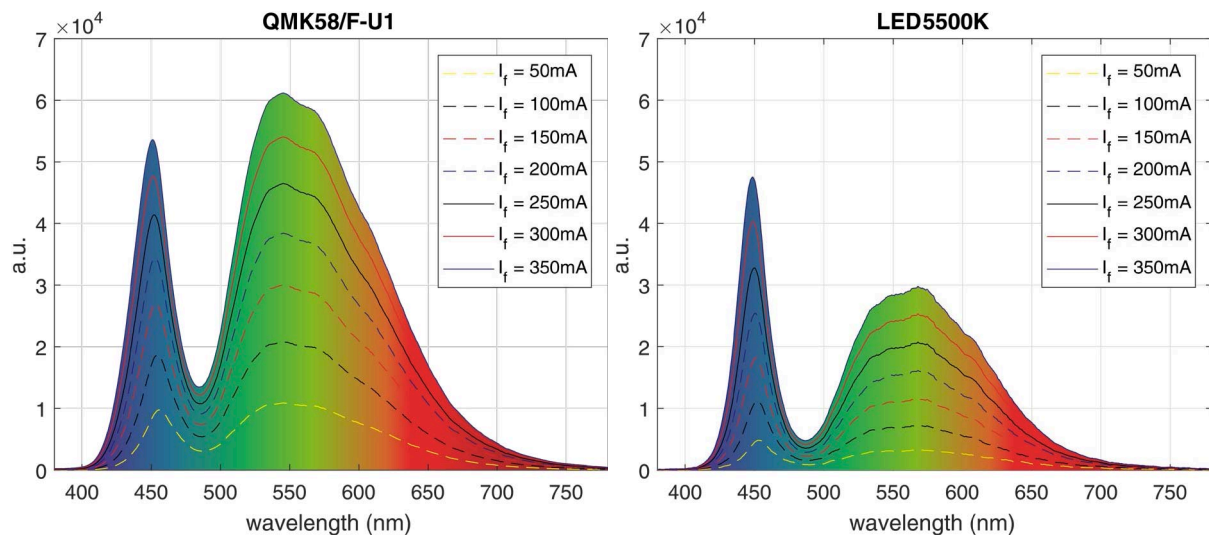


Figure 2. Emitted spectra for different forward currents.

4. RESULTS OF COMMUNICATION PROPERTIES

We used the square signal its parameters are mentioned above. The initial frequency of this signal was 1 MHz. The measurement showed that the rise time t_r of the blue LED with the external phosphor layer was 123.23 ns,

the fall time t_f was 126.26 ns. Based on these measured values, we reckoned the theoretical maximal frequency of modulation signal according to the relation:

$$f_{max} = \frac{1}{t_r + t_f}. \tag{1}$$

This frequency was 4.008 MHz for the blue LED.

The same measurement was repeated with the white LED5500K. The rise time t_r was 151.01 ns, the fall time t_f was 160.25 ns. The theoretical maximal frequency of modulation signal proceeds from the relation 3.212 MHz.

The next step was increasing of frequency of the square signal and observing the mentioned parameters. The frequency was increased with step 0.5 MHz. During the measurement we also recorded the amplitude of received signal for calculation of a voltage transmission. Results are summarized in Table 3. The transmission was calculated according the relation:

$$A = 20 \log \frac{U_{f>1MHz}}{U_{f=1MHz}}, \tag{2}$$

where $U_{f=1MHz}$ is voltage measured by the oscilloscope at 1MHz, $U_{f>1MHz}$ is voltage measured at higher frequencies.

Table 3. Comparison of two white light sources – rise and fall times, transmission.

Frequency (MHz)	H2A1-H450 + QMK58/F-U1			LED5500K		
	t_r (ns)	t_f (ns)	Transmission A (dB)	t_r (ns)	t_f (ns)	Transmission A (dB)
1.0	123.2	126.3	0.000	151.0	160.3	0,000
1.5	122.3	125.8	-0.015	149.1	154.9	-0.272
2.0	120.7	124.6	-0.160	132.5	136.8	-1.019
2.5	107.2	111.8	-0.812	118.7	120.9	-1.991
3.0	95.7	96.1	-1.814	102.9	104.5	-3.283
3.5	77.6	78.9	-3.139	82.8	84.5	-5.018
4.0	72.5	74.5	-3.701	73.4	75.0	-6.077
4.5	64.1	64.8	-4.651	63.6	64.8	-7.365
5.0	57.7	59.2	-5.977	56.3	57.4	-8.685
5.5	51.2	52.5	-7.108	50.3	51.4	-9.946
6.0	46.1	47.1	-8.175	45.2	46.0	-11.933
6.5	42.5	43.1	-8.897	39.9	40.5	-13.390

Figure 3 (left) shows the rise and fall times of signals for both two white light sources. Figure 3 (right) shows the voltage transmission expressed in dB. The rise times gradually shorten, because the rise time of excitation pulse also shortens with increasing frequency. The same deals for the fall times.

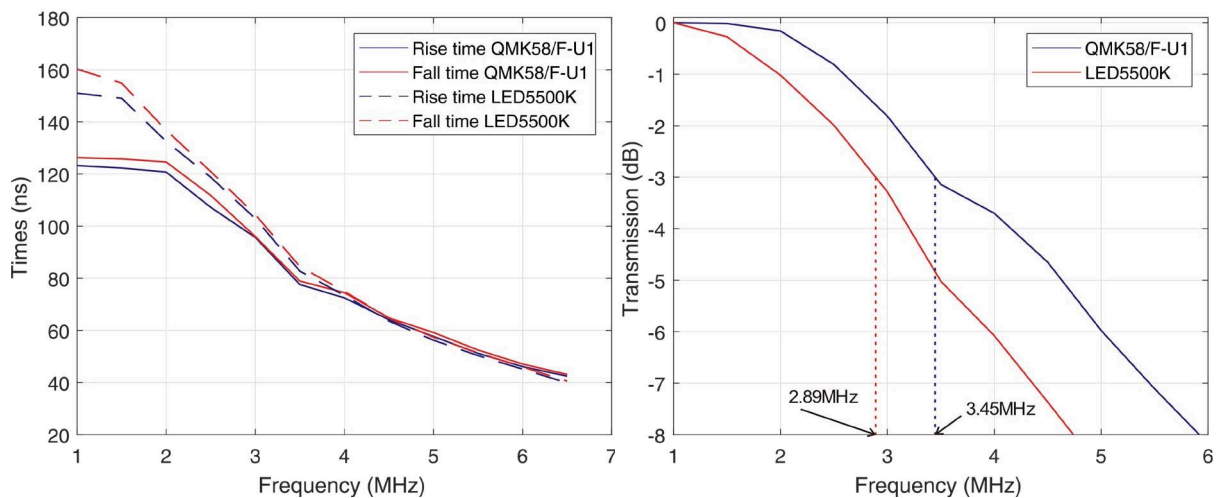


Figure 3. Rise and fall times (left), voltage transmission (right).

Figure 4 shows signals of white light detected by the photodetector after excitation by the square signal with frequencies 1 MHz and 4 MHz respectively. It is obviously from Fig. 4, that the rise and fall times of the blue

LED with the external phosphor layer are shorter than times of the white LED5500K. further, we can observe an amplitude drop of signal after excitation by the square signal with frequency 4 MHz. An amplitude ratio (Amp_{1MHz}/Amp_{4MHz}) is smaller for the blue LED with the external phosphor layer than for the white LED5500K. This is shown in Fig. 4(right).

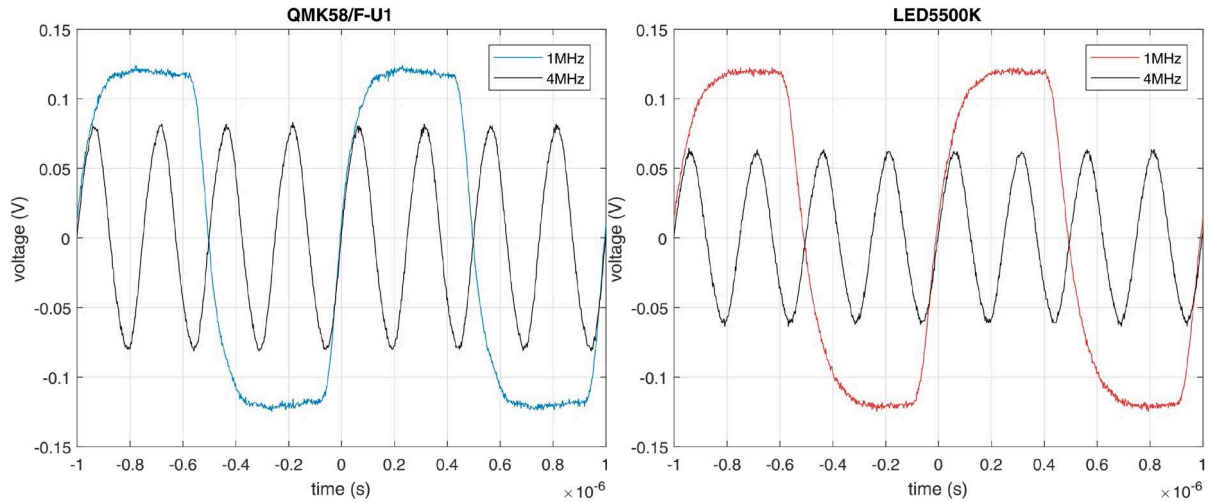


Figure 4. Signals received by the photodetector.

5. DISCUSSION

We measured the illumination properties of the phosphor powder QMK58/F-U1, which is suitable to white light creation together with the blue light emitting power LED. The white LED5500K was chosen for comparison. At first, we tested change of CCT with regard to the forward current. This parameter is important for the communication properties of white light, because the CCT should change minimally. The change of CCT can be evaluated by the relation (3), which is derived from relative error [11]:

$$\Delta(\%) = \frac{CCT_{I_f=350mA} - CCT_{I_f=50mA}}{CCT_{I_f=50mA}} \cdot 100, \quad (3)$$

where CCT are values measured for mentioned forward currents. The change Δ of CCT for QMK58/F-U1 was 2.2% and for LED5500K 6.9% respectively. These changes are not noticeable. However, the blue LED with the external phosphor layer has more stable illumination properties.

The communication properties of compared white light sources are expressed in rise and fall times. The next observed parameter was the frequency in which the voltage transmission decreases by 3 dB. The measurements showed that the blue LED with the external phosphor layer can transmit higher frequency than the white LED5500K. Before the measurement, we reckoned the maximal usable frequency based on rise and fall times. Finally, these assumptions did not come true, the results were slightly worse.

6. CONCLUSION

This article compared properties of the blue LED with the external phosphor layer and properties of the white LED5500K. At first, the illumination properties were tested. It was shown that the blue LED with the external phosphor layer has more stable CCT than the white LED regarding to the forward current. Testing of communication properties focused on measurement of rise and fall times. The next evaluated parameter was the voltage transmission at different frequencies. Measurement showed that the blue LED with the external phosphor layer can transmit higher frequencies than the white LED.

ACKNOWLEDGEMENT

The authors would like to acknowledge the financial support of the Ministry of Education, Youth and Sports of the Czech Republic under Projects No. SP2019/80 and SP2019/143 of VSB–Technical University of Ostrava, Czech Republic. Our research was also supported by Projects No. VI20172019071, VI20152020008, TA04021263, TK01020162 and TK01020178. The work has been partially supported by projects CZ.1.07/2.3.00/20.0217.

REFERENCES

- [1] G. Held: *Introduction to Light Emitting Diode Technology and Applications*, CRC Press, Boca Raton, 2009.

- [2] N. D. Q. Anh, T. H. Q. Minh, and N. H. K. Nhan: Active pre-equalizer for broadband over visible light, *Advances in Electrical and Electronic Engineering*, vol. 14, no. 5, pp. 609-614, Dec. 2016.
- [3] E. F. Schubert: *Light-Emitting Diodes*, Cambridge University Press, Cambridge, 2006.
- [4] T. Stratil, P. Koudelka, R. Martinek, and T. Novak: Active pre-equalizer for broadband over visible light, *Advances in Electrical and Electronic Engineering*, vol. 15, no. 3, pp. 553-560, Mar. 2017.
- [5] T. H. Do and M. Yoo: Visible light communication-based vehicle-to-vehicle tracking using CMOS camera, *IEEE Access*, vol. 7, pp. 7218-7227, Jan 2019.
- [6] M. Ahmad, Q. Chen, Z. Khan, M. Ahmad, and F. Khurshid: Infrastructure-based vehicular congestion detection scheme for V2I, *International Journal of Communication Systems*, vol. 32, no. 3, pp. 1-14, Feb. 2019.
- [7] A. F. Santamaria and C. Sottile: Smart traffic management protocol based on VANET architecture, *Advances in Electrical and Electronic Engineering*, vol. 12, no. 4, pp. 279-288, Nov. 2014.
- [8] Sylgard 184 Silicone Elastomer Kit, Dow Corning [online], available at: <http://www.dowcorning.com/applications/search/default.aspx?R=131EN>.
- [9] H2A1-H450, Roithner Lasertechnik [online], http://www.roithner-laser.com/datasheets/led_highsingle/h2a1-h450.pdf.
- [10] GT-P03W54101140, GM Electronic [online], <https://www.gme.cz/led-1w-white-140lm-120-hexagon-gt-p03w54101140>.
- [11] R. S. Witte, J. S. Witte: *Statistics*, Wiley, Hoboken, 2009.

Measurement of Influence of Total Rainfall on Modulated Optical Beam in Laboratory FSO System

Jan Latal*, Jan Vitasek*, Marian Bojko**, Lukas Hajek*, Zdenek Wilcek*, Jakub Kolar*,
Tomas Stratil*, and Filip Šarlej*

*Department of Telecommunications, Faculty of Electrical Engineering and Computer Science,
VSB-Technical University of Ostrava, 17. listopadu 15, 708 33 Ostrava, Czech Republic

**Department of Hydromechanics and Hydraulic Equipment, Faculty of Mechanical Engineering,
VSB Technical University of Ostrava, 17. listopadu 15, 708 33 Ostrava, Czech Republic

Tel.: +420 597 325 845, E-mail: jan.latal@vsb.cz

ABSTRACT

This article deals with an effect of a rainfall on modulated optical beams simulated in a laboratory environment in FSO systems. The aim of our study was to find out how much the rainfall can affect a communication. Different types of modulated light sources operating at different wavelengths in FSO links have been used. An integral part of the study is also a detailed analysis of the behavior of simulated atmospheric transmission conditions affecting over the entire length of the fibreless optical link in laboratory.

Keywords: FSO, MER, rain, refractive index, bit rate.

1. INTRODUCTION

Free Space Optic (FSO) systems are an important type of communication system that provides high transmission rates (Gbps) in unlicensed bandwidth, relatively easy to install, high security, minimal problem with electromagnetic compatibility etc. The FSO can connect distances up to 10 km or more, depending on used light sources, their power, configuration and additional optics. This makes the FSO as a very important technology usable also for space applications, including applications for businesses such as Facebook, Google, etc. However, what significantly degrades the FSO; it is the transmission environment, which is the atmosphere, precisely the troposphere for ground FSO systems. The troposphere extends from the surface of the Earth up to 7 km in the polar regions and 18 km around the equator. It is the lowest layer of the atmosphere. The temperature of the troposphere decreases with altitude. The impact of atmospheric phenomena on FSO systems is critical and can either completely interrupt or suppress the link reliability of the entire transmission system, which in turn affects the Quality of Service (QoS). The Earth's atmosphere consists of 21% oxygen, 78% nitrogen and 1% occupy noble gases and other elements. The atmosphere also includes water and aerosols. The most degrading effect affecting on the FSO systems is a fog, where the droplet/mist particle size is proportional to the wavelength of light. The heavy fog can reach an attenuation up to 300 – 315 dB·km⁻¹. The second major degrading effect on FSO systems is rain. However, this phenomenon is not as strong as the fog because the droplet radius is 200 – 2000 μm. The droplet radius is therefore higher than the wavelength of light sources [1, 4].

Typical values of attenuation of a water column of 25 mm·h⁻¹ are approximately 6 dB·km⁻¹. Therefore, commercially available FSO systems operating with a 25 dB reserve are not limited by rain. Especially in urban areas, because of the distance of the FSO is less than 1 km thus the FSO is resistant to rain. If the FSO system is working at a distance of 500 m, then the rain attenuation will be approximately 3 dB·km⁻¹. If it is a cloud burst, which corresponds to a water column value >100 mm·h⁻¹ [5], then it can cause problems in areas where the FSO distance is higher than in metropolitan areas. However, cloud bursts with a given intensity have a short duration, so the FSO connections do not endanger long term. Rainfall intensity is the amount of rainfall that falls to the ground over a period of time. The intensity can range from very weak (0.1 mm·h⁻¹ to 2.5 mm·h⁻¹) to very strong (more than 40 mm·h⁻¹). The FSO/RF combination is used to increase the reliability of the FSO link, but this may not be enough.

The aim of this work is to analyze the behavior of the FSO systems with different wavelengths and transmission rates. The evaluation parameter was the communication parameter Modulation Error Ratio (MER) depending on the total rainfall. These rainfalls are simulated using the made-up nozzle control system in an acrylate box in the laboratory. For a detailed analysis of the behavior of refractive index changes, a modified Edlen equation is used, where input variables (pressure, humidity, temperature) are required. As a result, a measuring system consisting of sensors along the optical beam path, which penetrated the acrylate box, was made.

2. ANALYSE OF RAIN EFFECT ON FSO SYSTEMS

Electromagnetic wave propagation in the troposphere is affected by hydrometeors, which are raindrops, hail or even clouds. Waves are scattered and attenuated. The raindrop influences the electromagnetic wave in two ways. The first way is characterized that the drop behaves as a lossy dielectric where the energy is absorbed. Therefore,

the raindrop can be considered a semiconducting environment. In this wave propagating environment, it induces sliding currents causing heat loss – attenuation occurs. In addition, the currents become induced in the drops of rain or mist by a source of secondary radio waves, thereby dissipating energy into undesirable directions [2].

It is necessary to approach this issue with the help of a statistical approach (in time and in space). The first method is microscopic. It is based on the description of the interaction of electromagnetic wave with a raindrop of specific dimensions and shape. The other method is macroscopic. This approach is based on long-term measurements in dependence of precipitation intensity and attenuations on given connections, where empirical models are valid for the particular destinations and for the annual or monthly probabilities of connections, or the occurrence of rain intensity.

Rain is the most common type of precipitation in temperate zone. The rain attenuation of FSO is caused by the absorption of energy by the raindrop and the scattering of the laser beam in all directions. The rain droplet diameter is between 0.1 mm and 7 mm. Smaller drops are drops of cloud. Larger raindrops are unstable and tend to fragment. Droplets smaller than 2 mm in diameter are spherical, larger droplets are flattened and droplets larger than 4 mm deepened at the bottom of the given Pruppacher-Pitter shape. The actual shape is approximated in order to derive the dispersion properties of electromagnetic waves [3].

However, some articles also deal with a study of rainfall effects on radio or FSO systems, which is a major benefit of this article. In 2002, a team around Maha Achour dealt with the simulation of total rainfall, which created rainfall attenuation models, total rainfall /intensity, the definition of falling droplet velocities of different sizes [6].

Another study of the rain effect on FSO systems was mainly addressed in Kuala Lumpur, where precipitation frequently occur. Fatin Hamimi Mustafa et al. analyzed the data for Heavy-Rain and Lighter Rain or Drizzle [7]. Another team [8] studied other types of rainfall attenuation models for FSO systems for one year at the same place. They created behavior prediction models from the measured precipitation values. These models were then compared to the already established models according to ITU-R P.838, R.

The effect of rain drop attenuation on the FSO link operating at wavelengths 532 and 655 nm was studied at work [9]. It was found that nonlinear attenuation increases with a linear increase in rainfall rate. It was also found that rain had a greater effect on 532 nm. Also, the influence of FSO/RF simulation link was studied based on long-term data in Pakistan, where it was found that CCDF (Complementary Cumulative Distribution Function) was used to determine the value of the monthly distribution function affecting such a communication system. The connection would have up to 99.99% reliability if the joint length was less than a few hundred meters. The aim was to point out the possibility of using FSO/RF for 5G networks [10].

In another article, the authors again focused on the use of FSO/RF link (1550 nm / 60 GHz) to maximize the availability of a hybrid link using a channel probabilistic model. This model was based on the observed attenuation characteristics of the link obtained from the power level measurement for a given hybrid link [11].

Rainfall attenuation behavior prediction models for FSO systems have been studied. The new very simple model has been set to 5 km long FSO communication link, where it refines the previously used models [12].

3. ANALYSE OF RAIN EFFECT ON FSO SYSTEMS

A measuring apparatus was constructed to simulate the total rainfall, which is partially automated and allows modifications. This makes it possible to study the behavior of the optical modulated FSO link in laboratory conditions. To ensure stable conditions of the simulated atmosphere, an acrylate box (250×50×50 cm) was used. A detailed description of the measuring configuration is described in [13]. However, we used only two calibrated nozzles for the experiment: 90B1FP3,5 (purple) 90B2FP6,5 (brown). The aim of the measurements was to determine the state of the simulated atmosphere from the point of view of measuring the basic parameters such as humidity, temperature and pressure, from which the value of the refractive index can be calculated. This is one of the basic parameters of the transmission medium. A set of IoT sensors based on BME280, which are stored in special boxes protecting them from a direct column of simulated rainfall with a NodeMCU central control unit Lolin V3 through a MQTT protocol transmitting through Wi-Fi wireless technology, was designed. Individual sensors for measuring of the atmospheric parameters are disposed within the box to follow the path of the optical modulated beam through the box along its length below it, see Fig. 1. The measured data are saved into a file from which the variables can be substituted into the modified Edlen equation for the refractive index calculation.

A LabVIEW application was created for controlling of valves to set the water flow. The valves were set to 50% or 100% of its maximum value. The application allows to adjust the flow and monitor the current pressure level in bar units within the hose distribution system. To calculate the rainfall, it is necessary to know the flow rate and the value of the water that has passed in an hour. For the purple nozzle and the 50% valve opening of the regulator, the precipitation intensity is $120 \text{ mm}\cdot\text{h}^{-1}$ and the flow rate is $5 \text{ l}\cdot\text{min}^{-1}$ and at 100% it is $216 \text{ mm}\cdot\text{h}^{-1}$ and the flow rate is $9 \text{ l}\cdot\text{min}^{-1}$.

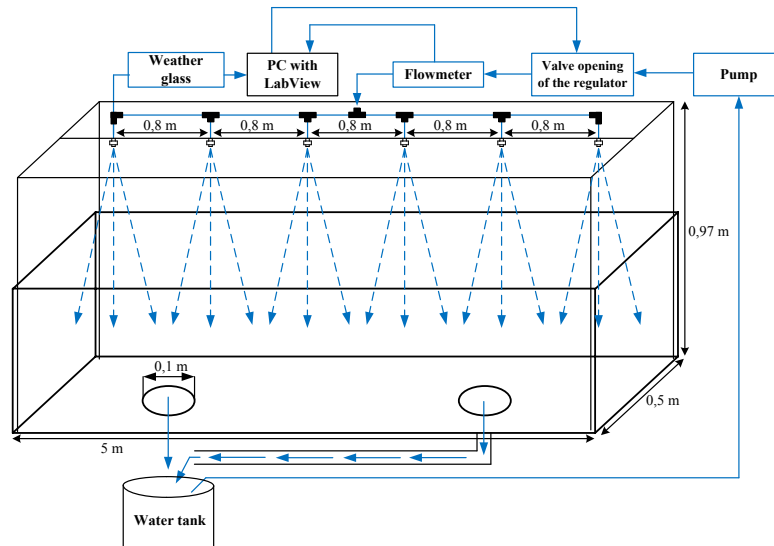


Figure 1. Laboratory acrylate box for rain simulation for FSO link.

For the brown nozzle and the 50% valve opening of the regulator, the rainfall intensity is $144 \text{ mm} \cdot \text{h}^{-1}$ and the flow rate is $6 \text{ l} \cdot \text{min}^{-1}$ and at 100% it is $240 \text{ mm} \cdot \text{h}^{-1}$ and the flow rate is $10 \text{ l} \cdot \text{min}^{-1}$. Measurement of atmospheric parameters during rain simulation was performed using a purple nozzle and a light source operating at 650 nm with a control valve opening of 50% and 100%. However, since the sensors were then damaged by a jet of water spouting onto a set of sensors, no measurements were made for the brown nozzle and another 850 nm wavelength. For this reason, it was not possible to realize measurements of atmospheric parameters for the wavelength of 850 nm and thus to calculate the refractive index in the acrylate box based on the modified Edlen equation.

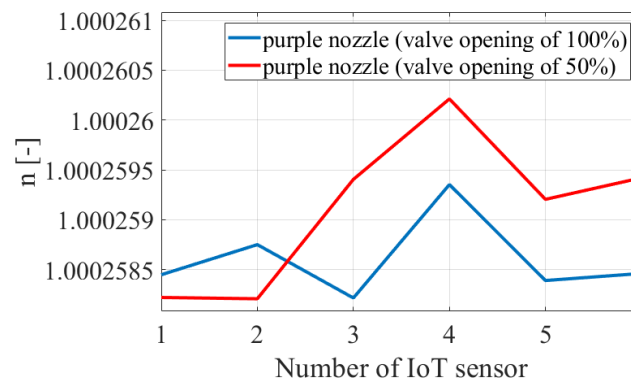


Figure 2. Refractive indices by rain simulation for purple nozzle and wavelength 650 nm .

The graph (Fig. 2) shows refractive indices during the rain simulation with purple nozzle. It is clear from the y-axis that the refractive index changes up to the fifth and seventh decimal place respectively. During the measurement, the humidity was constantly kept at 100%. Only the pressure and temperature were changed.

4. QUALITATIVE PARAMETER MER MEASUREMENT OF FSO LINK IN LABORATORY

As already mentioned, the modulated optical beam (OOK modulation) operating at 650 and 850 nm was measured through acrylate boxes where rain (varying intensity according to the opening of the control valve) affected on the beam. The main criterion for quality transmission was the MER parameter. At the start, the valve was open to 50% of its maximum value. It is clear from the graph (Fig. 3) that the MER value decreases with a higher speed value. The higher the MER value, the better the signal received. Based on this information, it can be argued that values of MER for purple nozzles are better, a received signal level is higher and thus communication property of the FSO link is less impaired. For the brown nozzle (red curve color), we observe lower MER values, resulting in worse communication capabilities of the FSO link. Although the transmission rate values are relatively low, there is a trend in the development of behavior of FSO link under the effect of rain for higher transmission rates depending on the wavelength of the light source used.

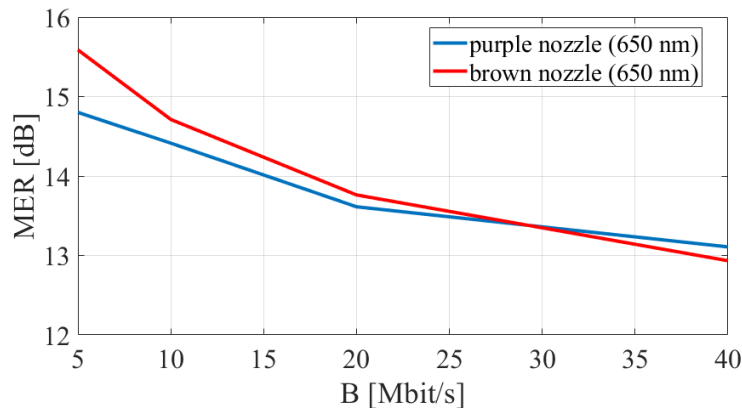


Figure 3. MER values for different transmission rates of FSO link with two nozzles (valve opening 50%).

Below is a graph (Fig. 4) with the dependence of the MER parameter on the transmission rate for different wavelengths labeled with a red curve (850 nm) and a blue curve (650 nm) with a 100% valve opening. There is a wavelength dependence. We can observe that MER is fundamentally different for the used wavelengths by more than 4.24 dB between them and this value is more or less similar with increasing transmission rate.

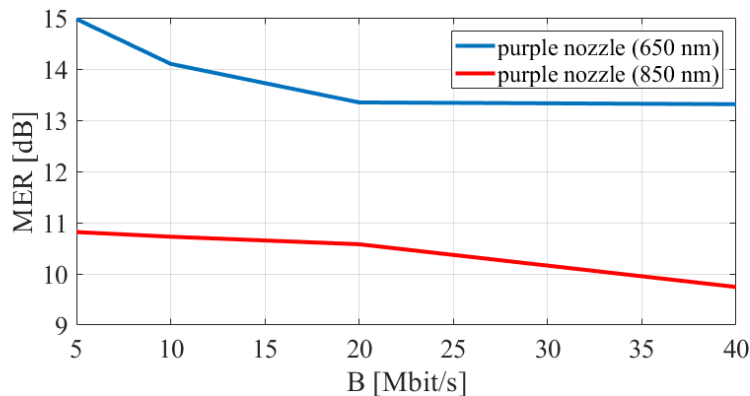


Figure 4. MER parameter in dependence on transmission rates and wavelengths (valve opening 100%).

4. CONCLUSIONS

The aim of this article was to acquaint readers with the problems associated with the effect of simulated rain on FSO link in laboratory conditions. Based on the done experimental work with the modulated optical beam using OOK modulation, the following conclusions are found through the qualitative parameter of MER communication. From the evaluation of the results of the MER parameter in the simulation of rain, it was found that the MER parameter decreases with increasing transmission rate at both purple and brown nozzles. Furthermore, it has been found that when the valve is opened at 50% with a wavelength of 650 nm, the brown nozzle causes a higher signal degradation than the purple nozzle. By comparing the same nozzle (purple) at different wavelengths, it was found that the 850 nm wavelength provides a better signal than the 650 nm wavelength. Measurement of atmospheric parameters during rain simulation was performed only using a purple nozzle at 650 nm at 50 and 100% opening due to sensor disfunction.

In the future, we want to focus on better protection of IoT sensors in order to perform further measurements of atmospheric quantities for refractive index modeling and hence refractive index structural parameter for other FSO link modulation formats. An integral part is also the modeling of the impact of rain using the software tool Ansys Fluent for a deeper understanding of the transmission space behavior inside the acrylate boxes.

ACKNOWLEDGEMENTS

The authors would like to acknowledge the financial support of the Projects No. SP2019/80 and SP2019/143, VI20172019071. This article was prepared within the frame of sustainability of the project No. CZ.1.07/2.3.00/20.0217 within the frame of the operation programme "Education for competitiveness" that was financed by the Structural Funds and from the state budget of the Czech Republic. This work was supported by the European Regional Development Fund in the Research Centre of Advanced Mechatronic Systems project, project number CZ.02.1.01/0.0/0.0/16_019/0000867.

REFERENCES

- [1] A. K. Majumdar and J. C. Ricklin: *Free-Space Laser Communications: Principles and Advances*, vol. 2. Springer Science & Business Media, 2010.
- [2] F. Nadeem *et al.*: Weather effects on hybrid FSO/RF communication link, *IEEE Journal on Selected Areas in Communications*, vol. 27, pp. 1687–1697, 2009.
- [3] P. Pechac and S. Zvanovec: *Zaklady sireni vln pro planovani pozemnich radiovych spoju*, CVUT, 2007.
- [4] V. Brazda, V. Schejbal, and O. Fiser: Rain impact on FSO link attenuation based on theory and measurement, in *Proc. 6th European Conference on Antennas and Propagation (EUCAP)*, Prague, Czech, 2012.
- [5] H. Willebrand and B. S. Ghuman: *Free Space Optics: Enabling Optical Connectivity in Today's Networks*, Indianapolis, SAMS, 2002.
- [6] M. Achour: Simulating atmospheric free-space optical propagation: Rainfall attenuation, in *Proc. SPIE, Free-Space Laser Communication Technologies XIV*, vol. 4635, San Jose, United States, 2002.
- [7] F. H. Mustafa, A. S. M. Supaat, and N. Charde: Effect of rain attenuations on free space optic transmission in Kuala Lumpur, *International Journal on Advanced Science, Engineering and Information Technology*, vol. 1, pp. 337-341, 2011.
- [8] A. Z. Suriza, I. Md. Rafiqul, W. Al-Khateeb, and A. W. Naji: Analysis of rain effects on terrestrial free space optics based on data measured in tropical climate, *IJUM Engineering Journal*, vol. 12, pp. 45-51, 2011.
- [9] P. Singh and M. L. Singh: Experimental determination and comparison of rain attenuation in free space optic link operating at 532 nm and 655 nm wavelength, *Optik-International Journal for Light and Electron Optics*, vol. 125, pp. 4599–4602, 2014.
- [10] U. A. Korai, L. Luini, R. Nebuloni, and I. Glesk: Statistics of attenuation due to rain affecting hybrid FSO/RF link: Application for 5G networks. in *Proc. 11th European Conference on Antennas and Propagation*, Paris, France, May 2017.
- [11] H. Wu, B. Hamzeh, and M. Kavehrad: Achieving carrier class availability of FSO link via a complementary RF link, in *Proc. Conference Record of the Thirty-Eighth Asilomar Conference on Signals, Systems and Computers*, Pacific Grove, USA, Mar. 2005.
- [12] U. A. Korai, L. Luini, and R. Nebulo: Model for the prediction of rain attenuation affecting free space optical links, *Electronics*, vol. 7, pp. 1-14, 2018.
- [13] J. Latal, J. Vitasek, L. Hajek, A. Vanderka, R. Martinek, and V. Vasinek: Influence of simulated atmospheric effect combined with modulation formats on FSO systems, *Optical Switching and Networking*, vol. 33C, pp. 184-193, 2019.

Adjustment of Radiation Pattern of Street Luminaire

Jan Vitasek, Tomas Stratil, Zdenek Wilcek, Jakub Kolar, and Michal Hub

Department of Telecommunications, Faculty of Electrical Engineering and Computer Science,
VSB–Technical University of Ostrava, 17. listopadu 15, 708 00 Ostrava, Czech Republic
Tel: +420 596 999 413, Fax: +420 596 991 650, e-mail: jan.vitasek@vsb.cz

ABSTRACT

This article deals with the analyze of the radiation pattern of the street luminaire Boos Naica and suggests its modifications by turning the LEDs and reflecting surfaces. The goal is to create a more uniform optical power distribution. The street luminaires can provide two functions at the same time, illumination and communication. It is important for communication purposes that the received optical power does not drop below 3dB. The aim of the adjustments was to extend and more uniform the radiation pattern of the real street luminaire and thus widen the distance between the luminaires resulting in saving money.

Keywords: LED, LightTools, radiation pattern, street luminaire.

1. INTRODUCTION

Illumination is one of the main topics which are currently developed. The illumination is used indoor or outdoor. This article focuses on the outdoor street illumination. The latest trend is the replacement of obsolete street luminaires with low pressure sodium bulbs by modern LED luminaires. There are several reasons to use LEDs for the illumination. The LEDs reach much higher efficiency than lightbulbs or fluorescent lamps and their further improvements are expected. Other advantages of the LEDs are smaller and compact size, longer lifetime, lower heat generation, higher tolerance to humidity, and lower power consumption. Moreover, the lightbulbs emit omnidirectional which causes light pollution and energy waste. Today, the LEDs can be found almost everywhere, they are used in indoor lightbulbs, in car headlamps and taillights or in the street luminaires [1-3,10].

The LEDs can have two functions, a basic illumination function and a communication function. Unlike traditional light sources, LEDs can be switched on and off very fast; human eye is not able to perceive these changes. This feature is a precondition for communication (data transfer). The street luminaires so can provide illumination and useful data for pedestrians or cars. The street luminaires can thus be “smart” and integrated into the “smart city” concept. Another option is to control the emitting power of street luminaires and reduce their energy consumption [4-5].

White light at about 2800 K or 5000 K is most used for illumination purposes. The LEDs produce white light using two methods: colour mixing or light conversion. The colour mixing method uses 3 (or more) colour chips: red, green, blue. Any light is created by setting the appropriate radiation power [1-2]. The other method is based on the conversion of blue light to higher wavelengths (green, yellow). The rest of the blue light and the spectrally shifted light create white light together. The most commonly used converter is Yttrium Aluminium Garnet (YAG) doped by Cerium $Y_3Al_5O_{12}:Ce^{3+}$. The second method is cheaper, but the communication properties are worse because the YAG has a relatively long photoluminescence decay reducing the bit rate [1,2,6-8].

Simulations described in this article were done in LightTools software. The LightTools (LT) is a 3D optical engineering and design software product that supports virtual prototyping, optimization and photorealistic renderings of illumination applications. Its unique design and analysis capabilities, combined with ease of use, support for rapid design iterations, and automatic system optimization, help to ensure the delivery of illumination designs according to specifications and schedule [9].

The aim of this article is to evaluate the radiation pattern of the real Boos Naica street luminaire and suggestions for improvement. All adjustments and suggestions were done in LightTools. The result is a geometric design whose radiation pattern is better compared to the original pattern.

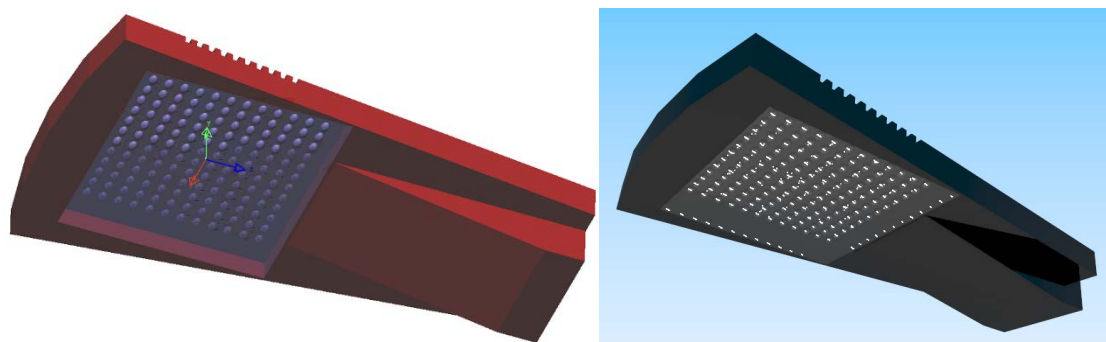


Figure 1. Boos lamp simulated in LightTools.

2. STREET LUMINAIRE BOOS NAICA

We have the real street luminaire Boos Naica for testing. The technical parameters of this luminaire are: colour temperature 4000 K, luminous flux 47000 lm, size 675×421×124 mm (L×B×H). The luminaire includes 144 LEDs [10]. A model of this luminaire was created in LightTools software for following simulations and evaluations.

The LEDs are arranged in a rectangle. Figure 2 shows the cross-section of the luminaire in the YZ plane. The luminaire model in the LT program was placed at a height of 5 m. The radiation pattern has a classical Gaussian shape, see Fig. 4. The full width at half maximum FWHM is 6.5 m.

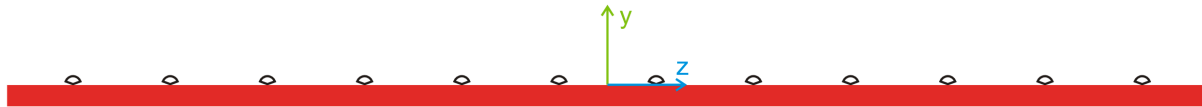


Figure 2. LED distribution in Boos lamp.

3. ADJUSTMENTS OF RADIATION PATTERN

The created Boos Naica luminaire was further modified in LT. There are several ways how to make the adjustments. Articles [11,12] solve a similar situation using TIR lens and microlens array. The LEDs are placed at the bottom of the reflecting cavity. Each LED has its own TIR lens. Light emitted by LED reflects on TIR lens and then passes through the microlens array, creating a uniform light distribution. Using a TIR lens and a microlens array is an expensive solution, but more accurate. We solve the adjustments by turning of LEDs and reflective surfaces, which is a cheaper solution but less efficient. The original LED distribution in the plane was changed to two planes with a slope of 30°. At the same time, the LEDs were turned. Further, small (20 mm) reflective surfaces were used to direct the transmitted light. The inclinations of the individual reflecting surfaces are described in Fig. 3. The radiation angle of the LEDs is 140°.

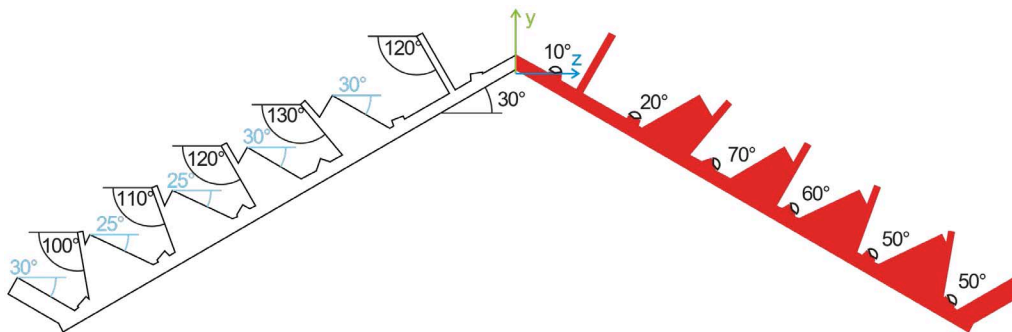


Figure 3. LED orientations and tilts of reflection surfaces.

Figure 4 compares the radiation pattern of Boos Naica and the radiation pattern of our proposed changes. The maximum peak was reduced and lateral distributed. The important parameter is full width at half maximum FWHM. The FWHM of Boos Naica luminaire is 6.5 m according to simulations in LT. After the modifications described above, FWHM is extended to 11.1 m, which is a significant improvement. The power drop can be compensated by increasing the supply current or other type of LED.

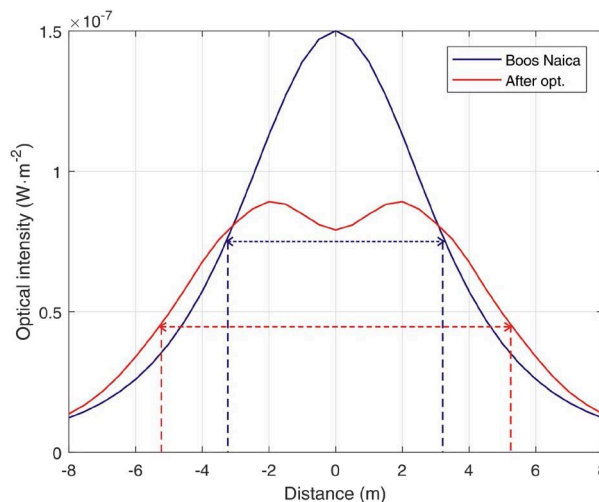


Figure 4. Comparison of illumination patterns.

4. ILLUMINATION OF STREET

The aim of other simulations was to find out how far you can place individual luminaires apart. The distance between the luminaires was gradually increased. It has been shown that a distance of 14 m is sufficient for the received optical power which does not drop below 3 dB. Next Fig. 5 shows the relative distribution of optical power along the pavement. The red curve shows the relative optical power distribution of our designed luminaire with reflective surfaces, the luminaire distance is 14 m. The blue curve shows the same situation, just with the original Boos Naica luminaires at distance of 14 m. The relative optical power dropped to value almost 6.4 dB in distance of 7 m from the luminaire. By comparison, to avoid a drop of optical power greater than 3 dB with Boos Naica luminaires, it would be necessary to place these luminaires 10 m apart. Therefore, a smaller number of our designed luminaires is needed to illuminate the same stretch than the original Boos Naica luminaires.

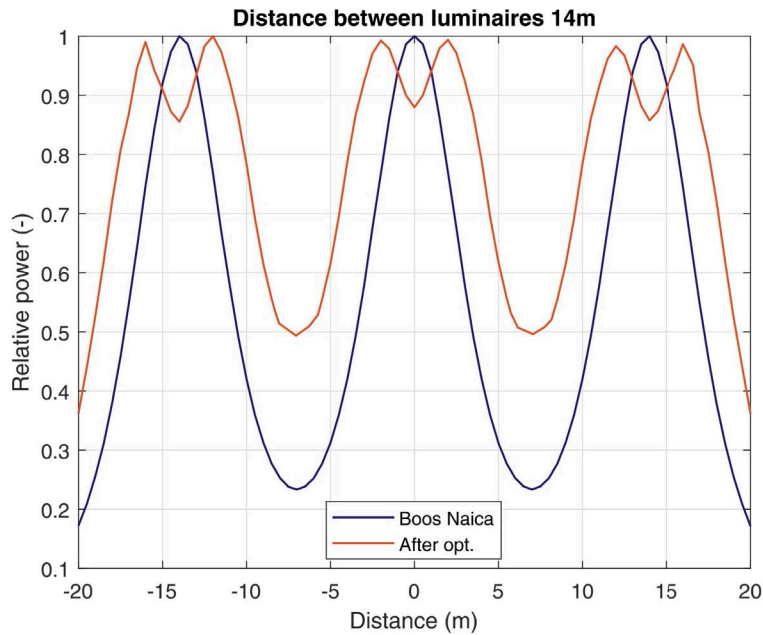


Figure 5. Comparison of illumination patterns of three luminaires in line.

The last Fig. 6 shows the relative distribution of the optical power after illumination by the three luminaires after the proposed modifications.

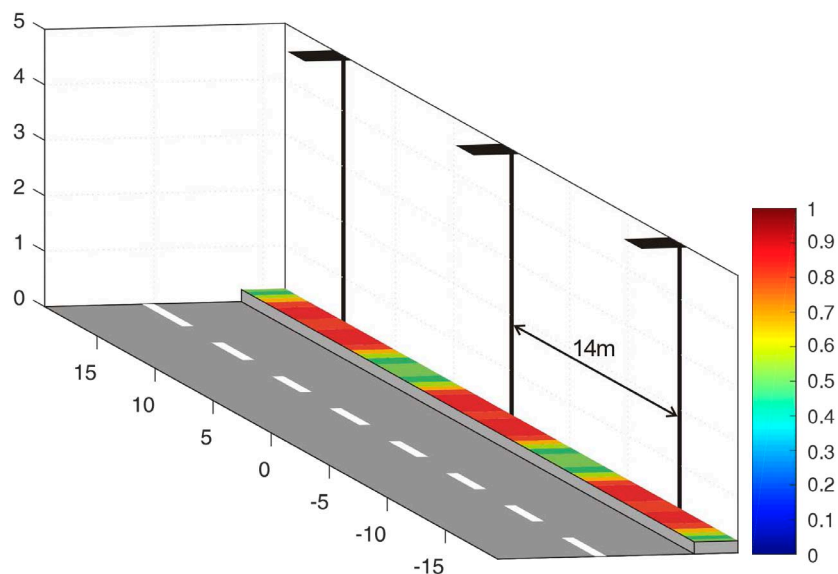


Figure 6. Illumination of pavement by three luminaires (after optimization).

5. CONCLUSION

The aim of this article was to propose modifications to a real street luminaire Boos Naica to make the distribution of optical performance more even. The radiation pattern was adjusted by turning the orientation of the LEDs and by reflecting surfaces. These adjustments are not expensive and allow to use the cover of

an existing luminaire Boos Naica. The original LED parameters are retained. The proposed adjustments reduce the main peak and extend the emitted power sideways. This makes it possible to use larger spacing between the luminaires without excessive decreasing the emitted power.

ACKNOWLEDGEMENT

The authors would like to acknowledge the financial support of the Ministry of Education, Youth and Sports of the Czech Republic under Projects No. SP2019/80 and SP2019/143 of VSB–Technical University of Ostrava, Czech Republic. Our research was also supported by Projects No. VI20172019071, VI20152020008, TA04021263, TK01020162 and TK01020178. The work has been partially supported by Project No. CZ.1.07/2.3.00/20.0217.

REFERENCES

- [1] E. F. Schubert: *Light-Emitting Diodes*, Cambridge University Press, Cambridge, 2006.
- [2] G. Held: *Introduction to Light Emitting Diode Technology and Applications*, CRC Press, Boca Raton, 2009.
- [3] R. Baleja, J. Sumpich, P. Bos, B. Helstynova, K. Sokansky, and T. Novak: Comparison of LED properties, compact fluorescent bulbs and bulbs in residential areas, in *Proc. 16th International Scientific Conference Electric Power Engineering*, 2015, Kouty nad Desnou, Czech Republic.
- [4] J. R. Oh, S. H. Cho, Y. H. Lee, and Y. R. Do: Enhanced forward efficiency of $Y_3Al_5O_{12}:Ce^{3+}$ phosphor from white light-emitting diodes using blue-pass yellow-reflection filter, *Optic Express*, vol. 17, pp. 7450-7457, Apr. 2009.
- [5] J. Li, J.-G. Li, X. Li, and X. Sun: Photoluminescence properties of phosphors based on Lu^{3+} -stabilized $Gd_3Al_5O_{12}:Tb^{3+}/Ce^{3+}$ garnet solid solutions, *Optical Materials*, vol. 62, pp. 328-334, Dec. 2016.
- [6] N. D. Q. Anh, T. H. Q. Minh, and N. H. K. Nhan: Enhancing lighting performance of white LED lamps by green emitting Ce,Tb phosphor, *Advances in Electrical and Electronic Engineering*, vol. 14, no. 5, pp. 609-614, Dec. 2016.
- [7] M. S. Jang, Y. H. Choi, S. Wu, T. G. Lim, and J. S. Yoo: Material properties of the Ce^{3+} -doped garnet phosphor for a white LED application, *Journal of Information Display*, vol. 17, pp. 117-123, 2016.
- [8] A. Liner, M. Papes, J. Jaros, F. Perecar, L. Hajek, J. Latal, P. Koudelka, and V. Vasinek: Software design of SMD LEDs for homogeneous distribution of irradiation in the model of dark room, *Advances in Electrical and Electronic Engineering*, vol. 12, no. 6, pp. 622-630, Dec. 2014.
- [9] LightTools, Synopsys [online], <https://optics.synopsys.com/lighttools/>.
- [10] Boos Naica, Boos [online], <http://www.booslight.com/products/naica/>.
- [11] X.-H. Lee, I. Moreno, and C.-C. Su: High-performance LED street lighting using microlens arrays, *Optics Express*, vol. 21, no. 9, pp. 10612-10621, Mar. 2013.
- [12] C. C. Sun, X. H. Lee, I. Moreno, C.-H. Lee, Y.-W. Yu, T.-H. Yang, and T.Y. Chung: Design of LED street lighting adapted for free-form roads, *IEEE Photonics Journal*, vol. 9, no. 1, pp. 1-13, Feb. 2017.

Effect of Carbon Dioxide on SDR-Based Modulated Optical Beams for Free Space Optical Link

1st Jan Latal

Department of Telecommunications
VSB–Technical University of Ostrava
Ostrava, Czech Republic
jan.latal@vsb.cz

2nd Zdenek Wilcek

Department of Telecommunications
VSB–Technical University of Ostrava
Ostrava, Czech Republic
zdenek.wilcek@vsb.cz

3rd Jakub Kolar

Department of Telecommunications
VSB–Technical University of Ostrava
Ostrava, Czech Republic
jakub.kolar@vsb.cz

4th Filip Sarlej

Department of Telecommunications
VSB–Technical University of Ostrava
Ostrava, Czech Republic
filip.sarlej@vsb.cz

5th Radek Martinek

Department of Cybernetics and Biomedical Engineering
VSB–Technical University of Ostrava
Ostrava, Czech Republic
radek.martinek@vsb.cz

Abstract—The basic atmospheric phenomena (mainly fog) influencing the optical beams, which were generated by a laser diode at a wavelength of 650 nm and 850 nm, will be introduced in this article. Also, the possibilities of the Software Defined Radio utilization, which can create different types of modulation (M-Quadrature Amplitude Modulation, M-Phase-Shift Keying) and can be used for evaluation of the influences of artificial atmospheric effect on the modulated optical beam in the acrylate box, will be presented. The Modulation Error Ratio is selected as the evaluation and communication parameter, depending on the Carbon dioxide exposure in the timeline. This is particularly strong communication jamming to the rise of wireless communication when the Carbon dioxide does not have an effect to such an extent.

Index Terms—FSO, carbon dioxide, fog, MER, QAM, PSK, modulation, scattering.

I. INTRODUCTION

Optical Wireless Communications (OWC) systems for outdoor called Free Space Optical Link (FSO) became a new type of telecommunication networks in recent years [1]. The OWC are not regulated by any national regulator of Radiofrequency (RF) spectrum and provide high bandwidth. This makes the OWC as an attractive transmission tool for telecommunication operators. The unlicensed bands of OWC are very advantageous, nevertheless, there are problems with the transmission environment, which is the atmosphere. The atmosphere compounds of several layers [2]. From 0 to 80–90 km of altitude, there is a homosphere, above the homosphere, there is the heterosphere. The atmosphere causes several problems in the form of plenty of physical phenomena which affect the optical beam. The atmosphere is a chaotic and unpredictable environment with dynamic changes. Many negative effects are in the atmosphere. Aerosols in the atmosphere cause the scattering of light, which happens on their particles. The scattering is described according to the Mie linear scattering which appears on particles comparable to the wavelength of light. These

effects degrade the optical power or the beam shape. The fog, mist, turbulences and other atmospheric phenomena can affect the FSO link [3], [4]. Modern methods of switching between FSO and RF are using for reliability and immunity improvement. Hybrid FSO/RF link has much better reliability and immunity against atmospheric effects [5]– [9].

With the arrival of new 5G networks the growth of data transmission, as well as the use of wireless systems for transport services, is also expected. The FSO may also be one of the available technologies when it acts as a proxy or main communication system based on the need or location. It is well-known that building technologically demanding communication networks poses many problems, whether legislative, administrative or time-related. On the contrary, building the FSO systems is simpler, brings high transfer rates, and a high level of security. Therefore, the FSO systems can be also used for traffic control and data transfer between individual control systems, or for the SMART public lightning networks. Nowadays, the public lightning networks represents one of the possibilities how to gain a comprehensive overview of the number of locations where they are located.

In this article, the author's team focused on the effect of the simulated atmospheric phenomenon, which was a carbon dioxide fog (CO₂), on the modulated optical beams Phase-Shift Keying or Quadrature Amplitude Modulation (M-PSK and M-QAM) with respect to the communication parameter Modulation Error Ratio (MER).

II. THEORETICAL DEFINITION AND DESCRIPTION OF MEASURING WORKPLACE FOR SIMULATION OF CARBON DIOXIDE EFFECT ON THE LABORATORY FSO LINK

A. Theory of Fog Effect on the FSO systems

Fog is the most negative phenomenon for the FSO link connections because it consists of small droplets of water with

a size close to the IR wavelengths in the FSO link [10]–[17]. Based on the size of particles, which the fog consists, we distinguish different fog levels. We talk about fog if the meteorological visibility is between 0 and 2 km. If the visibility is more than 2 km this state is referred to as a ‘mist’. It is well-known that the fog results in a reduction of the optical power of the FSO link, and, in some cases, the communication can be disrupted completely, in the visible and near-infrared part of the spectrum. Modelling attenuation due to fog is a relatively complex matter, as the distribution and density of fog particles may vary with the altitude, which makes modelling even more complex [6].

The three main parameters used to calculate the attenuation due to fog and mist are visibility, relative humidity and temperature. However, the most important parameter is the meteorological visibility. The visibility was originally defined by a human observer for meteorological needs. It is defined by means of so-called Kruse model. The meteorological distance is defined as the distance at which the air permeability reaches 2 % of its original value at the wavelength of 550 nm based on 1924, Koschmieder [1].

The attenuation depends on the meteorological visibility. The attenuation is very low if the sky is clear (high meteorological visibility), while if the fog is thick (the meteorological visibility is low) the attenuation is high. This phenomenon will be discussed in a separate chapter that will summarize the effect of fog and thereby emerging attenuation depending on the visibility [1], [6]. The relationship between the V_M meteorological visibility and the extinction coefficient α_e is following Eq. (1):

$$\alpha_e \approx \frac{3.91}{V_M \left(\frac{550}{\lambda}\right)^q}, \quad (1)$$

where q is the particle size distribution coefficient for example $V_M \leq 6$ km Eq. (2).

$$q = 0.585 \cdot V_M^{\frac{1}{3}} \quad (2)$$

The attenuation of the optical intensity in the FSO link at the distance L_{12} can be also determined according to the attenuation coefficient:

$$\alpha_1 = -\frac{1}{L_{12}} \cdot 10 \log \frac{I_2}{I_1}, \quad (3)$$

where I_1 is optical intensity of transmitter, I_2 is optical intensity of receiver and L_{12} is length path (distance) optical beam in the transmission environment, which is the atmosphere. The relationship between the extinction coefficient α_e (km^{-1}) Eq. (1) and the attenuation coefficient α_1 ($\text{dB} \cdot \text{km}^{-1}$) Eq. (3) is following (Eq. 4):

$$\frac{I_2}{I_1} = e^{-\alpha_e \cdot L_{12}}, \quad (4)$$

then Eq. (5):

$$\alpha_1 = -\frac{1}{L_{12}} \cdot \log e^{\alpha_e \cdot L_{12}}, \quad (5)$$

based on the mathematical formulation about logarithm, we can write Eq. (6):

$$\alpha_1 = -\frac{(-\alpha_e) \cdot L_{12}}{L_{12}} \cdot \log e \quad (6)$$

then Eq. (7):

$$\alpha_1 = \alpha_e \cdot 4.329, \quad (7)$$

and Eq. (8):

$$\alpha_e = \frac{1}{4.329} \cdot \alpha_1, \quad (8)$$

and the finally relationship is Eq. (9):

$$\alpha_e = 0.23 \cdot \alpha_1 \quad (9)$$

However, there are several models that enable the calculation of specific attenuation for different wavelengths based on the meteorological visibility. The two most widely used models are the Kruse and Kim models. But the define of meteorological distance based on World Meteorological Organization later adopted the value the air permeability reaches 5 % (13 dB) [6], [7]. The attenuation can be also calculated using this equation and, according to the model used, the appropriate coefficient q shall be applied Eq. (10):

$$\alpha_{fog} = \frac{\log \left(\frac{T}{T_0}\right)}{V_M} \cdot \left(\frac{\lambda \cdot 10^{-9}}{\lambda_0}\right) \cong \frac{13}{V_M} \cdot \left(\frac{\lambda \cdot 10^{-9}}{550 \cdot 10^{-9}}\right), \quad (10)$$

where T represent temperature of transmission of environment, T_0 is reference temperature of transmission environment, λ is wavelength emitted by a source through transmission environment, λ_0 is reference wavelength. Then q is the particle size distribution coefficient: q for the Kruse model Eq. (11):

$$q = \begin{cases} 1.6 & \text{for } V_M \geq 50 \text{ km} \\ 1.3 & \text{for } 6 \leq V_M \leq 50 \text{ km} \\ 0.585 \cdot V_M^{\frac{1}{3}} & \text{for } 0 \leq V_M \leq 6 \text{ km} \end{cases} \quad (11)$$

A new method for evaluating the particle size distribution coefficient that respects this fact was proposed by Kim q model Eq. (12):

$$q = \begin{cases} 1.6 & \text{for } V_M \geq 50 \text{ km} \\ 1.3 & \text{for } 6 \leq V_M \leq 50 \text{ km} \\ 0.16V_M + 0.34 & \text{for } 1 \leq V_M \leq 6 \text{ km} \\ V_M - 0.5 & \text{for } 0.5 \leq V_M \leq 1 \text{ km} \\ 0 & \text{for } V_M \leq 0.5 \text{ km} \end{cases} \quad (12)$$

It is possible to further sub-divide fog according to the Al-Naboulsi model as advective and convective [8]. The advective fog is created by warm and humid airflow above a cold surface. The air cools and water vapor condenses. This fog is characterized by the content of liquid water of more than $0.20 \text{ g} \cdot \text{m}^{-3}$ and a particle diameter close to $20 \mu\text{m}$. The visibility of this fog is about 200 meters. The attenuation for the advective type of fog is given by the following relation Eq. (13):

$$\gamma_{adv} = 4.343 \cdot \frac{0.18126 \cdot \lambda_\mu^2 + 0.13709 \cdot \lambda_\mu + 3.7205}{V_M}, \quad (13)$$

where λ_μ is the wavelength in microns. The convective fog is formed by cooling the warm earth's surface by cold air at a very slow wind speed and high humidity. The contact of the air with warm surface causes condensation of water vapor, mainly at night and at the end of the day, with a particle size of 1 to 3 μm and water content between 0.01 and 0.1 $\text{g} \cdot \text{m}^{-3}$. This affects shorter wavelengths (first and second transmission window). The attenuation of this type of fog is given by the relationship Eq. (14):

$$\gamma_{con} = 4.343 \cdot \frac{0.11478 \cdot \lambda_\mu + 3.8367}{V_M}. \quad (14)$$

The effect of fog on the FSO systems can be described by empirical and theoretical procedures.

B. Description of the measuring workplace for simulation of the dry ice effect on the laboratory FSO link

We used the measuring (acrylate) box (see Fig. 1) for our fog measurement experiment with the modulated FSO link in the laboratory. This acrylate box has a length of 2.5 m and 0.5 m in height and 0.5 m in width. The box is used for stable conditions during experimental measurements. The carbon dioxide generated the artificial fog. Subsequently, the acrylate

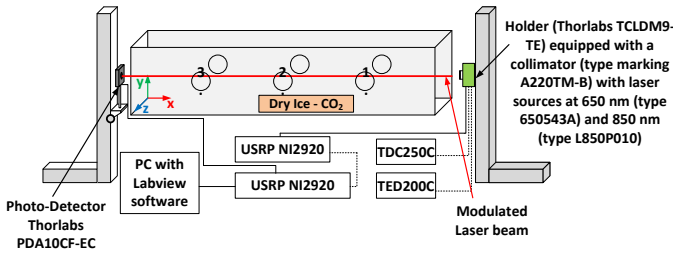


Fig. 1. Measurement of fog influence on FSO link.

box was placed on an iron mounting in front of it; the holder of the laser diode was installed on an aluminium structure, with the laser diode shooting at a right angle through the front of the measurement box. To ensure thermal and current stabilization of the laser diode (LD) on the transmission side, a Thorlabs set was used (TDC205C – setting regular part of the stream, TED200C – setting operating temperature, TLCLDM9 – holder of the laser diode with input for modulating voltage). One type of light source with a wavelength of 650 nm (type 650543A) was used a second at 850 nm (type L850P010). The LD 650 nm the output power was 5 mW and 850 nm has output power 10mW. To generate the PRBS (pseudo-random bit sequenced) signal, a USRP NI 2920 was used: its output was linked to the LD and could change the size of the modulation voltage for the laser diode. Modulation of the laser diode was achieved using the RF input on the holder Thorlabs TCLDM9-TE, which was driven by the current and thermal controller. The laser diode was placed inside laser driver Thorlabs TCLDM9-TE, where circuit Bias-T is placed. This circuit allows bringing together DC component from the current driver and modulation signal from RF input. This laser

driver is also stabilized by temperature driver. To the RF input that was supplied by an SMA connector with an impedance ending of about 50 Ω , the modulating signal with a frequency up to 50 MHz could be added and the sample rate is 500 kHz, number of symbols was set to 500, any shaping filter was not used and the gain of the signal was set to 0 dB. This signal directly modulated the laser diode installed in front of the holder (Thorlabs TCLDM9-TE) equipped with a collimator (type marking A220TM-B) to focus the optical beam. The fog generator fueled the fog into the acrylate box. The optical beams went through the box [18], [19].

On the receiver side, there was a photodetector InGaAs Fixed Gain Detector PDA10CF-EC. The photodetector bandwidth was 150 MHz. The affected laser beam was converted back to an electrical signal by stimulating a photodetector and then was demodulated in the second device (USRPNi 2920). A computer connected to the controlled device (USRPNi 2920) provided the reading of the changes in the symbol speed or modulation format and qualitative parameter MER.

C. Sublimation of solid carbon dioxide

The dry ice is a solid phase of carbon dioxide, which emerges from desublimation during cooling under 78.5 $^{\circ}\text{C}$. Dropping the solid carbon dioxide in hot water causes rapid sublimation of the solid carbon dioxide and very concentrated carbon dioxide (CO_2) gas is generated. The CO_2 is heavier than air and sticks to the bottom of the box. The concentration gradually and spontaneously decreases with increasing time. The sublimation of solid carbon dioxide at different levels could be considered as certain kinds of smog (CO_2 is an element of the smog). As many metropolitan cities in the world are burdened by smog pollution, this research could potentially contribute to a better understanding of optical communications in metropolitan area [19].

D. Modulation Error Ratio

As we observe, for example, the bit error rate parameter, we have the parameters for modulations that enable us to evaluate how much the modulated optical wave was affected by negative phenomena of the transmission environment during the transmission. These parameters include the Modulation Error Ratio (MER) parameter and Error Vector Magnitude (EVM) parameter. Both the parameters are related to the constellation diagram. The ideal constellation diagram contains only ideally positioned points, while in real conditions we cannot achieve this state due to various noise effects. Therefore, the individual points in the constellation diagram deviate from the ideal position and subsequently appear as if the given point was scattered. The MER parameter is defined as the ratio of the sum of amplitude squares of ideal symbol vectors to the sum of amplitude squares of error symbol vectors. This parameter is similar to the SNR in a digitally modulated signal and is

TABLE I
TIME VALUES AT WHICH THE M-PSK MODULATIONS REACHED THE ORIGINAL VALUES

Number of Measurement	Laser wavelength	Time (s)			
		QPSK	$\pi/4$ DQPSK	8PSK	16PSK
1	650 nm	42	45	78	43
	850 nm	74	71	80	81
2	650 nm	51	46	63	65
	850 nm	72	66	75	89
3	650 nm	46	50	45	57
	850 nm	51	63	62	71

TABLE II
TIME VALUES AT WHICH THE M-QAM MODULATIONS REACHED THE ORIGINAL VALUES

Number of Measurement	Laser wavelength	Time (s)			
		4QAM	16QAM	32QAM	64QAM
1	650 nm	42	41	43	78
	850 nm	58	43	38	123
2	650 nm	47	54	54	93
	850 nm	56	50	84	100
3	650 nm	37	51	40	50
	850 nm	46	65	47	59

usually expressed in the decibel level. It can be expressed as follows Eq. (15) [18], [19]:

$$MER = \frac{\sum_{j=1}^N (\tilde{I}_j^2 + \tilde{Q}_j^2)}{\sum_{j=1}^N \left[(I_j - \tilde{I}_j)^2 + (Q_j - \tilde{Q}_j)^2 \right]}, \quad (15)$$

where \tilde{I}_j is the component size of the ideal symbol on the I-axis of the constellation diagram, I_j is the component size of the real symbol on the I-axis of the constellation diagram, \tilde{Q}_j is the component size of the ideal symbol on the Q-axis of the constellation diagram, Q_j is the component size of the real symbol on the Q-axis of the constellation diagram [18].

III. THE MEASUREMENT PROCEDURE

The dry ice was used to simulate the fog generation. Its advantage is that there is no melting process, but it changes its solid state of matter into the gaseous one directly. This process is called sublimation. The measurement procedure was as follows. There is always the same amount of dry ice (150 ml) put into a container by means of a gauge. Consequently, half a litre of boiling water was poured over the dry ice, and the sublimation process started. Since the emerged fog is cold, it remains at the bottom of the box. Therefore, the fog was scattered after the sublimation by means of a fan all over the box and the measurement started. Since the emerged fog causes zero visibility, the modulation level of the MER parameter drops to zero. The subsequent fog dissolution results in the MER increase and the time, which was needed for the growth to the original maximum value, was determined for each modulation. The process of fog generation was shown in Fig. 2. The sublimated fog is on the left, which is held at the bottom of the box. The picture in the middle shows the process of the fog scattering and the picture on the right side shows the fog which is already scattered. The dry ice is a solid form of carbon dioxide (CO_2). As previously mentioned, the



Fig. 2. Process of fog generation by dry ice sublimation.

time courses of the MER parameter of fog dissolution were recorded. The time courses showed the period of time that was needed for the MER value to return to its original level. Each modulation was measured three times.

The testing of statistical hypotheses was carried out from final time courses in order to find out whether there is a statistically significant difference between the time courses.

A. Results for M-PSK modulation

The time courses of the M-PSK modulations were found out and are shown below in Fig. 3, along with the time courses for each modulation. It is obvious that individual courses are similar. Only the 16 PSK modulation was accompanied by oscillations as the values increased. We can observe substantial growth in the rise time from the minimum to maximum MER value for a given modulation type already from the $\pi/4$ DQPSK. The $\pi/4$ DQPSK is characterized by two advantages – since the information is hidden in the phase change, it allows incoherent reception. Moreover, it limits the effect of the parasitic amplitude modulation. Concerning the others, 8 PSK and 16 PSK, there are similar or longer delays in the MER parameter transition from the minimum to maximum level.

The following Tab. I shows the time at which the M-PSK modulations reached the original values.

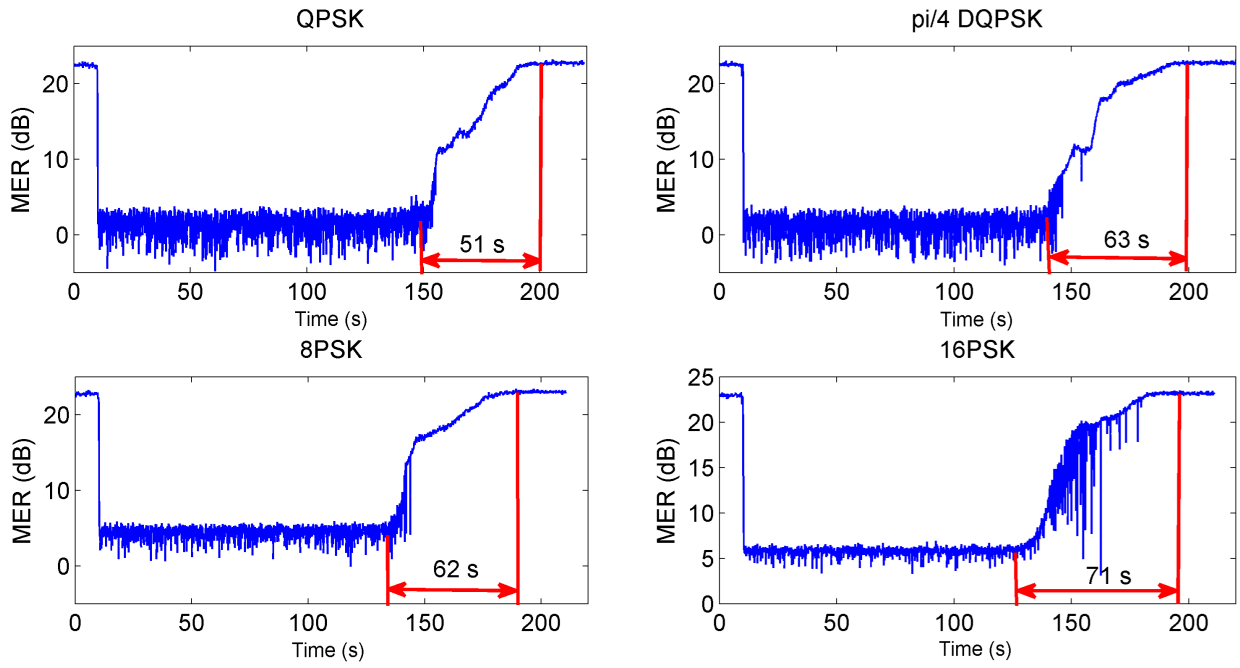


Fig. 3. Time courses of M-PSK modulations of fog activity that emerged from the dry ice sublimation.

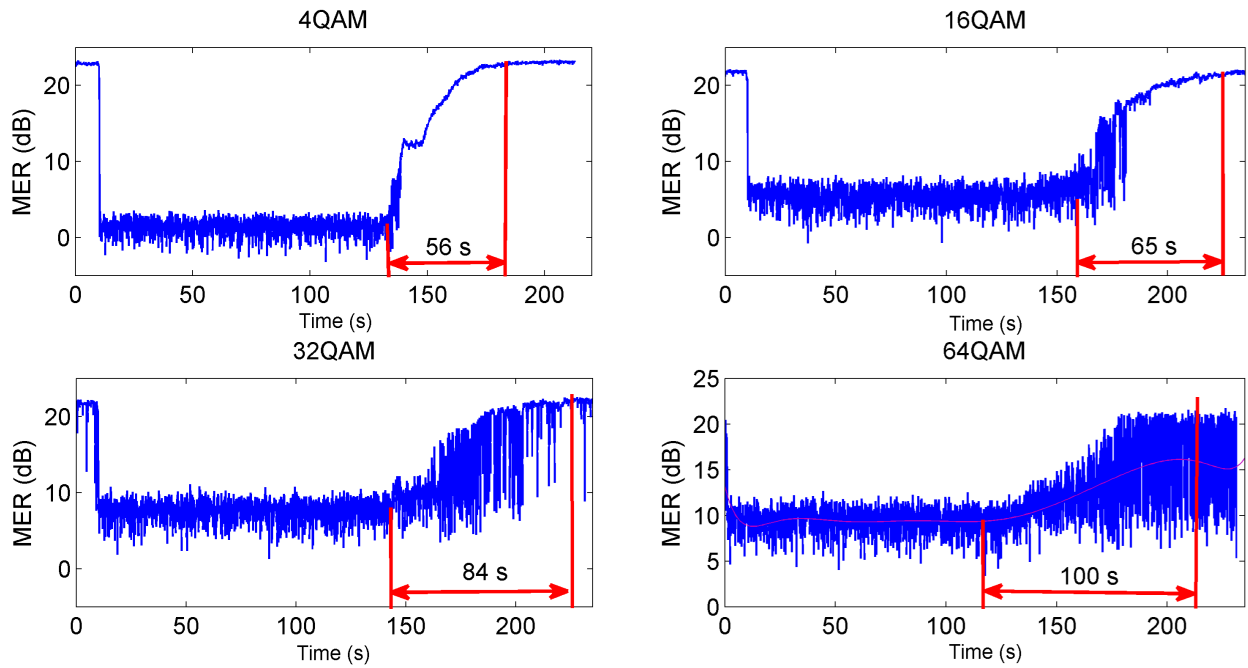


Fig. 4. Time courses of M-QAM modulations of fog activity that emerged from the dry ice sublimation.

Tab. I shows that higher wavelength of the used radiation source operating at 850 nm was more time consuming up to the point of stabilization of the MER value to the original value, so-called lossless. This clearly illustrates that wavelength was more sensitive to the type of generated fog inside the acrylic box and, therefore, the particle size also corresponded to the

transmitted wavelength.

B. Results for M-QAM modulation

The time courses for reaching the original MER value are shown below in Fig. 4, for the M-QAM modulation with a different number of states at different wavelengths used for

testing. Concerning the 16 QAM and higher modulations, the oscillation of the MER value occurred during the fog dissolution, while the 4 QAM modulation had smooth time rise up to the rise of the MER maximum level, i.e. to its original values, for both used wavelengths of the radiation sources at 650 and 850 nm testing. The red curve on Fig. 4 represent the average values of parameter MER dependent on time for 64-QAM modulation. Based on the measurement it is apparent that more complex types of modulation formats, such as M-QAM, are more demanding and the number of symbols has a major effect on the behaviour of the faultless communication through the MER parameter. Concerning the fibreless optical systems using the M-QAM higher state modulations it is necessary to provide additional RF link location which would be able to switch to lower frequencies in case of heavy fog, thus avoiding the loss of communication/reduced reliability of the link or complete link failure. The following chart shows the time courses at which the M-QAM modulations reached the original MER values.

The measurement showed (see Tab. II) that in case of more complicated types of modulation formats, such as the M-QAM, the MER value changes from its original value to the maximum value with respect to the wavelength of the radiation source very differently than in case of m-PSK modulations. The following Tab. II shows the time at which the M-QAM modulations reached the original values.

IV. CONCLUSION

During the research of the dry ice behaviour with respect to the FSO, it has been proved that modulations formats of the more complex character, such as M-QAM or multi-symbol modulations, are less able to cope with the generated fog in the box. However, it is necessary to take into account that, nowadays, it is also a standard to additionally install the RF link to the FSO links. The RF link has a role to increase the reliability of the FSO link and, at the same time, to act as an additional source of communication if the FSO link error rate gets worse. However, it is demonstrated that fog, as a major source of communication disruption for the FSO systems, has considerably different behaviour for different types of radiation sources operating at different wavelengths. This implies the need for deeper knowledge of fog tests in different locations in order to use them for the SMART systems in the future.

ACKNOWLEDGMENT

The research described in this article could be carried out thanks to the active support of the projects no. SP2019/80 and SP2019/143. The work has been partially supported by Project No. CZ.1.07/2.3.00/20.0217. This work was supported by the European Regional Development Fund in the Research Centre of Advanced Mechatronic Systems project, project number CZ.02.1.01/0.0/0.0/16 019/0000867 within the Operational Programme Research, Development and Education. This article was also a part of project VI20172019071.

REFERENCES

- [1] L. C. Andrews and R. L. Phillips, *Laser Beam Propagation through, Random Media*, SPIE, Bellingham, 1998.
- [2] M. H. Ibrahim, H.A. Shaban, M.H. Aly, "Effect of different weather conditions on BER performance of single-channel free space optical links," *Optik*, vol. 137, pp. 291–297, May 2017.
- [3] M. Z. Chowdhury, MD. T. Hossan, A. Islam, Y. M. Jang, "A Comparative Survey of Optical Wireless Technologies: Architectures and Applications," *IEEE Access*, vol. 6, pp. 9819–9840, January 2018.
- [4] H. Ivanov, T. Plank, L. Mustafa, E. Cernic, E. Leitgeb, "Estimation of Mie scattering influence for the FSO channel under artificially simulated fog conditions," in *Proceedings of SPIE - The International Society for Optical Engineering, Environmental Effects on Light Propagation and Adaptive Systems 2018*, Berlin, Germany, September 2018, vol. 10787, pp. 1–9.
- [5] H. Khalid, S. S. Muhammad, H. E. Nistazakis, G. S. Tombras, "Performance Analysis of Hard-Switching Based Hybrid FSO/RF System over Turbulence Channels," *Computation*, vol. 7, pp. 1–10, 2019.
- [6] A. Prokes, "Atmospheric effects on availability of free space optics systems," *Optical Engineering*, vol. 48, pp. 066001-1–066001-10, June 2009.
- [7] *Guide to Meteorological Instruments and Methods of Observation and Information Dissemination, CIMO-XIV/Doc. 6.3*, World Meteorological Organization, Geneva 1996.
- [8] M. Naboulsi, H. Sizun, F. de Fornel, "Fog attenuation prediction for optical and infrared waves," *Optical Engineering*, vol. 43, pp. 319–329, February 2004.
- [9] S. M. Yasir, N. Abas, A.M.S. Saleem, "Performance analysis of 10Gbps FSO communication link under suspended dust and rain conditions in Lahore, Pakistan," *Nonlinear Optics Quantum Optics*, vol. 50, pp. 235–252, 2019.
- [10] J. Libich, J. Perez, S. Zvanovec, Z. Ghassemlooy, R. Nebuloni, C. Capsoni, "Combined effect of turbulence and aerosol on free-space optical links," *Applied Optics*, vol. 56, pp. 336–341, January 2017.
- [11] Y. Golovachev, A. Etinger, A. G. Pinhasi, Y. Pinhasi, "Propagation properties of sub-millimeter waves in foggy conditions," *Journal of Applied Physics*, vol. 125, pp. 151612-1–151612-7, April 2019.
- [12] M.A. Ismail, H. Fathallah, M.-S. Alouini, "On the performance of optical wireless links over random foggy channels," *IEEE Access*, vol. 5, pp. 2894–2903, 2017.
- [13] B. Kebapci, F. Miramirkhani, H. Nouri, M. Uysal, "A custom-design atmospheric channel emulator for the performance evaluation of free space optical communication systems," in *Proceedings of 19th International Conference on Transparent Optical Networks, ICTON 2017*, Girona, Spain, September 2017, pp. 1–5.
- [14] M. H. Ibrahim, H.A. Shaban, M.H. Aly, "Effect of different weather conditions on BER performance of single-channel free space optical links," *Optik*, vol. 137, pp. 291–297, May 2017.
- [15] J. Perez, Z. Ghassemlooy, S. Rajbhandari, M. Ijaz, H. Le Minh, "Ethernet FSO communications link performance study under a controlled fog environment," *IEEE Communications Letters*, vol. 16, pp. 408–410, March 2012.
- [16] M. Ijaz, Z. Ghassemlooy, J. Pesek, O. Fiser, H. Le Minh, "Edward Bentley Modeling of fog and smoke attenuation in free space optical communications link under controlled laboratory conditions," *Journal of Lightwave Technology*, vol. 31, pp. 1720–1726, April 2013.
- [17] J. Toth, L. Ovsenik, J. Turan, "Advanced wireless communication systems - Free space optics: Atmosphere monitoring proposal (Fog and Visibility)," in *Proceedings of 13th IEEE International Scientific Conference on Informatics, INFORMATICS 2015*, Poprad, Slovakia, November 2015, pp. 281–285.
- [18] J. Latal, J. Vitasek, M. Bojko, J. Skrinisky, T. Stratil, Z. Wilcek, J. Kolar, "Simulation and Measurement of Atmospheric Effect on Optical Beam," in *Proceedings of 2018 20th International Conference on Transparent Optical Networks (ICTON)*, ICTON 2018, Bucharest, Romania, July 2018, pp. 1–7.
- [19] J. Vitasek, R. Martinek, A. Vanderka, L. Hajek, J. Latal, Z. Lu, B. Li, "Effects of carbon dioxide on different PSK modulation formats of Optical Wireless Communications using USRP," in *Proceedings of 2016 18th International Conference on Transparent Optical Networks (ICTON)*, ICTON 2016, Trento, Italy, August 2016, pp. 1–5.

VLC channel equalization simulator based on LMS algorithm and virtual instrumentation

1st Radek Martinek, 2nd Lukas Danys,
3rd Rene Jaros, 4th David Mozny

*Department of Cybernetics and Biomedical Engineering
Faculty of Electrical Engineering and Computer Science
VSB-Technical University of Ostrava
Ostrava, Czech Republic
radek.martinek@vsb.cz, lukas.danys@vsb.cz,
rene.jaros@vsb.cz, david.mozny@vsb.cz*

5th Petr Siska, 6th Jan Latal

*Department of Telecommunications
Faculty of Electrical Engineering and Computer Science
VSB-Technical University of Ostrava
Ostrava, Czech Republic
petr.siska@vsb.cz, jan.latal@vsb.cz*

Abstract—This article focus on experimental evaluation of least mean squares (LMS) algorithm functionality in the form of software defined channel equalizer. Transmission channel is modelled for deployment in visible light communications (VLC), which can be impaired by multiple elements such as multi-path transmission, intersymbol interference (ISI), etc. Equalizer is thoroughly tested in designed virtual device that allows modelling of different disturbance types, respectively different signal propagation models. Experiments are performed on multi-state quadrature amplitude modulation (M-QAM). Results are evaluated by error vector magnitude (EVM) and modulation error rate (MER). In the conclusion, simulated results are compared to the real measured values of VLC technology.

Index Terms—Channel equalization, visible light communication (VLC), quadrature amplitude modulation (QAM), virtual instrumentation, least mean squares algorithm (LMS).

I. INTRODUCTION

There are many approaches to channel equalization. Equalization itself is generally divided into analog or digital. Nowadays, we are mainly interested in digital system equalization. Currently, so called adaptive equalization is one of the main methods among the group of digital system equalizations [1]–[3]. In mobile communications, where multi-path transmission occurs (causing intersymbol interference) radio channel parameters tend to constantly changing in time [4]. Adaptive Equalization is therefore used to reduce various disturbing effects and their consequences. Equalizer parameters (adaptive equalizer is designed most often as the finite impulse response (FIR) filter) can vary greatly according to the current parameters of the radio channel. Properties of adaptive equalizers can be advantageously used even in the field of visible light communications (VLC).

The basic idea of visible light communication is to employ light not only for lighting purposes, but concurrently also for data transmissions). The visible light spectrum ranges approximately from 390 to 700 nm [5], [6].

In the frequency domain, the visible light spectrum can be defined approximately in range of 400 to 800 THz. During day, the human eye is most sensitive to 555 nm, but in case of

worse light conditions (during night), the eye adapts to lower wavelengths, which correspond to green color.

The great advantage of visible light communication is that its bandwidth is more than 10000 times higher than that of conventional radio communications (radio communications: 3 kHz–300 GHz; VLC: 400–800 THz) [7]–[9].

Main advantages of VLC systems:

- Wide unlicensed band - channels in radio systems tend to be overused, therefore its highly likely some technologies tend to lack free channels.
- Lower costs when compared to radio communication systems.
- Higher security. Transmission safety and safe use in areas, where radio communication is not possible (aviation, petrochemical industry, hospitals). Light also does not pass through walls, therefore its difficult to eavesdrop on ongoing communications. However it is still possible by redirecting beam of light elsewhere. However this scenario is unlikely, as the mirror has to be in direct visibility to transmitting light source.

It is possible to achieve high data rates by utilizing light-emitting diode (LED) sources (maximal modulation bit rate of LED diode is 1 Gbit/s). Deployment of multiple LEDs in multiple input multiple output (MIMO) scenarios can lead to increased bit rates, while maintaining the same bandwidth [10]. This technology is nowadays used in Wi-Fi. MIMO has much better utilization of spectrum, thus achieving even better transmission properties.

Possible deployment of VLC systems:

- Intelligent lighting – intelligent lighting with VLC capabilities can provide infrastructure for conventional lighting, control and data communication, which can also significantly decrease power consumption [11].
- Cellphone connectivity – visible light communication can offer higher bit rate than Wi-Fi. It is also much harder to eavesdrop VLC systems [12].

- Deployment in dangerous environments – mainly in areas with significant risk of explosions possibly caused by RF technologies (mines, petrochemical industry, oil platforms).

II. METHODS

There are many types of adaptive equalizers that are nowadays used in radio communication systems. However their implementation is based on the same principle. Received distorted data are corrected by adaptive filters that are changing their coefficients based on current radio channel parameters.

When the correct filter coefficients are selected, the output of the equalizer should be the same, or vary slightly from the original transmitted data. It is necessary to pick the right parameters of adaptive equalizers. The correct choice of adaptive equalizer parameters is most often determined by periodic transmission of so called training sequence. The training sequence is predetermined in advance and the equalizer therefore knows what data should appear on its input.

Equalizer works in two modes - training mode and tracking mode. In training mode, the transmitter transmits predetermined training sequence, which is distorted by disturbance. By evaluating this sequence, filter coefficients for the best possible correction of data are obtained. The training mode is then followed by a tracking mode in which the data sequence is transmitted and corrected according to parameters obtained by training mode [13], [14].

The most frequently used adaptive equalizers can be divided in two main groups, linear and non-linear. Linear adaptive equalizers are based on transversal or grid filter and are not using reconstructed output signal $d(t)$. On contrary the non-linear adaptive equalizers are using the output signal $d(t)$ in feedback path. They are used when distortion caused by channel is too high for linear equalizers. Non-linear equalizers are based on these three methods:

- Decision feedback (DFE).
- Maximum likelihood sequence detection (MLSD).
- Maximum likelihood sequence estimation (MLSE).

III. FEEDFORWARD EQUALIZER

Feedforward equalizer is a linear equalizer with either transversal or grid filter. Linear equalizer with transversal filter is the simplest implementation. It consists of branched delay lines, with a delay time τ (TD) that is the same as the symbol period of the data signal. Simplest equalizer is using direct branching (it is a FIR filter, also called as a transversal filter). If the equalizer also consist of feedback branches it is called a infinite impulse response (IIR) filter. This type of filter is not used in radio channels as its tend to be unstable. This type of equalizer is discrete, but intersymbol interference (ISI) distortion is continual. As it has a finite number of states, it is not long enough to provide the right correction of continuous signal. It uses only information from previous and actual states and therefore might amplify noise instead of reducing it [15], [16]. Linear equalizers are not suitable for transmission channels with spectral zeroes. These channels are often found

in radio communications, for example ionospheric wave with frequency lower than 30 MHz or modern mobile communications. This equalizer is adjusting signal based on actual state and is not making logic value adjustments (differentiate between "1" and "0"). It only deals with correction of voltage levels themselves. Following mathematical description is for 3-tap feedforward equalizer (FFE) (1), where $e(t)$ is equalized voltage waveform in time, T_D is delay, c_n is correction coefficient, $r(t - nT_D)$ is input waveform before correction in individual taps. Taps are correction factors applied to voltage levels to correct them accordingly. 3-tap FFE use three bits for correction of one bit - one bit which is currently adjusted and two previous bits. For example 5-tap FFE would use two more bits for evaluation.

$$e(t) = c_0.r(t - (0.T_D)) + c_1.r(t - (1.T_D)) + c_2.r(t - (2.T_D)). \quad (1)$$

Fig. 1 represents block scheme of FFE. It is a graphical representation of previously mentioned equation (1). It is noticeable that 3-tap FFE has 3 evaluation branches, where the signal is delayed differently. The signal in the respective tap is multiplied by the correction coefficient and then the signals are added together into the resulting equalized signal $e(t)$.

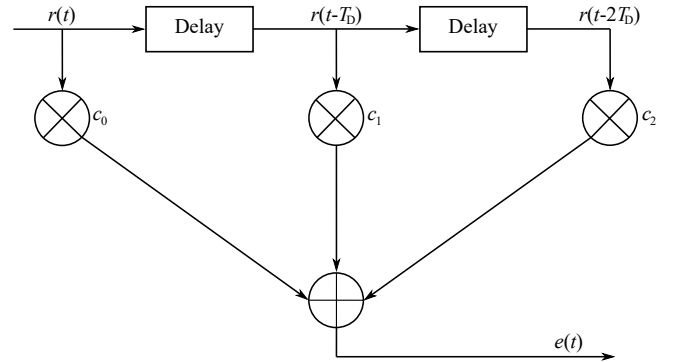


Fig. 1. Block scheme of FFE.

IV. VIRTUAL DEVICE DESIGN

The simulation program is written in LabVIEW using the Modulation Toolkit and Adaptive Filter Toolkit libraries. The Front Panel (user interface) can be seen in Fig. 2. It consists of two buttons, one for storing data in a pre-created text file and the other for stopping the program.

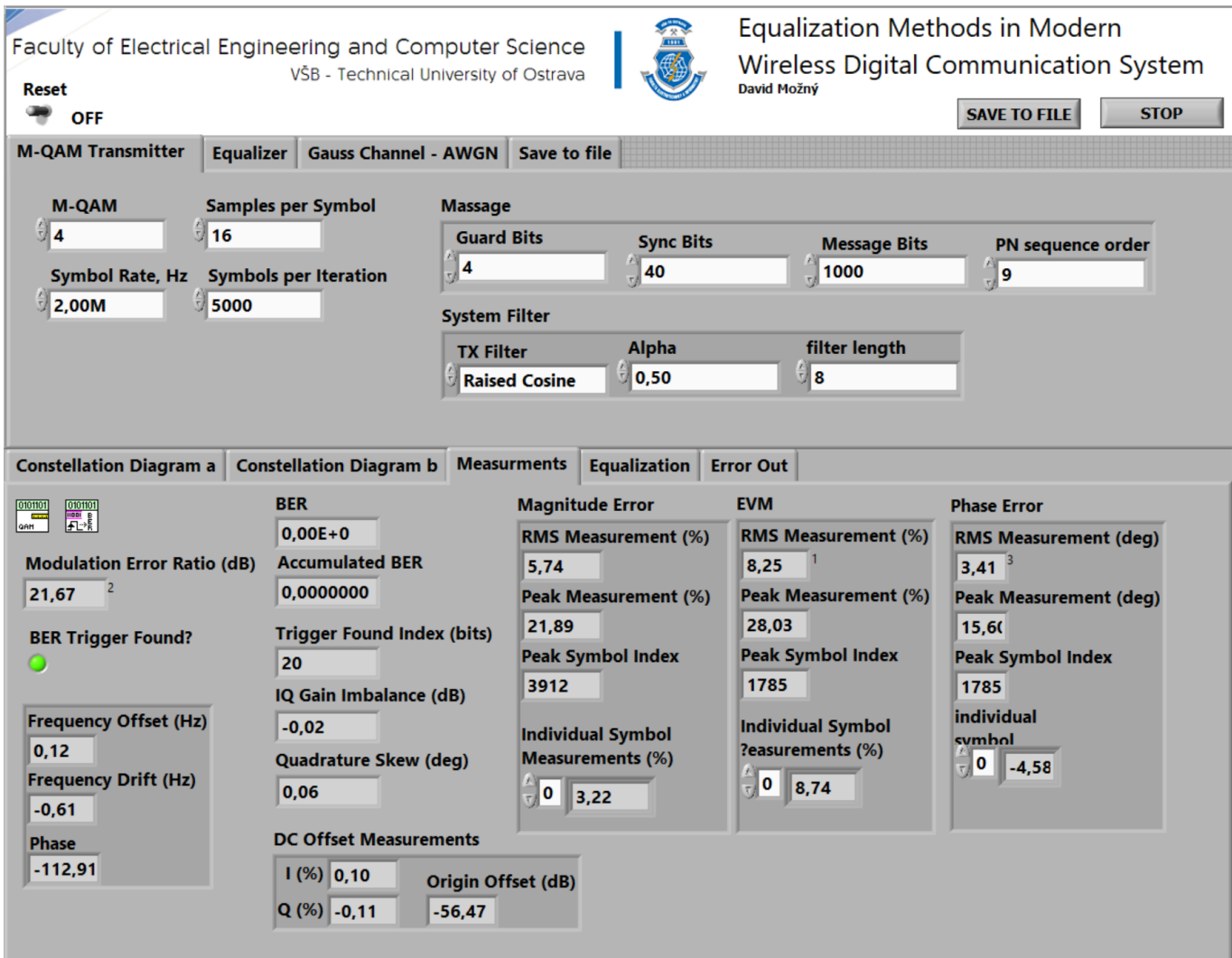


Fig. 2. Virtual device comparing properties of channel equalization with the help of adaptive least mean squares (LMS) algorithm utilizing multi-state quadrature amplitude modulation modulation for the VLC needs.

V. EXPERIMENTS

Simulations were performed in the following manner. The parameter E_b/N_0 [17] was changed in range from 20 to 40 dB and then modulation error rate (MER) [18] and error vector magnitude (EVM) [19] parameters were measured. During simulations the value of E_b/N_0 was changed by block which insert Gaussian noise. This approach was chosen based on real measurements as we have also observed Gaussian noise reducing E_b/N_0 . Simulations were performed for multi-state quadrature amplitude modulation (M-QAM), mainly from four state to sixty-four state QAM modulations. Figures of MER and EVM dependency on E_b/N_0 were created. Fig. 3 represent dependence of MER on E_b/N_0 . Fig. 4 is than symbolizing dependence of EVM. All presented graphs contain simulated values of 4QAM, 8QAM, 16QAM, 32QAM and 64QAM modulations.

The setting of simulation parameters was following: Bandwidth was set to 1 MHz (simulation was performed for one

bandwidth only), number of symbols was set to 5000 (limited by performance of computer).

TABLE I
RESULTS OF PERFORMED SIMULATIONS FOR 4-QAM MODULATION.

E_b/N_0	Without EQ		LMS	
	EVM	MER	EVM	MER
40	2,67	31,46	2,99	30,47
38	3,38	29,43	3,28	29,67
36	4,18	27,57	3,65	28,76
34	5,24	25,62	4,19	27,56
32	6,65	23,54	4,74	26,48
30	8,38	21,54	5,45	25,26
28	10,49	19,59	6,37	23,92
26	13,09	17,66	7,49	22,51
24	16,68	15,56	8,64	21,27
22	20,36	13,83	10,17	19,85
20	26,03	11,69	12,04	18,39

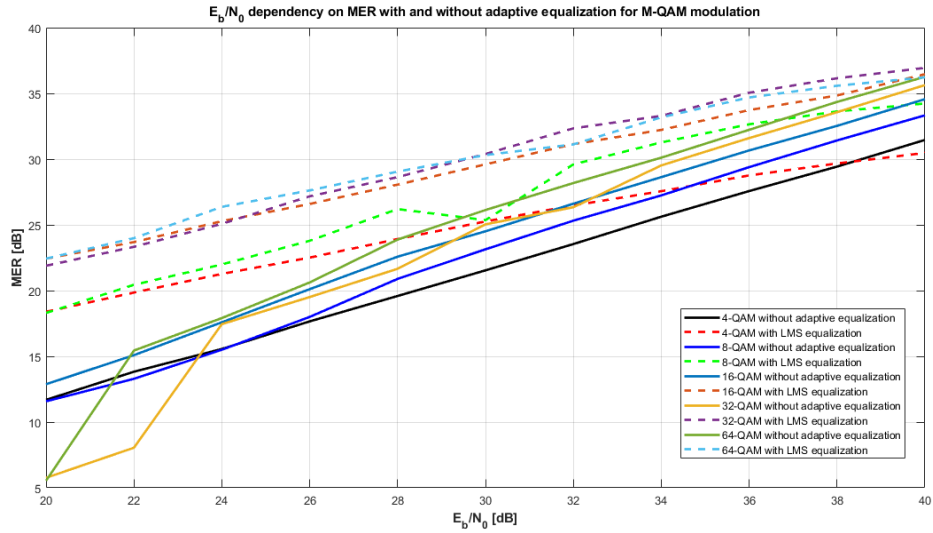


Fig. 3. Comparison of LMS algorithm efficiency for M-QAM based on MER.

TABLE II
RESULTS OF PERFORMED SIMULATIONS FOR 8-QAM MODULATION.

Without EQ			LMS	
E_b/N_0	EVM	MER	EVM	MER
40	1,87	33,33	1,68	34,23
38	2,33	31,42	1,81	33,63
36	2,94	29,39	2,01	32,65
34	3,76	27,24	2,37	31,27
32	4,68	25,32	2,88	29,6
30	6,01	23,14	4,66	25,36
28	7,86	20,89	4,24	26,2
26	10,94	18	5,61	23,79
24	14,65	15,5	6,89	21,99
22	18,94	13,29	8,23	20,44
20	23,23	11,58	10,54	18,3

TABLE IV
RESULTS OF PERFORMED SIMULATIONS FOR 32-QAM MODULATION.

Without EQ			LMS	
E_b/N_0	EVM	MER	EVM	MER
40	1,27	35,63	1,09	36,94
38	1,6	33,57	1,19	36,15
36	2,02	31,6	1,36	35,05
34	2,56	29,52	1,67	33,29
32	3,66	26,34	1,85	32,34
30	4,31	25,04	2,32	30,39
28	6,3	21,66	2,82	28,63
26	8,14	19,51	3,37	27,17
24	10,33	17,45	4,29	25,08
22	30,55	8,05	5,22	23,33
20	39,96	5,76	6,18	21,89

TABLE III
RESULTS OF PERFORMED SIMULATIONS FOR 16-QAM MODULATION.

Without EQ			LMS	
E_b/N_0	EVM	MER	EVM	MER
40	1,39	34,56	1,12	36,46
38	1,77	32,53	1,34	34,84
36	2,2	30,66	1,53	33,73
34	2,76	28,63	1,82	32,22
32	3,49	26,61	2,06	31,14
30	4,45	24,51	2,46	29,6
28	5,57	22,58	2,94	28,06
26	7,35	20,11	3,47	26,59
24	9,82	17,59	4,04	25,28
22	13,17	15,09	4,87	23,69
20	17,15	12,88	5,62	22,43

TABLE V
RESULTS OF PERFORMED SIMULATIONS FOR 64-QAM MODULATION.

Without EQ			LMS	
E_b/N_0	EVM	MER	EVM	MER
40	1,01	36,26	1,01	36,22
38	1,26	34,35	1,1	35,58
36	1,6	32,23	1,2	34,69
34	2,03	30,11	1,43	33,18
32	2,56	28,18	1,81	31,12
30	3,22	26,13	1,99	30,31
28	4,19	23,88	2,32	29,05
26	6,08	20,62	2,73	27,62
24	8,32	17,91	3,16	26,37
22	11,03	15,44	4,14	23,99
20	34,43	5,54	4,95	22,43

The shape of individual graphs more or less corresponds to theoretical assumptions. With decreasing values of E_b/N_0 , MER and EVM worsen as well. Modulation formats without equalization have a much higher error rate in comparison to adaptive equalization (Table I to V). Fig. 5 represents comparisons of various constellation diagrams with and without equalization. Based on performed simulations it can be

said that adaptive equalization significantly improves measured parameters in comparison to situation without equalization, especially in case of lower values of E_b/N_0 . In case of higher signal to noise ratio (E_b/N_0), the algorithm might even have negative effects on communication.

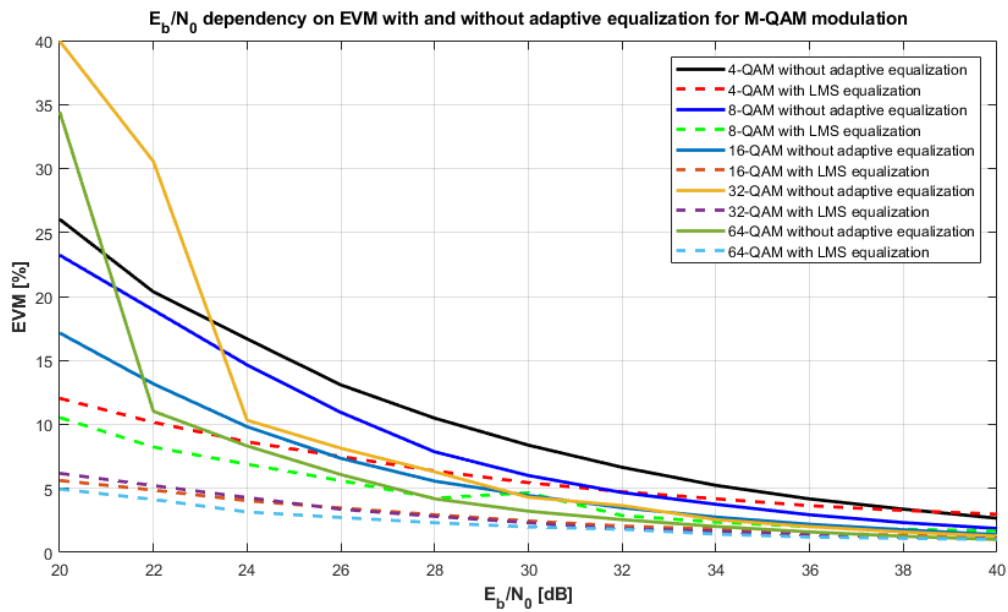


Fig. 4. Comparison of LMS algorithm efficiency for M-QAM based on EVM.

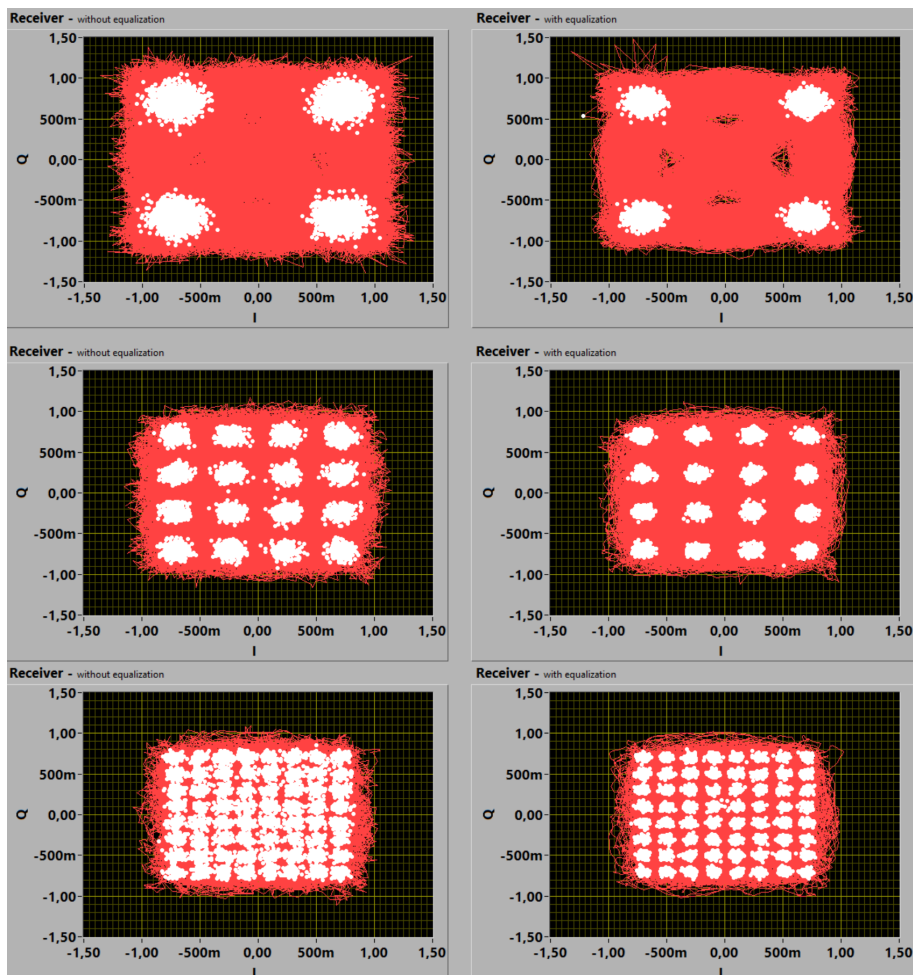


Fig. 5. Comparison of constellation diagrams before (left) and after applying of equalization (right).

By analysing Fig. 4, which is showing comparison of EVM, it can be seen that for E_b/N_0 values of 34 to 40 dB there is no difference between applied adaptive algorithm and measurements without equalization. In range of 30 to 34 dB, equalizer is slowly affecting communication, improving EVM. At lowest measured value of E_b/N_0 (equal to 20 dB), the equalizer effect is evident. In case of four state QAM modulation, the difference between situation with and without equalization is approximately 14 %. Difference between individual adaptive equalizers is about 1.4 %. In case of 8-QAM, the difference between equalized signal and signal without equalization approximately 12 %.

VI. CONCLUSION

This article introduced the possibilities of software defined channel equalizer based on LMS algorithm. The experimental results clearly show the effectiveness of the tested equalizer. On the basis of both MER and EVM, it can be concluded that all tested modulations have significantly improved. The proposed virtual instrument is usable for designing and testing of new or existing channel equalization methods without supplementary expensive SDR-based measurement systems. High modularity of whole system offers possible testing on various different modulation formats.

ACKNOWLEDGMENT

This article was supported by the Ministry of Education of the Czech Republic (Project No. SP2019/85 and SP2019/118). This work was supported by the European Regional Development Fund in the Research Centre of Advanced Mechatronic Systems project, project number CZ.02.1.01/0.0/0.0/16 019/0000867 within the Operational Programme Research, Development and Education. This work was supported by the European Regional Development Fund in A Research Platform focused on Industry 4.0 and Robotics in Ostrava project, CZ.02.1.01/0.0/0.0/17 049/0008425 within the Operational Programme Research, Development and Education. This article was also a part of project VI20172019071.

REFERENCES

- [1] R. Martinek, J. Vanus, M. Kelnar, P. Bilik, and J. Zidek, "Application of recursive least square algorithm to adaptive channel equalization," in *XXI IMEKO World Congress "Measurement in Research and Industry"*. IMEKO-International Measurement Federation Secretariat Budapest, Hungary, 2015, pp. 1–4.
- [2] P.-F. Cui, Y. Yu, Y. Liu, W.-J. Lu, and H.-B. Zhu, "Joint RLS and LMS adaptive equalization for indoor wireless communications under staircase environments," in *2015 International Conference on Wireless Communications & Signal Processing (WCSP)*. IEEE, 2015, pp. 1–5.
- [3] S. M. Shah, R. Samar, N. M. Khan, and M. A. Z. Raja, "Design of fractional-order variants of complex LMS and NLMS algorithms for adaptive channel equalization," *Nonlinear Dynamics*, vol. 88, no. 2, pp. 839–858, 2017.
- [4] Q. Liu, P. He, K. Yang, and S. Leng, "Inter-symbol interference analysis of synaptic channel in molecular communications," in *2014 IEEE International Conference on Communications (ICC)*. IEEE, 2014, pp. 4424–4429.
- [5] R. Martinek, L. Danys, and R. Jaros, "Visible Light Communication System Based on Software Defined Radio: Performance Study of Intelligent Transportation and Indoor Applications," *Electronics*, vol. 8, no. 4, p. 433, 2019.

- [6] M. Rahaim, A. Miravakili, S. Ray, V. Koomson, M. Hella, and T. Little, "Software defined visible light communication," in *Wireless Innovation Forum Conference on Communications Technologies and Software Defined Radio (WInnComm SDR)*, vol. 5, 2014.
- [7] Z. Ghassemlooy, L. N. Alves, S. Zvanovec, and M.-A. Khalighi, *Visible light communications: theory and applications*. CRC press, 2017.
- [8] S. Arnon, *Visible light communication*. Cambridge University Press, 2015.
- [9] P. H. Pathak, X. Feng, P. Hu, and P. Mohapatra, "Visible light communication, networking, and sensing: A survey, potential and challenges," *IEEE communications surveys & tutorials*, vol. 17, no. 4, pp. 2047–2077, 2015.
- [10] C.-H. Chang, C.-Y. Li, H.-H. Lu, C.-Y. Lin, J.-H. Chen, Z.-W. Wan, and C.-J. Cheng, "A 100-Gb/s multiple-input multiple-output visible laser light communication system," *Journal of Lightwave Technology*, vol. 32, no. 24, pp. 4121–4127, 2014.
- [11] K. Warmerdam, A. Pandharipande, and D. Caicedo, "Connectivity in IoT indoor lighting systems with visible light communications," in *2015 IEEE Online Conference on Green Communications (OnlineGreenComm)*. IEEE, 2015, pp. 47–52.
- [12] M. Ayyash, H. Elgala, A. Khreishah, V. Jungnickel, T. Little, S. Shao, M. Rahaim, D. Schulz, J. Hilt, and R. Freund, "Coexistence of WiFi and LiFi toward 5g: concepts, opportunities, and challenges," *IEEE Communications Magazine*, vol. 54, no. 2, pp. 64–71, 2016.
- [13] R. Martinek, J. Vanus, P. Bilik, M. Al-Wohaishi, J. Zidek, and H. Wen, "The implementation of equalization algorithms for real transmission channels," in *2016 IEEE International Instrumentation and Measurement Technology Conference Proceedings*. IEEE, 2016, pp. 1–6.
- [14] V. R. Krstić and M. L. Dukić, "Decision feedback blind equalizer with tap-leaky whitening for stable structure-criterion switching," *International Journal of Digital Multimedia Broadcasting*, vol. 2014, 2014.
- [15] E. Z. Tabasy, A. Shafik, K. Lee, S. Hoyos, and S. Palermo, "A 6 bit 10 GS/s TI-SAR ADC with low-overhead embedded FFE/DFE equalization for wireline receiver applications," *IEEE Journal of Solid-State Circuits*, vol. 49, no. 11, pp. 2560–2574, 2014.
- [16] J. M. Kizer, J. A. Slavick, R. R. Kennedy, and P. J. Meier, "Modal PAM2/4 Pipelined Programmable Receiver Having Feed Forward Equalizer (FFE) And Decision Feedback Equalizer (DFE) Optimized For Forward Error Correction (FEC) Bit Error Rate (BER) Performance," US Patent US20150085914A1, Mar., 2015.
- [17] H. A. Mahmoud and H. Arslan, "Error vector magnitude to SNR conversion for nondata-aided receivers," *IEEE Transactions on Wireless Communications*, vol. 8, no. 5, pp. 2694–2704, 2009.
- [18] J. D. Terry, "Method and apparatus for controlling out-of-band interference and error vector magnitude (EVM) using peak-to-average-power-ratio (PAPR) reduction with constraints," Patent, Aug., 2018.
- [19] R. Schmogrow, B. Nebendahl, M. Winter, A. Josten, D. Hillerkuss, S. Koenig, J. Meyer, M. Dreschmann, M. Huebner, and C. Koos, "Error vector magnitude as a performance measure for advanced modulation formats," *IEEE Photonics Technology Letters*, vol. 24, no. 1, pp. 61–63, 2011.